NOTE TO USERS

This reproduction is the best copy available.

MESOSPHERIC OZONE DENSITIES RETRIEVED FROM OSIRIS

OBSERVATIONS OF THE O$_2$ A-BAND DAYGLOW

PATRICK SHEESE

A DISSERTATION SUBMITTED TO THE FACULTY OF GRADUATE

STUDIES IN PARTIAL FULFILLMENT OF THE REQUIREMENTS

FOR THE DEGREE OF

DOCTOR OF PHILOSOPHY

GRADUATE PROGRAM IN EARTH AND SPACE SCIENCE

YORK UNIVERSITY

TORONTO, ONTARIO

SEPTEMBER 2009

Library and Archives
Canada

Published Heritage
Branch

395 Wellington Street
Ottawa ON K1A 0N4
Canada

Bibliothèque et
Archives Canada

Direction du
Patrimoine de l'édition

395, rue Wellington
Ottawa ON K1A 0N4
Canada

Canada

MESOSPHERIC OZONE DENSITIES RETRIEVED FROM OSIRIS

OBSERVATIONS OF THE O_2 A-BAND DAYGLOW

by **Patrick Sheese**

By virtue of submitting this document electronically, the author certifies that this is a true electronic equivalent of the copy of the dissertation approved by York University for the award of the degree. No alteration of the content has occurred and if there are any minor variations in formatting, they are as a result of the conversion to Adobe Acrobat format (or similar software application).

Examination Committee Members:

1. Ian McDade
2. Brian Solheim
3. Jack McConnell
4. Jim Whiteway
5. Jian-Guo Wang
6. Don Hastie
7. Kimberly Strong

Abstract

The Odin satellite was launched into orbit in early 2001 with one of its main objectives being to investigate ozone and ozone-related chemistry in the middle atmosphere. One of Odin's two instruments is the OSIRIS instrument, which scans the Earth's limb, observing Rayleigh-scattered sunlight with high vertical resolution and near-global coverage. An important feature that OSIRIS observes in the mesosphere is the emission of molecular oxygen A-band dayglow, the intensity of which is dependent on local ozone density.

A kinetic-photochemical model of the A-band dayglow has been developed in order to forward model the OSIRIS observations. The model takes into account the most current measurements of photochemical reaction coefficients, line strengths, and incident solar flux, and assumes an MSIS background atmosphere. The observations and forward model are used in an iterative optimal estimation technique to solve the inverse problem of retrieving ozone density profiles between altitudes of 70 – 95 km. The results form a climatological database of upper mesospheric ozone, which is compared with near-coincident ozone retrievals from the SABER instrument aboard the TIMED satellite.

A detailed error analysis is performed on the retrievals determining the sensitivity of the results to different sources of error, such as instrument noise, errors in the forward model parameters, and errors in the retrieval method itself. The retrievals are also examined to determine vertical, latitudinal, and seasonal variations. Variations are compared to previous and concurrent measurements from a number of other sources.

Acknowledgements

There are many people to whom I am very grateful,

- My supervisor, Ian McDade, for his guidance and support over the past few years.

- My committee members, Brian Solheim and Jack McConnell, for all their advice and assistance.

- Ted Llewellyn, for his encouragement and many helpful comments.

- All my friends at York—especially Brynle Barrett, Stephanie Conway, and Salvatore Paneduro—for all of their help and support.

- All of my family—especially my parents Ron and Susan, my sister Kate, my Grandmother Sheila, my Grandfather Bud, and my wife Val—for all their love and encouragement.

Contents

List of tables

List of figures

List of symbols

A	Averaging kernels of a retrieval.
A	Einstein coefficient.
A_p	Area of CCD pixel p.
a	Height argument in the Chapman function.
b	Forward model parameter.
$Bias_p$	Correction factor for DC bias of pixel p.
C	Relative quenching rate for Barth-type reactions.
c	Speed of light.
Ch	Chapman function.
D	Doppler profile.
$Dark_p$	Correction factor for assumed dark current generated by pixel p.
DN	Digital count units of the OS—datanumbers.
E_j''	Energy of the lower state of absorption transition at line j.
F	Forward model function.
F	Atmospheric solar flux.

f	Fraction of baffle scatter contribution to the Rayleigh-scattered contribution for an OSIRIS observation.
g	Atmospheric Bands' photochemical reaction coefficient.
$\mathbf{G}_y$	The gain matrix of for a given retrieval.
H	Scale height of an atmospheric species.
h	Planck's constant.
i	Index of vector or matrix row elements.
I_p	Generated CCD photocurrent.
I_p'	OS Level 0 signal for pixel p converted to radiance values and corrected for the dark current and DC bias.
I_p''	OS Level 0 signal for pixel p converted to radiance values and corrected for the dark current, DC bias, and internal scattering.
I_λ	Radiance incident on the CCD array.
J	Photolysis coefficient.
j	Index of emission/absorption line or matrix column elements.
$\mathbf{K}$	Weighting functions relating the state vector to the measurement vector.
k	Collisional quenching coefficient.
k_B	Boltzmann's constant.
$\mathbf{K}_n$	Weighting functions evaluated at the nth iteration.
L	Photochemical loss rate of a given atmospheric constituent.
lat	Geographic latitude.
lon	Geographic longitude.

M	A molecule, either O_2 or N_2.
m	Mass.
n	Iteration step.
nd	Total number density of assumed background atmosphere.
N_{off}	Number of times OS signal is binned off-chip.
N_{on}	Number of pixels in a column on the OS CCD that are binned on-chip.
OE	OS CCD optical efficiency.
P	Photochemical production rate of a given atmospheric constituent.
p	Pixel.
PB	Percentage of the assumed linear A-band background to be subtracted from the Level 1 radiances.
$PL(th, z)$	Path length through a 1 km atmospheric shell at altitude z at an observed tangent height th.
QE	OS CCD quantum efficiency.
R	Retrieval function.
R	Radius of Earth.
ROE	OS readout error.
R_p	OS CCD pixel response function.
S	Covariance matrix.
S_j	Line strength of the jth line.
S_p	OS Level 0 signal for pixel p.
S_T	Total band strength.

S_x Photochemical source function of atmospheric constituent x.

T Temperature.

t Time.

$T(th, z)$ Transmission function through an element along the OSIRIS line-of-sight at an altitude of z at an observed tangent height th.

T_{baffle} Assumed total atmospheric transmission of baffle scatter radiation within the A-band region.

t_e OS exposure time.

$T_f(th, z)$ Transmission function along the OSIRIS line-of-sight from an element at altitude z on the far side of the line-of-sight to the OSIRIS instrument at an observed tangent height th.

th OSIRIS observed tangent height.

$T_n(th, z)$ Transmission function along the OSIRIS line-of-sight from an element at altitude z on the near side of the line-of-sight to the OSIRIS instrument at an observed tangent height th.

T_S Standard temperature, 296 K.

UT   Universal time.

v Molecular vibrational level.

W Transmission function calculation weighting factor.

$\mathbf{x}$ State vector.

$\hat{\mathbf{x}}$ Optimal estimate of the state vector.

x Atmospheric constituent.

$\mathbf{x}_a$	*A priori* state vector.
$\mathbf{x}_n$	Retrieved state vector at the nth iteration.
$\mathbf{y}$	Measurement vector.
$\hat{\mathbf{y}}$	Forward model evaluated with the optimal estimate retrieval.
$\mathbf{y}_n$	Forward model evaluated at the nth iteration.
z	Altitude.
z_f^*	Altitude at the top of the atmosphere on the far-side of the OSIRIS line-of-sight.
z_n^*	Altitude at the top of the atmosphere on the near-side of the OSIRIS line-of-sight.
α	OS analog-to-digital conversion factor.
α_D	Doppler line width.
γ	Modelled fraction of total signal of a pixel column that is due to internal scattering.
$\boldsymbol{\varepsilon}$	Uncertainty in the measurement vector.
η	Volume emission rate.
λ	Wavelength.
$\boldsymbol{\mu}_e$	Mean value of an ensemble of retrievals.
ν	Frequency or wavenumber.
ν_0	Wavenumber at the center of an absorption line.
$\sigma(\nu)$	Absorption cross-section at wavenumber ν.
σ	Standard deviation.

σ_e Standard deviation of an ensemble of retrievals.

φ, ϕ Quantum yield.

χ Solar zenith angle.

Ω_p Solid angle observed by pixel p.

Chapter 1

Introduction

As has been noted by countless others, ozone is one of the most important trace constituents in the Earth's atmosphere. Not only does it play a dominant role in the energy budget of the lower to middle atmosphere, but it also absorbs highly energetic ultraviolet (UV) solar radiation, which would otherwise be extremely harmful to life on the surface. In fact, it is now widely believed that it was the formation of the ozone layer in Earth's early atmosphere that allowed for the evolution of life on the Earth's surface. It is therefore vital that atmospheric ozone and ozone-related chemistry be fully understood in all regions of the atmosphere, especially the mesosphere—the least well understood region of the atmosphere.

There are only a few satellite missions that currently measure ozone concentrations on a regular basis in the upper mesosphere, each with different retrieval methods and spatial and temporal coverage. Because of this, there is a lack of available ozone concentration datasets available for inter-comparison, and the motivation behind this

study is to create a new database of upper mesospheric ozone density profiles in order to further elucidate the physics and chemistry of ozone in the region.

1.1   Introduction to atmospheric ozone

Ozone was first detected in a laboratory, simply by its smell, due to its pungent odour, by the German chemist Christian Schönbein in 1839 (*e.g. Schönbein*, [1840]). However, it wasn't until 1863 that the suggestion was made that the chemical make-up of ozone was O_3 [*Rubin*, 2001]. Chemical analysis of atmospheric ozone started as early as 1853, and spectroscopic observations began to be made in the late 19th century by many scientists worldwide, among who were such notable figures as Chappuis, Hartley, and Huggins [*Brasseur and Solomon*, 2005].

Detection of ozone has come a long way since the first laboratory detections of ozone by Christian Schönbein in the mid-19th century that relied mainly on odour. From then until 1920, the only other ozone detection experiments, including attempts to measure atmospheric ozone, were conducted using metals and dyes that were found to oxidize in the presence of ozone. As one would expect, quantitative studies using these methods were incredibly difficult, to say the least [*Rubin*, 2001; *Dobson and Harrison*, 1926].

Earlier in 1879 it had been proposed by Alfred Cornu [*Cornu*, 1879] that the solar UV spectrum exhibited broadband absorption at wavelengths below roughly 330 nm, and it was William Hartley in 1880 [*Hartley*, 1880] who suggested that this absorption was due to ozone. This absorption band later came to be known as the Hartley band. It was in 1912 that the vertical thickness of ozone was first inferred from measurements of the

2

solar absorption coefficients in the Hartley band. The ozone vertical thickness is a measure of how thick a layer of ozone would be at standard temperature and pressure (STP). It was determined at the time that the vertical thickness of ozone in the atmosphere was roughly 5 mm [*Dobson*, 1968].

Fabry and Buisson in 1920 [*Fabry and Buisson*, 1921] took 14 days worth of UV spectrographic data in Marseilles for the express purpose of measuring atmospheric ozone. They determined a steady vertical thickness of 3 mm. Later, in 1925, Gordon Dobson began taking long-term daily measurements of the atmospheric ozone vertical thickness in Oxford using a specifically designed ozone spectrophotometer [*Dobson*, 1968]. Such instruments today are commonly referred to as Dobson spectrophotometers and measure total ozone column densities (the mass or number density of a column of air) in Dobson units (1 Dobson unit is equivalent to a vertical thickness of 10 μm). Ground-based spectroscopic measurements of atmospheric ozone column densities quickly became more common worldwide and are still commonplace today, such as Environment Canada's Arctic Stratospheric Ozone Observatory (ASTRO) and Experimental Studies Unit (ARQX), and the international Network for the Detection of Atmospheric Composition Change (NDACC). Other ground-based sites and aircraft- and satellite-based spectrometers observing in the nadir (observing downward towards the surface) are also frequently employed, such as the Total Ozone Mapping Spectrometer (TOMS) aboard Nimbus-7 and Meteor-3 [*Heath et al.*, 1975].

For some monitoring purposes total ozone column density is a sufficient measurement; however, for the majority of present day applications knowledge of the

ozone vertical distribution is essential. A typical vertical ozone profile is shown in Fig. 1.1. Some of the first successful attempts to measure vertical ozone concentration profiles used a method whereby a spectrophotometer was attached to an ascending balloon. This type of radiosonde is now commonly referred to as an ozonesonde. The concentration of ozone at a specific altitude can be determined by differentiating the curve of partial column ozone versus height. The difficulty with this method however is that local ozone concentrations are still difficult to retrieve at lower altitudes where total column densities vary little with height. This method was later adapted for rocket measurements, and also for horizontal lines-of-sight (in the Earth's limb) and for observing various other spectral bands where ozone is now known to absorb or emit radiation. Direct *in situ* methods of measuring ozone using ozonesondes began in the early 1960's via *in situ* chemiluminescent [*Regener*, 1960] and electrochemical [*Brewer and Milford*, 1960] detection techniques.

Since then, a wide variety of new techniques to monitor atmospheric ozone have been developed. One of the most recent innovations involves measurement of ozone absorption signatures in the spectrum of Rayleigh-scattered sunlight as observed in Earth's limb from a satellite platform. This technique is exploited by the Canadian Optical Spectrograph and Infra-Red Imaging System (OSIRIS) on board the Odin Satellite [*Warshaw et al.*, 1998], which was launched in February 2001 and is still currently in operation. The main objective of OSIRIS is to measure stratospheric ozone profiles at altitudes of 20 – 50 km, and the results have been very impressive (*e.g. von Savigny et al.* [2003], *Petelina et al.* [2004], *Haley et al.* [2004]). This dissertation reports

4
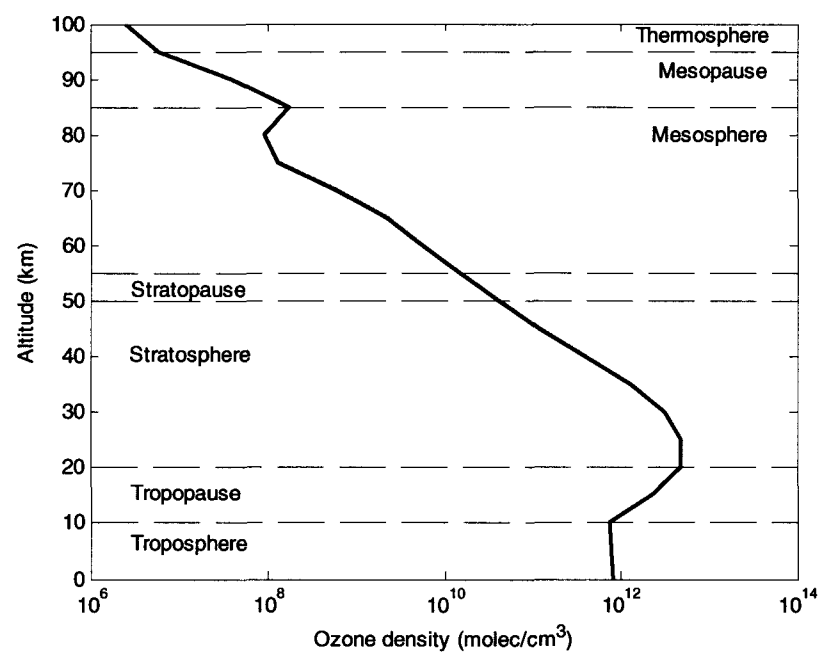
Figure 1.1: Typical vertical distribution of ozone densities in varying atmospheric layers (layer boundaries are approximate). The ozone data was obtained from *Brasseur and Solomon* [2005].

on the development of a technique for exploiting the OSIRIS observations to determine ozone density profiles in the much less well understood upper mesosphere, between altitudes of 70 and 95 km.

1.2 Structure of thesis

Chapter 2 discusses the necessary background information. The composition, dynamics, and energetics of the mesosphere are discussed, along with the relevant ozone chemistry and mesospheric ozone retrieval methods. The Odin mission and the OSIRIS instrument are also described in detail.

Chapter 3 provides details on the relationship between a specific daytime airglow

5

emission feature, namely the molecular oxygen A-band dayglow at 762 nm, and the local ozone densities. The developed kinetic-photochemical model relating the A-band emissions to the local ozone densities is described, as well as the method used to forward model OSIRIS observations given the results of the kinetic-photochemical model.

The details of the ozone density profile retrieval process, an iterative Newtonian Optimal Estimation technique [*Rodgers*, 2008], and its implementation are discussed in Chapter 4. A discussion of the error analysis of the retrieval is also presented in this chapter.

Retrieved daytime mesospheric ozone density profiles are presented to highlight vertical, longitudinal, and seasonal variations in Chapter 5, along with a detailed discussion of the results.

Chapter 6 discusses the results of comparison studies between the OSIRIS A-band results and ozone densities determined from mid-IR thermal emission observations made with the SABER instrument aboard TIMED [*Mlynczak*, 1997]. Comparisons with observations made with the 1.27 μm spectrometer on the Solar Mesosphere Explorer (SME) [*Thomas et al.*, 1983] are also presented.

Chapter 7 presents conclusions drawn from this study and provides suggestions for areas of improvement and future work.

Chapter 2

Background

2.1 Physics and chemistry of the mesosphere

The mesosphere is the atmospheric layer located between altitudes of approximately 50 and 100 km. Temperatures in the mesosphere typically decrease with increasing altitude up to the mesopause, located between 80 and 100 km depending on season and latitude, where they reach the lowest temperatures in Earth's atmosphere, as illustrated in Fig. 2.1. The region of altitudes near the mesopause is also commonly referred to as the mesosphere-lower thermosphere (MLT), which is the region to be discussed in this section. More comprehensive studies of the physics and chemistry of this region can be found in *Smith* [2004], *Andrews et al.* [1987], and *Brasseur and Solomon* [2005].
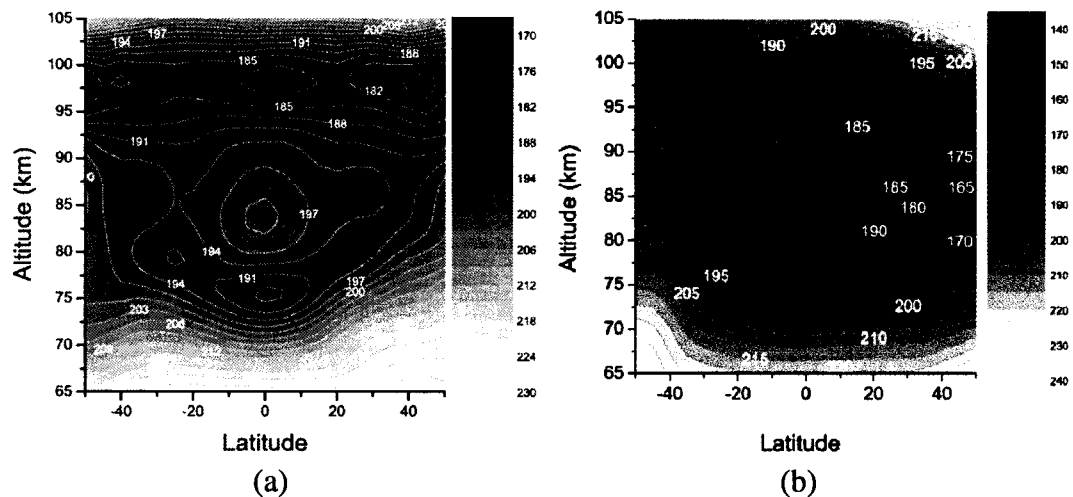
Figure 2.1: Retrieved SABER temperature distributions, in Kelvin, zonally-averaged, highlighting the vertical, latitudinal and seasonal variability of the mesopause boundaries. (a) Day 80 and (b) day 170 of 2003, from *Xu et al.* [2007].

2.1.1 Composition

The composition of the MLT, like the stratosphere and troposphere below, consists mainly of N_2 and O_2 with respective mixing ratios of ~78% and ~21%, which are generally independent of altitude (the constituents are "well mixed"). The majority of the larger molecules that are common in the lower atmosphere (*e.g.* N_2O, hydrocarbons, etc.) are typically not found in the MLT, with the exception of CO_2, H_2O, and, to a lesser extent, CH_4. However, the concentrations of these molecules all decrease rapidly with altitude, as illustrated in Fig. 2.2.

The third most abundant species in the MLT is atomic oxygen, which is produced in the thermosphere mainly through the photolysis of O_2 by ultraviolet (UV) light. Since three-body reactions such as,

8

$$O + O_2 + M \rightarrow O_3 + M \qquad (2.1)$$

and

$$O + O + M \rightarrow O_2 + M \qquad (2.2)$$

are less likely in the thermosphere due to the decrease in total density with altitude, the lifetime of O is much longer in this region. Atomic oxygen is transported downward from the thermosphere into the MLT through diffusion and/or downward vertical wind. As can be seen in Fig. 2.2, atomic oxygen mixing ratios tend to increase with height in the MLT.
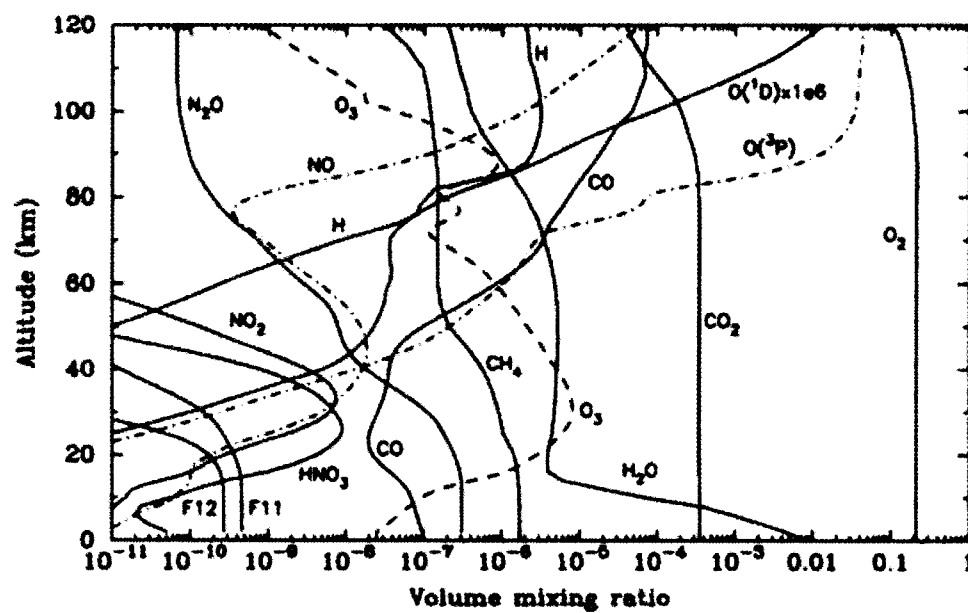
Figure 2.2: Typical daytime volume mixing ratio profiles of chemical species in the atmosphere at mid-latitudes, from *Lopez-Puertas and Taylor* [2001].

Since atomic oxygen is increasing in the MLT, Reaction 2.1 leads to the secondary ozone peak, typically located between altitudes of 85 and 90 km [*Sica*, 1993]. The leading loss process near the secondary ozone maximum is due to the presence of H in the catalytic reaction,

$$OH + O \rightarrow H + O_2 \tag{2.3}$$

$$H + O_3 \rightarrow OH + O_2, \tag{2.4}$$

which corresponds to a net reaction of,

$$O + O_3 \rightarrow 2O_2. \tag{2.5}$$

However, photolysis in the Hartley band also leads to the destruction of ozone, at wavelengths less than 310 nm[1],

$$O_3 + h\nu \; (\lambda < 310 \text{ nm}) \rightarrow O_2(a^1\Delta) + O(^1D). \tag{2.6}$$
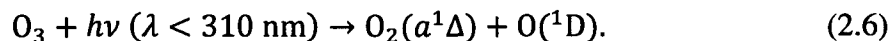
There are also many excited species found in the MLT, such as $O(^1D)$, $O_2(a^1\Delta)$, $O_2(b^1\Sigma)$, $N(^2D)$, etc. that are integral to the chemistry of the region.

2.1.2 Dynamics

The dynamics and energetics of the MLT highly influence the vertical and seasonal variations of ozone. An understanding of both is required in order to interpret retrieval results.

It is now widely accepted [*Lindzen*, 1981; *Holton*, 1982; *Nappo*, 2002] that the mean circulation of the MLT region is significantly influenced by deposited energy and momentum that has been transported upwards from the lower atmosphere by both tides and gravity waves. The subject of gravity waves is complex, and a full quantitative review of their physical properties and atmospheric effects is beyond the scope of this dissertation. A brief qualitative synopsis of such a review, *Nappo* [2002], is given here.

Gravity waves are caused in the lower atmosphere due to a wide variety of

---

[1] Ozone photolysis also occurs at wavelengths up to ~330 nm, producing $O(^3P)$. See Reactions 2.18 and 2.19.

atmospheric disturbances. Sources include ground terrain, storms, volcanic eruptions, etc. When a parcel of air that is in equilibrium with its surroundings is adiabatically displaced, assuming the parcel and its surroundings do not mix, the fluid buoyancy force will act upon the parcel to bring it back to equilibrium. When the parcel is displaced and then released, assuming the displacement is not entirely horizontal, the resulting motion is described by simple harmonic oscillation—a gravity wave. Energy and momentum from the source of the disturbance can be transported away, upwards or downwards, by gravity waves, and the deposited energy and momentum reflect those of the original disturbance.

Gravity wave amplitudes grow with height until they are convectively unstable, causing the wave to break. This process regularly transports momentum and energy from the lower atmosphere up into the mesosphere and above. A significant proportion of these waves are believed to originate in the stratosphere due to disturbances acting against the mean flow; and, in the MLT, deposited momentum from gravity waves is great enough as to reverse the direction of the mean zonal wind. Therefore, near summer solstice, when stratospheric zonal winds are typically directed westward, internal gravity waves tend to force the upper atmosphere mean zonal winds eastwards. Conversely, around winter solstice when the mean zonal winds in the stratosphere are directed eastward, westward zonal winds are typically observed in the upper atmosphere, as can be seen in Fig. 2.3. Due to the Coriolis force, the acceleration caused by the deposited momentum in the zonal direction results in an additional meridional acceleration. The atmospheric dynamics described above set up a meridional flow directed from the summer pole to the

11
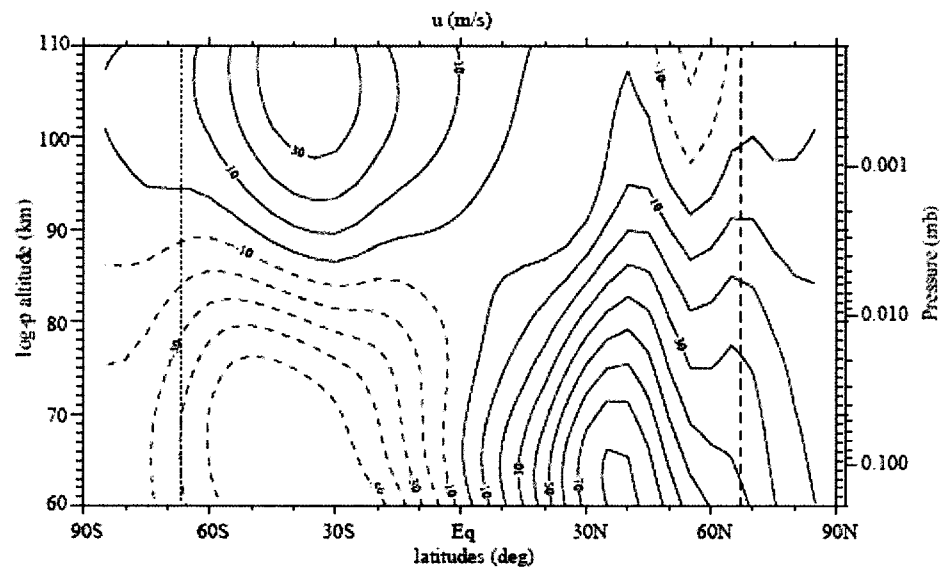
Figure 2.3: Zonal wind speed component in m/s (positive values indicate a westward direction) for January as determined by the SOCRATES 2-D circulation model [*Gruzdev and Brasseur*, 2005], adapted from *Smith* [2004].
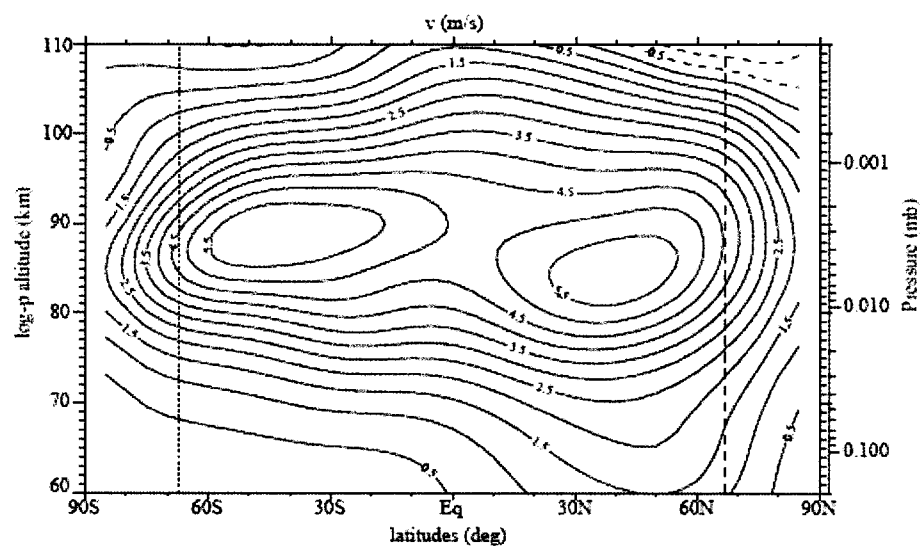
Figure 2.4: Meridional wind speed component in m/s (positive values indicate a northward direction) for January as determined by the SOCRATES 2-D circulation model, adapted from *Smith* [2004].

winter pole, seen in Fig. 2.4. A requirement for mass continuity during this outflow of air

in the summer hemisphere leads to rising air, which leads to adiabatic cooling. The opposite is true in the winter hemisphere, where the inflow of air results in sinking air and adiabatic warming. Fig. 2.5 shows typical vertical winds in the middle atmosphere near winter solstice. This process of dynamic heating in the mesosphere is the main driver of the region's seasonal thermal variations, mainly cold summers and warm winters, which is discussed further in the following section.
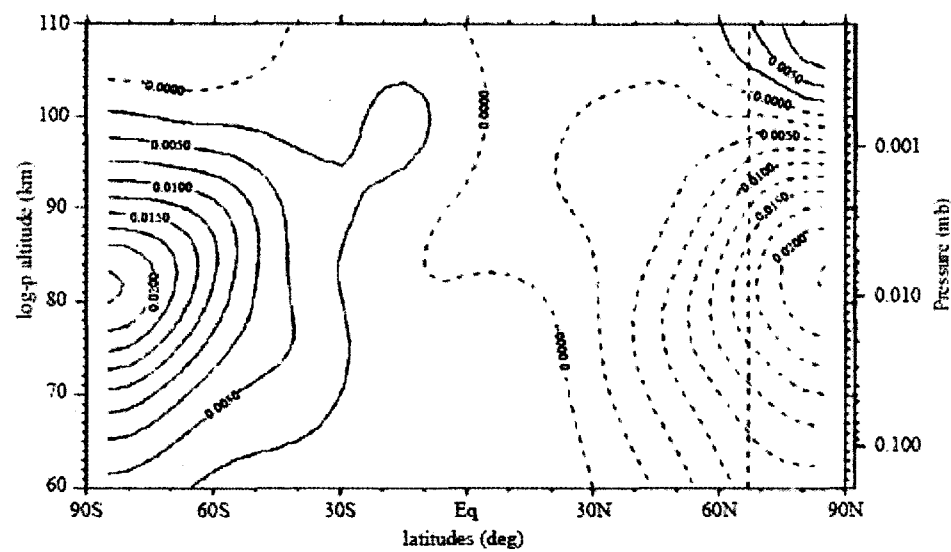
Figure 2.5: Vertical wind speed component in m/s (positive values indicate an upward direction) for January as determined by the SOCRATES 2-D circulation model, adapted from *Smith* [2004].

This process also has an effect on the seasonal variations of trace species in the MLT. Mixing ratios of trace species that tend to decrease with altitude in the MLT, such as O_3, H_2O, and CO_2, are typically larger in the summer MLT than in the winter. Mixing ratios that tend to increase with altitude in the MLT, mainly O and H, are typically larger in the winter MLT than in the summer.

13

Tides also play a significant role in the dynamics of the MLT region. An atmospheric tide is any wave structure that is on a global scale with a period that is an integral fraction of 24 hours. Tides are generally sinusoidal in longitude and/or local time and are characterized by a wavenumber, which corresponds to the number of wave periods that span the Earth. There are two classifications of tides: migrating tides are westward-propagating waves and are the direct consequence of solar heating, and non-migrating tides, which can be stationary or westward- or eastward-propagating, are primarily due to meteorological effects in the troposphere, such as latent heat released from water vapour during precipitation.

In the mesosphere tide amplitudes increase with height due to decreasing density, and the most dominant tide in the atmosphere is the diurnal tide, which can have horizontal wind amplitudes upwards of 50 m/s and temperature amplitudes of 20 K. As well, vertical transport is affected by the vertical velocity amplitudes of tides, especially the larger velocities associated with the diurnal tide. The effects of the diurnal tide on vertical transport are strongest near the equator throughout the mesosphere, and are present at all latitudes above 80 km. Calculated vertical wind perturbations due to the diurnal tide in April can be seen in Fig. 2.6. Many studies, such as *Burrage et al.* [1995] and *McLandress* [2002], have shown that tidal amplitudes are greatest in the equatorial regions, decreasing with latitude, and tend to peak shortly after equinox (April and October), and are at their lowest around solstice. Tidal amplitudes also tend to be at their greatest at the spring (April) peak. Seasonal variations of the diurnal tide amplitude as observed by the High Resolution Doppler Imager (HRDI) instrument aboard the Upper

14

Atmosphere Research Satellite (UARS) are shown in Fig. 2.7.
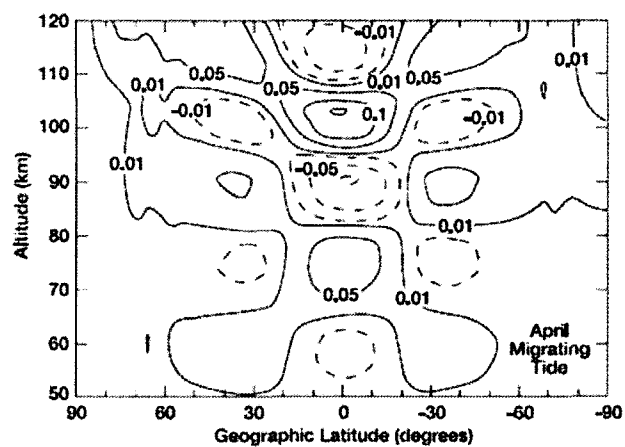
Figure 2.6: Calculated variations of vertical wind perturbations in m/s at 12 LT due to the diurnal tide, from *Brasseur and Solomon* [2005].
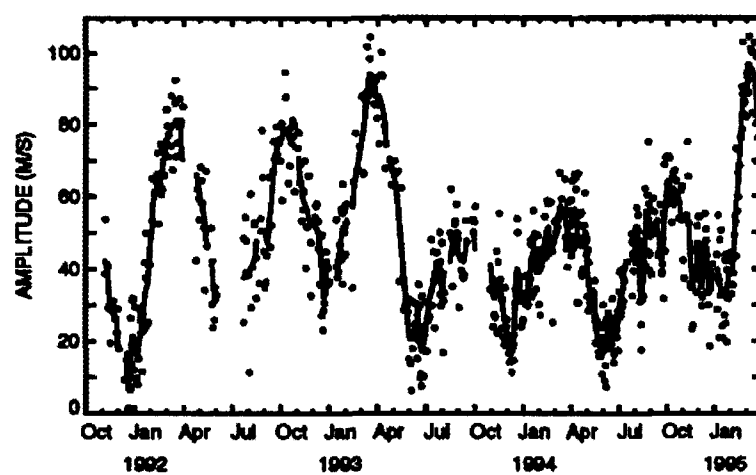
Figure 2.7: Seasonal variations of the meridional wind amplitudes of the solar diurnal tide observed by HRDI at an altitude of 95 km and at a latitude of 20°, adapted from *Burrage et al.* [1995].

2.1.3 Energetics

There are a number of sources of energy exchange in the MLT that lead to the heating and cooling of the region. As mentioned above, dynamical heating plays a major role in

15

the thermal budget of the MLT and is the main driver of the cool mesospheric summers and warm winters. However, chemical heating can play a significant role as well. A detailed discussion of the energetics of the upper atmosphere is given by *Mlynczak and Solomon* [1993], and is summarized below.

The major source of the input of energy into the MLT is the absorption of solar radiation by molecular oxygen and ozone (although it should be noted that due to the efficient absorption of UV radiation by O_2 in the thermosphere, as well as the low densities of O_3 in the MLT, direct solar heating is at a minimum in this region). For instance, when a photon at 265 nm photodissociates an O_3 molecule,

$$O_3 + h\nu \ (\lambda = 265 \text{ nm}) \rightarrow O_2(a^1\Delta) + O(^1D), \tag{2.7}$$
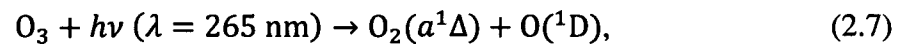
24% of the energy goes into dissociation, 21% goes into the excitation of $O_2(a^1\Delta)$, 42% into the excitation of $O(^1D)$, and 13% is converted to heat. Chemical energy can also be stored in the products of photodissociation to be released as heat later in exothermic chemical reactions and in quenching of excited species. Since these end products, such as O and H, can have long lifetimes in the MLT, it is not uncommon for this chemical energy to be released in a completely different geographic location, days after the initial absorption. Some common exothermic reactions that take place in the MLT are,

$$O + O + M \rightarrow O_2 + M \tag{2.8}$$

$$O + O_2 + M \rightarrow O_3 + M \tag{2.9}$$

$$H + O_3 \rightarrow OH + O_2. \tag{2.10}$$
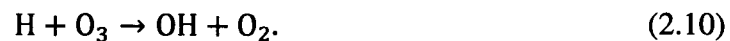
When the photolysis of a molecule leads to products in excited states, *e.g.* Equation 2.7, there are three pathways the absorbed energy can take; it can be released as heat

during quenching of the excited product, *e.g.*,

$$O_2(a^1\Delta) + O_2 \rightarrow O_2 + O_2 + \text{heat}, \qquad (2.11)$$
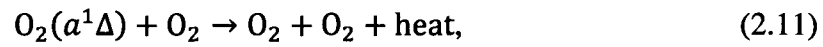
it can be transferred to a different molecule, *e.g.*,

$$O(^1D) + O_2 \rightarrow O(^3P) + O_2(b^1\Sigma), \qquad (2.12)$$
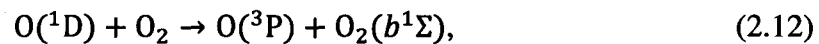
or, as in the case of Reaction 2.7, it can be radiated away, *e.g.*,

$$O_2(a^1\Delta) \rightarrow O_2 + h\nu \; (\lambda = 1.27 \; \mu m) \qquad (2.13)$$

$$O_2(b^1\Sigma) \rightarrow O_2 + h\nu \; (\lambda = 762 \; nm). \qquad (2.14)$$
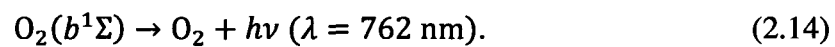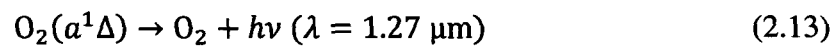
This last type of loss occurs when the excited species transitions to either a lower electronic state or a lower vibrational level, or a combination of the two. A wide range of excited atmospheric species radiate in a wide range of bands.

Another contributor to the energy budget of the MLT is radiative cooling due to vibrational de-excitation, or relaxation, of CO_2 [*López-Puertas et al.*, 1998; *Castle et al.*, 2006]. When CO_2 is excited into various vibrational states through collisional excitation, it is relaxed through spontaneous emission in the infrared, *e.g.* 4.3 and 15 μm. This process acts to remove thermal energy from the MLT. Figs. 2.8 – 2.10 show model results of the different processes that contribute to the heating of the MLT.

17
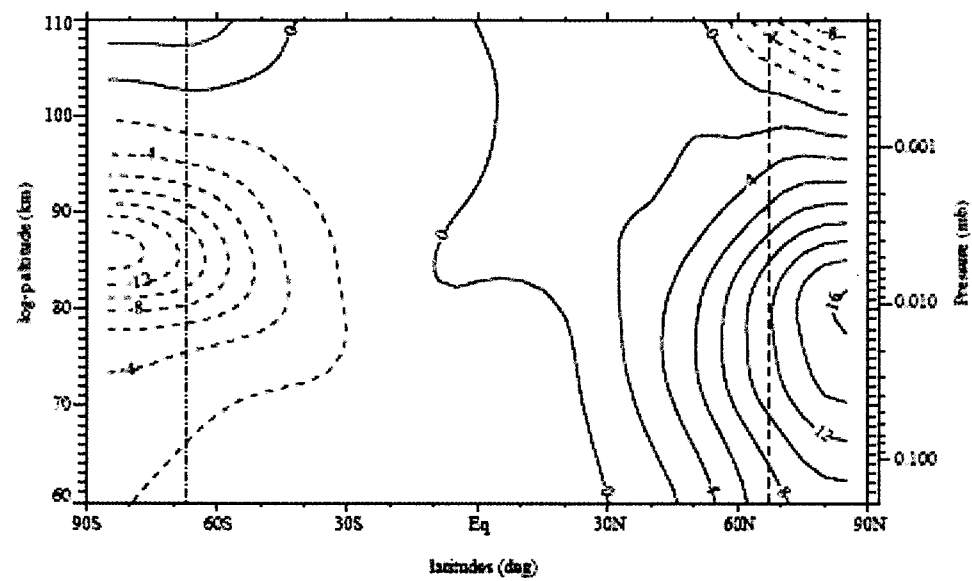
Figure 2.8: Dynamical heating contribution to the thermal budget in the MLT in K/day (negative values indicate cooling) for January, as calculated by the SOCRATES 2-D circulation model, adapted from *Smith et al.* [2004].
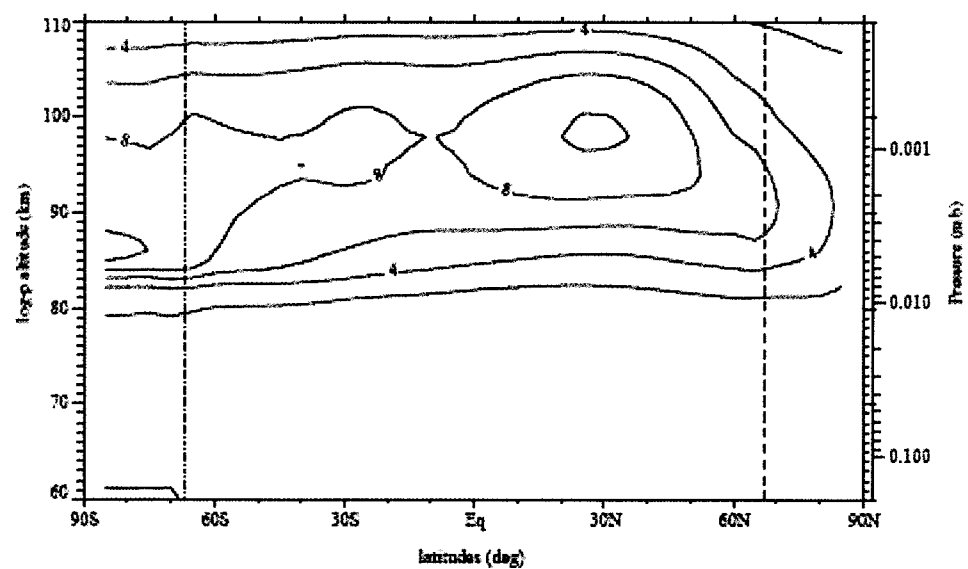
Figure 2.9: Chemical heating contribution to the thermal budget in the MLT in K/day for January, as calculated by the SOCRATES 2-D circulation model, adapted from *Smith et al.* [2004].

18
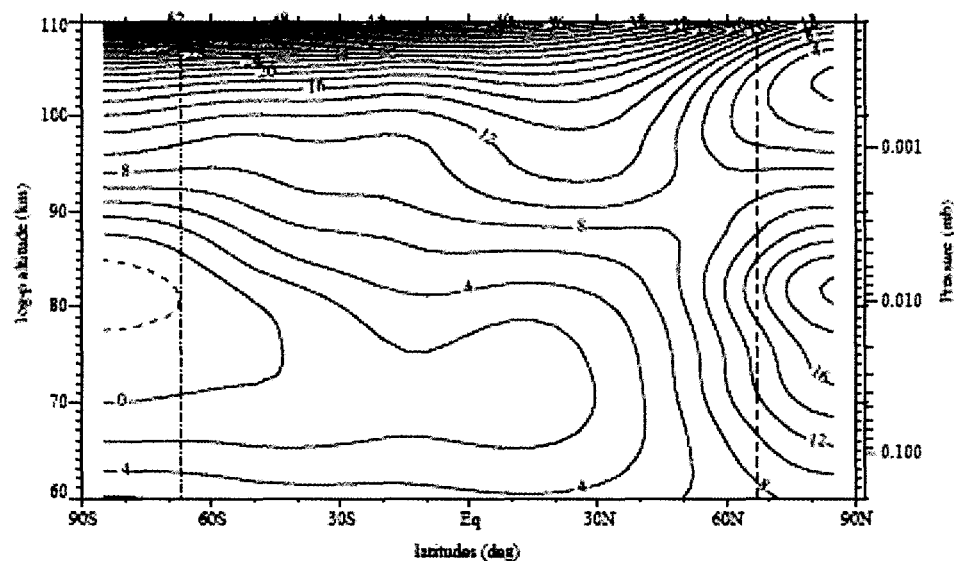
Figure 2.10: Radiative cooling contribution to the thermal budget in the MLT in K/day for January, as calculated by the SOCRATES 2-D circulation model, adapted from *Smith et al.* [2004].

2.2 Mesospheric ozone

2.2.1 Ozone chemistry

The basic model for the production and loss of atmospheric ozone was originally outlined by *Chapman* [1930]. The main mechanism leading to the formation of ozone in the middle atmosphere begins with the photodissociation of molecular oxygen by UV light,

$$O_2 + h\nu \ (\lambda < 242 \text{ nm}) \rightarrow O + O. \tag{2.15}$$
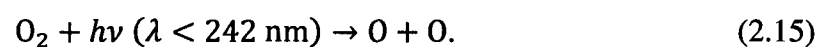
The atomic oxygen atoms produced in Reaction 2.15 can either both be in the ground $O(^3P)$ state or one can be in the ground state and the other in the excited $O(^1D)$ state, depending on the wavelength of the absorbed photon. The atomic oxygen produced can then either self-recombine,

19

$$O + O + M \rightarrow O_2 + M, \tag{2.16}$$

or combine with molecular oxygen to produce ozone,

$$O + O_2 + M \rightarrow O_3 + M, \tag{2.17}$$

where M is a third body, required to conserve energy and momentum, either N_2 or O_2. Chapman also outlined two mechanisms that lead to the net loss of ozone. First, is the photodissociation of ozone, which can lead to either ground state or electronically excited oxygen species depending on the wavelength of the incident radiation,

$$O_3 + h\nu \ (\lambda > 310 \text{ nm}) \rightarrow O_2(X^3\Sigma) + O(^3P) \tag{2.18}$$

$$O_3 + h\nu \ (\lambda \leq 310 \text{ nm}) \rightarrow O_2(a^1\Delta) + O(^1D). \tag{2.19}$$
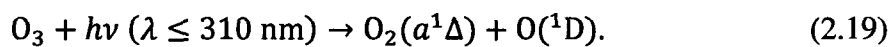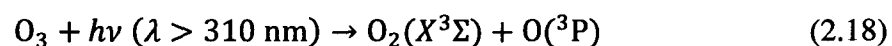
Second, is the recombination of ozone with atomic oxygen, producing two oxygen molecules,

$$O_3 + O \rightarrow 2O_2. \tag{2.20}$$

However, the chemical reaction coefficient for Reaction 2.20 originally proposed by Chapman was much greater than subsequently measured values, which resulted in lower than expected observed odd oxygen densities. It was *Bates and Nicolet* [1950] who first showed that there must be catalytic mechanisms possibly involving hydrogen species compensating for this reaction, *e.g.*,

$$OH + O \rightarrow H + O_2 \tag{2.21}$$

$$H + O_3 \rightarrow OH + O_2 \tag{2.22}$$

$$\text{NET } O_3 + O \rightarrow 2O_2. \tag{2.23}$$
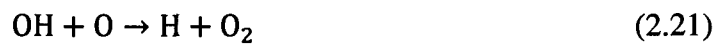
This process, along with other catalytic reactions involving atomic hydrogen, plays an important role in the MLT where atomic hydrogen densities are at their greatest. Other

20

such catalytic mechanisms were later discovered involving species of NO_x, chlorine, and bromine; although, these heavier species play a much more significant role in the chemistry of the stratosphere than in that of the mesosphere.

2.2.2 Mesospheric retrievals

The *in situ* methods for measuring atmospheric ozone described in Chapter 1 are feasible for tropospheric and stratospheric studies; however, *in situ* mesospheric retrievals are much more difficult and/or impractical. This is mostly due to its location of 50 – 90 km above the surface. Aircraft generally cannot fly at altitudes greater than ~13 km, the upper limit of balloons is typically around 35 km, and the lower limit of satellites in low-Earth orbit is roughly 200 km. Rocket-borne instruments can provide *in situ* measurements, and were used extensively in the 1960's – 1980's. However, due to their low spatial and temporal coverage, the use of rockets has since become much less desirable in light of advancements in satellite-based measuring techniques.

Any method of retrieving atmospheric parameters from a satellite platform will undoubtedly require an indirect measurement, typically a measurement of radiation, the intensity of which is dependent on the parameter of interest. An indirect method already mentioned is to measure the radiation that is transmitted through the atmosphere in an absorption band in order to determine the concentration of the absorbing species. Satellite-based instruments perform these types of retrievals while directly observing solar radiation transmitted through the atmosphere, a method known as solar occultation, and also while observing stellar radiation (stellar occultation). Solar occultation

retrievals of ozone have been performed by a number of satellite-based instruments, such as the Stratospheric Aerosol and Gas Experiments (SAGE) [*McCormick and Zawodny*, 1989] and the ACE-FTS (Atmospheric Chemistry Experiment Fourier Transform Spectrometer) aboard the Canadian SCISAT satellite [*Walker et al.*, 2005]. SAGE measured extinction profiles at a variety of wavelengths in the visible and near-infrared region, whereas the ACE-FTS measures in the mid-infrared region. The Global Ozone Monitoring by Occultation of Stars (GOMOS) instrument aboard the Envisat satellite [*Kyrola et al.*, 2004] exploits stellar occultation measurements in the UV to near-IR in order to retrieve density profiles of ozone and other key atmospheric constituents.

Solar occultation instruments, however, are limited to taking measurements only twice per orbit, and stellar occultation instruments are limited by number of stars available. Another similar technique is to observe scattered sunlight in the Earth's limb. One of the first experiments to make use of this method was performed by *Cunnold et al.* [1973], using an aircraft-based instrument that measured aerosols in the stratosphere. Satellite instruments that have made use of this technique to retrieve ozone concentrations include the Solar Mesosphere Explorer (SME) [*Rusch et al.*, 1984], and OSIRIS [*Llewellyn et al.*, 2004].

Another indirect method of sounding the atmosphere is to observe atmospheric emission of radiation from excited atmospheric species. Common ozone-related emissions measured by satellite-based instruments are the O_3 9.6 µm band emission (*e.g.*, LIMS (Limb Infrared Monitor of the Stratosphere) aboard Nimbus 7 [*Remsberg et al.*, 1984], SABER aboard TIMED [*Mlynczak*, 1997]), the O_2 Infrared Atmospheric Bands

22

(*e.g.* SME [*Thomas et al.*, 1983], SABER aboard TIMED [*Mlynczak*, 1997], OSIRIS aboard Odin [*Degenstein et al.*, 2005]) and the O_2 Atmospheric Bands, *e.g.* the High Resolution Doppler Imager instrument (HRDI) aboard the Upper Atmospheric Research Satellite (UARS) [*Marsh et al.*, 2002], and the ACE-MAESTRO (Measurement of Aerosol Extinction in the Stratosphere and Troposphere Retrieved by Occultation) instrument [*McElroy et al.*, 2007].

The inherent disadvantage of indirectly measuring ozone via atmospheric emissions is that the atmospheric processes that lead to the emission can be rather complex. Retrievals require the use of inverse and/or forward models, which themselves require precise knowledge of the state of the atmosphere and many key photolysis and reaction coefficients, and/or the use of complex non - local thermodynamic equilibrium (non-LTE) band models.

2.3 The OSIRIS instrument aboard Odin

2.3.1 The Odin mission

The Odin satellite was developed in a collaboration between the space agencies of Sweden, Canada, Finland, and France, and was launched into orbit on February 20th, 2001 with a Russian Start-1 InterContinental Ballistic Missile (ICBM) from Svobodny, Siberia. A detailed description of the Odin satellite and its instruments are presented in *Warshaw et al.* [1998], *Murtagh et al.* [2002], and *Llewellyn et al.* [2004]. Although the planned duration of the mission was originally only two years, Odin continues to be operational, and in early 2007 the European Space Agency (ESA) began its support of

Odin as one of its Third Party Missions. On board the Odin satellite are two instruments, the Sub-Millimetre Radiometer (SMR) and the Optical Spectrograph and Infra-Red Imaging System (OSIRIS). The objectives of the Odin mission were originally two-fold, 50% of the mission was to be dedicated to Astronomy and 50% was to be dedicated to Aeronomy. The SMR was used in both Astronomy and Aeronomy modes, whereas OSIRIS was used solely in Aeronomy mode. However, once ESA began its support, the Odin observing schedule was modified to focus solely on Aeronomy. The original and current Aeronomy mission objectives are to further the understanding of processes in the stratosphere and mesosphere, especially in relation to ozone-related chemistry, and to elucidate the mechanisms that couple these two regions.

The satellite is classified as a small satellite, with a mass of 235 kg and measuring 1.1 m in height and 1.8 m in length and width when its solar panel arrays are deployed, as illustrated in Fig. 2.11.
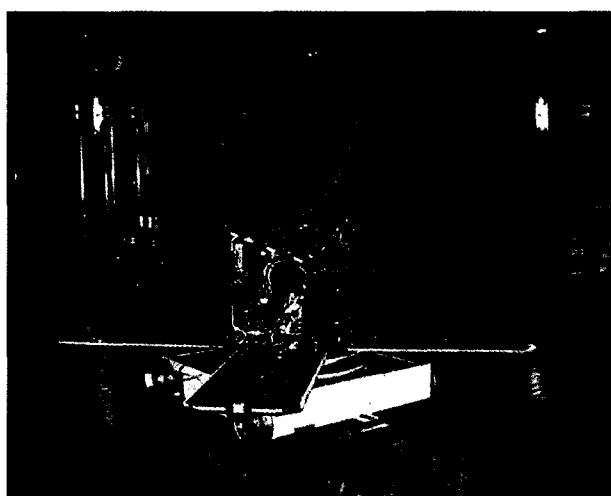
Figure 2.11: Photograph of the Odin satellite, pre-launch, with solar panel array deployed, from aerospace-technology.com.

Odin was launched into a near-circular, near-sun-synchronous orbit at an altitude of ~620 km with an ascending node at 18:00 LT and a descending node at 06:00 LT. Fig. 2.12 illustrates the nominal change of local time with observed latitude, where individual circles of latitude are always observed at the same local time. As Odin ascends (Northward) between latitudes of 60°S and 60°N the tangent point local time remains essentially constant at 18:00. As Odin observes higher latitudes in the northern hemisphere observed local times sweep through local noon, and in the southern hemisphere at high latitudes Odin sweeps through local midnight. With an inclination of 97.8° global coverage is only slightly limited to latitudes nominally between 82.2°N and 82.2°S given the standard in-orbit forward view of OSIRIS and the SMR; however both instruments aboard the satellite are able to be directed to look ±32° out of the orbital plane, increasing their nominal latitudinal coverage. Odin has a period of 96 minutes, sweeping 24° of longitude per orbit, and had a nominal precession period of 365 days.
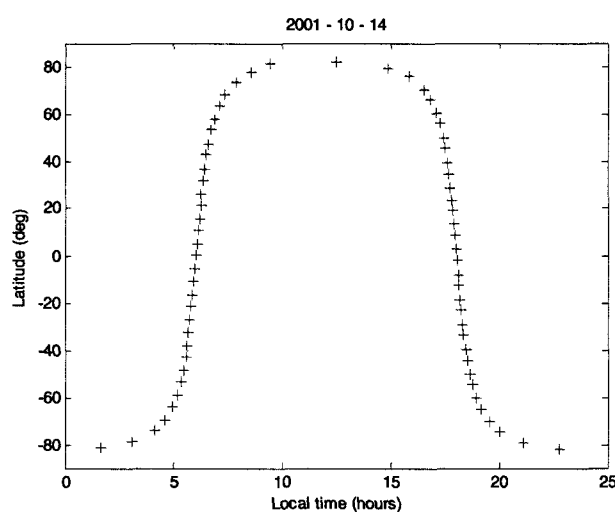
Figure 2.12: Local time observed by Odin as a function of latitude. Orbital motion in plot is from right to left.

25

2.3.2 The OSIRIS instrument

The Canadian OSIRIS instrument is comprised of two different instruments. One is an optical spectrograph (OS) and the other is an infrared (IR) imager, both of which are limb-viewing instruments with pointing directions bore-sighted with each other and with that of the SMR in order to provide simultaneous co-located measurements. Odin nods up and down in orbit so that the on-board instruments do not require moving parts in order to scan the Earth's limb. OSIRIS scans between tangent heights of approximately 10 to 110 km. Since the ozone retrievals in this study are made with the OS observations, more of the discussion will be devoted to the details of the OS and only a brief synopsis of the IR imager follows.

The IR imager consists of three InGaAs detectors at 1.263 μm, 1.273 μm, and 1.520 μm, each with a 10 nm full-width half-maximum, a horizontal field-of-view of 2 km, and a vertical field-of-view of 90 km. The detectors were chosen to be oriented vertically in order to be able to produce tomographic inversions. The 1.263 and 1.273 μm channels detect $O_2(a^1\Delta)$ airglow emission. The 1.520 μm channel was chosen in a band without any significant absorption features primarily to measure the background scattered sunlight; however, there are some nighttime OH emissions within the band that can be exploited in order to recover O and H densities.

The OS is a diffraction grating spectrograph that measures Rayleigh-scattered sunlight at wavelengths between 275 and 810 nm with a spectral resolution of ~1 nm. Typical OS spectra at different tangent heights are shown in Fig. 2.13, and Table 2.1 lists a few of the relevant absorption and emission features observed in the OS spectral

window.
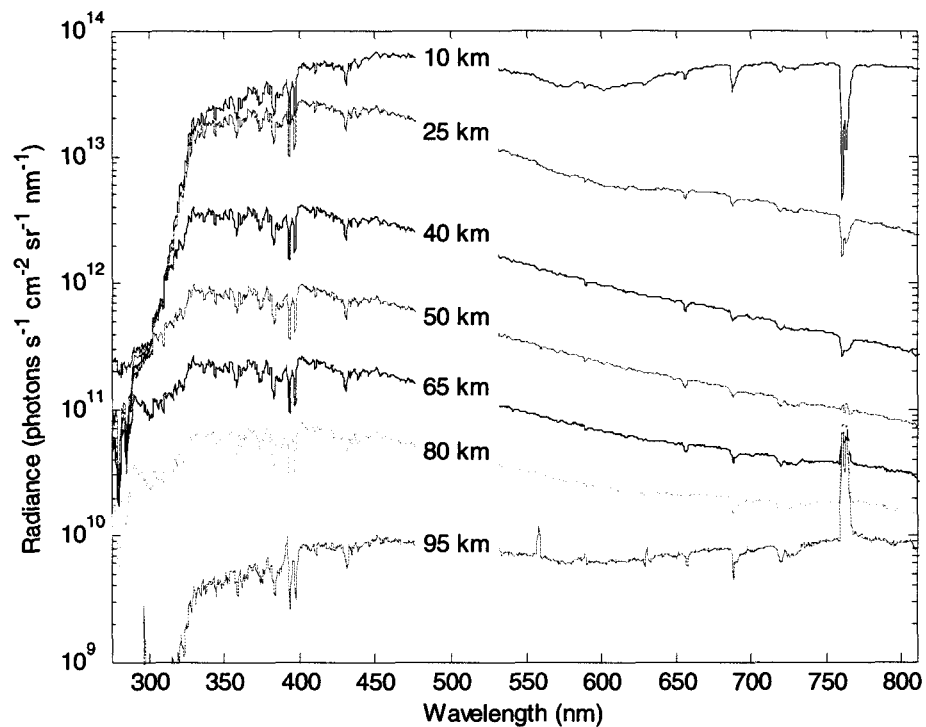
Figure 2.13: OSIRIS spectra at various observed tangent heights for one scan (spectra observed at intermediate tangent heights have been omitted).

Species	Observed features
O_3	Absorption in the Hartley-Huggins band (<330 nm) and in the Chappuis band around 600 nm.
NO_2	Absorption around 400 nm.
BrO	Absorption between 300 and 370 nm.
OClO	Absorption between 300 and 450 nm.
O_2	Absorption and emission in the Atmospheric A-bands at 762 nm, and absorption in the B-bands at 687 nm.

Table 2.1: Relevant absorption/emission features in the OS spectral range.

Unlike the IR imager, the OS does not make tomographic recoveries as it has a horizontal slit allowing for a ~40 km horizontal field-of-view (assuming the viewing

layer is homogenous this allows for a greater signal-to-noise ratio) and a 1 km vertical field-of-view. The OSIRIS fields-of-view are shown in Fig. 2.14. With a finite integration time, typically under 2 seconds, the vertical resolution is slightly greater than 1 km. The incoming signal, after passing through the initial set of baffles, is guided through the optical setup, as seen in Fig. 2.15, and is dispersed onto a 1353 x 286 pixel array CCD camera. Only 32 of the 286 columns are actually illuminated by the in-field signal corresponding to the nominal 40 km horizontal field-of-view. Other active viewing columns are used to determine the intensity of internal stray light within the instrument. All 1353 rows are illuminated by the spectrally dispersed signal with a dispersion function, $\frac{d\lambda}{dp}$, of roughly 0.49 nm/pixel throughout the OS spectral range.
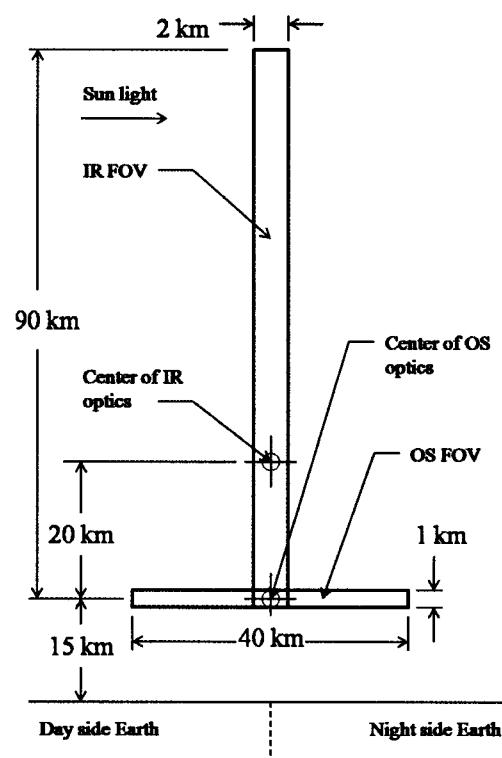
Figure 2.14: Nominal OSIRIS fields-of-view, adapted from *Warshaw et al*, [1998].

28
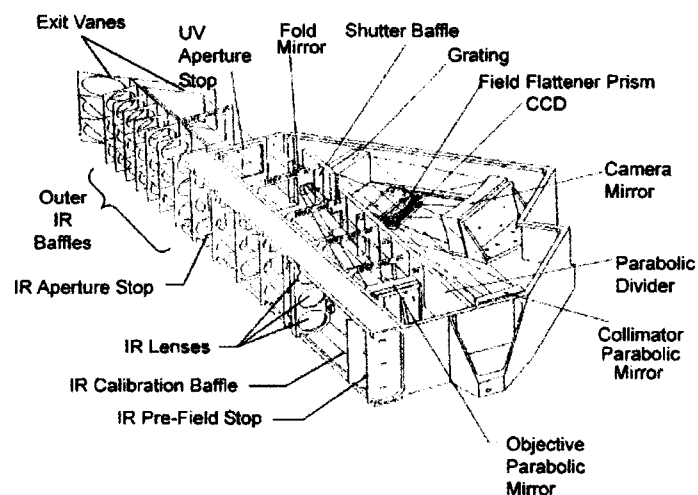
Figure 2.15: OSIRIS optical design, from *Llewellyn et al.* [2004].

2.3.3 OSIRIS viewing geometry

The original geometry of the Odin orbit was such that OSIRIS would orbit the terminator on February 28th and October 18th each year, labelled as terminator days in Fig. 2.16, such that both the OSIRIS sun-scattering angle and the observed tangent point solar zenith angle would be equal to 90° on those days. Between March 1st (February 29th) and October 17th, in plane, OSIRIS would only observe daytime conditions in the Northern hemisphere and nighttime conditions in the Southern hemisphere, and vice versa between October 19th and February 27th.

However, Odin's orbit has not been perfectly sun-synchronous and the orbital precession has been slowing. As a consequence, OSIRIS is observing more nighttime conditions while in the ascending phase (the observed tangent-point-latitude is increasing northward) of its orbit, whereas OSIRIS is observing more daytime conditions while in the descending phase (the observed tangent-point-latitude is decreasing southward).

a) Spring and Autumnal equinox b) Terminator days

c) December solstice d) June solstice
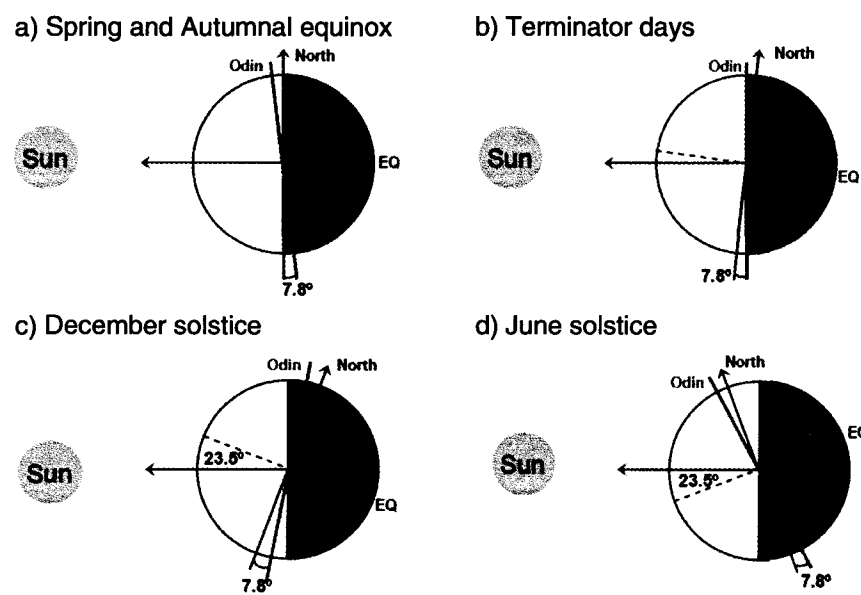
Figure 2.16: Nominal Odin orbital geometry throughout the year, adapted from *Wiensz* [2005].

Presently, on terminator days OSIRIS observe sun-scattering and solar zenith angles greater than 90° throughout the ascending phase and less than 90° throughout the descending phase. Fig. 2.17 shows a comparison of observed local time as a function of observed latitude for two near-terminator days, October 14th, seven years apart. In order to quantify the change in OSIRIS daytime/nighttime coverage, Fig. 2.18 shows the observed local time as a function of observed latitude for the same orbits as in Fig. 2.17, only local time is measured in hours from previous sunrise.
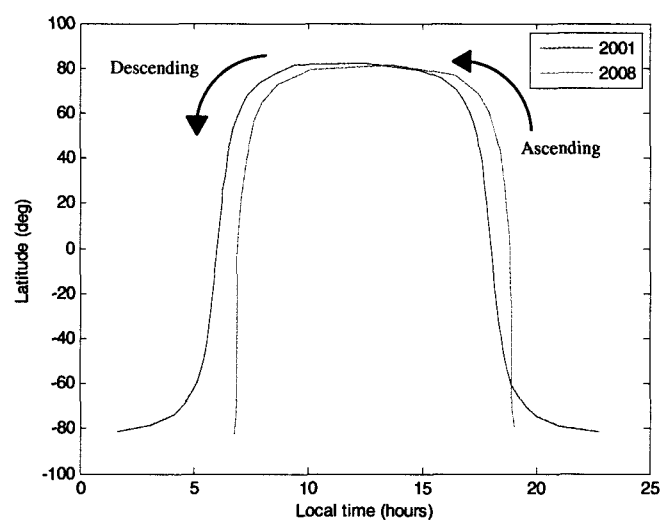
Figure 2.17: Local time observed by OSIRIS as a function of latitude for 14 October 2001 at an observed tangent height of approximately 35 km (blue), and 14 October 2008 at an observed tangent height of approximately 60 km (green). Orbital motion in plot is from right to left.
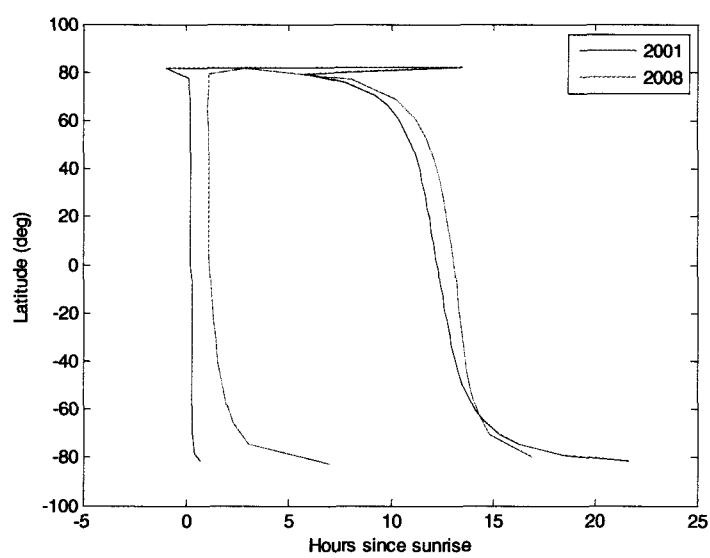
Figure 2.18: Local time (in hours since sunrise) observed by OSIRIS as a function of latitude for the same conditions as in Fig. 2.17.

2.3.4 OSIRIS viewing schedule

The nominal viewing schedule for Odin was such that the Astronomy and Aeronomy

31

teams would have equal viewing time. The schedule, seen in Fig. 2.19, had OSIRIS scanning tangent heights between ~10 and 60 km (strat basic mode) once every three days; once every 10 days OSIRIS would observe the entire range of possible tangent heights (strat-meso mode); and in July two weeks were devoted to observing the summer mesosphere, scanning tangent heights from ~70 to 110 km (summer meso mode).
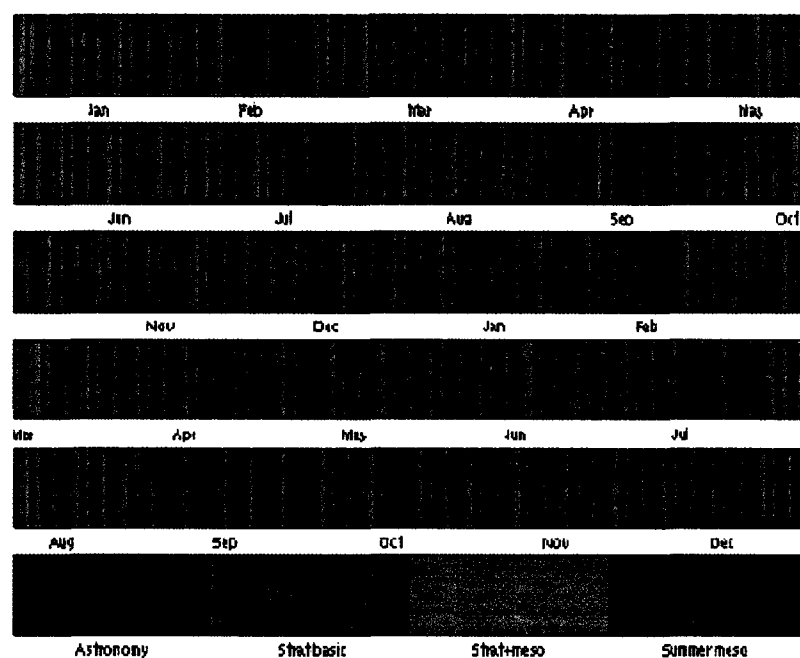
Figure 2.19: Nominal Odin viewing mode schedule, from *Murtagh et al.* [2002].

The viewing schedule has changed over the years due to shifting interests in the Aeronomy team. In 2004, OSIRIS began observing the mesosphere more days in the southern summer hemisphere, and in mid-2007, when ESA began funding the OSIRIS mission and the Astronomy mission ended, OSIRIS began to make mesospheric observations on a near-daily basis. Fig 2.20 shows a plot of days OSIRIS made mesospheric observations.
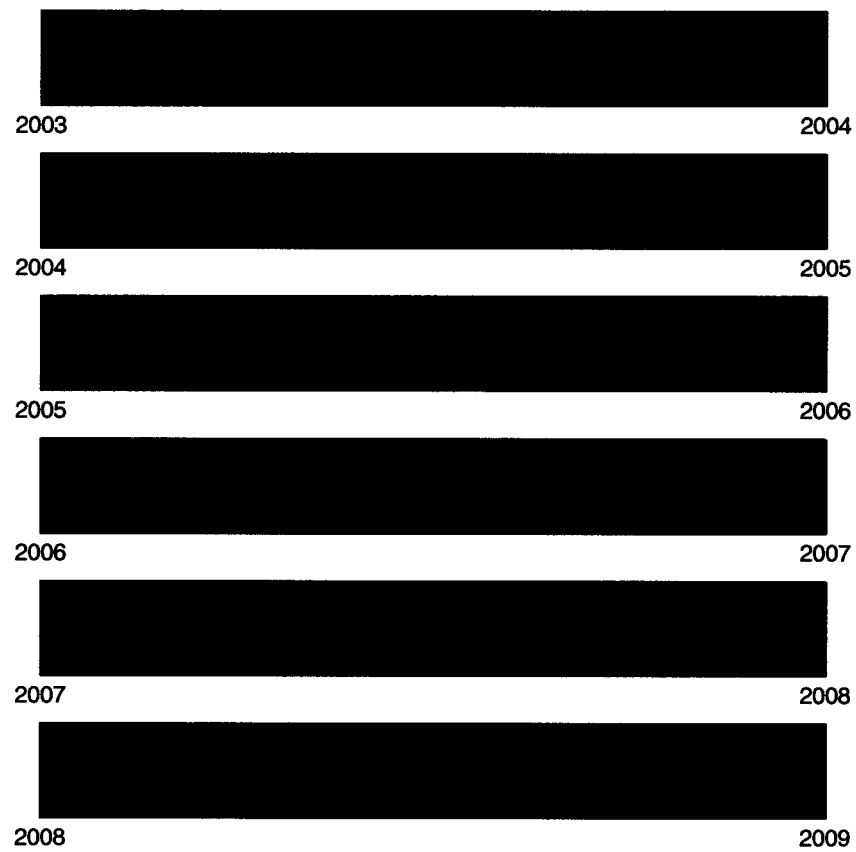
Figure 2.20: Illustration of days between January 2003 and December 2008 that OSIRIS observed the mesosphere (red) and days that OSIRIS did not observe the mesosphere (blue).

Chapter 3

OSIRIS A-band observation model

In this chapter the properties of the O_2 Atmospheric Band system are discussed, along with the production and loss mechanisms that lead to atmospheric O_2 A-band dayglow. The kinetic-photochemical and forward models that have been developed in order to simulate OSIRIS observations in the A-band region are also discussed in detail.

3.1 The molecular oxygen Atmospheric Bands

3.1.1 The O_2 Atmospheric Bands

As outlined in *Goody and Yung* [1989] there are many different electronic states that molecular oxygen can occupy, including the ground state $O_2(X^3\Sigma)$, the first excited electronic state $O_2(a^1\Delta)$, and the second excited electronic state $O_2(b^1\Sigma)$. Within each electronic state, the molecule can also occupy different vibrational levels. Transitions between different electronic-vibrational levels through photon absorption/emission within the atmosphere lead to a wide range of observable absorption and emission bands. The

more common of these O_2 transitions are illustrated in Fig. 3.1.
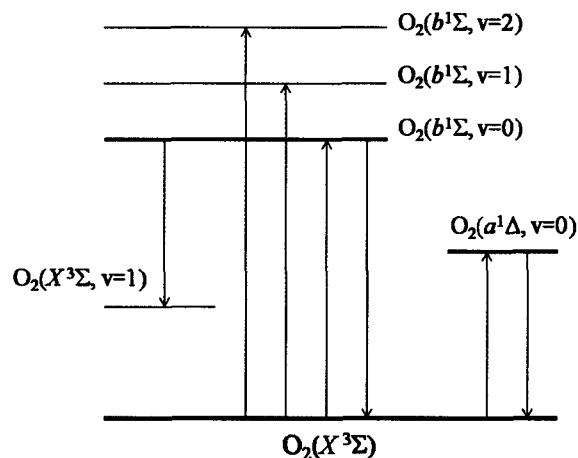
Figure 3.1: Energy level diagram of molecular oxygen including the ground state and the first two excited electronic states. Common transitions observed in the atmosphere are shown. Illustrated transitions, from left to right, are the (0-1) band, γ-band, B-band, A-band (absorption/emission), Infrared Atmospheric (0-0) band (absorption/emission).

The electronic-vibrational transitions between the molecular oxygen ground state and second excited state $\left(X \leftrightarrow b \right)$ give rise to the Atmospheric Band system. In the Atmospheric Bands there are three electronic-vibrational transitions that are of relevance to this study: the A-, B-, and γ-bands, which are detailed in Table 3.1.

Band	Electronic-Vibrational transition	Associated energy wavelength (nm)
A-band	$O_2(X^3\Sigma, v=0) \rightarrow O_2(b^1\Sigma, v=0)$	762
B-band	$O_2(X^3\Sigma, v=0) \rightarrow O_2(b^1\Sigma, v=1)$	689
γ-band	$O_2(X^3\Sigma, v=0) \rightarrow O_2(b^1\Sigma, v=2)$	629

Table 3.1: Important electronic-vibrational bands in the Atmospheric Band system.

A molecule undergoing this type of transition does not emit and absorb photons at a single wavelength due to varying rotational states within the molecule. Transitions between rotational states, along with electronic and vibrational states, correspond to energy wavelengths at discrete lines, centered on the electronic-vibrational transition

energy wavelength. Absolute transition intensities are different for absorption and emission, however both are directly proportional to the line strength [*Herzberg*, 1950], which is defined as the intensity per absorbing molecule, commonly measured in cm^{-1} / (molec cm^{-2}). The line strengths of the A-band, as given by the 2004 edition of the HITRAN spectroscopic database [*Rothman et al.*, 2005], are plotted in Fig. 3.2.
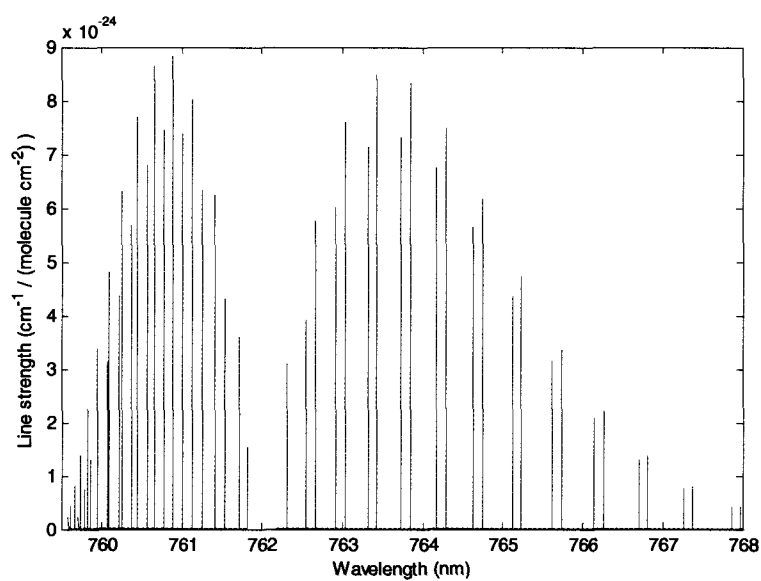
Figure 3.2: Atmospheric A-band rotational line strengths. Line strength values are for temperatures of 296 K, taken from the 2004 HITRAN database.

The Atmospheric Bands are observed for the $^{16}O_2$ molecule and similarly for the isotopic molecules $^{16}O^{17}O$ and $^{16}O^{18}O$, the latter of which have different rotation line strengths and positions. Given the relative abundances for $^{16}O^{16}O$, $^{16}O^{17}O$, and $^{16}O^{18}O$ of 99.76%, 0.037%, and 0.204%, respectively [*Slanger et al.*, 1997], OSIRIS does not have the necessary sensitivity for the isotopic emissions or absorptions to be of any great significance in this study. However, isotopic O_2 A-band lines are included in transmission function and O_2 absorption cross-section calculations.

3.1.2 Observations of the Atmospheric Bands

The first reported dayglow observations of the O_2 Atmospheric Bands, shown in Fig. 3.3, were provided by *Wallace and Hunten* [1968]. They observed dayglow in the A-band between altitudes of 35 and 128 km and the (0-1) band, at 864 nm, between altitudes of 59 and 95 km, using rocket-borne spectrometers and photometers. They also identified the primary production and loss mechanisms of $O_2(b^1\Sigma)$. Ground-based observations of the (0-1) band at twilight were later used to infer O_3 densities in the lower thermosphere [*Noxon*, 1975]; however, reports of subsequent dayglow observations did not begin until over 15 years later [*e.g. Skinner and Hays*, 1985; *Torr et al.*, 1986]. Following these observations, $O_2(b^1\Sigma)$ dayglow began to be used to retrieve atmospheric temperatures and densities of important species in the middle atmosphere. *Sica* [1991] presented a method to infer ozone densities using simultaneous ground-based measurements of $O_2(b^1\Sigma)$ and $O_2(a^1\Delta)$ during twilight, *Heller et al.* [1991] inferred mesospheric temperatures from rocket-borne spectrometer measurements of the A-band, and *López-González et al.* [1992] proposed a method of retrieving O_3 densities from $O_2(b^1\Sigma)$ dayglow.
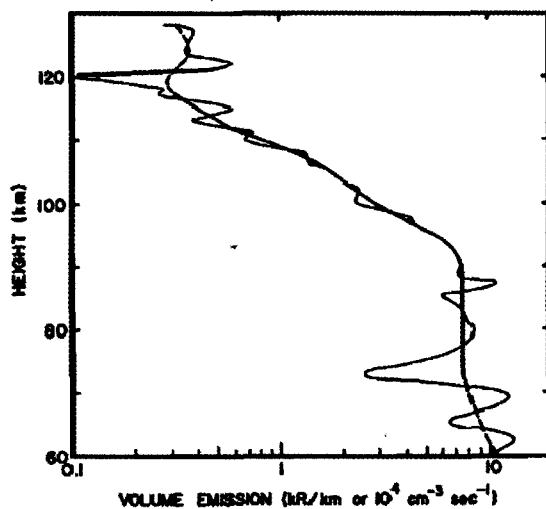
Figure 3.3: Rocket-borne photometer measurements and model of the oxygen A-band dayglow, from *Wallace and Hunten* [1968].

3.1.3 A-band Production and Loss Mechanisms

A detailed description of the production and loss mechanisms of A-band dayglow is given by *Bucholtz et al.* [1986], and is summarized in this section. A schematic diagram of the production of the A-band dayglow can be seen in Fig. 3.4, and Table 3.2 lists the significant reactions and all corresponding rate constants.

There are three primary sources of the $O_2(b^1\Sigma)$ in the mesosphere. The first source is photon absorption in the Atmospheric Bands,

$$O_2(X^3\Sigma, v = 0) + h\nu \ (762, 689, 629 \ \text{nm}) \rightarrow O_2(b^1\Sigma, v = 0, 1, 2), \qquad (3.1)$$
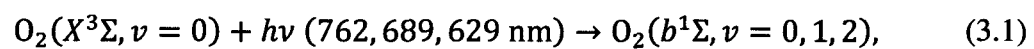
where O_2 in the ground state absorbs photons in the A-, B-, and γ-bands. The production rates through these processes are,

$$P_{resA} = g_A[O_2] \qquad (3.2)$$

$$P_{resB} = g_B[O_2], \qquad (3.3)$$

38
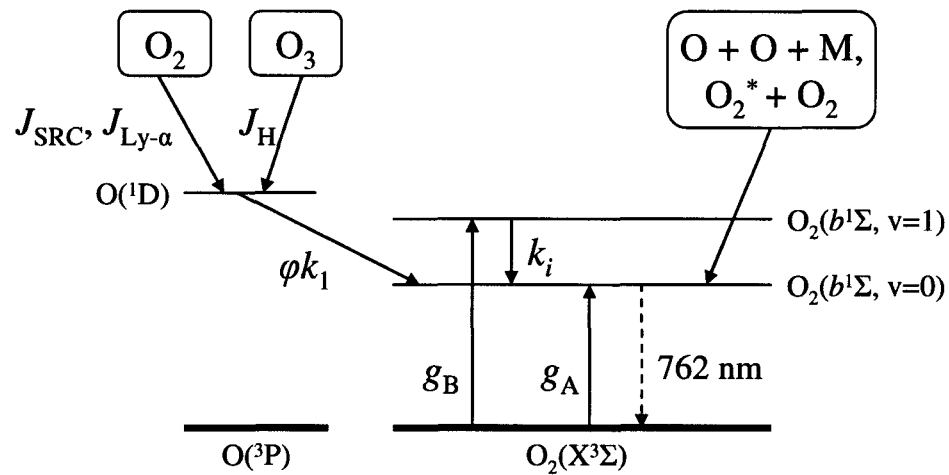
Figure 3.4: Schematic of processes accounted for in the kinetic-photochemical model that contribute to the production of A-band dayglow. J and g terms are photochemical reaction coefficients, and k terms are collisional quenching rates.

where g_A and g_B, in units of s^{-1}, are the photochemical reaction coefficients in the A- and B-bands, respectively (also known as g-factors), and [ ] refers to the number density of the species within the brackets, in molec/cm^3. A detailed discussion of the calculation of the g-factors, is given in Section 3.3.5. *Bucholtz et al.* [1986] showed that absorption in the γ-band is insignificant in comparison to that of the A- and B-bands, and hence is not considered in this study. The B-band however is considered due to the fact that $O_2(b^1\Sigma)$ in the $v=1$ state is rapidly collisionally deactivated into the $v=0$ state, subsequently leading to A-band emission. From the equations given in Table 3.2 the production rate of $O_2(b^1\Sigma, v=0)$ due to deactivation of $O_2(b^1\Sigma, v=1)$ can be written as,

$$P_B = K[O_2(b^1\Sigma, v = 1)], \tag{3.4}$$

where

$$K = k_{0B}[O] + k_{1B}[O_2] + k_{2B}[N_2] \tag{3.5}$$

and

39

$$[O_2(b^1\Sigma, v = 1)] = \frac{P_{resB}}{A_{771} + K + k_{3B}[O_3]}. \qquad (3.6)$$

The k values given in Equations 3.5 and 3.6 are the reaction coefficients for the reactions given in the corresponding equations in Table 3.2, and A_{771} is the Einstein coefficient for spontaneous emission of a photon for the $O_2(1-1)$ band at 771 nm. Therefore,

$$P_B = \frac{K\, P_{resB}}{A_{771} + K + k_{3B}[O_3]}. \qquad (3.7)$$

Another loss mechanism of $O_2(b^1\Sigma, v{=}1)$ is through emission at 686 nm into the O_2 ground state. However, as discussed by *Slanger et al.* [1997], this mechanism is insignificant in comparison to collisional quenching, and is therefore not considered in the kinetic-photochemical model.

The second source is collisional excitation of O_2 in the ground state by $O(^1D)$,

$$O(^1D) + O_2(X^3\Sigma) \rightarrow O(^3P) + O_2(b^1\Sigma). \qquad (3.8)$$
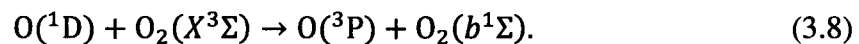
Lee and Slanger [1978] found that this process will lead to nearly equal populations of both the $v{=}0$ and $v{=}1$ states. However, as *Bucholtz et al.* [1986] point out, the deactivation rate of the $O_2(b^1\Sigma, v{=}1)$ state into the $O_2(b^1\Sigma, v{=}0)$ state is much faster than the electronic quenching rate of $O_2(b^1\Sigma, v{=}0)$ into the ground state; and therefore the reaction given in Equation 3.8 can be considered to produce solely $O_2(b^1\Sigma, v{=}0)$ molecules. The production rate of $O_2(b^1\Sigma)$ from this source is,

$$P_{O(^1D)} = \varphi k_1 [O(^1D)][O_2], \qquad (3.9)$$

where φ and k_1 are the efficiency and rate constant, respectively, of Reaction 3.8. In test cases, when the model was modified to include the pathway of $O(^1D)$ exciting O_2 into the $O_2(b^1\Sigma, v{=}1)$ state, it was found that retrievals of ozone varied by less than 0.05%.

There are only two significant sources of $O(^1D)$ in the mesosphere, photolysis of O_2 in the Schumann-Runge Continuum (SRC) and photolysis of O_3 in the Hartley band,

$$O_2 + h\nu \ (\lambda \leq 175 \text{ nm}) = O(^1D) + O(^3P) \tag{3.10}$$

$$O_3 + h\nu \ (\lambda \leq 310 \text{ nm}) = O(^1D) + O_2(a^1\Delta). \tag{3.11}$$
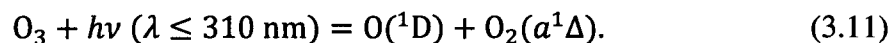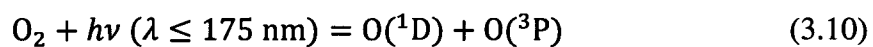
Due to the long radiative lifetime of $O(^1D)$, spontaneous emission of a photon at 630 nm is much less likely than the dominant loss processes of $O(^1D)$ in the mesosphere, namely electronic quenching by N_2 and O_2 molecules. Thus, the $O(^1D)$ concentration in the mesosphere is given by,

$$[O(^1D)] = \frac{J_2[O_2] + J_3[O_3]}{A_{1D} + k_1[O_2] + k_2[N_2]}, \tag{3.12}$$

where J_2 and J_3 are the photolysis coefficients of O_2 and O_3, respectively, A_{1D} is the Einstein coefficient for emission of $O(^1D)$ at 630 nm, and k_1 and k_2 are the quenching rates of $O(^1D)$ due to O_2 and N_2, respectively. The calculation of the photolysis coefficients are discussed in detail in Section 3.3.

The third source of $O_2(b^1\Sigma)$ is a chemical source that was first proposed by *Wallace and Hunten* [1968] to be due to the 3-body recombination of atomic oxygen; however, subsequent work [*Campbell and Gray*, 1973; *Slanger and Black*, 1977] suggested, and it is now widely accepted, that laboratory and nightglow observations are more consistent with a two-step Barth-type process,

$$O + O + M \rightarrow O_2^* + M, \tag{3.13}$$

where M is an O_2 or N_2 molecule. Then,

$$O_2^* + O_2 \rightarrow O_2(b^1\Sigma) + O_2. \tag{3.14}$$

41

The unidentified O_2^* state can also be quenched by atomic oxygen. From *McDade et al.* [1986], the production rate of $O_2(b^1\Sigma)$ from this process can be approximated as,

$$P_{Barth} = \frac{k_5[O]^2[O_2][M]}{C_{O2}[O_2] + C_O[O]},$$

(3.15)

where k_5 is the reaction coefficient of Reaction 3.13 and C_{O2} and C_O are relative quenching rates of O_2^* by O_2 and O, respectively, derived by *McDade et al.* [1986] from rocket-borne observations of the nightglow. These relative quenching rates are unitless and take into account the efficiencies of Reactions 3.13 and 3.14 as well as the quenching rates of O_2^* due to O_2, N_2, and O.

$O_2(b^1\Sigma,\ v=0)$ molecules, as well as spontaneously emitting photons in the A-band region, may undergo electronic quenching by N_2, O_3, O_2, and O. The A-band volume emission rate, η, in photons/s/cm^3, is thus,

$$\eta = F_c \frac{A_{1\Sigma}\left(P_{res} + P_{O(^1D)} + P_{Barth}\right)}{A_{1\Sigma} + k_0[N_2] + k_3[O_3] + k_4[O_2] + k_6[O]},$$

(3.16)

where F_c is the A-band Franck-Condon factor, which has a value of 0.93 [*Nicholls*, 1965], $A_{1\Sigma}$ is the A-band Einstein coefficient, and k_0, k_3, k_4, and k_6 are the quenching rates for N_2, O_3, O_2, and O, respectively. Fig. 3.5 shows a typical modelled volume emission rate vertical profile, along with the contributions of each source detailed above. The model takes into account all processes described above; the background atmosphere (O_2, N_2, and T), which is determined by a locally run MSIS-E-00 model [*Hedin*, 1991]; and assumed *a priori* O_3 and O profiles (discussed in Sections 3.4 and 4.2, respectively).

42
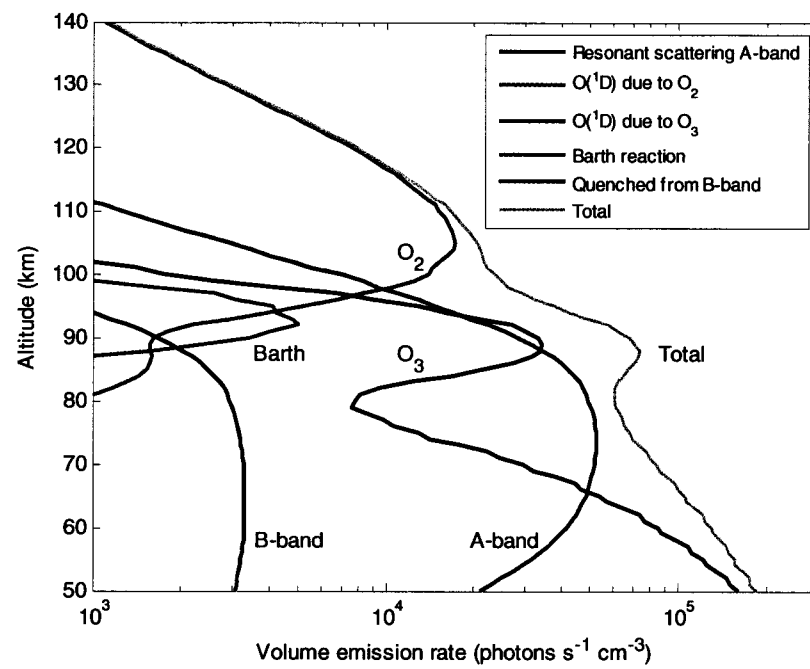
Figure 3.5: Typical modelled volume emission rates and contributions from the different photochemical sources.

Reaction	Rate	Value	Reference
$O_2 + h\nu(762\ nm) \rightarrow O_2(b, v=0)$	g_A	See text	n/a
$O_2 + h\nu(689\ nm) \rightarrow O_2(b, v=1)$	g_B	See text	n/a
$O_2(b, v=1) \rightarrow O_2(X, v=1) + h\nu(771\ nm)$	A_{771}	0.070	*Yankovsky et al., 2006*
$O_2(b, v=1) + O \rightarrow O_2(b, v=0) + O$	k_{0B}	4.5(-12)	*Yankovsky et al., 2006*
$O_2(b, v=1) + O_2 \rightarrow O_2(b, v=0) + O_2$	k_{1B}	4.2(-11)exp(-312/T)	*Yankovsky et al., 2006*
$O_2(b, v=1) + N_2 \rightarrow O_2(b, v=0) + N_2$	k_{2B}	5(-13)	*Yankovsky et al., 2006*
$O_2(b, v=1) + O_3 \rightarrow 2O_2 + O$	k_{3B}	3(-10)	*Yankovsky et al., 2006*
$O_2 + h\nu(\lambda \leq 176\ nm) \rightarrow O(^1D) + O(^3P)$	J_2	See text	n/a
$O_3 + h\nu(\lambda \leq 310\ nm) \rightarrow O(^1D) + O_2(a)$	J_3	See text	n/a
$O(^1D) \rightarrow O + h\nu(630\ nm)$	A_{1D}	6.81(-3)	*Kernahan and Pang, 1975*
$O(^1D) + O_2 \rightarrow O + O_2(b, v=0)$	φk_1	φ=0.95	*Green et al., 2000*
$O(^1D) + O_2 \rightarrow O + O_2$	k_1	3.3(-11)exp(55/T)	*Sander et al., 2006*
$O(^1D) + N_2 \rightarrow O + N_2$	k_2	2.15(-11)exp(110/T)	*Sander et al., 2006*
$O + O + M \rightarrow O_2^* + M$	k_5	4.7(-33)exp(300/T)^2	*Campbell and Gray, 1973*
$O_2^* + O_2 \rightarrow O_2(b, v=0) + O_2$	C_{O2}	7.5	*McDade et al., 1986*
$O_2^* + O \rightarrow O_2 + O$	C_O	33	*McDade et al., 1986*
$O_2(b, v=0) \rightarrow O_2 + h\nu(762\ nm)$	$A_{1\Sigma}$	0.085	*Burch and Gryvnak, 1969*
$O_2(b, v=0) + N_2 \rightarrow$ products	k_0	1.8(-15)exp(45/T)	*Sander et al., 2006*
$O_2(b, v=0) + O_3 \rightarrow$ products	k_3	3.5(-11)exp(135/T)	*Sander et al., 2006*
$O_2(b, v=0) + O_2 \rightarrow$ products	k_4	3.9(-17)	*Sander et al., 2006*
$O_2(b, v=0) + O \rightarrow$ products	k_6	8(-14)	*Sander et al., 2006*

Table 3.2: Chemical reactions relevant in the production and loss of $O_2(b^1\Sigma)$ in the mesosphere. J, g, and A values are all in units of s^{-1}, all k values with the exception of k_5, which is in units of cm^6/s, are in units of cm^3/s, and values for C_{O2} and C are unitless. In the "Value" column, numbers given as $m(n)$ should be read as $m \times 10^n$.

3.2 The continuity equation

Modelling the total band volume emission rate of the O_2 A-band requires a determination

of the $O_2(b^1\Sigma)$ density profile. This can be derived from the continuity equation [*Brasseur*

and Solomon, 2005], which is an expression of how the density of a chemical species changes with time due to both local photochemical reactions and transport processes,

$$\frac{\partial [x]}{\partial t} + \nabla \cdot ([x]\mathbf{v}) = S_x,$$ (3.17)

where $\mathbf{v}$ is the velocity of mass flow through a volume of air, again [ ] refers to the number density of the chemical species x within the volume, and S_x is the source function of the species x, in molec/cm^3/s, which takes into account all photochemical production mechanisms, P_x, also in molec/cm^3/s, and loss mechanisms L_x, in units of s^{-1},

$$S_x = P_x - L_x[x].$$ (3.18)

In the case of $O_2(b^1\Sigma)$, the Einstein coefficient is 0.085 s^{-1}, which corresponds to a radiative lifetime of approximately 12 s. This means that the effects of transport can be considered negligible, and $O_2(b^1\Sigma)$ to be considered in rotational equilibrium; thus making the chemistry of the band relatively simple. From Equations 3.17 and 3.18, the density of $O_2(b^1\Sigma)$ reduces to,

$$[O_2(b^1\Sigma)] = \frac{P_{O2(b)}}{L_{O2(b)}}.$$ (3.19)

The production and loss mechanisms are modelled using the equations presented in the previous section.

3.3 Calculation of photochemical reaction coefficients

3.3.1 Photolysis coefficients

The photolysis rate of a gas over a given spectral interval at a specific altitude is determined by,

$$J(z) = \int F(\lambda, z)\sigma(\lambda)\phi(\lambda)d\lambda, \tag{3.20}$$

where $J(z)$ is in units of s^{-1}, $F(\lambda,z)$ is the spectral flux at altitude z in photons/s/cm^2, $\sigma(\lambda)$ is the absorption cross-section of the gas in cm^2/molec, and $\phi(\lambda)$ is its quantum yield in molec/photon. This can be calculated numerically with the approximation,

$$J(z) \approx \sum_{i=1}^{N} F(\lambda_i, z)\sigma(\lambda_i)\phi(\lambda_i)\Delta\lambda_i, \tag{3.21}$$

where N is the number of spectral intervals. Assuming the attenuation of the spectral solar flux at a given altitude is solely due to absorption, $F(\lambda,z)$ can be determined via the Lambert-Beer law,

$$F(\lambda, z) = F(\lambda, \infty)\exp\left(-\sec\chi \int_{z}^{z_\infty} \sum_{x}[x]\sigma_x(\lambda)dz'\right), \tag{3.22}$$

where $F(\lambda,\infty)$ is the solar flux at the top of the atmosphere, χ is the solar zenith angle, and $[x]$ and $\sigma_x(\lambda)$ are the molecular density and absorption cross-section of absorber x, respectively. As detailed in *Brasseur and Solomon* [2005], at solar zenith angles between 75° and 95° the curvature of the Earth must be considered in determining the attenuation, and the secχ term in Equation 3.22 must be replaced by the Chapman function, which *Smith and Smith* [1972] showed can be approximated as,

$$Ch(a, \chi) = \left(\frac{\pi a}{2}\right)^{\frac{1}{2}}\left(1 - \text{erf}\left[\left(\frac{a}{2}\right)^{\frac{1}{2}}\cos\chi\right]\right)\exp\left(\frac{a}{2}\cos^2\chi\right), \tag{3.23}$$

where $a = (R + z)/H$, R is Earth's radius, and H is the scale height of the absorbing species.

46

3.3.2 Solar flux values

All calculations of atmospheric photochemical reaction coefficients require the knowledge of the incident solar flux at the top of the atmosphere. Measurements of these values were taken from the Solar Radiation and Climate Experiment (SORCE) instruments' [*Sparn et al.*, 2005] time series published on the NASA website, http://lasp.colorado.edu/sorce/index.htm. For molecular oxygen and ozone photolysis coefficient calculations, to be described in Sections 3.3.3 and 3.3.4, daily average solar flux values at the Lyman-α line and between 137 and 310 nm were measured by the Solar Stellar Irradiance Comparison Experiment (SOLSTICE) instruments. For the g-value calculations, as detailed in Section 3.3.5, daily average solar flux values at 689 nm and 762 nm were measured by the Spectral Irradiance Monitor (SIM) instrument. A typical solar spectrum from a composite of these instruments is seen in Fig. 3.6.

(a)   (b)
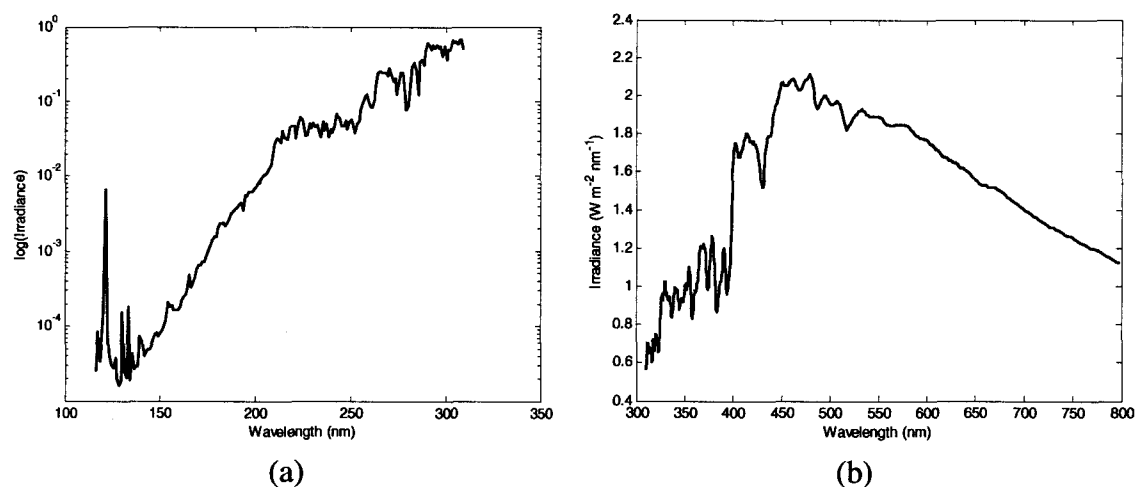
Figure 3.6: A typical daily average solar spectrum as seen by the instruments aboard the SORCE satellite, (a) UV spectrum from SOLSTICE instruments, values are the log10 values of the measured irradiance in W/m^2/nm (b) visible spectrum from SIM instrument.

3.3.3 Molecular oxygen photolysis coefficient calculations

One of the major sources of $O(^1D)$ in the upper atmosphere is photolysis of molecular oxygen in the SRC, between 137 and 175 nm, and also at the solar Lyman-α line at 121.6 nm, as seen in Fig. 3.7. O_2 absorption at wavelengths greater than 175 nm, *i.e.* in the Schumann Runge Bands (SRB), leads to predissociation, which results in two oxygen atoms in the ground state [*Brasseur and Solomon*, 2005].
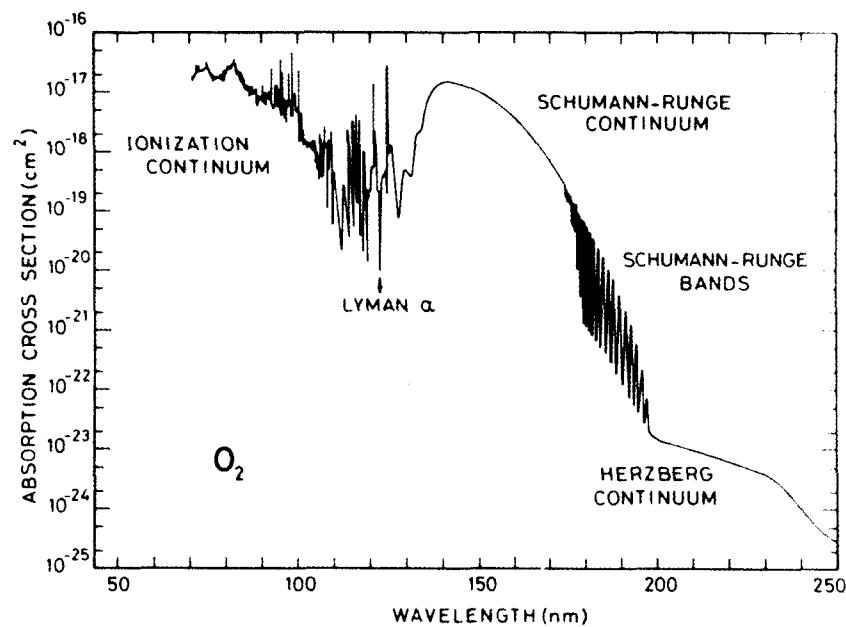
Figure 3.7: Absorption cross-sections of O_2, from *Brasseur and Solomon* [2005] (note that extracted figure ordinate units are different from general thesis usage of cm^2/molec).

In the kinetic-photochemical model, the photolysis coefficients at a given altitude for the reaction,

$$O_2 + h\nu \ (\lambda \leq 175 \text{ nm}) \xrightarrow{J_2} O(^1D) + O(^3P) \tag{3.24}$$
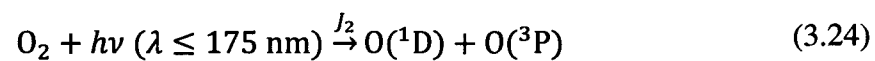
are calculated numerically according to Equations 3.21 and 3.22. The O_2 densities are

obtained from the MSIS model. The O_2 absorption cross-sections in the SRC were taken from *Yoshino et al.* [2004] for 1 nm intervals between 130 – 175 nm, and the absorption cross-section for the Lyman-α line at 121.6 was taken from *Reddmann and Uhl* [2003]. The O_2 photodissociation quantum yield at all wavelengths in the SRC is 1.0 [*Brasseur and Solomon*, 2005], and the average value is 0.48 at the Lyman-α line [*Lacoursière et al.*, 1999]. Fig. 3.8 shows the calculated J_2 values for different solar zenith angels.
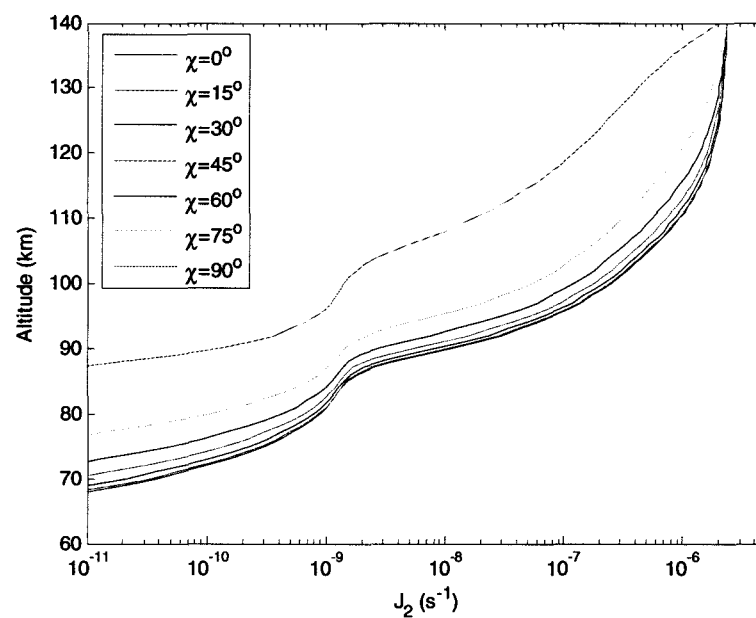
Figure 3.8: Calculated O_2 photolysis rates for a typical atmosphere at varying solar zenith angles.

3.3.4 Ozone photolysis coefficient calculations

The other major source of $O(^1D)$ in the middle atmosphere is through the photolysis of O_3 in the Hartley bands, between 198 and 310 nm. At wavelengths greater than 310 nm, in the Huggins bands, the photolysis of O_3 results in atomic oxygen in the ground state [*Brasseur and Solomon*, 2005].

49

At the altitudes and solar zenith angles of interest in this study, above 70 km and less than 85°, respectively, J_3 values in the Hartley bands does not vary significantly with height from the J_3^∞ value (the photolysis coefficient at zero optical depth, in s^{-1}). Thus, the calculated J_3 profile is simply the J_3^∞ value, which can be determined numerically via,

$$J_3^\infty = \sum_{i=1}^{N} F(\lambda_i, \infty) \sigma(\lambda_i) \phi(\lambda_i) \Delta \lambda_i. \tag{3.25}$$

The O_3 absorption cross-sections in the Hartley bands were obtained from *Daumont et al.* [1992], *Brion et al.* [1993], and *Malicet et al.* [1995] for the spectral region of 198 – 309 nm. The O_3 photodissociation quantum yields used were obtained from *Nishida et al.* [2004] for 1 nm intervals between 198 – 225 nm, from *Takahashi et al.* [2002] for 1 nm intervals between 230 – 288 nm, and from *Talukdar et al.* [1998] for 1 nm intervals between 289 – 309 nm. For typical conditions, the photolysis coefficient of the Hartley bands is roughly,

$$J_3^\infty = 7.1 \times 10^{-3} \text{ s}^{-1}. \tag{3.26}$$

3.3.5 Photochemical reaction coefficients in the Atmospheric Bands

One of the two most significant sources of A-band dayglow in the mesosphere is resonant scattering in the Atmospheric Bands. The production rate of $O_2(b^1\Sigma)$ due to this source, P_{res}, in units of molec/cm^3/s, is given by,

$$P_{res} = g(z, \chi)[O_2], \tag{3.27}$$

where $g(z)$ is the photochemical reaction coefficient in the Atmospheric Bands at altitude

z, also known as the g-factor. Calculations of both A-band and B-band g-factors were carried out line-by-line, similar to the method of *Bucholtz et al.* [1986] where,

$$g(z,\chi) = \int F(v,z) \sum_j S_j(T)D(v)dv. \tag{3.28}$$

The solar flux at wavenumber v, $F(v,z)$, is dependent on the solar zenith angle χ and was determined in the same manner as detailed in Section 3.3.1, $S_j(T)$ is the jth line strength of the band system at temperature T, and $D(v)$ is a Doppler line shape at wavenumber v. A Doppler line shape was used in place of the Voigt profile used in similar calculations [*Bucholtz et al.*, 1986, *Mlynczak*, 1993], because above 40 km both natural and pressure-broadening of the lines can be ignored as Doppler broadening is the dominant effect.

The Doppler line profile is a normalized Gaussian distribution, unitless, and is given by *Goody and Yung* [1989] as,

$$D(v) = \frac{1}{\alpha_D \sqrt{\pi}} \exp\left[-\left(\frac{v - v_0}{\alpha_D}\right)^2\right], \tag{3.29}$$

where v_0 is the line center and the Doppler line width α_D, in wavenumbers, is given by,

$$\alpha_D = \frac{v_0}{c}\left(\frac{2k_B T}{m}\right)^{\frac{1}{2}}, \tag{3.30}$$

where, c is the speed of light, k_B is Boltzmann's constant, and m is the mass of an O_2 molecule.

The relationship between line strength at temperature T and line strength at standard temperature T_s (296 K) is given by *McClatchey et al.* [1973] and is simplified by *Bucholtz et al.* [1986]. This relationship, where E_j'' are the respective energies of the lower states, is given as,

51

$$S_j(T) = \frac{S_j(T_s)T_s}{T} \exp\left(\frac{1.439E_j''(T - T_s)}{TT_s}\right). \tag{3.31}$$

All A- and B-band system line strengths, line centres, and lower state energies listed in the 2004 HITRAN database were used in the summation in Equation 3.28. As previously mentioned, absorption in the γ-band was shown by *Bucholtz et al.* [1986] to be insignificant in comparison to the absorption of the A- and B-bands, and thus has not been included in this study.

When calculating the *g*-factors, the integration over wavenumber was performed from 12964 to 13166 cm^{-1} with a step size of 0.01 cm^{-1}. Similar to *Bucholtz* [1986], it was determined that a step size of 0.001 cm^{-1} made no significant difference in the results. The integration over altitude was performed from 40 to 120 km with a 1 km step size. It was found that including altitudes above 120 km in the integration made no significant difference, and the *g*-factors above this altitude were essentially equal to the corresponding values at 120 km.

The *g*-factors were tabulated for solar zenith angles between 0 and 90° and for altitudes between 40 and 120 km. These values were approximately 17 – 20% greater than those of *Mlynczak* [1993], due to differences in solar flux values and the incorporation of additional spectral lines in the integration that have been added to the HITRAN database since that time. *Mlynczak et al.* [2000] found a 15% increase in their *g*-factor calculations when incorporating additional spectral lines added to the 1996 edition of the HITRAN database. Tables of the *g*-factor results can be seen in Appendix C. From Fig 3.9, it can be seen that the *g*-factor values decline with solar zenith angle due

to the increased attenuation of the solar flux. It can also be seen that $O_2(b^1\Sigma)$ production due to absorption in the Atmospheric Bands is dominated by the A-band with g-factors roughly an order of magnitude greater than those of the B-band.
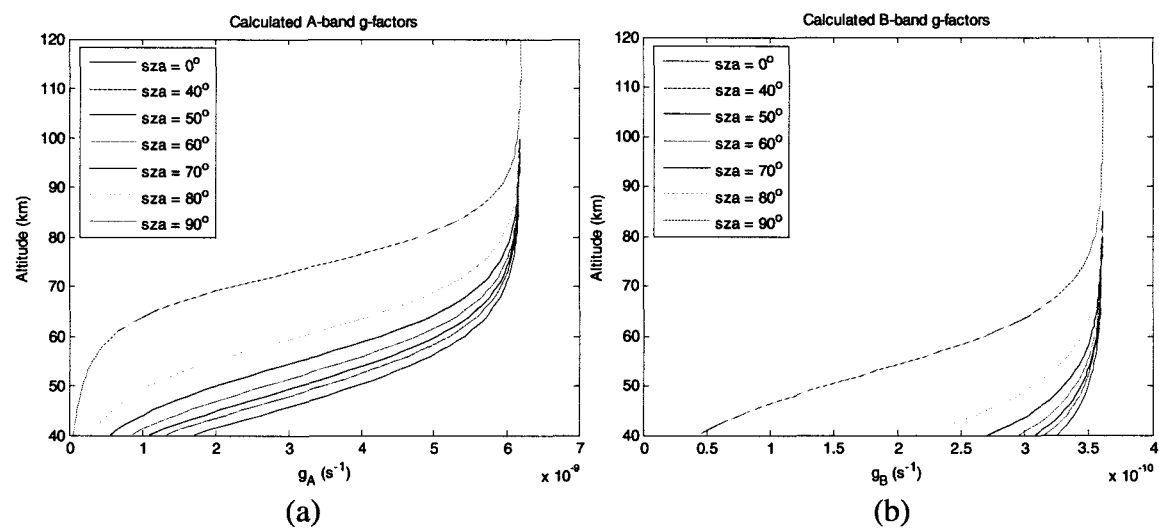
Figure 3.9: Calculated g-factors for solar zenith angles between 0° and 90° for (a) the A-band, and (b) the B-band.

The temperature and O_2 density profiles used in the calculations were obtained from the MSIS model and $F(v,\infty)$ was assumed to be a flat spectrum for each band system, the values of which were obtained from daily band-averaged solar irradiance data measured by the SIM instrument between July 2002 and December 2007. A $F(v,\infty)$ value of 2.75×10^{-13} photons cm^{-2} $(cm^{-1})^{-1}$ sec^{-1} was used for the A-band and 2.41×10^{-13} photons cm^{-2} $(cm^{-1})^{-1}$ sec^{-1} for the B-band.

The overall uncertainty in the calculated g-factors is typically less than 10%. Sources of error include uncertainty of the line strengths, which is typically ~5%; differences in the temperature profile from the profile used in the calculations, <7%; and error and variation in the solar flux values, <1%.

53

3.4 The *a priori* ozone density profile

Since the OSIRIS viewing geometry is such that daytime measurements are only possible in the summer hemisphere, the assumed *a priori* O_3 density profile should be representative of a typical summer O_3 profile, seen in Fig. 3.10. This was achieved by averaging all retrieved SABER [*Mlynczak*, 1997] ozone profiles from July 2004 that were near-coincident with OSIRIS observations. The SABER instrument is discussed in more detail in Chapter 6. The conditions for coincidence were that same day observations of the two instruments must be observing regions within 2° of latitude, 5° of longitude, 1° of solar zenith angle, and the measurements were taken within one hour of each other.
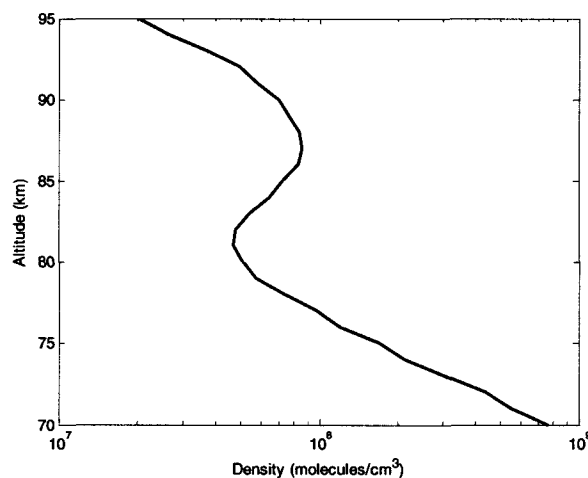
Figure 3.10: The *a priori* O_3 density profile for altitudes between 70 and 95 km, based on summer SABER observations.

3.5 Modelled volume emission rates

Sample results of the kinetic-photochemical model described above are compared here to observations of A-band volume emission rates that were measured by the HRDI

instrument, described by *Hays et al.* [1993]. One of ten instruments on board the UARS satellite, HRDI is a limb-scanning instrument that observes the oxygen A-band with high spectral resolution between 50 and 115 km with near-global coverage. *Ratnam et al.* [2004] presented observed HRDI A-band volume emission rates, which exhibited a semi-annual oscillation at lower latitudes in both hemispheres, peaking around equinox. They observed a decrease in the amplitude of this oscillation with increasing latitude, whereas at mid-latitudes they observed a more predominant annual oscillation peaking in the summer. The observed peak height, around 87 – 90 km, did not tend to vary with season at a given location, but varied slightly with latitude. Their observations for different seasons are shown in Fig. 3.11.
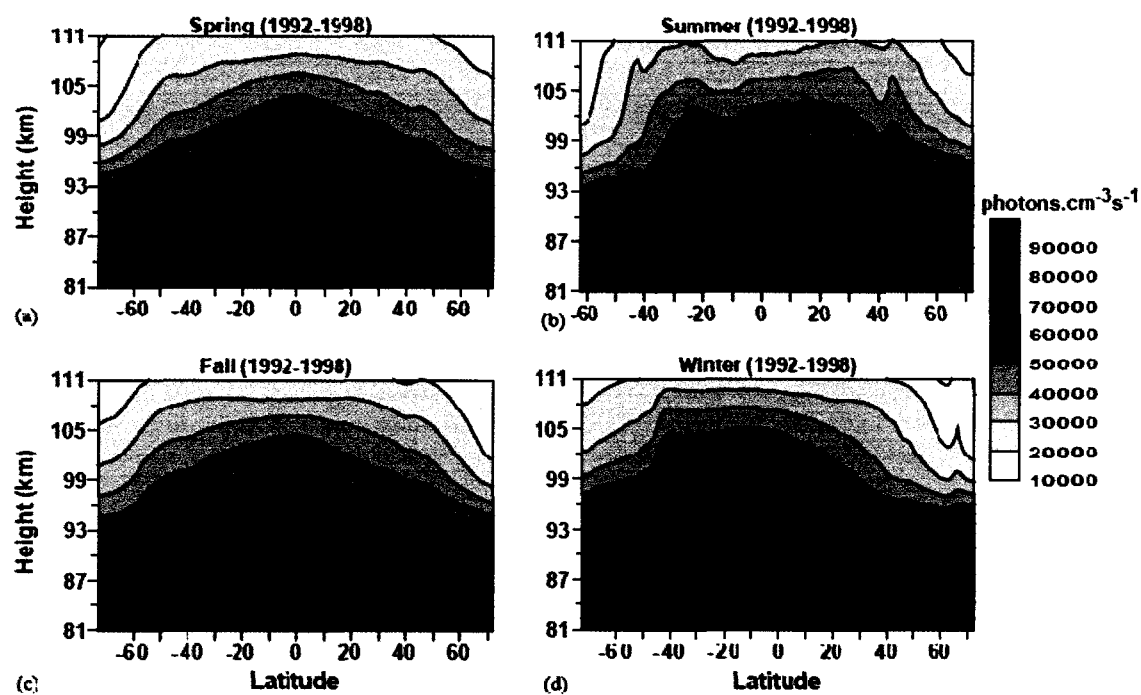
Figure 3.11: HRDI yearly and zonally-averaged observations of A-band VER for different seasons at noon, (a) March – April, (b) May – August, (c) September – October, (d) November – February, from *Ratnam et al.* [2004].

Volume emission rates were modelled to simulate the HRDI observations using the kinetic-photochemical model discussed in this chapter. For the model runs, an MSIS background atmosphere was assumed for all atmospheric constituents with the exception of ozone and atomic oxygen, which were the *a priori* ozone and atomic oxygen density profiles, described in Sections 3.4 and 4.2.3, for all days and latitudes. Day 1 and 15 of every month in each seasonal interval were modelled for the six-year average, and the results are shown in Fig. 3.12.
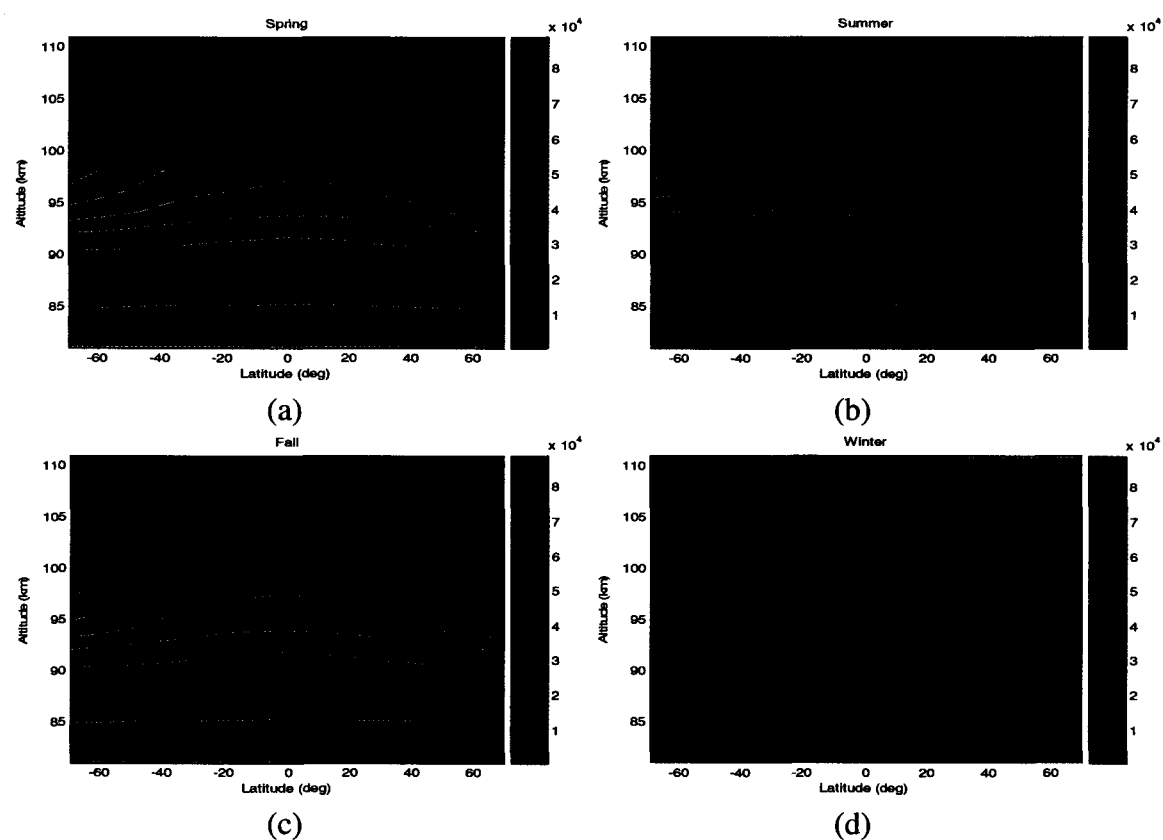
Figure 3.12: Modelled volume emission rates in photons/cm^3/s for the same conditions as Fig. 3.11.

Overall the latitudinal and seasonal structures are in good agreement, as well as the

absolute magnitudes. Both the observed and the modelled data show an increase in volume emission at the winter pole at slightly lower altitudes. Both show little difference between spring and fall at all latitudes. The differences between the observed and modelled datasets are assumed to be due to differences in the ozone and atomic oxygen profiles, errors in the MSIS background atmosphere, and possible uncertainties in the HRDI recovery transmission. Maximum HRDI A-band VER uncertainties were given by *Ratnam et al.* [2004] to be on the order of 10%.

3.6 Forward model

3.6.1 Forward modelling OSIRIS limb irradiances

The kinetic-photochemical model predicts local A-band volume emission rate profiles, $\eta(z)$. These values are then used to simulate observed OSIRIS total band limb irradiances in the A-band region, $I(th)$, in photons/s/cm^2,

$$I(th) = \sum_{z=z_f^*}^{th} \eta(z)PL(th,z)T_f(th,z) + \sum_{z=th+1}^{z_n^*} \eta(z)PL(th,z)T_n(th,z), \quad (3.32)$$

where z_f^* and z_n^* are the top of the atmosphere at the far and near sides of the OSIRIS line-of-sight respectively, $PL(th,z)$ is the path length through a 1 km shell at altitude z when observing tangent height th, and $T_f(th,z)$ and $T_n(th,z)$ are the far and near side transmission functions, respectively, along the OSIRIS line-of-sight from an element at an altitude z to the OSIRIS instrument. Fig. 3.13 illustrates the geometry represented by Equation 3.32. The top of the atmosphere in the forward model is assumed to be located at an altitude of 140 km. In test cases where the model was extended up to a maximum

57
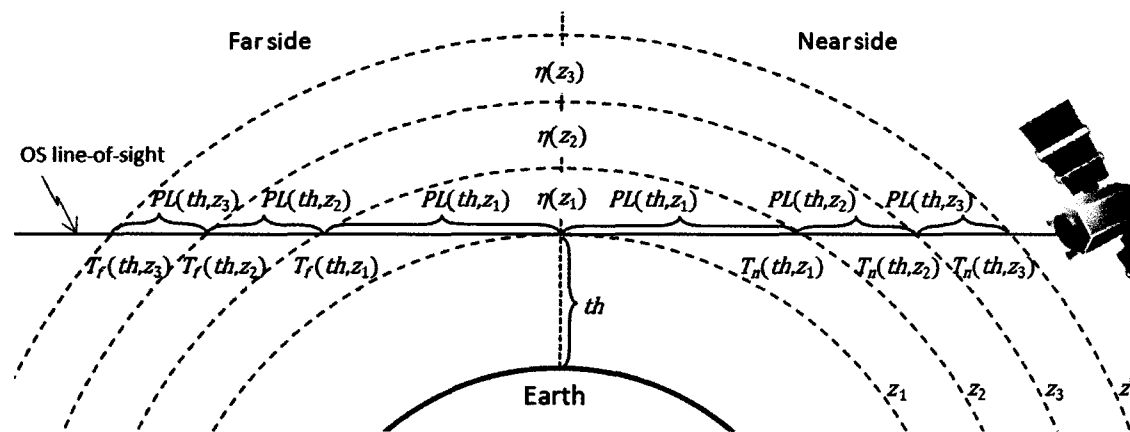
Fig 3.13: Diagram of the OSIRIS viewing geometry represented in the forward model.

altitude of 240 km there was no significant difference in the calculated limb irradiances—differences in the final retrievals were less than 0.1%. Equation 3.32 is analogous to the solution of the general radiative transfer equation where the source function is equal to the total band volume emission rate determined by the kinetic-photochemical model and the transmission function is the average band transmission function as discussed in the proceeding section. Such an approximation is common in radiative transfer models, such as the BANDPAK radiative transfer model [*Marshall et al.*, 1994].

3.6.2 Transmission calculations

The atmospheric transmission function within the A-band region from a given element to the OSIRIS instrument is the product of all transmission functions of subsequent elements within the OSIRIS line-of-sight,

$$T_n(th, z) = \prod_{h=z}^{z_n^*} T(th, h) \tag{3.33}$$

58

$$T_f(th, z) = T_n(th, th) \prod_{h=th}^{z} T(th, h), \quad (3.34)$$

where $T(th, z)$ is the weighted average band transmission through an element at an altitude z for a viewing tangent height of th, given by,

$$T(th, z) = \sum_{i=1}^{N} W(v_i, z) \exp[-[O_2]PL(th, z)\sigma(v_i, z)]\Delta v_i, \quad (3.35)$$

where N is the number of spectral intervals. The weighted band average transmission function and the O_2 absorption cross-sections are calculated line-by-line between 12898 and 13166 cm^{-1} with a spacing of 0.01 cm^{-1}. Results using a spacing of 0.005 cm^{-1} show no significant difference. The absorption cross-sections, again in cm^2/molec, are determined using the 371 A-band line strengths at standard temperature, $S_j(T_s)$, given in the 2004 HITRAN database and assuming a Doppler profile,

$$\sigma(v, z) = \sum_j S_j(T)D_j(v). \quad (3.36)$$

Fig. 3.14 shows the calculated absorption cross-sections at different temperatures for a sample spectral interval within the A-band.

The weighting factor $W(v,z)$, unitless, is the normalized absorption spectrum,

$$W(v, z) = \frac{\sum_j S_j(T)D_j(v)}{S_T}, \quad (3.37)$$

where S_T is the total band strength, in cm^{-1} / (molec cm^{-2}), is calculated using,

$$S_T = \sum_v \sum_j S_j(T)D_j(v). \quad (3.38)$$

In the forward model a fast line-by-line calculation is implemented by storing a pre-

59

calculated array of absorption cross-sections and weighting functions for temperatures between 100 and 600 K with 1 K spacing and wavenumbers between 12898 and 13166 cm^{-1} with a spacing of 0.01 cm^{-1}. However, at a given temperature, cross-sections and weighting functions at wavenumbers where the cross-section values are less than 1×10^{-27} cm^2/molec are omitted from the array. These omissions reduce computation time in each transmission calculation by roughly 80% and show no significant difference in calculated transmission in comparison to calculations using all absorption cross-sections within the spectral interval.
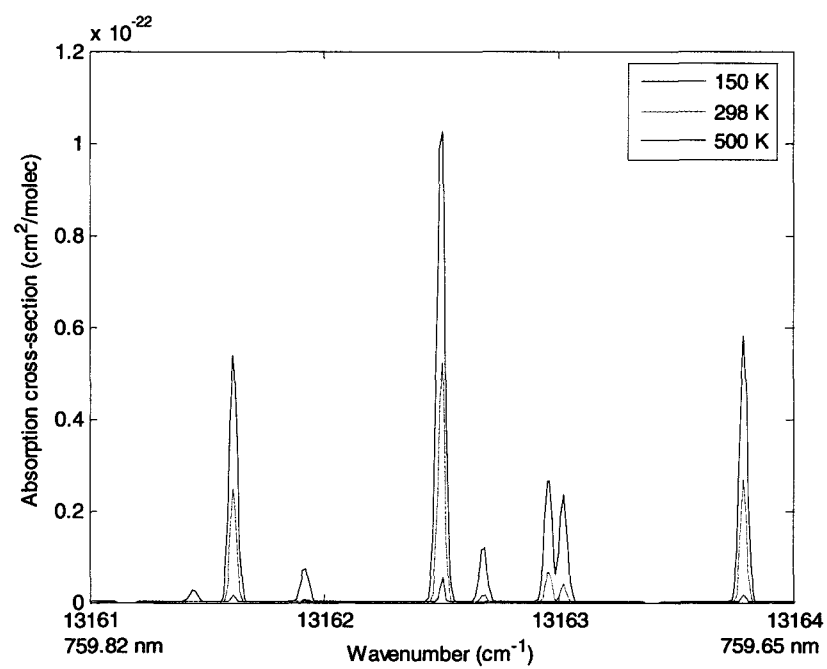
Figure 3.14: Calculated A-band absorption cross-sections at 150 K, 298 K, and 500 K. The increase in line strength with temperature is typical of lines in the wings of the band (shown here), whereas near the band center line strength decreases with temperature.

Fig. 3.15 shows the calculated transmission for all contributing elements at different tangent heights for a typical atmosphere, where the white sections are regions where $z >$

140 km. It can be seen from Fig. 3.16 that very little is transmitted from the far side for an observed tangent height of 65 km, and 50% is transmitted from the far side at an observed tangent height of ~77 km.
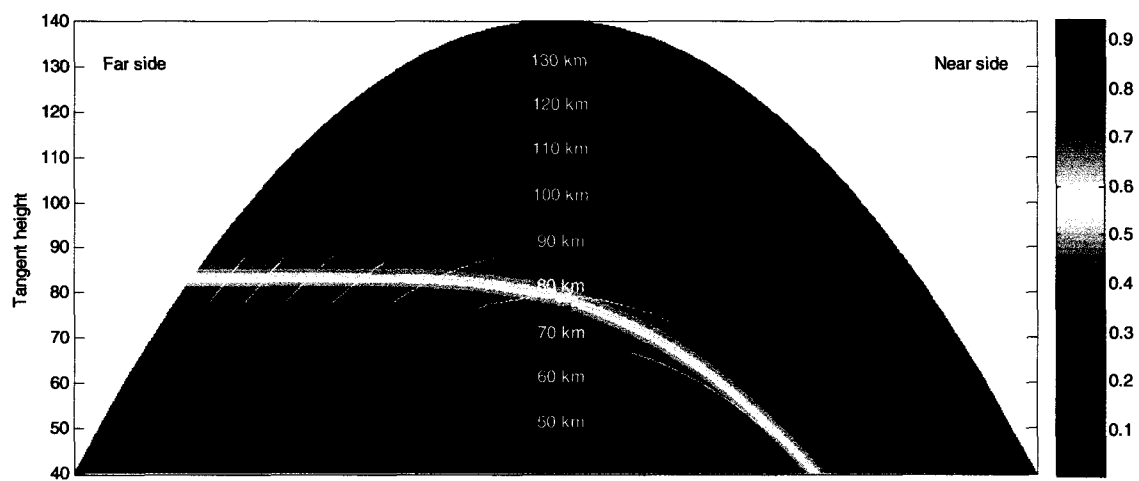
Figure 3.15: Atmospheric cross-section displaying transmission of A-band dayglow for different observed tangent heights, calculated along line-of-sight from element to top of atmosphere. The white curves indicate element height.
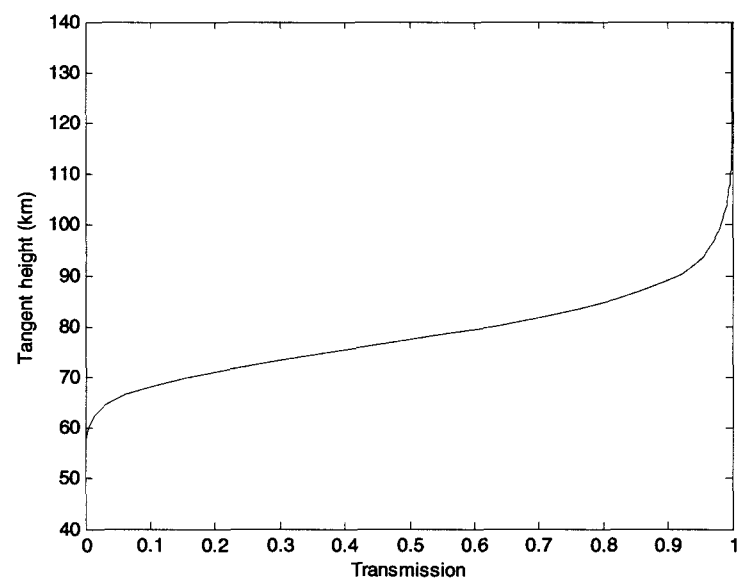
Figure 3.16: Line-of-sight transmission of A-band dayglow, from observed tangent point to top of atmosphere as a function of tangent height.

3.6.3 Comparisons with OSIRIS observations

In Figs. 3.17 and 3.18, forward modelled limb irradiances, in photons/s/cm^2, assuming *a priori* O_3 and associated O profiles, are compared to typical OSIRIS observations of limb irradiances integrated over the A-band region (the integration method is described in Section 4.1.4). The absolute magnitudes of the modelled results are in agreement with the OSIRIS observations. This implies that the kinetic-photochemical and forward models are behaving well and are effective tools for predicting A-band volume emission rates and the OSIRIS line-of-sight transmission. There are however some differences between the forward model and the observations. As previously mentioned, these differences are due to differences between the *a priori* and actual ozone and atomic oxygen densities, which are the quantities to be retrieved in this study.
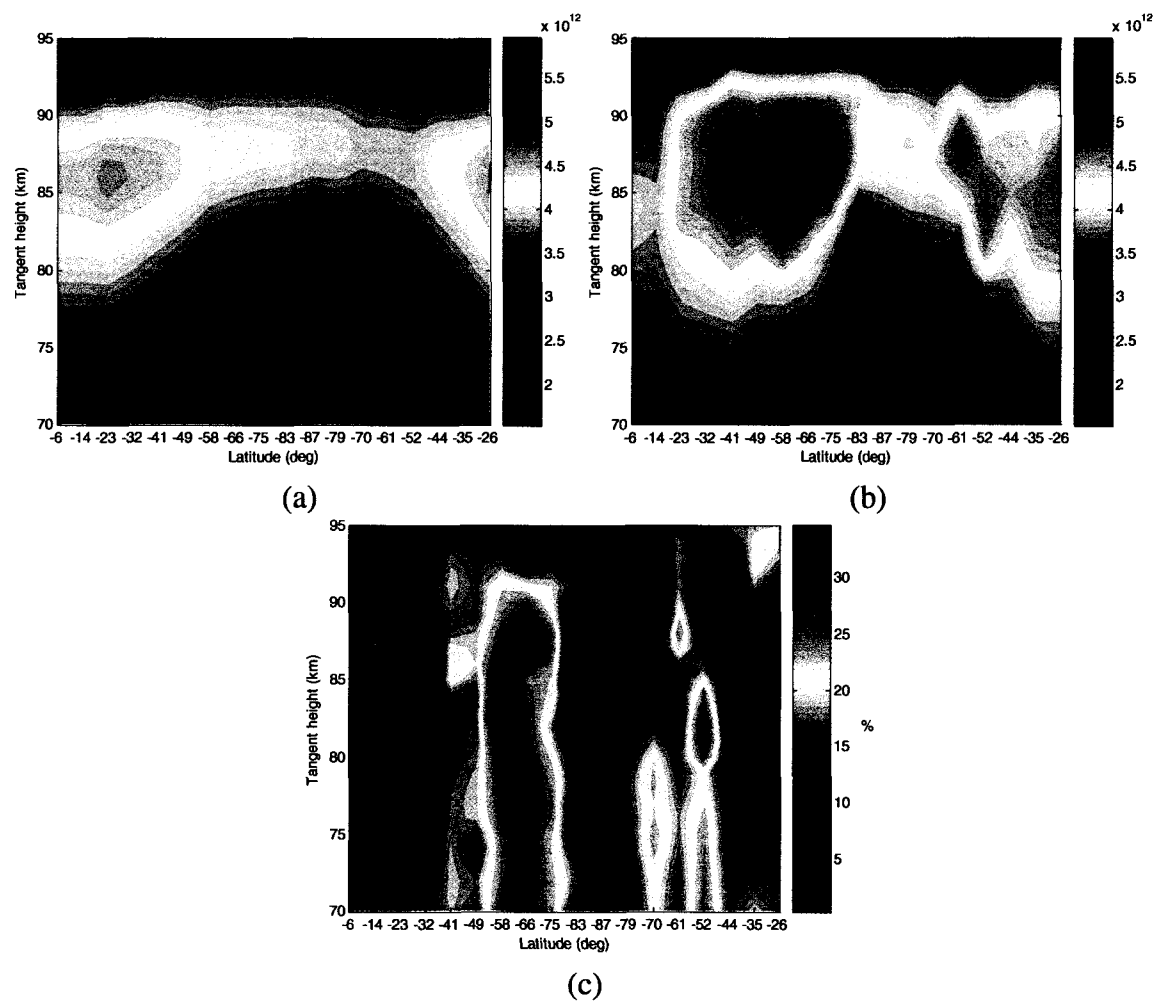
Figure 3.17: Integrated limb irradiances in photons/s/cm^2 for orbit 21033 on 2 Jan. 2005, (a) forward modelled with *a priori* O_3 and (b) OSIRIS observations. (c) Shows the percent difference between the model results and OSIRIS observations.

(a)

(b)

(c)
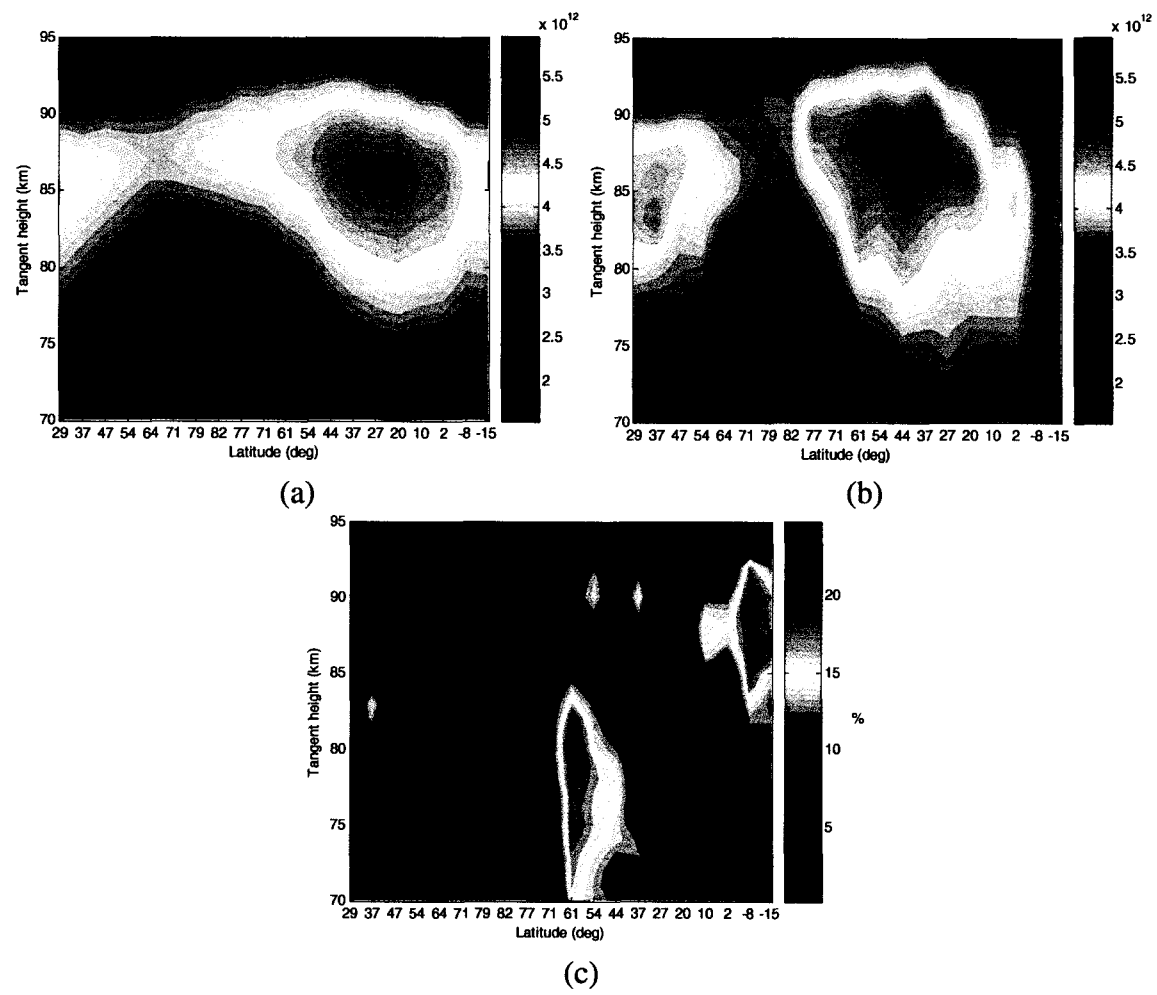
Figure 3.18: Integrated limb irradiances in photons/s/cm^2 for orbit 39695 on 4 June 2008, (a) forward modelled with *a priori* O_3 and (b) OSIRIS observations. (c) Shows the percent difference between the model results and OSIRIS observations.

Chapter 4

Retrieval of ozone densities from OSIRIS observations

This chapter discusses the observed OS Level 1 radiances and details how they were manipulated to produce A-band limb irradiance profiles. The retrieval method that exploits these profiles in order to retrieve ozone density profiles is also described, along with the results of a study that investigates the uncertainties associated with the retrievals.

4.1 OSIRIS observations

4.1.1 OS Level 1 pre-processing

The radiances used in the ozone retrievals are taken from the OS Level 1 data, given in photons/s/cm^2/sr/nm. The Level 1 data is converted from the Level 0 data, given in digital count units of data numbers (DN), a process that also corrects for internal scattering and the OS CCD dark current and DC bias. The following describes the conversion/correction

process, as detailed by *Haley and Sioris* [2001].

Each pixel p in the OS CCD array generates a photocurrent I_p, in electrons/s, that is induced by the incident radiance, I_λ, in photons/s/cm^2/sr/nm. The generated photocurrent is related to the radiance through the pixel response function R_p,

$$I_p = I_\lambda R_p, \qquad (4.1)$$

where R_p is the product of the pixel area A_p, the solid angle of the pixel Ω_p, the dispersion function $\frac{d\lambda}{dp}$, and the optical and quantum efficiencies of the array OE and QE, respectively, and has units of electons cm^2 sr nm/pixel/photon,

$$R_p = A_p \Omega_p \frac{d\lambda}{dp} OE * QE. \qquad (4.2)$$

Before the pixel photocurrent is read off the array, the pixel columns are binned on-chip. N_{on} is the number of pixels binned within the column. For each OS observation the binned signal (in electrons) is read off the array, digitized, and can be binned a number of times, N_{off}, before being stored as the final Level 0 signal associated with that observation, S_p, in DN. Each pixel has an associated dark current, the correction factor of which is $Dark_p$, in units of electrons/s, and each pixel column has an associated DC bias, the correction factor of which is $Bias_p$, in units of DN. A portion of the signal from a given pixel is due to internally scattered light. The portion of the signal due to internal scattering is expressed as a fraction, γ, of the total signal of the entire pixel column.

Therefore the Level 0 signal at a given pixel column can be expressed as,

$$S_p = \sum_{N_{off}} \left[\sum_{N_{on}} \alpha \left(\int_0^{t_e} I_\lambda R_p dt + \gamma \int_0^{t_e} \int I_\lambda R_p dt \, dp + \int_0^{t_e} Dark_p dt \right) + Bias_p \right], \quad (4.3)$$

where t_e is the OS exposure time and the analog-to-digital conversion factor α has a value

of 0.0699 DN/electron. Equation 4.3 can be approximated as,

$$S_p = N_{off} \left[N_{on} \alpha \left(I_\lambda R_p t_e + \gamma \sum I_\lambda R_p t_e + Dark_p t_e \right) + Bias_p \right]. \quad (4.4)$$

As discussed by *Haley and Sioris* [2001], the difference between the terms $\gamma \sum I_\lambda R$ and

$\gamma \sum I'_p$ is on the order of 0.5%, where I'_p, in electrons/s, is defined as,

$$I'_p = \left(\frac{S_p}{N_{off}} - Bias_p \right) \frac{1}{N_{on} t_e \alpha} - Dark_p, \quad (4.5)$$

and therefore, solving Equation 4.4 for I_λ yields,

$$I_\lambda = \frac{\left(\frac{S_p}{N_{off}} - Bias_p \right) \frac{1}{N_{on} t_e \alpha} - Dark_p - \gamma \sum I'_p}{R_p}. \quad (4.6)$$

Equation 4.6 describes the process that is undergone to convert OS Level 0 data, in DN,

to the corresponding Level 1 radiances, in photons/s/cm^2/sr/nm.

4.1.2 OS Level 1 radiance uncertainty

The signal uncertainty for a given pixel, δS_p, is due to uncertainties in pixel dark current

and internal scattering, and due to photon and electron shot noise. *Haley and Sioris*

[2001] show that the pixel signal uncertainty, in DN, can be approximated as,

$$\delta S_p = \sqrt{ \left[\left(\frac{S_p}{N_{off}} - Bias_p \right) \alpha + (ROE)^2 + \left(\frac{1}{2} \right)^2 \right] N_{off} }, \quad (4.7)$$

where the readout noise, *ROE*, has a value of 1.2 DN RMS, and the factor of ½ is due to DN rounding.

Substituting Equation 4.5 into Equation 4.6 gives,

$$I_\lambda = \frac{I_p' - \gamma \sum I_p'}{R_p}. \tag{4.8}$$

From Equation 4.5 it can be seen that the uncertainty in I_p', in electrons/s, is given by,

$$\delta I_p' = \sqrt{\left(\frac{\delta S_p}{N_{off} N_{on} t_e \alpha}\right)^2 + \left(\frac{\delta Bias_p}{N_{off} N_{on} t_e \alpha}\right)^2 + \left(\delta Dark_p\right)^2}, \tag{4.9}$$

and the uncertainty in the signal due to the internal scattering, in electrons/s, is given by,

$$\delta\left(\gamma \sum I_p'\right) = \gamma \sum I_p' \sqrt{\left(\frac{\delta\gamma}{\gamma}\right)^2 + \left(\frac{\sqrt{\sum(\delta I_p')^2}}{\sum I_p'}\right)^2} \tag{4.10}$$

$$\approx \delta\gamma \sum I_p'. \tag{4.11}$$

Then, given the definition,

$$I_p'' = I_p' - \gamma \sum I_p', \tag{4.12}$$

and using the result of Equation 4.11, the uncertainty of I_p'', also in electrons/s, is given by,

$$\delta I_p'' = \sqrt{\left(\delta I_p'\right)^2 + \left(\delta\gamma \sum I_p'\right)^2}. \tag{4.13}$$

Then finally, from Equation 4.8 it can be seen that the uncertainty in the OS Level 1 radiance, δI_λ, in photons/s/cm^2/sr/nm, is given by,

$$\delta I_\lambda = I_\lambda \sqrt{\left(\frac{\delta I_p''}{I_p''}\right)^2 + \left(\frac{\delta R}{R}\right)^2}. \qquad (4.14)$$

This value is given in the OS Level 1 data as the radiance error.

4.1.3 Background subtraction

Determining the amount of the observed signal that is solely due to O_2 A-band emission is not a trivial matter. When the A-band emission is observed, depending on the observation tangent height, the background can be anywhere from 5 – 40% of the observed signal.

At lower tangent heights, around 65 km, the background source is mainly solar radiation scattered within the line-of-sight due to Rayleigh-scattering. As the multiple scattering contribution (radiation that has previously been scattered by the atmosphere prior to scattering within the line-of-sight) to the Rayleigh-scattered signal above 40 km in the A-band is only ~5%, as seen in Fig. 4.1, the background can be considered to be due solely to single scattering. At these heights, only a small fraction of a spectrally continuous radiation source in the A-band region, such as the Rayleigh-scattered background source, is absorbed by the narrow A-band absorption lines. Therefore, nearly all of the radiation is considered to be transmitted and observed by OSIRIS.

At higher tangent heights, around 95 km, the background signal is dominated by baffle scatter due to off-axis radiation reflected from the bright Earth below [*Llewellyn and Gattinger*, 1998]. This source is also considered spectrally continuous over the A-band region. Simulations of the transmission function for this source, assumed to emit
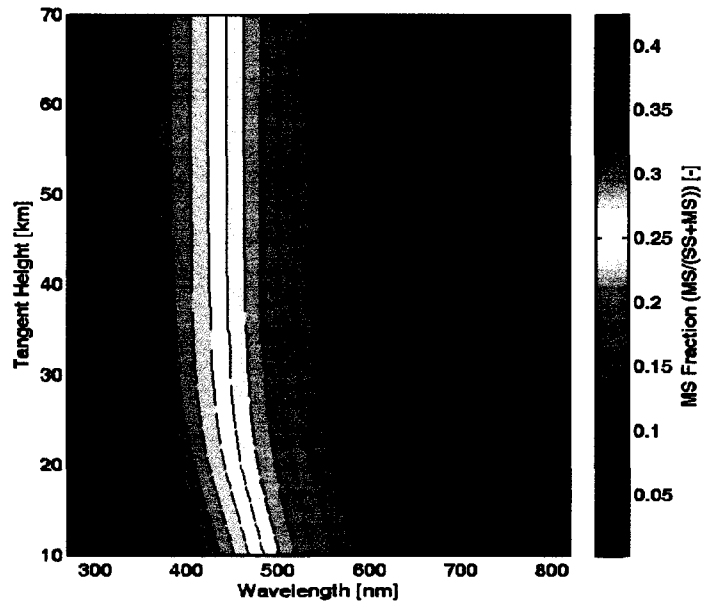
Figure 4.1: Contribution of multiple-scattered light to the total limb-scatter radiance, calculated using the LIMBTRAN model for a solar zenith angle of 70°, from *Haley* [2008].

normal to the Earth's surface, show that the effects of pressure-broadening of the absorption lines lead to an atmospheric transmission, integrated over the A-band region, of 95%, as seen in Fig. 4.2.

These simulations show that pressure-broadened A-band lines are narrow enough to allow significant transmission of radiation at wavelengths between the lines. This is consistent with the findings of *Slanger et al.* [1997], where ground-based instruments were able to observe both the nightglow continuum in the A-band region and distinct $^{18}O^{16}O$ (*b-X*) 0-0 nightglow emission lines between $^{16}O_2$ A-band absorption lines. The transmission, however, needs to be corrected for the slant path of the incoming radiation incident on the source surface. For example, with a solar zenith angle of 60°, the total transmission of incoming radiation in the A-band region is ~90%, giving a final observed

70
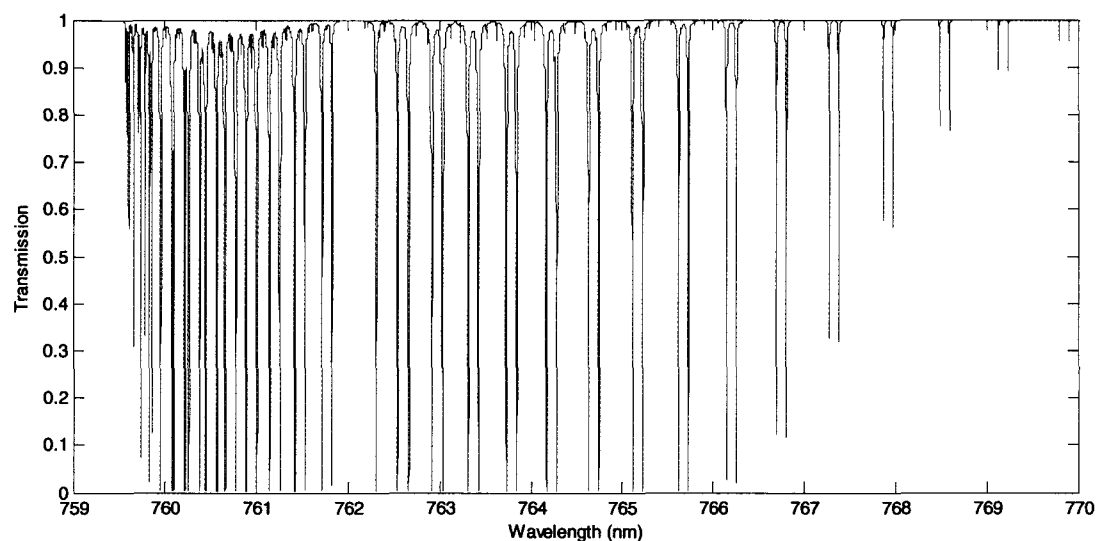
Figure 4.2: Atmospheric transmission in the A-band region calculated in the nadir from Earth's surface to top of atmosphere. Spectrally integrated transmission is equal to 0.95.

transmission of ~86%.

Therefore, at all observed tangent heights, an initial background is interpolated from the observed radiances just beyond the wings of the A-band where any additional sources of emission and absorption are assumed insignificant. Since the A-band region corresponds to pixel numbers 1215 – 1238 (758.8 – 768.2 nm), to determine the background within that region a least squares linear fit is taken of the signal values for pixels 1200 – 1214 (752.8 – 758.4 nm) and 1239 – 1253 (768.6 – 774.2 nm). It is then necessary to determine how much of the background signal is due to Rayleigh-scatter and how much is due to baffle scatter.

Values for the fraction of baffle scatter contribution to the Rayleigh-scattered contribution at 700 nm, f, are given by *Llewellyn et al.* [2004] and can be fit to the exponential equation,

71

$$f(th) = 0.0013e^{0.1157th}, \tag{4.15}$$

where *th* is the observed tangent height in km. Using Equation 4.15, the percentage of the calculated linear background to be subtracted from the A-band radiances, *PB*, at a specific tangent height is given by,

$$PB(th) = 1 - \frac{1 - T_{baffle}}{1 + 1/f(th)}, \tag{4.16}$$

where T_{baffle} is the assumed total atmospheric transmission of the baffle scatter radiation within the A-band. Fig. 4.3 shows the observed OSIRIS A-band spectra at different tangent heights along with the corresponding background and corrected signals.
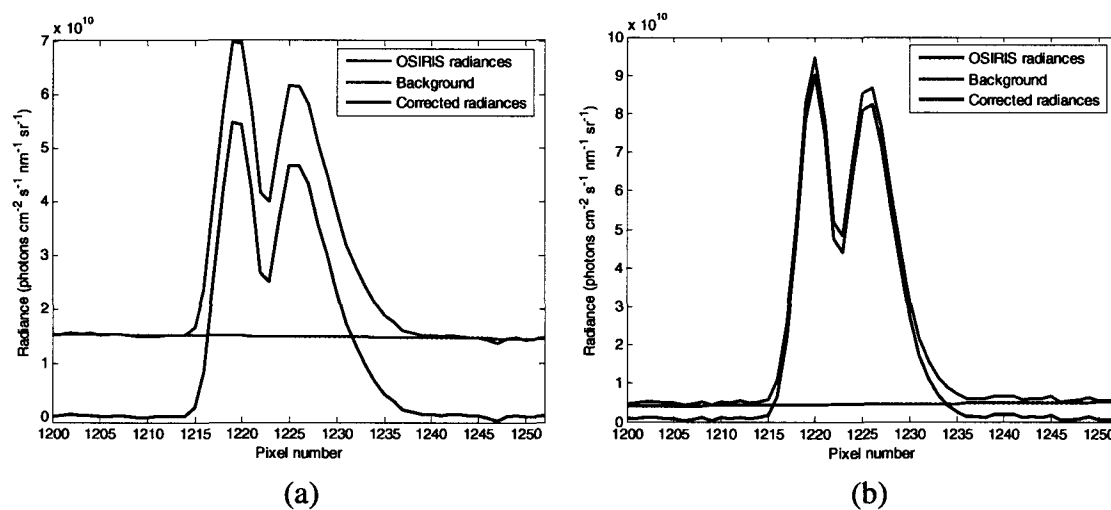
Figure 4.3: Background subtracted radiances from observed OSIRIS data at a tangent height of (a) 65 km and (b) 95 km.

4.1.4 Limb irradiance and error profiles

Total band radiances are calculated by summing over the observed pixelated OSIRIS A-band spectrum between pixels 1215 and 1238. Band radiance errors are calculated by

72

summing the corresponding pixelated radiance errors in quadrature. Limb irradiance profiles (and their corresponding error profiles) are then calculated by simply multiplying the band radiance values by 4π steradian and by the OSIRIS dispersion function, $\frac{d\lambda}{dp}$, which has a value of 0.49 nm/pixel, as determined by the Level 1 data. Typical total band limb irradiances and their associated error estimates, including the assumed background subtraction error discussed in the previous section, are plotted in Fig. 4.4. The limb irradiance profile is also referred to as the measurement in the following sections. As well, the error in the limb irradiance is referred to as the measurement error, and tends to be greater at lower tangent heights. However, overall, the error is typically quite low, <10%.

The nine OSIRIS scans that are used in Fig 4.4. are used throughout the study to display typical retrieval properties. Table 4.1 displays relevant viewing properties of these nine scans.

OSIRIS scan number	Date (yy/mm/dd)	Average latitude (°)	Average longitude (°)	Average solar zenith angle (°)	Average local time (h)
7450007	02/07/06	72	335	61	16.4
12913012	03/07/08	73	153	61	16.4
18802015	04/08/05	21	150	78	6.6
21030035	05/01/02	-81	249	69	18.6
26936026	06/02/01	-21	305	78	6.6
36888033	07/11/14	-63	138	78	18.9
36911027	07/11/30	-76	125	66	6.8
42444022	08/12/05	-41	63	64	6.9
42444023	08/12/05	-48	63	63	6.9

Table 4.1: Relevant viewing properties of the nine OSIRIS scans displayed in Fig. 4.4. Average values refer to values at the observed tangent point.
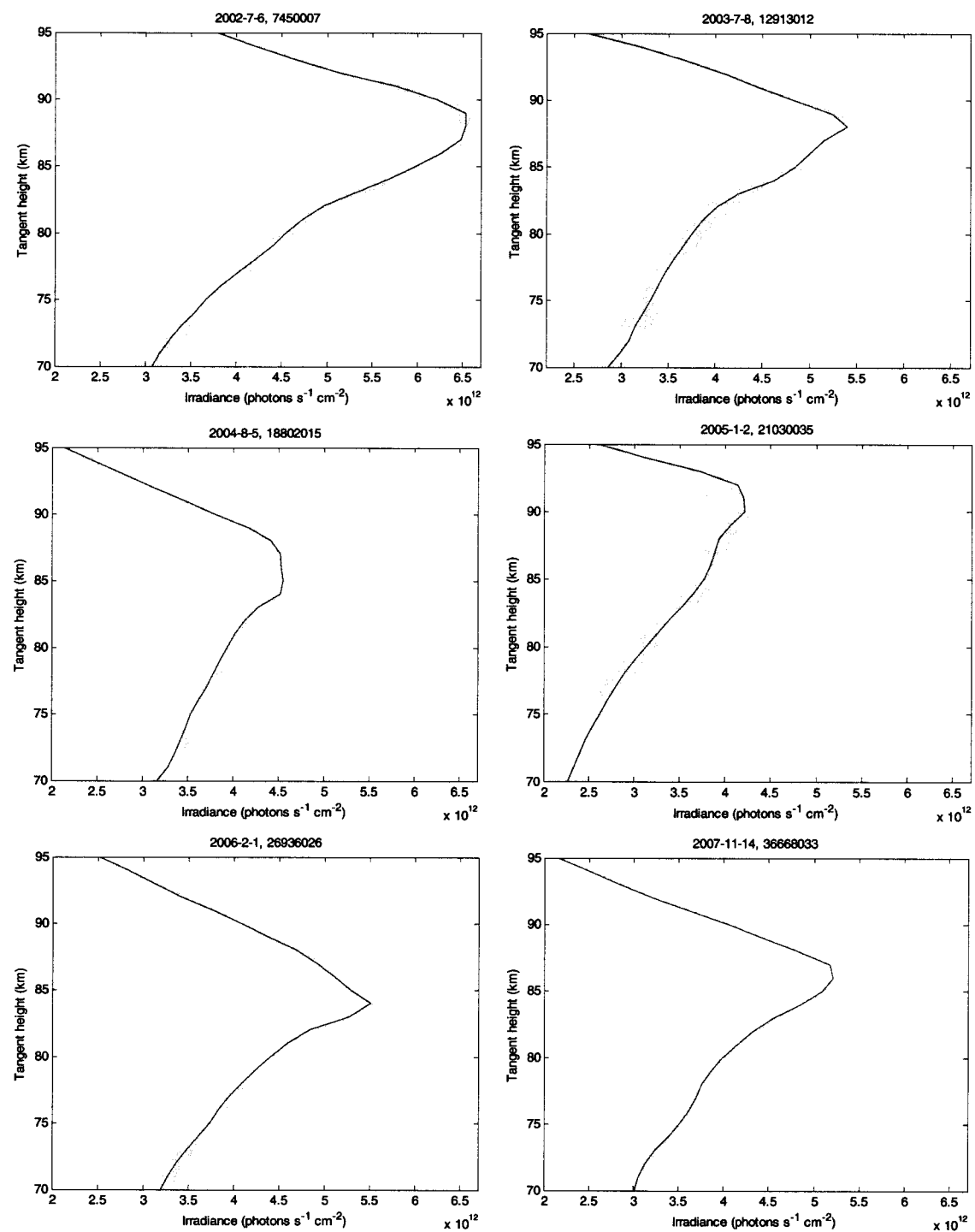
Figure 4.4: Total A-band limb irradiances (blue) and corresponding measurement error (shaded) for typical scans throughout the dataset.

74
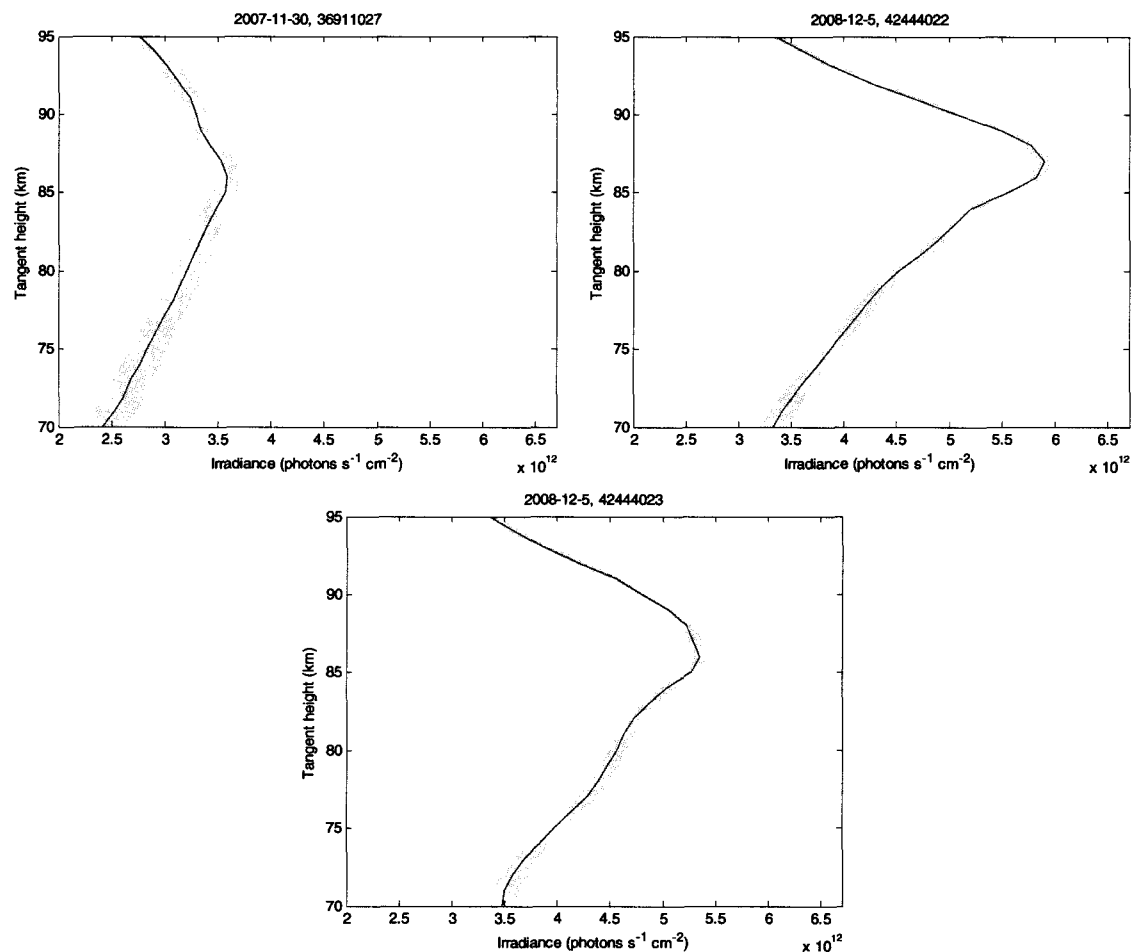
Figure 4.4: Total A-band limb irradiances (blue) and corresponding measurement error (shaded) for typical scans throughout the dataset (cont'd).

4.2 Optimal estimation

The retrieval of atmospheric constituent densities from indirect measurements of an associated property requires solving an inverse problem. One method of retrieving the state of the atmosphere from indirect measurements exploits Optimal Estimation techniques, whereby a statistically optimal solution of the state is determined from an ensemble of possible states without solving the inverse problem directly. The optimal

estimation theory described in this section has been adapted from *Rodgers* [2008]. As in *Rodgers* [2008], variables in bold lowercase denote vectors and variables in bold uppercase denote matrices.

4.2.1 Background theory

In the ideal case, the quantity being retrieved, known as the state vector $\mathbf{x}$, is related to the measurement vector $\mathbf{y}$ via a forward model $\mathbf{F}(\mathbf{x})$,

$$\mathbf{y} = \mathbf{F}(\mathbf{x}). \tag{4.17}$$

In this study the state vector will be the local ozone density profile, and the measurement vector will be the observed OSIRIS limb irradiance profile. Ideally, given the measurement vector, the inverse of the forward model could be used to retrieve the state vector,

$$\mathbf{x} = \mathbf{F}^{-1}(\mathbf{y}). \tag{4.18}$$

A major issue with inverse problems however, is that quite often the solution $\mathbf{x}$ is highly sensitive to various sources of error. Errors in the measurement and/or model parameters can be greatly amplified in the solution resulting in an unreasonable "exact" solution. An "exact" solution is one that returns the exact measurement when substituted back into Equation 4.17, however may be unrealistic due to the propagation of errors. Furthermore, measurement errors inherently lead to an infinite ensemble of possible solutions for $\mathbf{x}$ within the measurement error. To improve the solution, *a priori* knowledge of the state, $\mathbf{x}_a$, can be introduced as a constraint.

An optimal estimate of the state vector $\hat{\mathbf{x}}$ can be obtained by using the weighted

average of two independent measurements of the quantity, x_1 and x_2, with associated error covariance matrices of S_1 and S_2,

$$\hat{x} = (S_1^{-1} + S_2^{-1})^{-1}(S_1^{-1}x_1 + S_2^{-1}x_2). \qquad (4.19)$$

This is analogous to the scalar case using the inverse of standard deviation values, σ, as weights,

$$\hat{x} = \left(\frac{1}{\sigma_1^2} + \frac{1}{\sigma_2^2}\right)^{-1}\left(\frac{x_1}{\sigma_1^2} + \frac{x_2}{\sigma_2^2}\right). \qquad (4.20)$$

In the case where there is a linear relationship between x and y, the measurement y with experimental error ε would be related to the true state x through the weighting functions K,

$$y = Kx + \varepsilon, \qquad (4.21)$$

where $K = \frac{\partial y}{\partial x}$ and y has an error covariance matrix of S_ε. Using the state measurement of $K^{-1}y$ as the first measurement, and the *a priori* constraint x_a with a corresponding error covariance matrix S_x, as the second virtual measurement, the optimal estimate is given as,

$$\hat{x} = (S_x^{-1} + K^T S_\varepsilon^{-1} K)^{-1}(S_x^{-1}x_a + K^T S_\varepsilon^{-1} y), \qquad (4.22)$$

with the covariance of the estimate being,

$$\hat{S} = (S_x^{-1} + K^T S_\varepsilon^{-1} K)^{-1}. \qquad (4.23)$$

In the case where the forward model is non-linear, which is the case in this study, the optimal estimate can be found by using the Newtonian iteration method. The forward model is linearized by considering only the first order terms in the Taylor series expansion of the forward model about the estimate x_n,

$$y = F(x_n) + \frac{\partial F}{\partial x}(x - x_n) + 0(x - x_n)^2. \qquad (4.24)$$

As this is an iterative approach, the subscript n is used for the estimate to indicate the iteration step. In this study $x_{n=1}$ is equal to the *a priori*, however this criterion is not required. Equation 4.17 is equivalent to,

$$y = y_n + K_n(x - x_n), \qquad (4.25)$$

where y_n and K_n are the forward model and the weighting functions, respectively, evaluated at x_n. In this case, the two measurements to be combined for the optimal estimation are, $K_n^{-1}(y - y_n + K_n x_n)$ and x_a.

In this iterative approach $x_n \rightarrow \hat{x}$ as $n \rightarrow \infty$, where,

$$x_{n+1} = (S_x^{-1} + K_n^T S_\varepsilon^{-1} K_n)^{-1}[S_x^{-1} x_a + K_n^T S_\varepsilon^{-1}(y - y_n + K_n x_n)]. \qquad (4.26)$$

This can be rearranged, as shown in Appendix A, such that the number of inverse matrices that need to be calculated is minimized, to give,

$$x_{n+1} = x_a + S_x K_n^T (S_\varepsilon + K_n S_x K_n^T)^{-1}[(y - y_n) - K_n(x_a - x_n)]. \qquad (4.27)$$

The covariance of the estimate at each iteration is given by,

$$\hat{S} = (S_x^{-1} + K_n^T S_\varepsilon^{-1} K_n)^{-1} \qquad (4.28)$$

and can be rearranged (also shown in Appendix A) to give,

$$\hat{S} = S_x - S_x K_n^T (S_\varepsilon + K_n S_x K_n^T)^{-1} K_n S_x. \qquad (4.29)$$

This solution is often also referred to as the maximum *a posteriori*, or MAP, solution. As seen in the following section, the same solution for the optimal estimate is reached using Bayes' Theorem, as demonstrated in Appendix B.

78

4.2.2 Implementation

In this study, ozone was retrieved using the Newtonian iteration optimal estimation technique described in the above section. Specifically, the state vector $\mathbf{x}$ in this case represented the local ozone density profile in molec/cm^3, and the measurement vector $\mathbf{y}$ represented the observed OSIRIS A-band profile, as described in Section 4.1.4, measured in photons/s/cm^2. The optimal estimate of the state, or the retrieved ozone profile, $\hat{\mathbf{x}}$ was determined using,

$$\hat{\mathbf{x}} = \mathbf{x}_a + \mathbf{S}_x \mathbf{K}_n^T (\mathbf{S}_\epsilon + \mathbf{K}_n \mathbf{S}_x \mathbf{K}_n^T)^{-1} [(\mathbf{y} - \mathbf{y}_n) - \mathbf{K}_n (\mathbf{x}_a - \mathbf{x}_n)], \qquad (4.30)$$

given the convergence criterion,

$$\frac{|(x_n)_i - (x_{n-1})_i|}{(x_n)_i} < 0.001 \qquad (4.31)$$

for all i elements of the retrieval vector.

As discussed by *Von Savigny* [2002], in cases where the true state differs greatly from the *a priori*, this approach can lead to negative values within the retrieved ozone profiles. Results were thus forced to remain positive by using the logarithmic values of the *a priori* and measurements.

The *a priori* ozone profile $\mathbf{x}_a$ and forward model profile $\mathbf{y}_n$ that were used were the logarithmic values of those described in Chapter 3. As previously mentioned, it is not necessary for the value used for $\mathbf{x}_{n=1}$, or the "first guess", to be the same as the *a priori*, however this was the case in this study for all retrievals.

The covariance matrix $\mathbf{S}_\varepsilon$ is determined in a straightforward manner. It is a diagonal matrix where the diagonal values correspond to the estimated variance at each height of

the logarithmic OSIRIS limb irradiance profile. The relative variance was determined by adding in quadrature an assumed 5% error in the measurement due to estimated errors in the background subtraction and the percent error of the error in the measurement due to instrument noise. This is the measurement error as discussed in Section 4.1.4.

The covariance matrix $\mathbf{S}_x$ is also assumed to be a diagonal matrix with diagonal elements corresponding to the estimated variance at each height of the *a priori* state. Typically this value was determined to be the square of the *a priori* value multiplied by an "uncertainty factor" of 10. However, such a large variance would lead to non-convergence in some retrievals, and the "uncertainty factor" would be lowered to anywhere between ~5 and 0.1, until convergence was met.

Weighting function matrices were calculated numerically by manually perturbing $\mathbf{x}_n$ at each height, running the forward model for the unperturbed and perturbed state, and then comparing the results. The matrix elements were determined using,

$$(K_n)_{ij} = \frac{\partial (y_n)_j}{\partial (x_n)_i} \approx \frac{\Delta (y_n)_j}{\Delta (x_n)_i}, \tag{4.32}$$

where both x_n and y_n refer to the logarithmic values of the elements of $\mathbf{x}_n$ and $\mathbf{y}$, respectively, and i and j are the row and column indices, respectively. Since the problem was found to be only moderately non-linear, in order to save computing time $\mathbf{K}_n$ was only computed at the first iteration. Typical weighting functions are plotted in Fig. 4.5 and a schematic of the entire retrieval process is illustrated in Fig. 4.6.
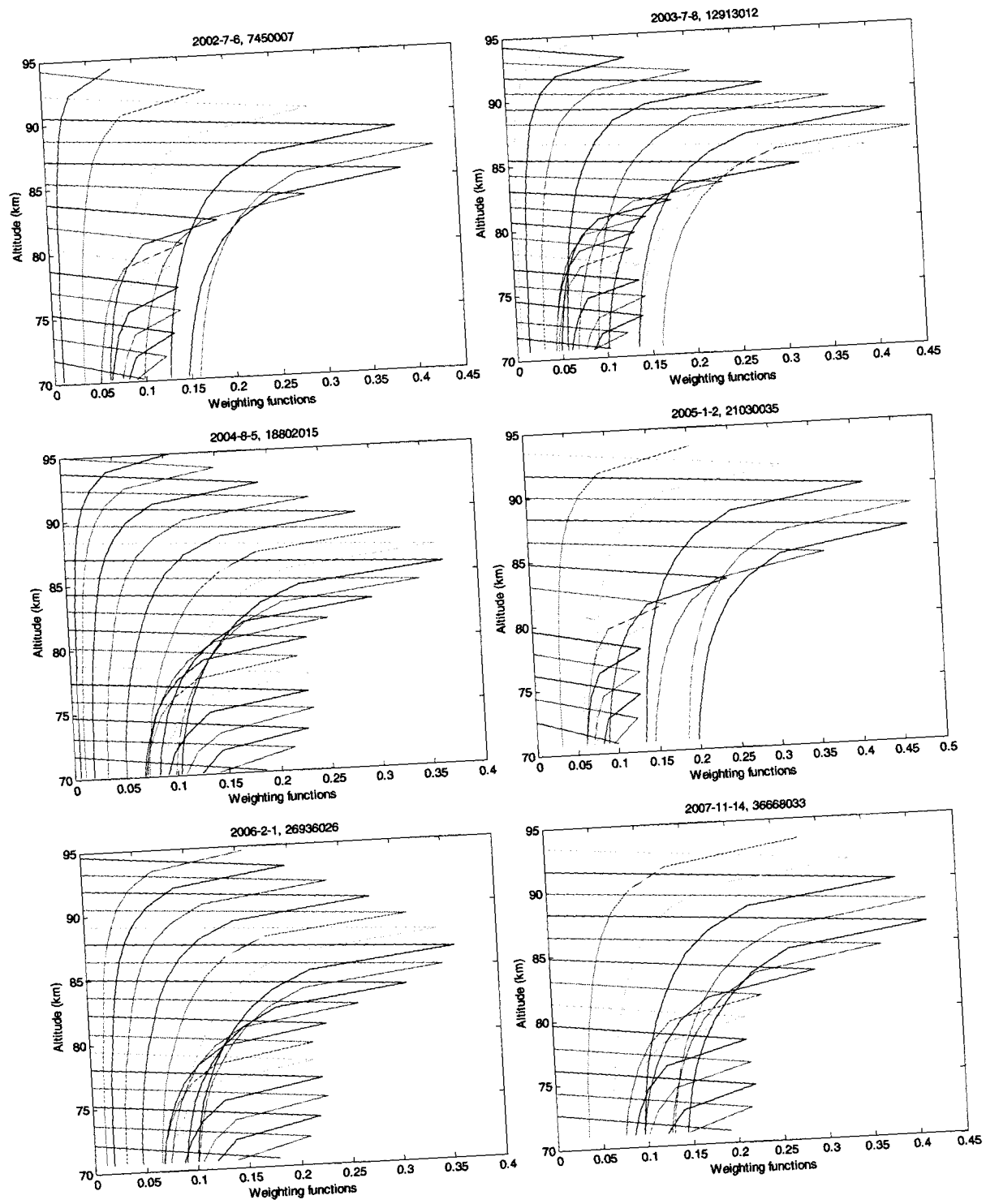
Figure 4.5: Weighting functions for scans corresponding to those of Fig. 4.4. Different colours represent rows of $\mathbf{K}_n$, where the weighting function for a specific tangent height is the row that peaks at that altitude.
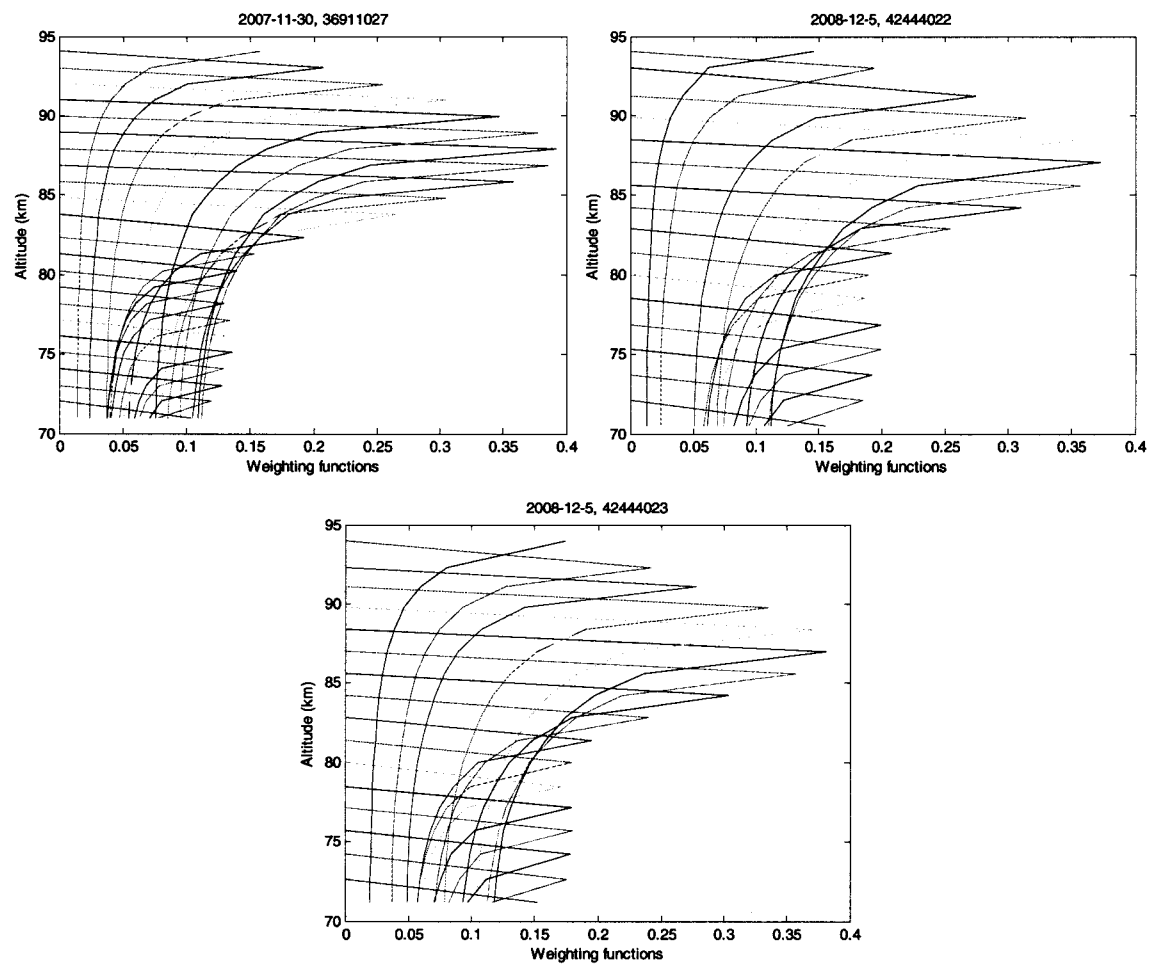
Figure 4.5: Weighting functions for scans corresponding to those of Fig. 4.4. Different colours represent rows of $\mathbf{K}_n$, where the weighting function for a specific tangent height is the row that peaks at that altitude (cont'd).
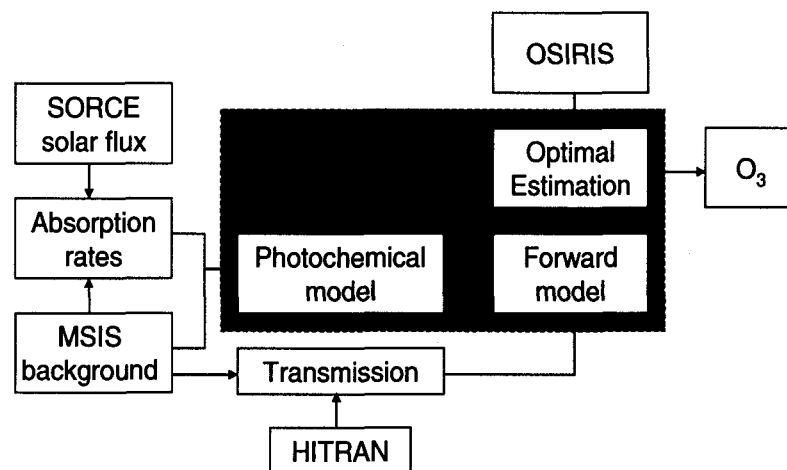
Figure 4.6: Illustration of the overall ozone retrieval process. Steps inside the dashed box indicate an iterative process.

4.2.3 Atomic oxygen retrievals

Atomic oxygen density profiles are inferred from retrieved ozone densities x_n and are updated at each iteration. It is assumed that the retrieved ozone densities are in steady state, and therefore ozone is in photochemical equilibrium with atomic oxygen [*Evans and Llewellyn*, 1973], whereby,

$$[O] = \frac{[O_3](J_3 + k_{O3}[H])}{k_{O2}[O_2][M]},$$ (4.33)

where, $k_{O3} = 2.9 \times 10^{-11} \exp(120/T)$ s^{-1} [*Sander et al.*, 2006] is the reaction coefficient for the reaction,

$$O_3 + H \rightarrow OH + O_2,$$ (4.34)

and $k_{O2} = 6.0 \times 10^{-34} \exp(T/300)^{2.4}$ s^{-1} [*Sander et al.*, 2006] is the reaction coefficient for the reaction,

$$O + O_2 + M \rightarrow O_3 + M.$$ (4.35)

The retrieval begins with an *a priori* atomic oxygen profile that is derived from the *a priori* ozone profile using the method described above, and the atomic hydrogen densities were obtained from the MSIS model.

4.2.4 Incorporating supplemental OSIRIS observations

At altitudes greater than 95 km the A-band volume emission rate is very weakly dependent on the ozone concentration, and therefore ozone is only retrieved up to a height of 95 km. However, OSIRIS does observe a significant amount of A-band airglow above this height, up to roughly 110 km. These contributions need to be incorporated into the retrieval, as dayglow from altitudes greater than the observed tangent height are in the OSIRIS line-of-sight. To allow for this it was assumed that in this region the only significant source of $O_2(b^1\Sigma)$ is due to $O(^1D)$ from the photolysis of molecular oxygen. It was also assumed that above 95 km the atmosphere is not as well mixed as below, and therefore a change in the assumed MSIS O_2 densities at these heights did not represent a similar change in N_2 densities. A similar optimal estimation routine to the one outlined above was developed to retrieve molecular oxygen, using the ozone *a priori* as the assumed ozone profile and the MSIS O_2 densities as the *a priori* for the retrieval. The "retrieved" O_2 densities at these heights were then used in the main ozone retrieval instead of the MSIS values so that the results of the forward model would be consistent with the OSIRIS observations. This method is an alternative to solving for the volume emission rates by inverting the observed OSIRIS radiances. Figure 4.7 shows typical results for these O_2 retrievals. This retrieval method could easily be adapted to retrieve

neutral densities in the lower thermosphere by retrieving the optimal estimate of both O_2 and N_2 densities simultaneously. In this study however, it is sufficient to assume the MSIS N_2 to be correct and only "retrieve" O_2 densities, as the only result required is that of the forward model, and not the true O_2 densities.

(a)   (b)
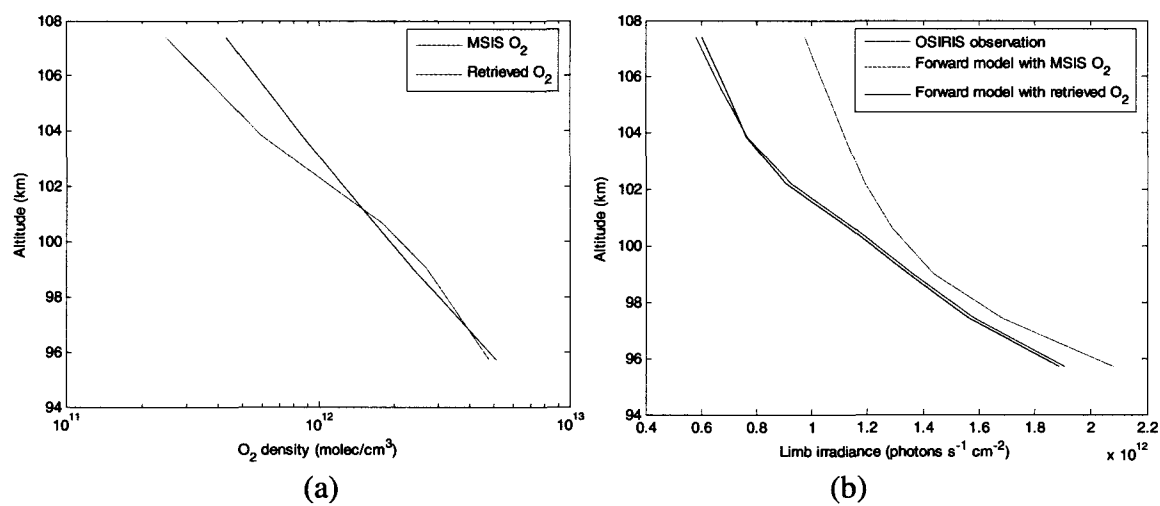
Figure 4.7: Typical results for O_2 density retrievals at tangent heights above the maximum height for O_3 retrievals. (a) Comparison of O_2 densities given by MSIS and the retrieval. (b) Comparison of OSIRIS observations, results of forward model using MSIS, and results of forward model using retrieval densities.

4.3 Error analysis

There are many different sources of error in any type of retrieval and a good understanding and characterization of the errors is essential for interpreting the results. The error analysis methods described in the following sections have been adapted from *Rodgers* [2008].

4.3.1 Quality control

There are two different tests performed on the retrievals to ensure the validity of the results. The first is a test carried out during the retrieval itself to ensure the retrieval agrees with the observation. The forward model is evaluated using the retrieved ozone to find the retrieved measurement $\hat{\mathbf{y}}$, which is then compared with the observation $\mathbf{y}$. The average percent deviation of the retrieved measurement from the observations is determined, and retrievals with an average percent deviation above 5% are assumed to have converged on an erroneous minimum and are therefore rejected.

$$\frac{\sum |\mathbf{y} - \hat{\mathbf{y}}| ./ \mathbf{y}}{N} < 0.05, \tag{4.36}$$

where N is the number of heights in the retrieval and $./$ refers to the division of the corresponding elements within the vectors. Less than 1% of all retrievals were rejected due to this criterion, and comparisons of typical observations with retrieved measurements are shown in Fig. 4.8. The fraction of the retrieved measurement that is attributable to A-band dayglow due to O_3 photolysis can be determined by inputting the retrieval into a modified version of the forward model that only accounts for this source. Fractional contributions to the retrieved measurement from the ozone source for different scans are shown in Fig. 4.9. Contributions are typically between 20 – 40%, slightly greater than typical differences between modelled and OSIRIS observations.

The second test for the purpose of quality control is performed after the retrieval to determine which retrieval vectors contain outliers. For each day's worth of data the ensemble is assumed to be represented by a Gaussian distribution with an ensemble mean

μ_e and standard deviation σ_e. Each retrieval within the ensemble is compared with the mean and if the difference between the two is greater than 3x the standard deviation the retrieval is flagged as containing an outlier,

$$|\mu_e - \hat{x}| > 3\sigma_e. \tag{4.37}$$

Less than 1% of the retrieved data (at individual altitudes) are outliers, and 8% of the retrieved profiles have been flagged.
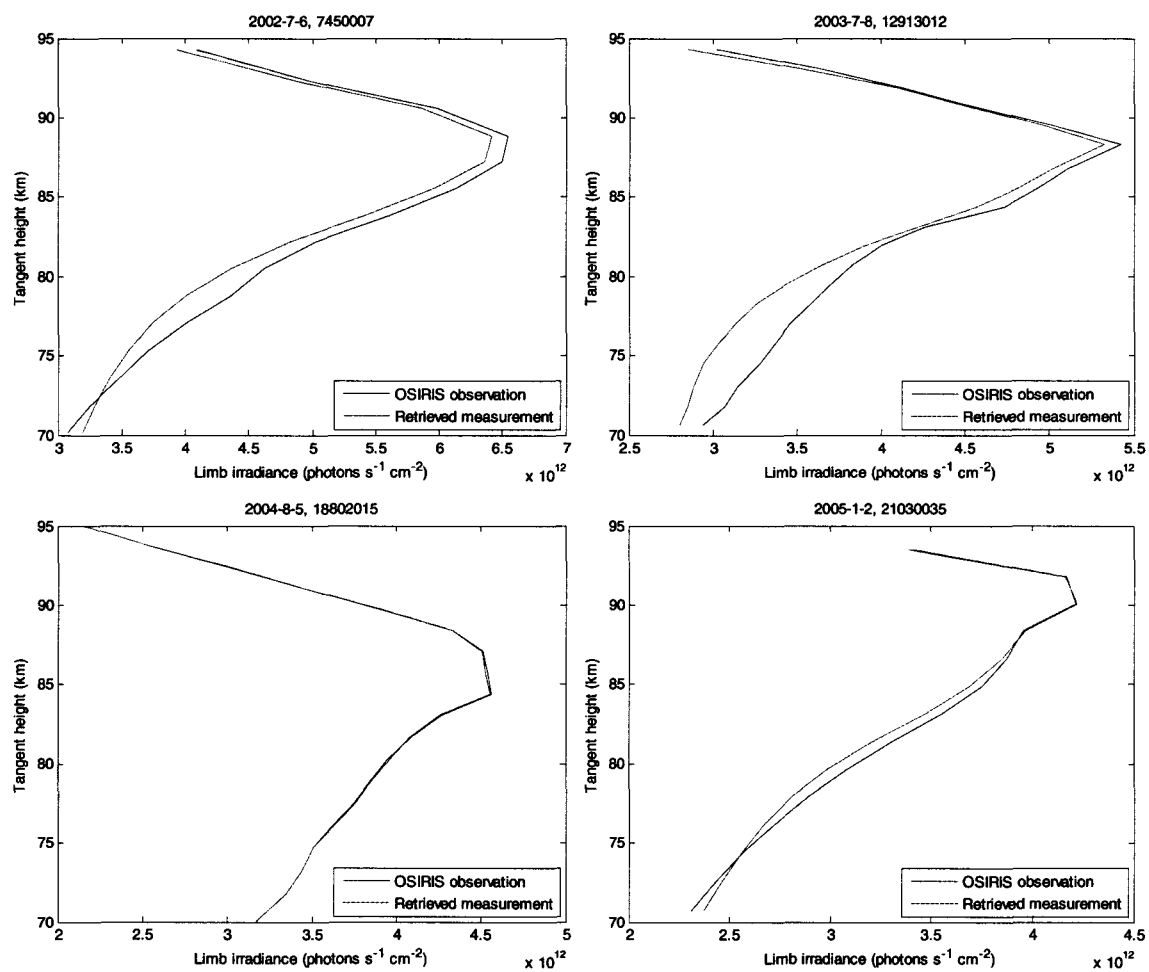
Figure 4.8: Comparisons of OSIRIS observations and retrieved measurements for scans corresponding to those of Fig. 4.4.
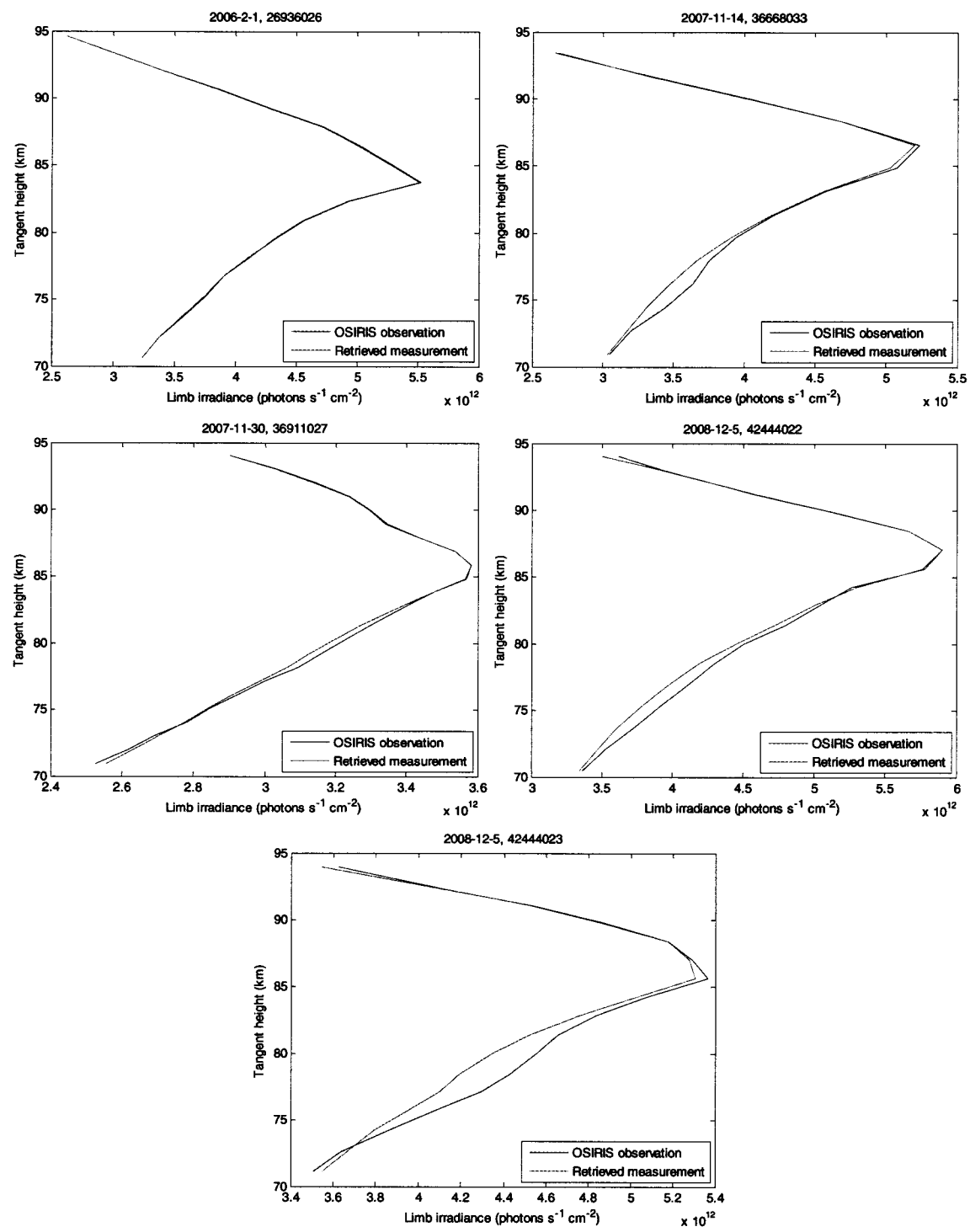
Figure 4.8: Comparisons of OSIRIS observations and retrieved measurements for scans corresponding to those of Fig. 4.4 (cont'd).
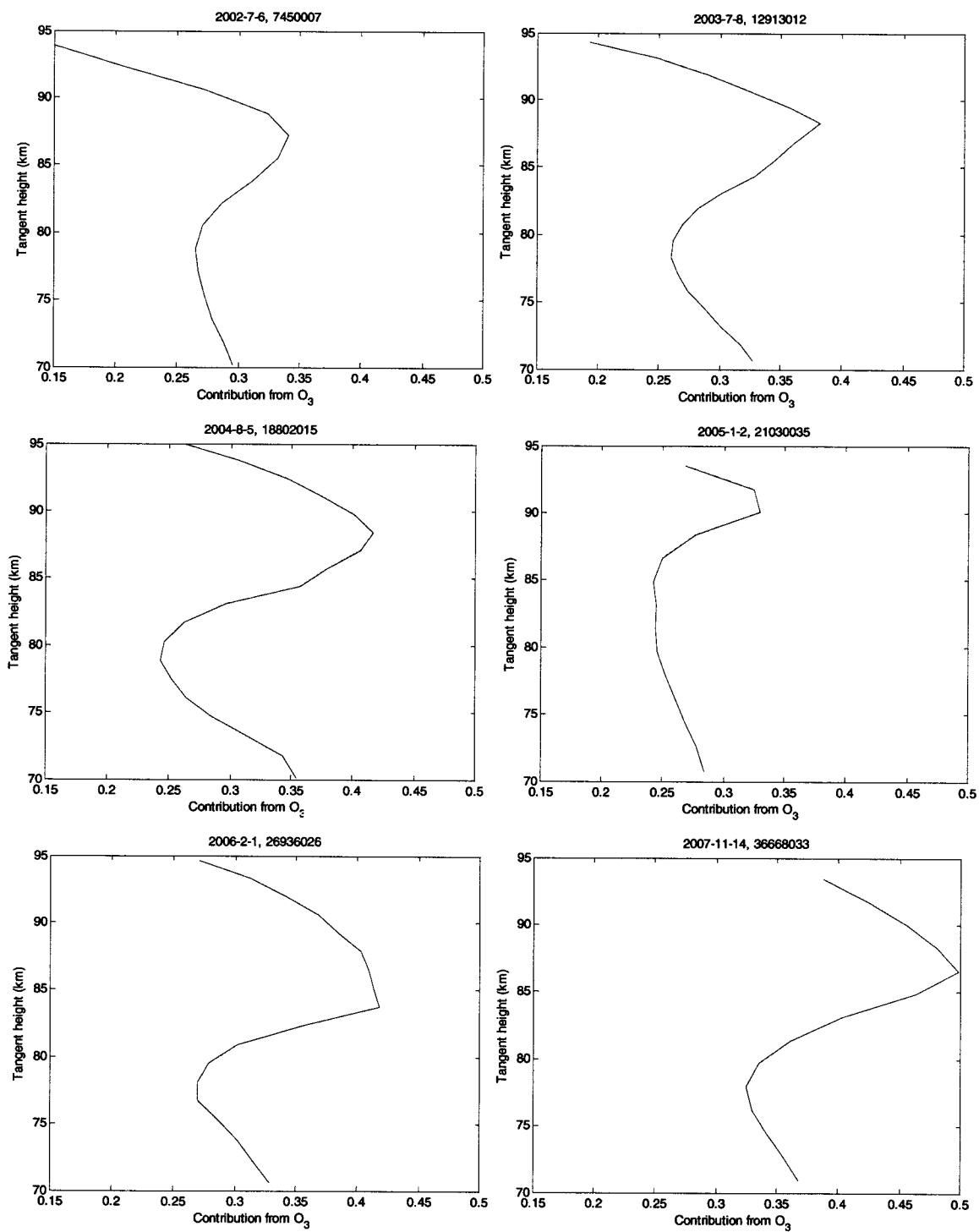
Figure 4.9: Fractional contribution to the retrieved measurement that is attributable to ozone photolysis for scans corresponding to those of Fig. 4.4.
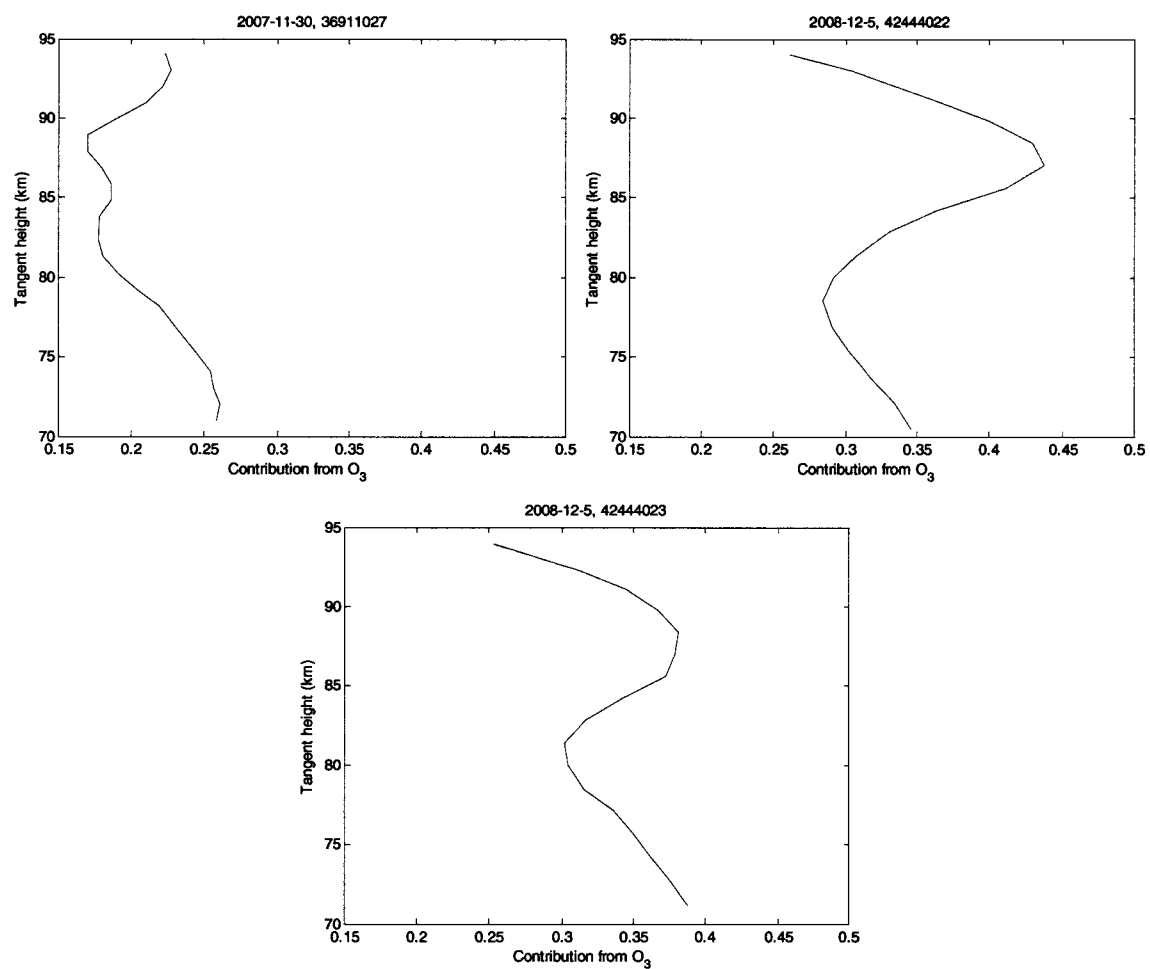
Figure 4.9: Fractional contribution to the retrieved measurement that is attributable to ozone photolysis for scans corresponding to those of Fig. 4.4 (cont'd).

4.3.2 Averaging kernels

A quick method of characterizing the retrievals is to examine the averaging kernels.

Analytically, the averaging kernels are defined as,

$$A = \frac{\partial R}{\partial y}\frac{\partial F}{\partial x} = \frac{\partial \hat{x}}{\partial x}, \tag{4.38}$$

where R is the retrieval function and $\frac{\partial R}{\partial y}$ is known as the contribution function, or the gain

matrix, $\mathbf{G}_y$. It can be seen from Equation 4.38 that the averaging kernels are a measure of the retrieval's dependence on, or response to, the true state. From Equation 4.27 the averaging kernels can be shown to be,

$$\mathbf{A} = \mathbf{G}_y \mathbf{K}_n = \mathbf{S}_x \mathbf{K}_n^T (\mathbf{S}_\varepsilon + \mathbf{K}_n \mathbf{S}_x \mathbf{K}_n^T)^{-1} \mathbf{K}_n. \tag{4.39}$$

Typical retrieval averaging kernels are plotted in Fig. 4.10, and are discussed below in terms of the retrieval response and resolution.
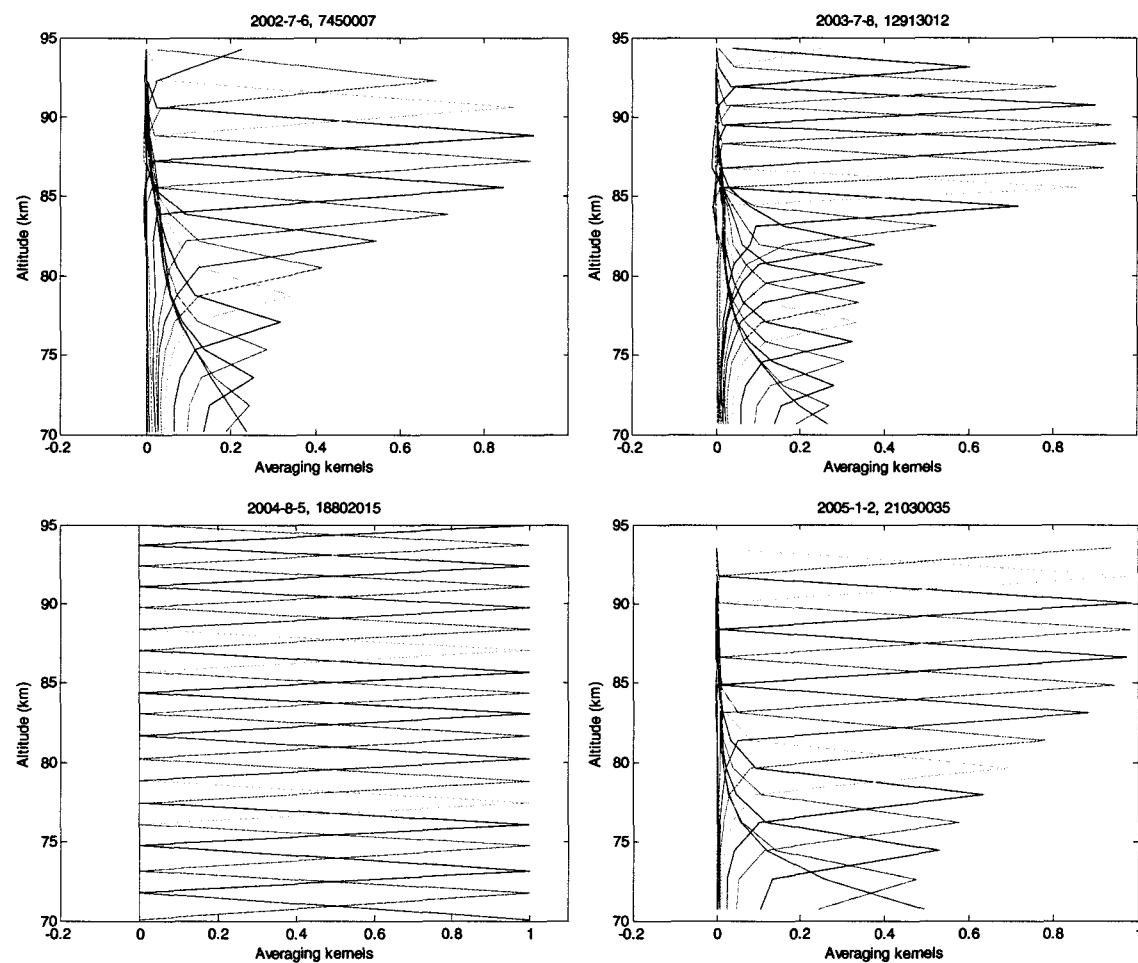
Figure 4.10: Averaging kernels for scans corresponding to those of Fig. 4.4. Different colours represent rows of $\mathbf{A}$, where the averaging kernel for a specific tangent height is the row that peaks at that altitude.
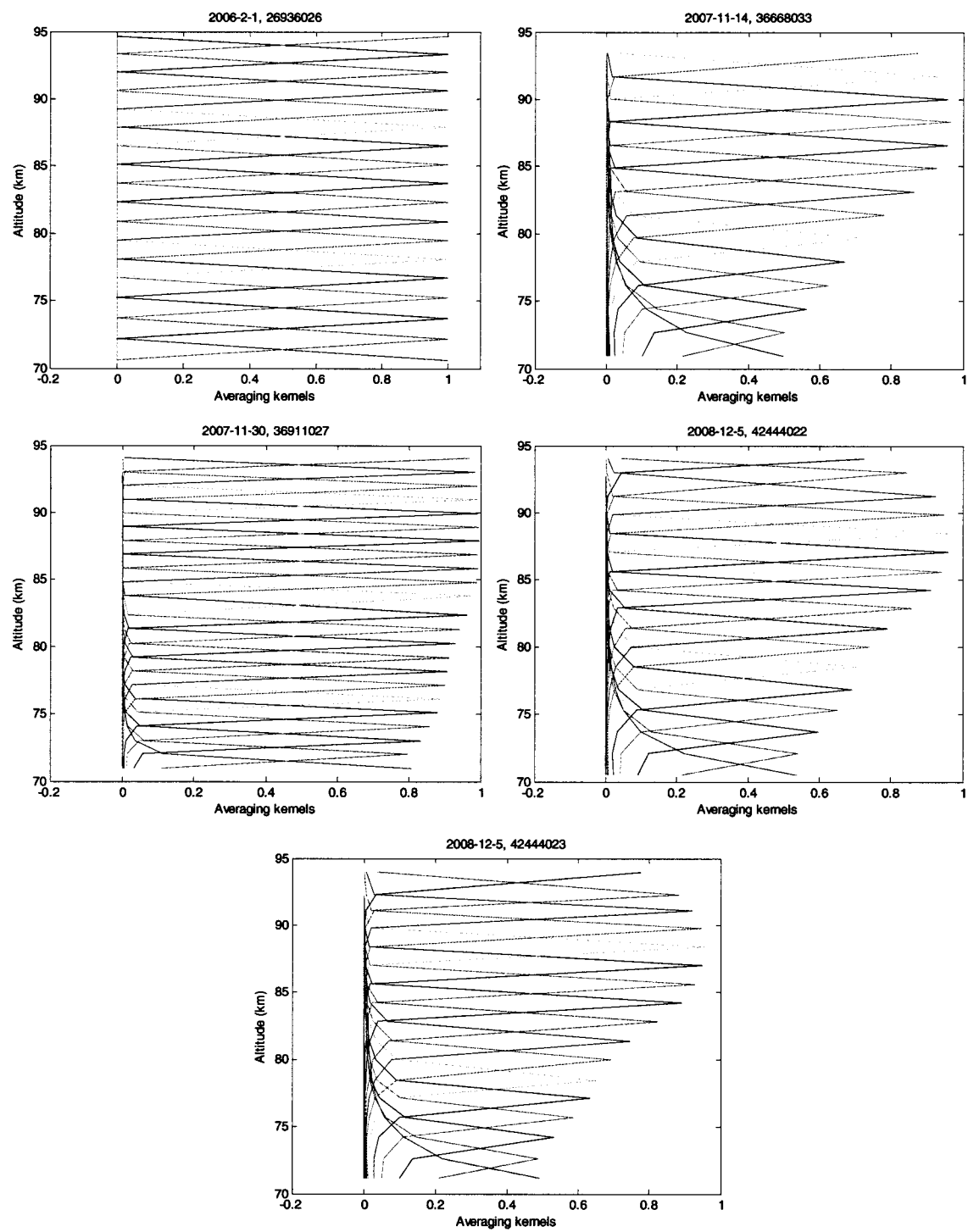
Figure 4.10: Averaging kernels for scans corresponding to those of Fig. 4.4. Different colours represent rows of **A**, where the averaging kernel for a specific tangent height is the row that peaks at that altitude (cont'd).

The averaging kernels are used to determine two characteristics of the retrieval. First is the retrieval response, which is determined at a given altitude by the sum of all averaging kernel values at that height. A response closer to unity at a given height implies that the retrieval is more dependent on the true state, whereas a response closer to zero implies the retrieval is more dependent on the *a priori*. Typically, it is desirable to have a response greater than ~0.7. The calculated retrieval responses corresponding to the averaging kernels seen in Fig. 4.10 are plotted in Fig. 4.11, and show typical responses are close to unity.
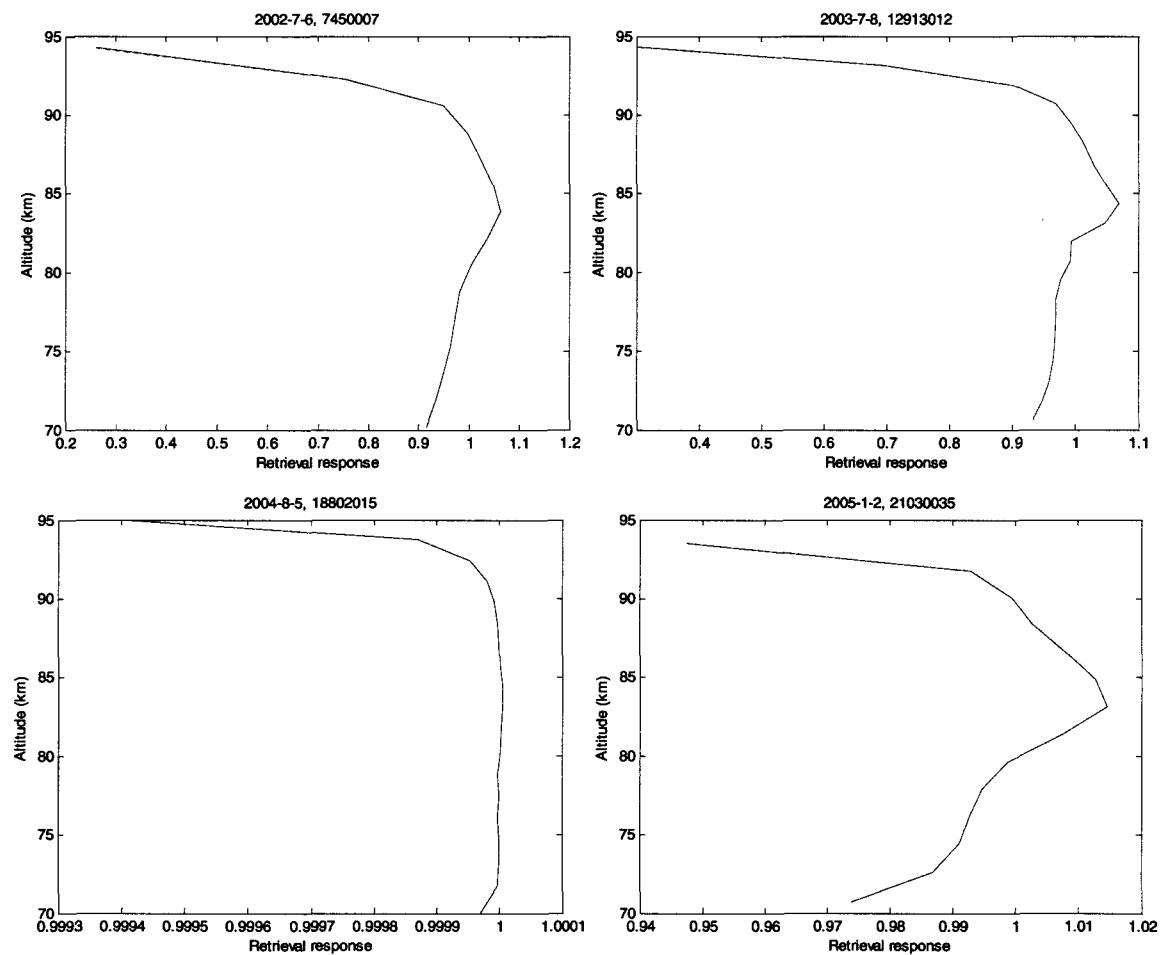
Figure 4.11: Retrieval response for averaging kernels plotted in Fig. 4.10.
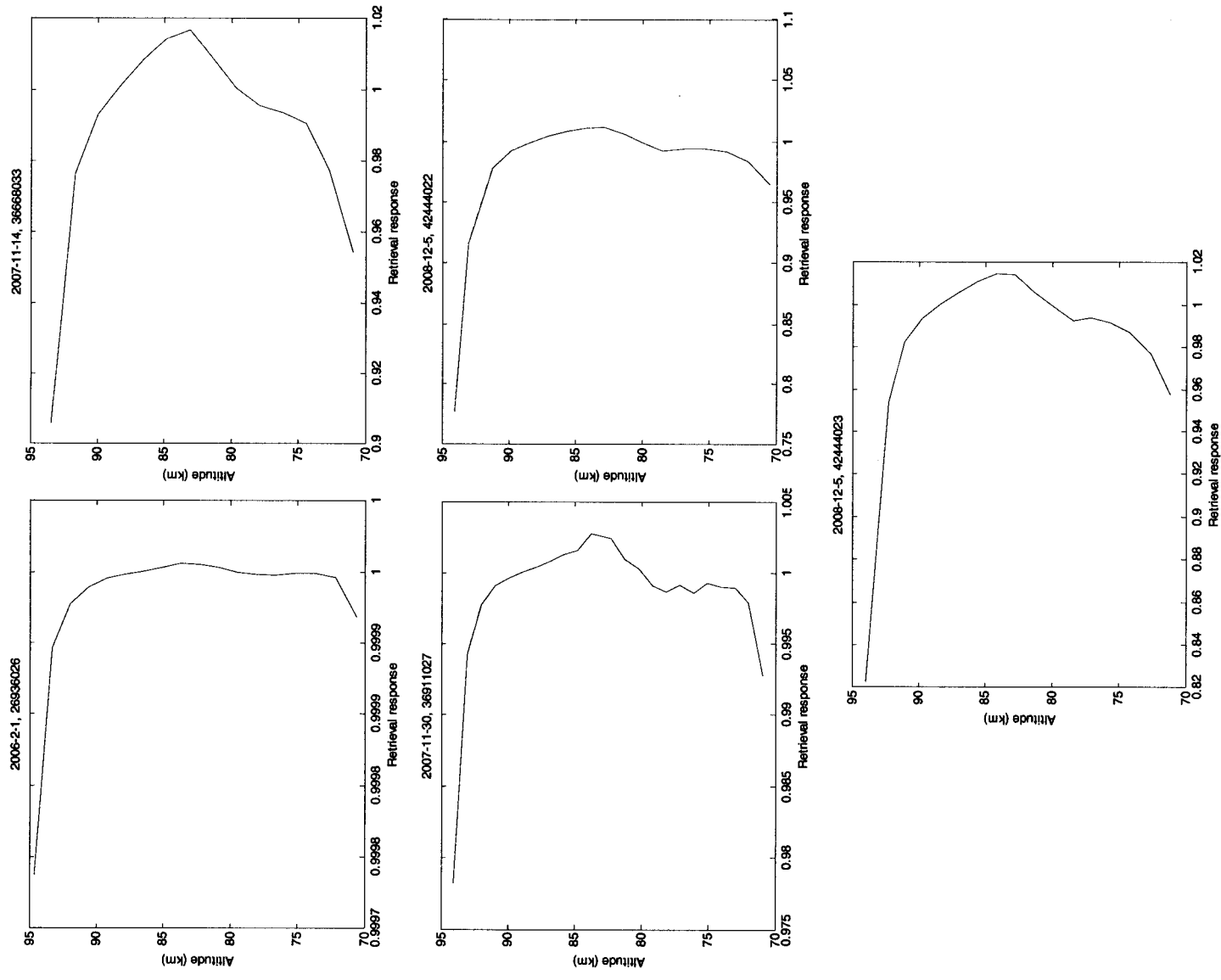
Figure 4.11: Retrieval response for averaging kernels plotted in Fig. 4.10 (cont'd).

The response is quite close to unity for the typical retrieval, and tends to decrease

slightly with decreasing altitude; however, for most retrievals response remains above 0.9. Also, above ~92 km, the retrieval response tends to drop off significantly with altitude.

The second characteristic is the retrieval resolution, which is determined by the width of the averaging kernels. The individual averaging kernels (rows of **A**) are essentially smoothing functions. In an ideal retrieval the averaging kernel matrix would simply be an identity matrix, *i.e.* delta functions, with zero smoothing. The width of the averaging kernel can be defined in different ways; here it is simply defined as the full-width half-maximum (FWHM). The retrieval resolutions corresponding to the averaging kernels in Fig. 4.10 are plotted in Fig. 4.12.

Retrieval resolution tends to decrease with altitude and increases at both the upper and lower limits of the retrieval altitudes. Away from the height limits resolution is typically between 1.2 and 2.5 km, which is slightly greater than the typical OSIRIS vertical resolution.
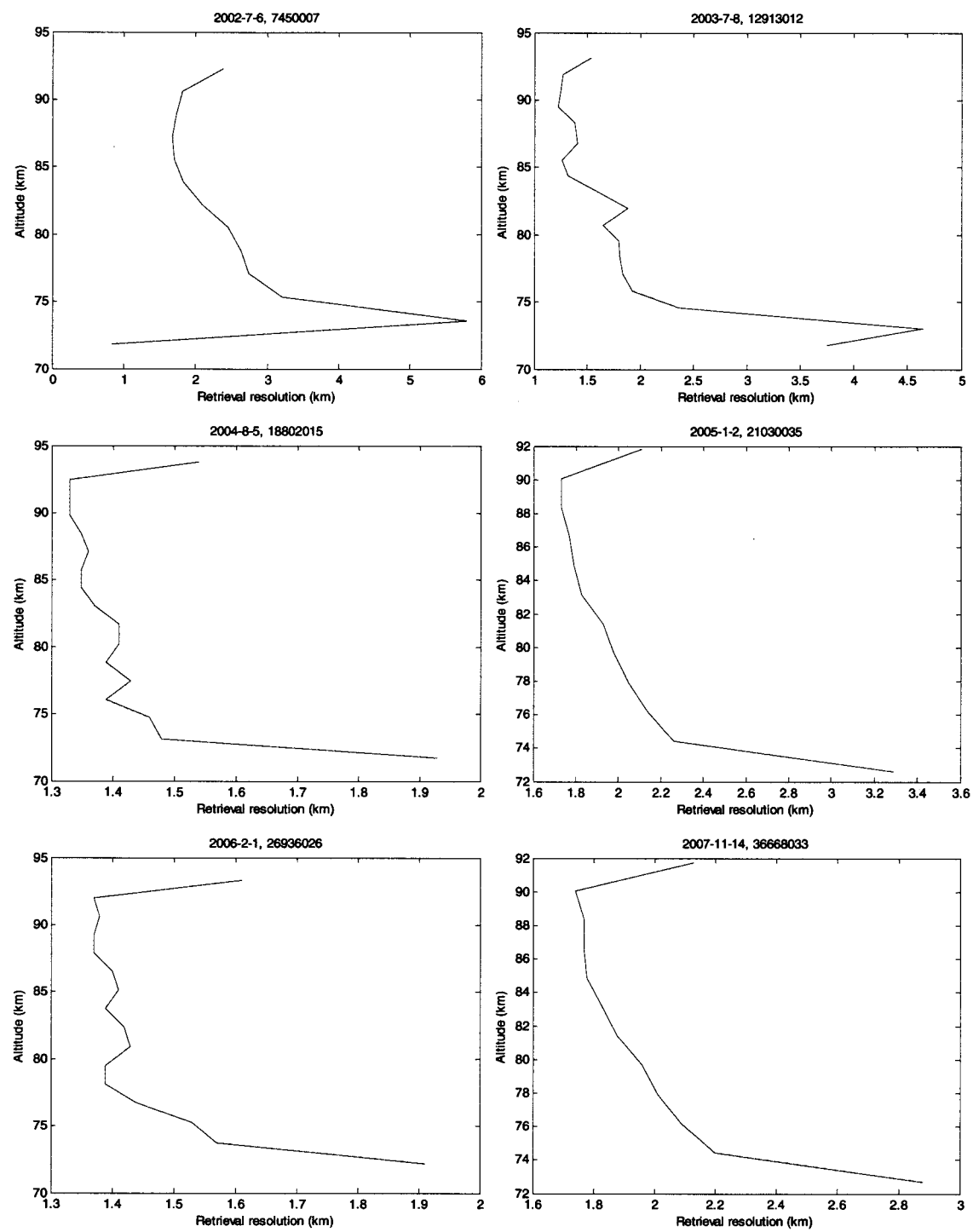
Figure 4.12: Retrieval resolution for averaging kernels plotted in Fig. 4.10.
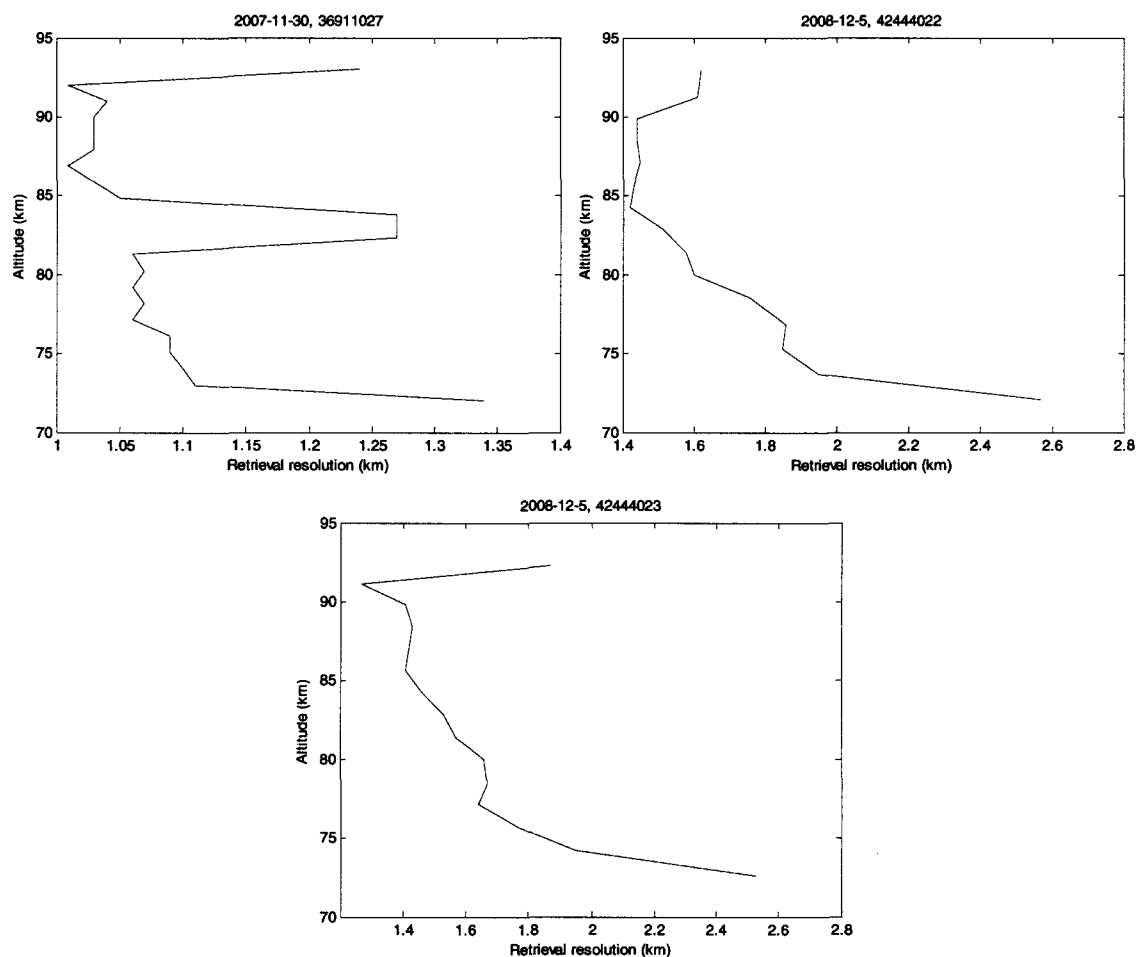
Figure 4.12: Retrieval resolution for averaging kernels plotted in Fig. 4.10 (cont'd).

4.3.3 Forward model bias and error

One of the simplest sources of error to check for is forward model bias. It is essential that the retrieval, **R**, of the forward model, **F**, with the *a priori* as the input, results in the *a priori*. That is to say, that there is no bias in the forward model,

$$\mathbf{R}[\mathbf{F}(\mathbf{x}_a)] - \mathbf{x}_a = 0 \text{ molec/cm}^3. \tag{4.40}$$

This is indeed the case for the forward model of this study. Fig. 4.13 shows the results of the forward model bias test.

97
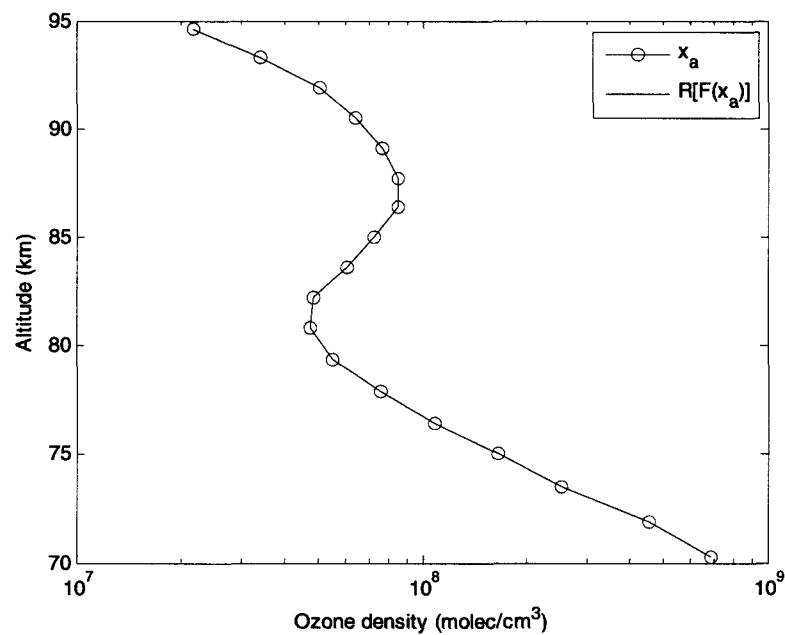
Figure 4.13: A comparison of the *a priori* ozone profile and the retrieved ozone profile when using the forward model as the measurement profile.

Another source of error, which is not as simple to characterize, is the forward model error. This is error that arises due to approximations of the physics and/or chemistry of the forward model, such as not taking transport into account, assuming cloud cover at a height of 0 km for the baffle correction, etc. In order to properly estimate the forward model error a model would need to be constructed that did take into account the entire physics and chemistry of the problem, which is simply not feasible. However, in this case, it is assumed that the forward model error is insignificant in comparison to the other sources of error discussed below.

4.3.4 Retrieval error

Retrieval error, in this case, refers to the types of error that are recovered within the retrieval itself. The two types of error are smoothing error and measurement error, which

98

are characterized by covariance matrices S_s and S_m, respectively, where,

$$\hat{S} = S_s + S_m. \tag{4.42}$$

The smoothing error arises from the finite widths of the averaging kernels, *i.e.* the limited

vertical resolution of the retrieval, and its covariance matrix is given by,

$$S_s = (A - I)S_x(A - I)^T, \tag{4.43}$$

where I is the identity matrix. The measurement error is the error in the retrieval due to

the propagation of error in the measurement, which, as mentioned Section 4.2.3, includes

both the OSIRIS observation error and errors due to background subtraction,

$$S_m = G_y S_y G_y^T. \tag{4.44}$$

The retrieval error for typical retrievals can be seen in Fig. 4.14. As can be seen in Fig.

4.14, the typical retrieval error, which includes measurement noise, is greater at heights

where OSIRIS observes lower A-band emission and lower where OSIRIS observes

greater A-band emission. Retrieval error values can reach up to 100% in some cases,

however typical values are below 25%.
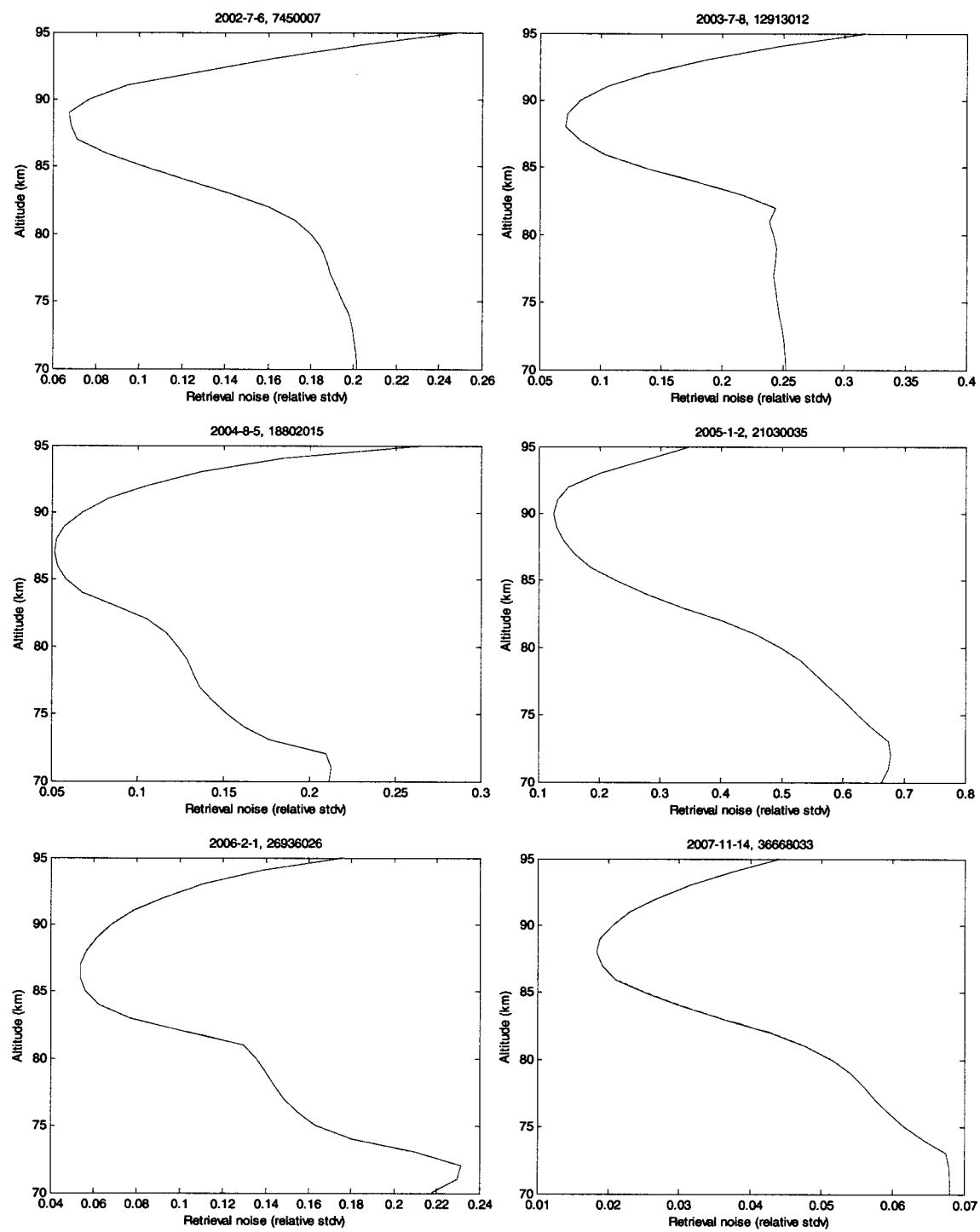
Figure 4.14: Retrieval error in terms of relative standard deviation for scans corresponding to those of Fig. 4.4.

100
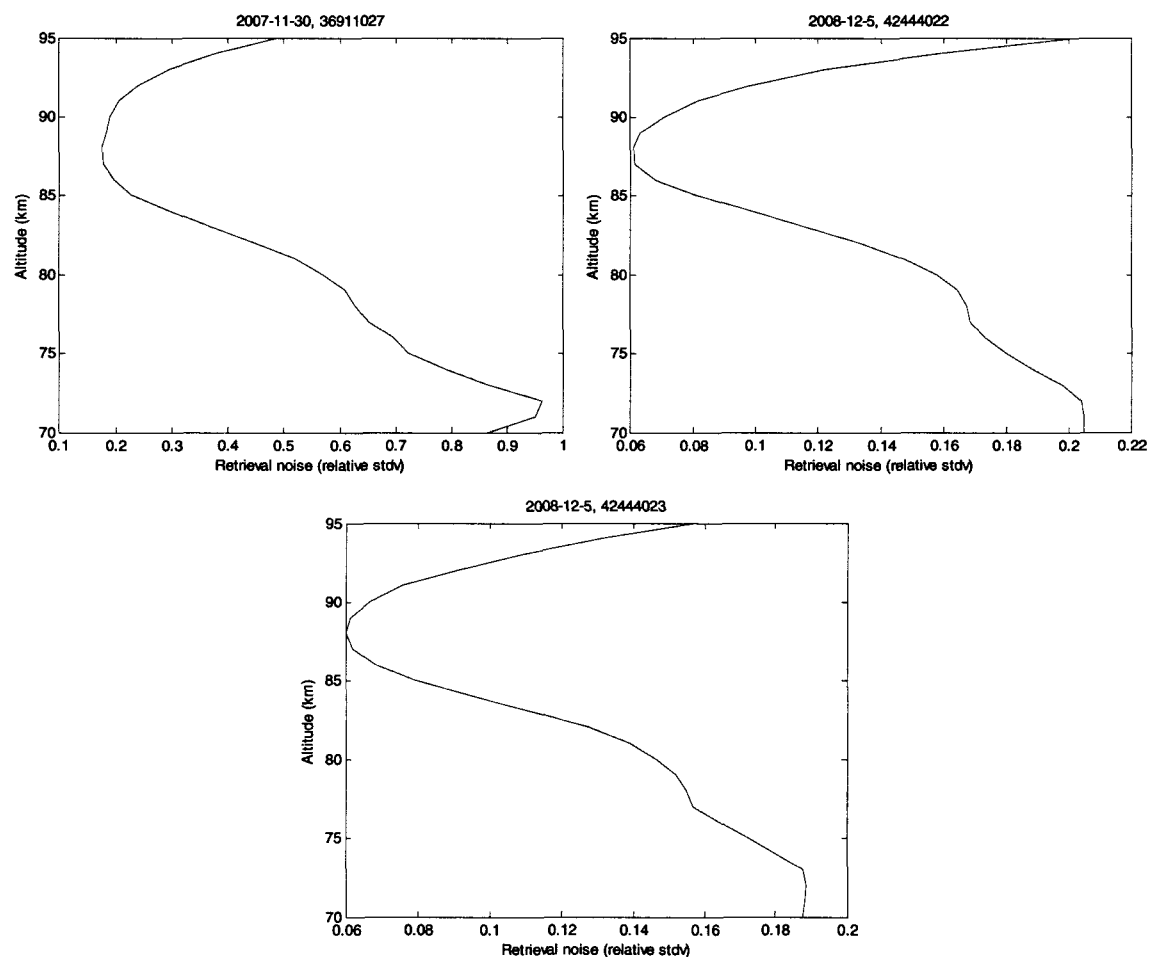
Figure 4.14: Retrieval error in terms of relative standard deviation for scans corresponding to those of Fig. 4.4 (cont'd).

4.3.5 Forward model parameter error

The final error component that needs to be estimated is the forward model parameter error, which is the total error that propagates through the retrieval due to uncertainties in the forward model parameters, and is determined numerically for each individual parameter, post-retrieval. The forward model parameter error of each parameter vector **b** has a covariance matrix S_f given by,

101

$$S_f = G_y K_b S_b K_b^T G_y^T, \qquad (4.45)$$

where $K_b = \frac{\partial y}{\partial b}$ is calculated numerically as well, and S_b is a diagonal matrix with the

diagonal elements corresponding to the variance of the model parameter. Table 4.2 lists

the average error, in terms of standard deviation, for model parameters that are the

greatest contributors to the overall forward model parameter error. Unless previously

discussed, the uncertainty values of the different parameters (first row of Table 4.2) are

those given by the individual sources for the parameters, as listed in Table 3.2.

Typical forward model parameter error for a given parameter ranges from

approximately <0.01% - 100% depending on the parameter and tangent height; however,

at tangent heights around the ozone minimum and/or at the lowest retrieval tangent

heights, forward model parameter error can occasionally be found in the 200% range.

The greatest contributors to the overall forward model parameter error are the

uncertainties in the A-band g-factors, uncertainty in k_0, and uncertainty in the MSIS

temperature and number density. The error could be greatly reduced with online

calculations of the A-band g-factors (although this would increase computation time), and

by using more reliable temperatures—perhaps coincident measurements from the SMR

aboard Odin.

Parameter: Uncertainty:	g_A 10%	S 5%	k_0 10%	k_1 10%	k_2 5%	$A_{1\Sigma}$ 5%	φ 5%	T 10%	nd 5%
Altitude (km)									
70	0.187	0.149	0.358	0.065	0.061	0.148	0.171	0.164	0.223
71	0.189	0.120	0.312	0.022	0.063	0.147	0.159	0.171	0.184
72	0.193	0.102	0.275	0.009	0.065	0.147	0.148	0.177	0.155
73	0.205	0.107	0.266	0.012	0.068	0.149	0.139	0.182	0.155
74	0.226	0.092	0.237	0.034	0.069	0.152	0.131	0.184	0.140
75	0.265	0.100	0.243	0.028	0.074	0.158	0.128	0.187	0.161
76	0.319	0.097	0.243	0.035	0.081	0.170	0.126	0.198	0.168
77	0.372	0.105	0.259	0.032	0.089	0.193	0.128	0.219	0.176
78	0.403	0.109	0.258	0.048	0.097	0.236	0.129	0.260	0.141
79	0.415	0.147	0.336	0.051	0.106	0.276	0.139	0.284	0.177
80	0.410	0.219	0.599	0.049	0.119	0.338	0.161	0.324	0.296
81	0.398	0.296	0.995	0.039	0.137	0.343	0.192	0.319	0.470
82	0.336	0.208	0.595	0.017	0.153	0.260	0.201	0.231	0.313
83	0.268	0.158	0.429	0.013	0.171	0.171	0.213	0.132	0.244
84	0.166	0.154	0.344	0.043	0.194	0.105	0.231	0.059	0.223
85	0.110	0.149	0.286	0.032	0.210	0.075	0.242	0.029	0.212
86	0.091	0.136	0.253	0.022	0.202	0.071	0.236	0.021	0.195
87	0.089	0.117	0.239	0.021	0.180	0.078	0.218	0.017	0.171
88	0.113	0.085	0.238	0.043	0.137	0.092	0.189	0.025	0.132
89	0.147	0.056	0.225	0.058	0.112	0.091	0.174	0.027	0.095
90	0.109	0.028	0.146	0.004	0.097	0.071	0.163	0.020	0.059
91	0.086	0.016	0.106	0.025	0.087	0.062	0.157	0.011	0.042
92	0.076	0.014	0.088	0.035	0.083	0.058	0.159	0.002	0.038
93	0.067	0.012	0.069	0.042	0.082	0.054	0.164	0.002	0.038
94	0.056	0.003	0.042	0.049	0.078	0.045	0.159	0.002	0.043
95	0.047	0.006	0.013	0.055	0.075	0.036	0.155	0.004	0.048

Table 4.2: Fractional errors due to uncertainty in forward model parameters that are the greatest contributors to the total forward model parameter error. The first seven listed parameters are systematic errors and refer to the parameters defined in Chapters 2 and 3. The final two parameters, T and nd, refer to the MSIS temperature and total number density, respectively, and are random errors.

4.3.6 Summary of error analysis

The greatest source of error in the retrievals is due to forward model parameter error, which can range between <5% and 200%. The total error of the retrieved ozone profiles, in standard deviation, is typically in the 10 – 100% range, and retrieved ozone profiles

with corresponding error are plotted in Fig. 4.15. This range of error is typical of upper mesospheric retrievals, especially ozone retrievals.
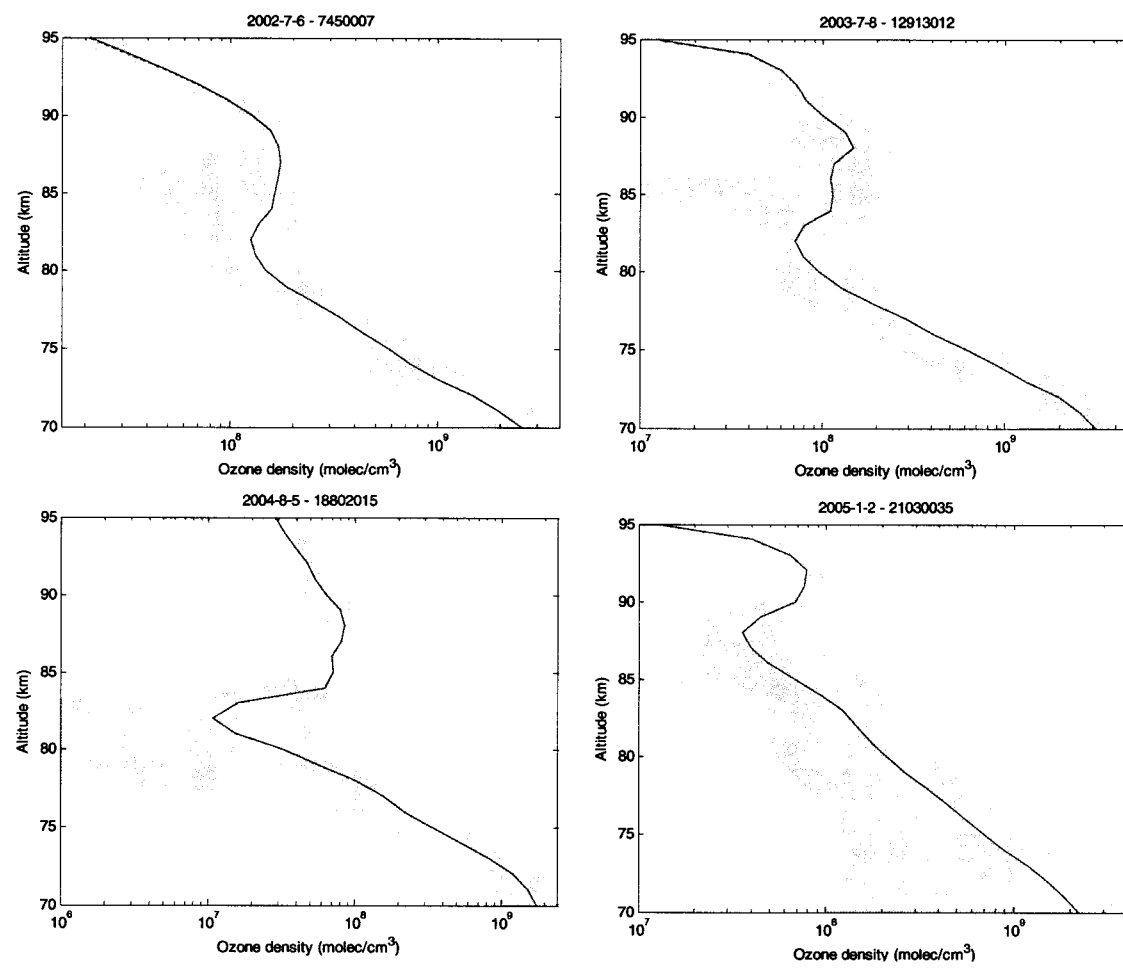
Figure 4.15: Retrievals (blue) and total error (shaded) for scans corresponding to those of Fig. 4.4.
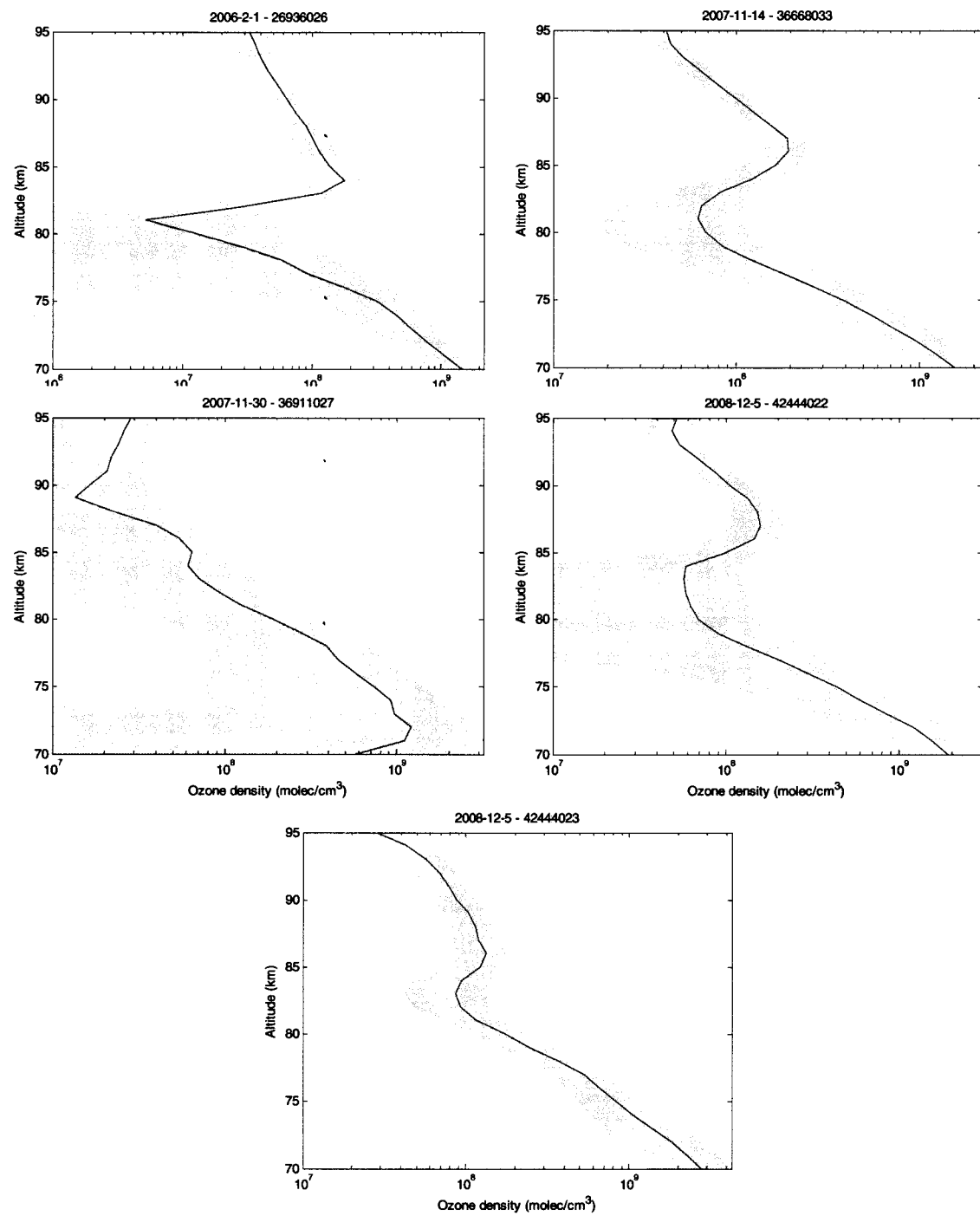
Figure 4.15: Retrievals (blue) and total error (shaded) for scans corresponding to those of Fig. 4.4 (cont'd).

Chapter 5

Results

5.1 Description of the dataset

Daytime ozone densities were retrieved in an altitude range of 70 – 95 km from OSIRIS observations between July 2002 and December 2008. Above 95 km the production of A-band dayglow due to ozone decreases significantly with altitude, due to decreasing ozone densities, and retrievals cannot be made with any significant accuracy. Below 70 km the production of A-band dayglow due to ozone is sufficient for performing ozone retrievals, however, the atmosphere in the A-band becomes increasingly optically thick with decreasing altitude and very little of the observed signal is actually originating from the observed tangent point. As can be seen in Fig. 5.1, less than 5% of the photons that are emitted within the OSIRIS line-of-sight at an observed tangent height of 65 km are transmitted to the instrument.

Although OSIRIS began taking measurements in early 2001, useful mesospheric observations were not made until July 2002. In the first year of observation, the

106

instrument exposure time was varied with tangent height in order to obtain data with a consistent signal-to-noise ratio at each tangent height. In the upper mesosphere this required much longer exposure times, up to 10 seconds, which led to altitude smearing. For this reason the time series of ozone retrievals does not begin until July 2002, when the exposure time in the mesosphere began to be kept constant at ~2 seconds.
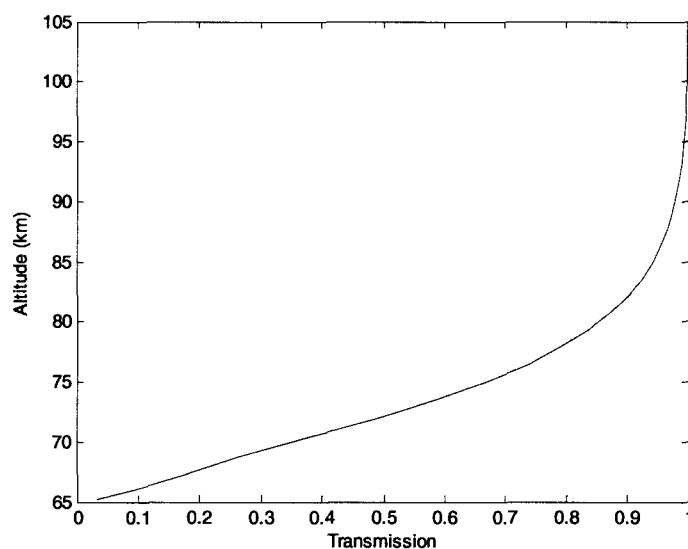
Figure 5.1: Modelled total A-band transmission function along OSIRIS line-of-sight while observing a tangent height of 65 km.

5.2 Analysis of the dataset

5.2.1 Daytime coverage of ascending and descending nodes

As mentioned in Chapter 3, the amount of daytime coverage during the separate ascending (observed tangent-point-latitude is increasing northward) and descending (observed tangent-point-latitude is decreasing southward) orbital phases has been changing over the course of the mission due to perturbations in Odin's orbit. Figs. 5.2 and

5.3 illustrate the amount of daytime coverage for the separate phases by plotting a latitudinal cross-section of daytime OSIRIS observations throughout the mission. It can be seen that observations during the descending phase are covering a much wider range of latitudes. As time progresses, observations during the descending phase are gaining daytime coverage in the lower latitudes, while observations during the ascending phase are losing daytime coverage. Due to the lack of data in the ascending phase all displays of results will be of retrievals in the descending phase, hence morning conditions.
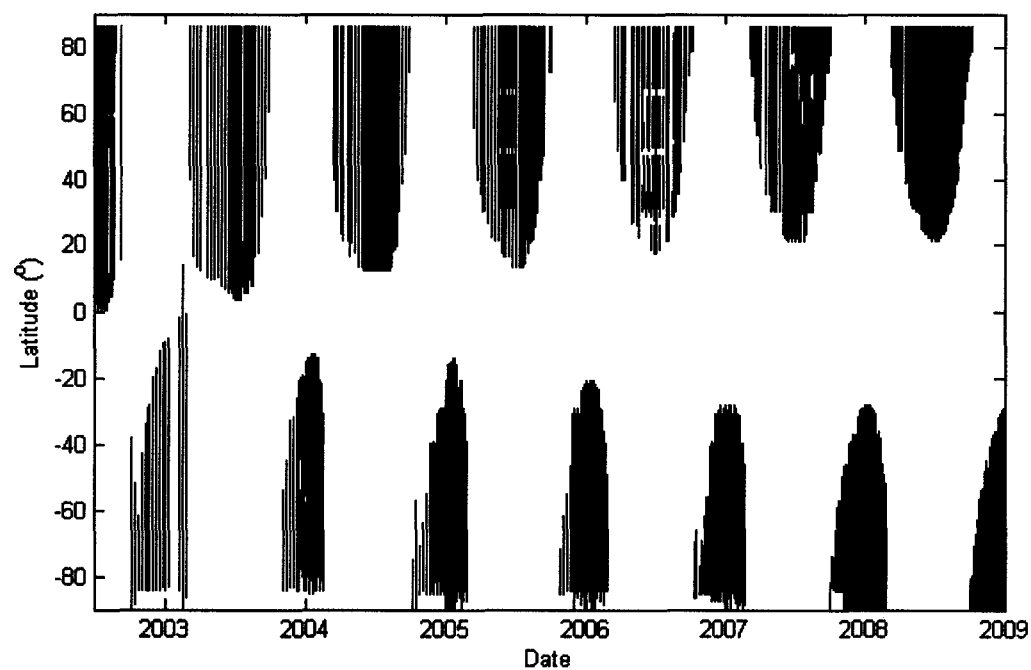
Figure 5.2: Ascending phase observations between July 2002 and December 2008, where coloured sections indicate areas observed by OSIRIS.
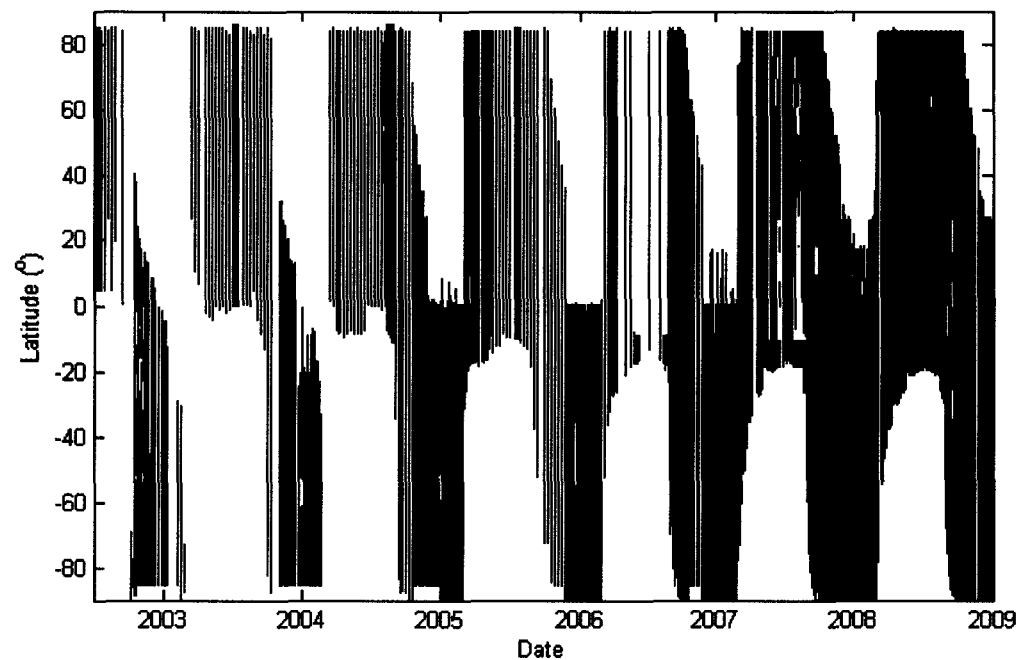
Figure 5.3: Descending phase observations between July 2002 and December 2008, where coloured sections indicate areas observed by OSIRIS.

5.2.2 Vertical profiles

Annual composites of ozone density profiles for the entire dataset are plotted for different latitude regions in Figs. 5.4 – 5.6. Composites were constructed by calculating 5-day average profiles for each day of the year for individual years, and taking the average of the yearly time-series. Due to fewer observations between 2002 and 2006, the composites are biased towards the 2007 - 2008 data. At all latitudes and seasons the same basic profile is observed: ozone densities decrease exponentially from an altitude of 70 km to a local minimum around 80 – 85 km, from $\sim2 \times 10^9$ molec/cm^3 to $\sim1 \times 10^7$ – 1×10^8 molec/cm^3. Ozone densities then begin to increase with altitude and peak around 87 km (ozone secondary maximum), where densities then begin to once again decrease

109

exponentially with altitude. In the tropics, the ozone secondary maximum is more pronounced (*i.e.* a greater difference in density between density minimum and maximum) around solstice, and at all other latitudes the maximum is more pronounced around equinox. These results are discussed further in Section 5.2.4.
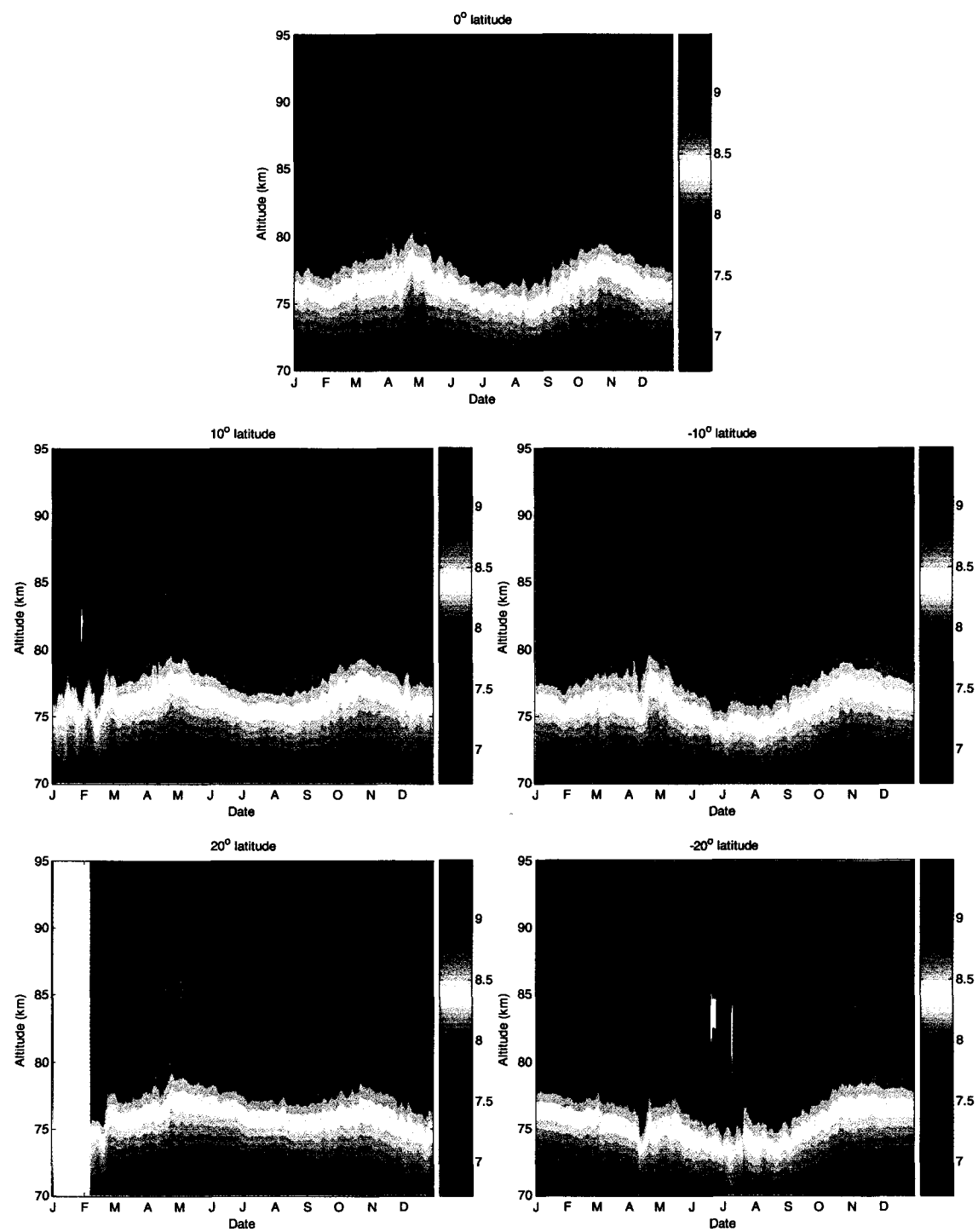
Figure 5.4: Height profile composites of the log of zonally-averaged ozone densities in molec/cm^3 for data from 2002 – 2008. Profiles are smoothed by a 5-day running average. Different latitudes in the tropics, representing 10° averages, are shown (*i.e.* 0°±5, *etc.*).

111
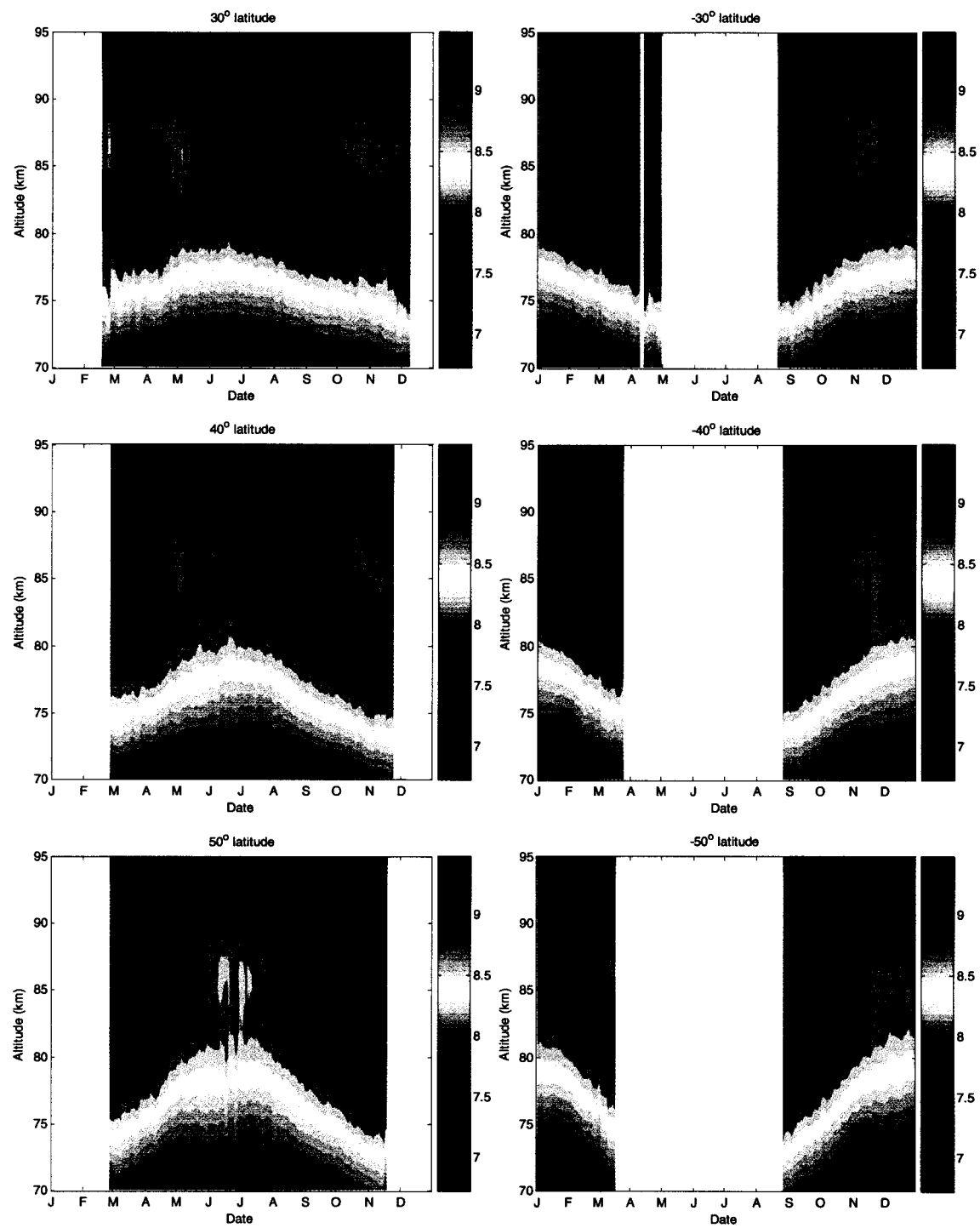
Figure 5.5: Same conditions as Fig. 5.4 are shown, only for mid-latitudes.
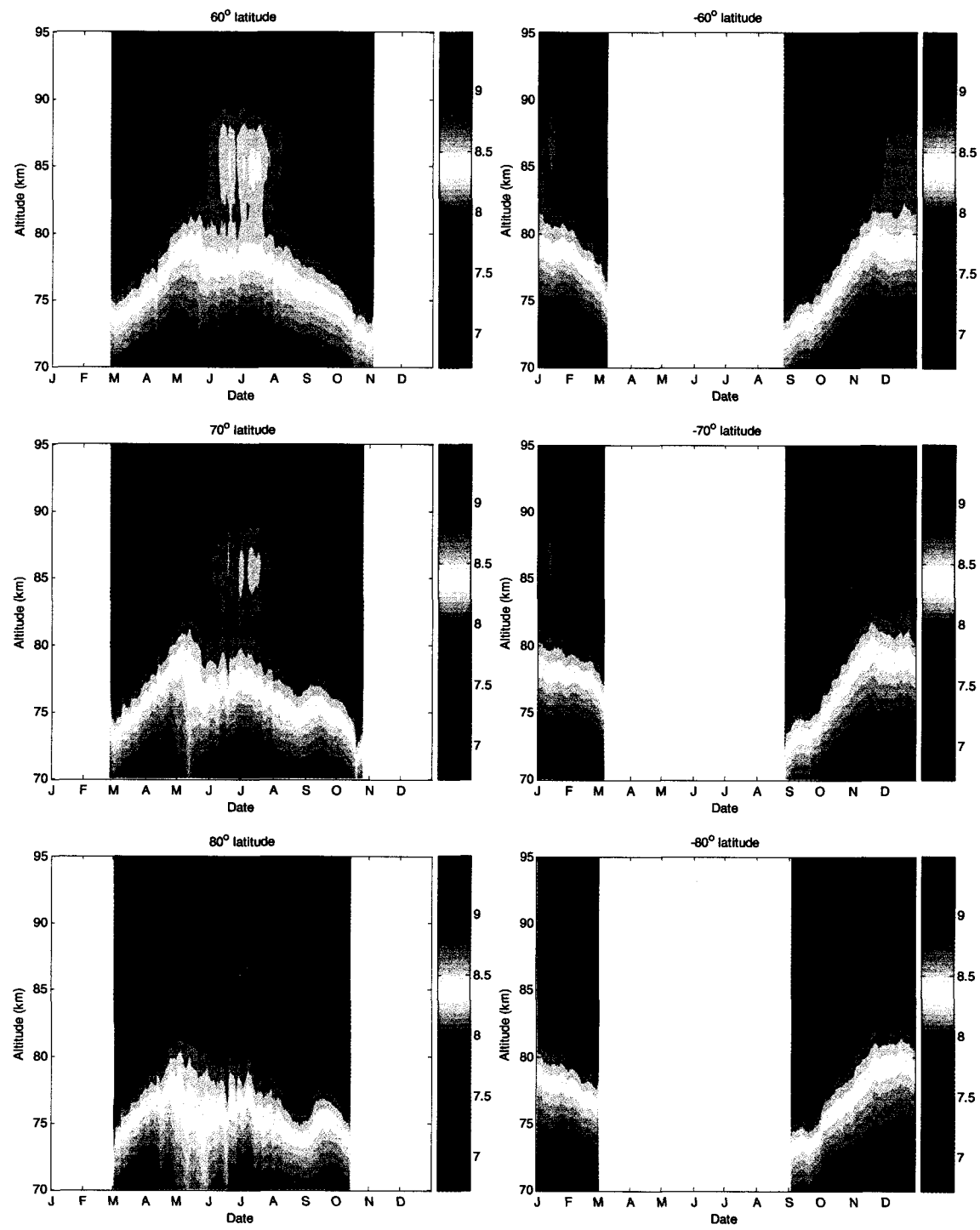
Figure 5.6: Same conditions as Fig. 5.4 are shown, only for high latitudes.

113

5.2.3 Latitudinal cross-sections

Annual composite latitudinal cross-sections are plotted in Fig. 5.7 for four different altitudes: below the ozone minimum (72 km), near the ozone minimum (82 km), near the ozone secondary maximum (87 km), and above the secondary ozone maximum (93 km). Ozone densities tend to peak between latitudes of $40 - 70°$ in the summer hemispheres at all altitudes. Around equinox, below ~82 km, ozone densities tend to peak around the equator, and above 82 km they tend to peak around $20 - 30°$ latitude.
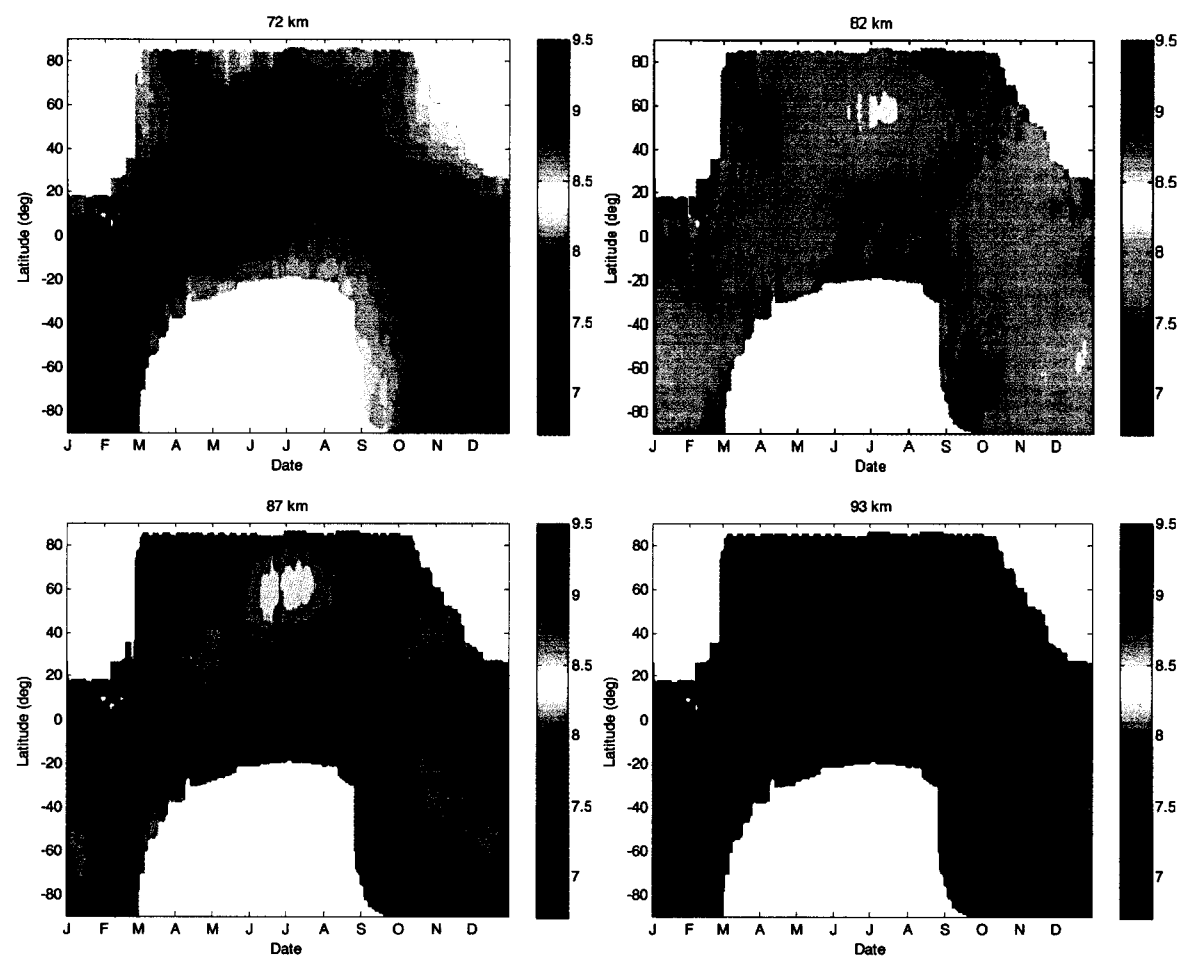
Figure 5.7: Zonally-averaged latitudinal cross-section composites of the log of ozone densities in molec/cm^3 for data between 2002 and 2008. 1-degree latitudinal bins represent 10-degree averages and 1-day bins represent 5-day averages.

5.2.4 Seasonal variations

The percent deviation of the annual composite vertical profiles (Section 5.2.2) from their respective annual means was determined in order to highlight the seasonal variations in each latitudinal region. Percent deviation plots are shown in Figs. 5.8 – 5.10. A Lomb-Scargle harmonic analysis [*Press and Rybicki*, 1989] was performed on the dataset to determine the amplitudes of the different components of the seasonal variations. The

115

Lomb-Scargle method produces a Fourier power spectrum (periodogram) by using a least-squares approach to fitting the dataset to a Fourier series. The advantage of this method is that it provides greater accuracy than straightforward Fourier analysis when dealing with unequally spaced data (which is certainly the case in this study). The details of determining the amplitudes and phases of the periodograms using Lomb-Scargle harmonic analysis is discussed by *Press and Rybicki* [1989] and *Hocke* [1998]. Periodograms have only been calculated for observations in the lower latitudes and are shown in Fig. 5.11. At latitudes poleward of ±30° there are too many seasonal gaps in the OSIRIS observations for this type of analysis to be reliable.

In the tropics there is a clear semi-annual oscillation (SAO) that peaks mid-April and mid-October. There is also a clear symmetry between the Northern and Southern hemispheres, with the SAO peak being 30 – 60% greater in the spring than in the fall. This is consistent with the effects of the diurnal tide, which is a predominant feature in the tropics, as described in Chapter 2.

In the mid-latitudes above approximately 82 km the SAO is still present; however, its amplitude is decreasing with increasing latitude. Below 82 km a strong annual oscillation becomes more prevalent, peaking around summer solstice. As latitude increases the annual oscillation is also present at altitudes above 82 km. This increase of ozone in the summer is consistent with the dynamics of the MLT, where rising air in the summer would act to increase ozone densities, as discussed in Chapter 2. Again, there is a similar symmetry between the Northern and Southern hemispheres.

In the high latitudes seasonal variations are more difficult to determine due to a

116

complete lack of winter observations. However, as latitude increases, the annual oscillation seen at the mid-latitudes tends to persists at all altitudes, which is consistent with the dynamics; but, interestingly, as well as the SAO remaining present above ~82 km, the SAO begins to become present at altitudes below ~78 km as well. Around 80°N it appears as though there is a superposition of the SAO and the annual oscillation.

In the higher latitudes, at an altitude of approximately 80 km, another interesting feature is observed. There is a peak in ozone density isolated to ~78 – 82 km occurring in early to mid-May, and a trough occurring roughly 4 months later in September at a slightly higher altitude. This feature is investigated further and discussed in Section 5.2.5.

Similar seasonal variations in ozone concentrations to those described above in the lower- to mid-latitudes were observed with the HRDI instrument aboard UARS [*Marsh et al.*, 2002], which also retrieved ozone from O_2 A-band observations from 1992 to 1997. The HRDI ozone time series covers an altitude range of approximately 65 – 100 km, a latitudinal range of 72°S – 72°N, and spans local times between 1500 and 1700 LT. Long-term HRDI ozone concentrations, illustrated in Fig. 5.12, also exhibited a more predominant SAO in the equatorial regions, peaking around equinox, and a more predominant annual oscillation in the mid-latitudes, peaking around summer solstice.
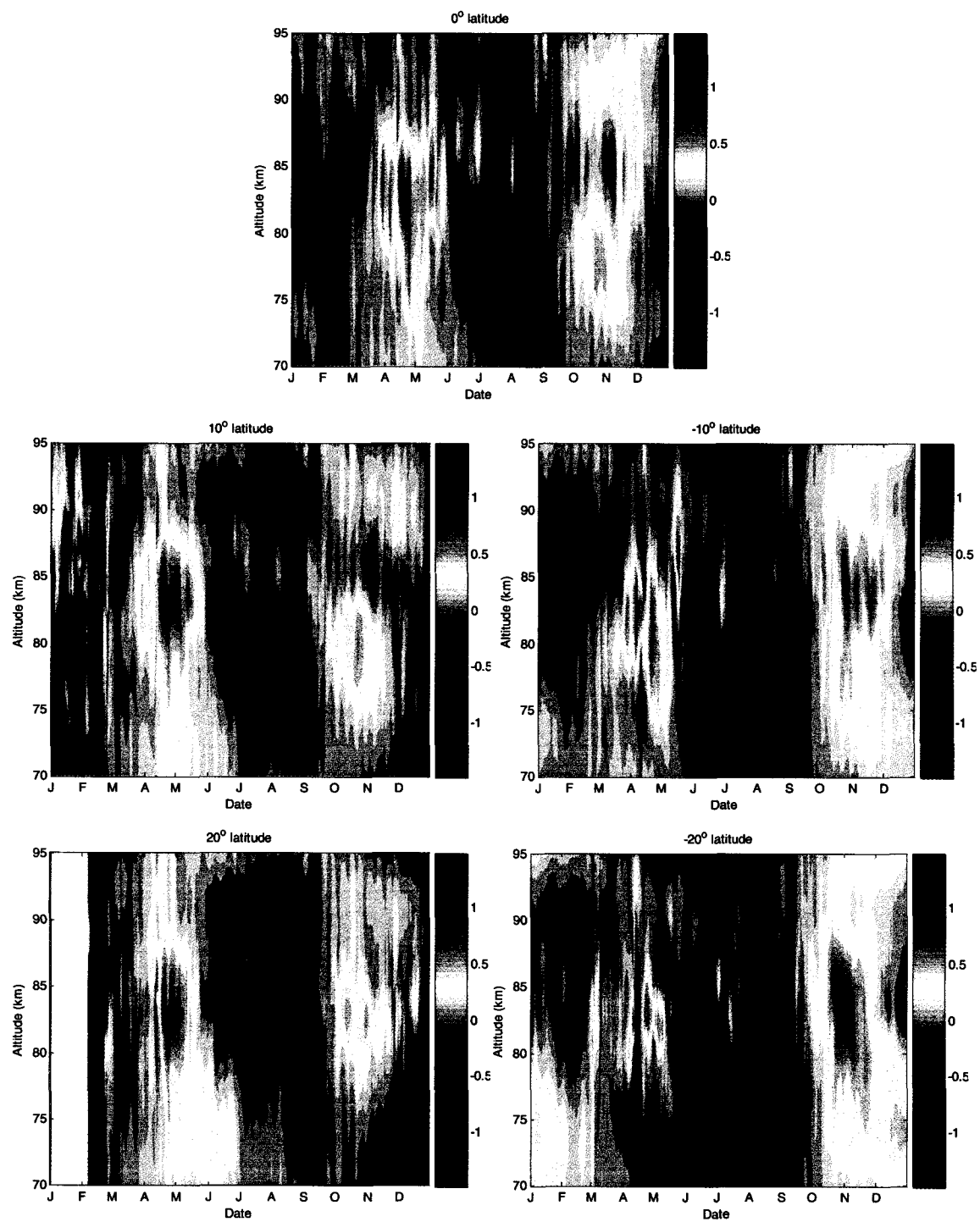
Figure 5.8: Percent deviations (unitless) of values shown in Fig. 5.4 from their respective annual means.

118
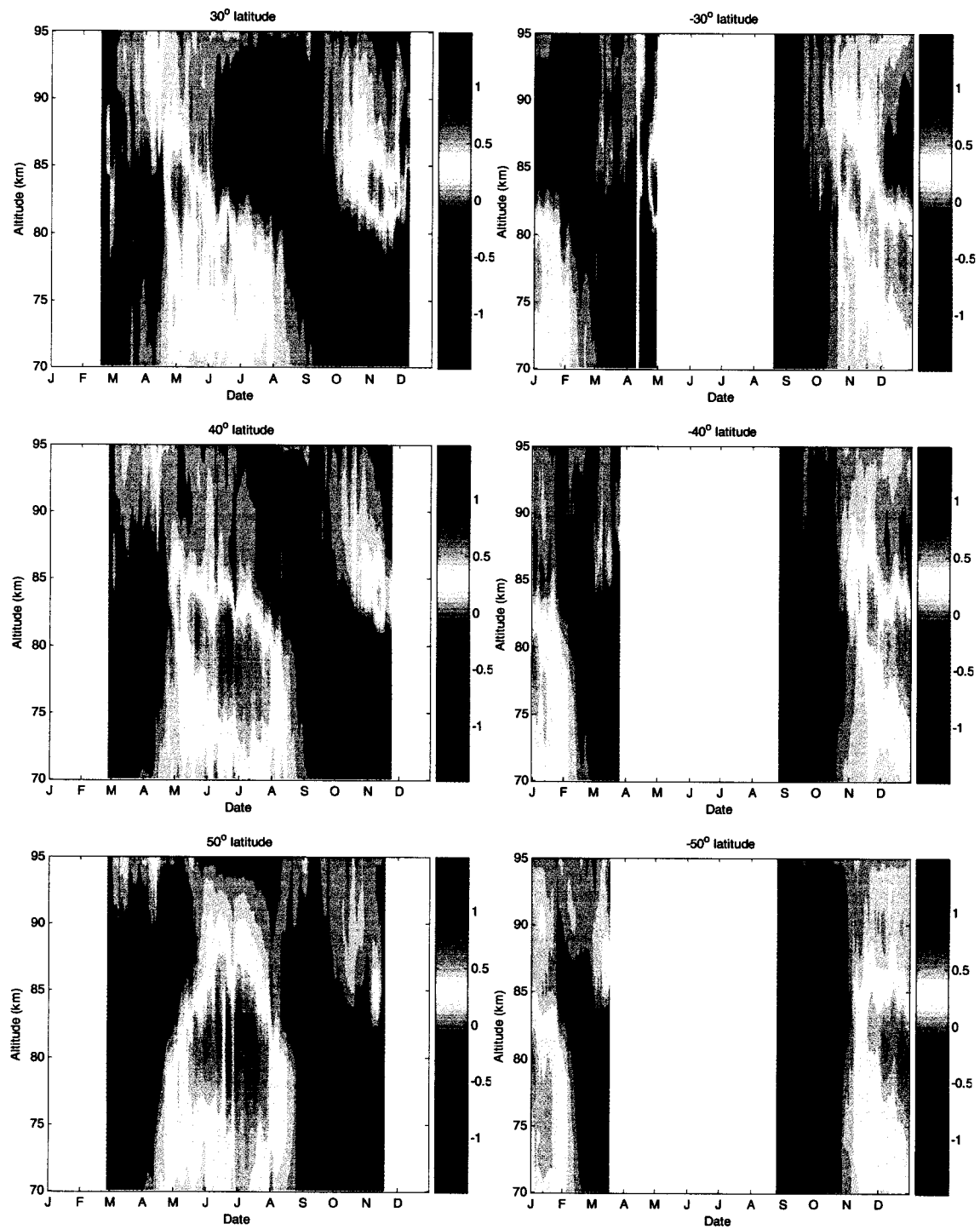
Figure 5.9: Percent deviations (unitless) of values shown in Fig. 5.5 from their respective annual means.

119
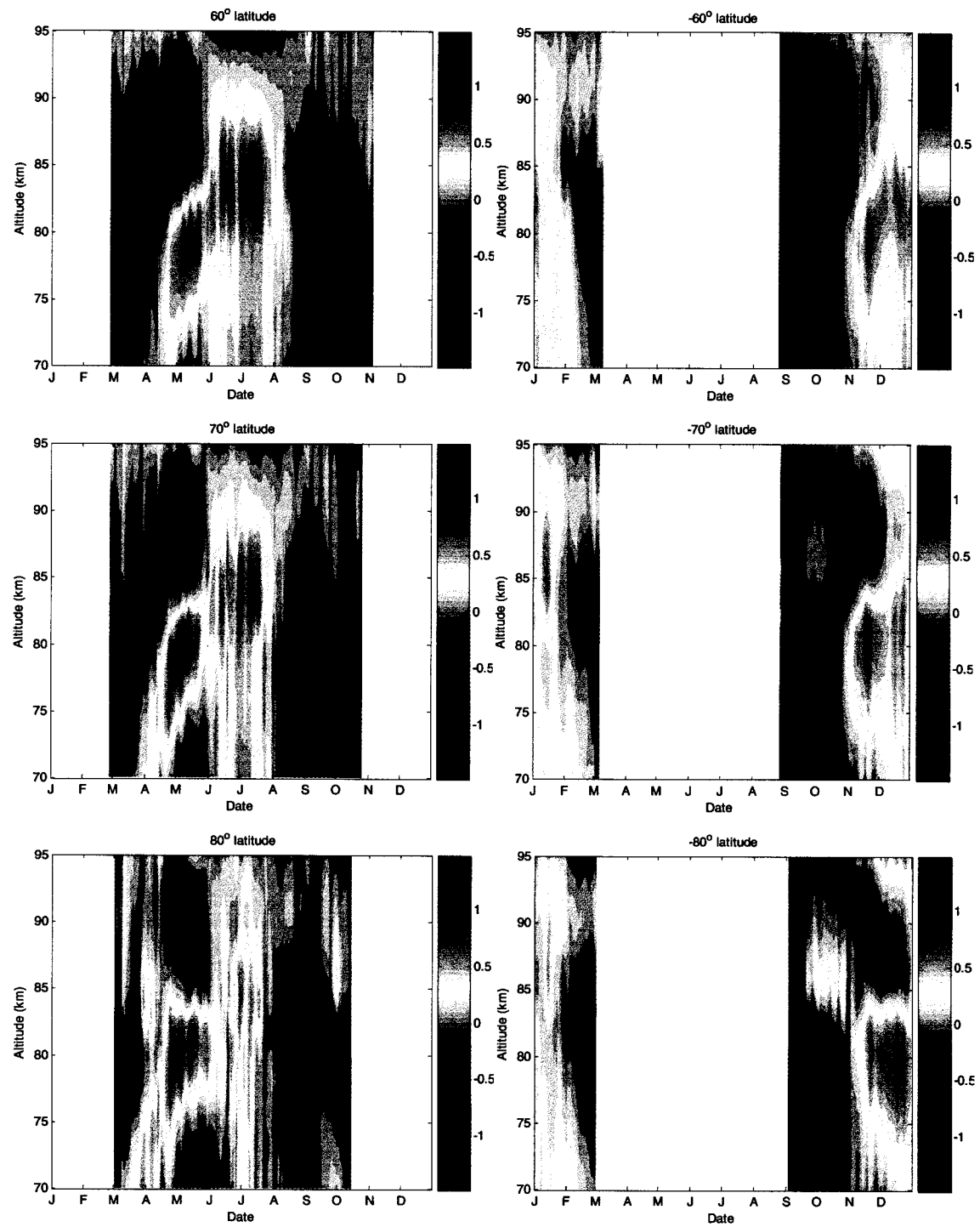
Figure 5.10: Percent deviations (unitless) of values shown in Fig. 5.6 from their respective annual means.
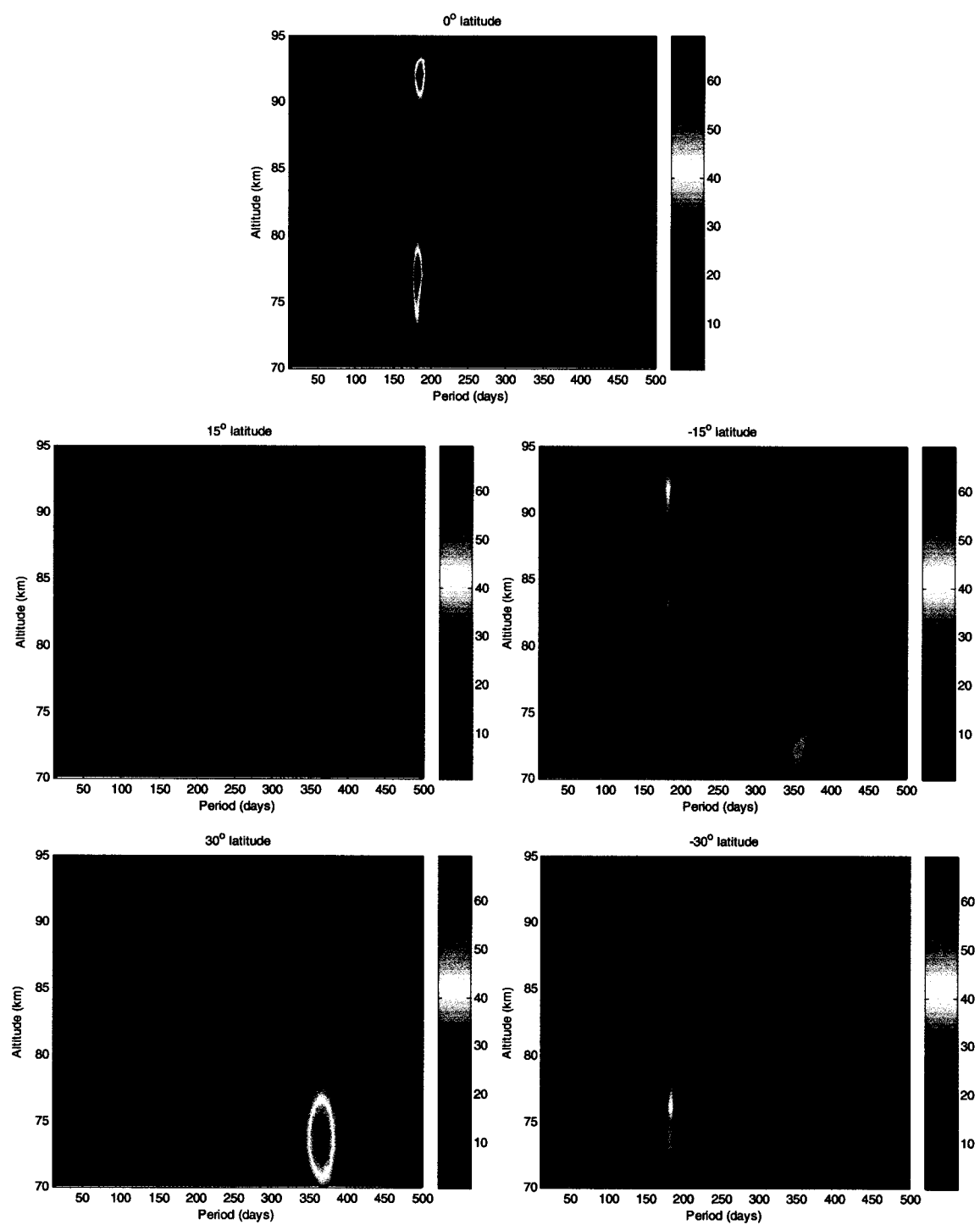
Figure 5.11: Lomb-Scargle harmonic analysis periodogram profiles of zonally-averaged ozone data for different low latitudes. Colour indicates the amplitude of the altitude dependent Fourier spectra.

121
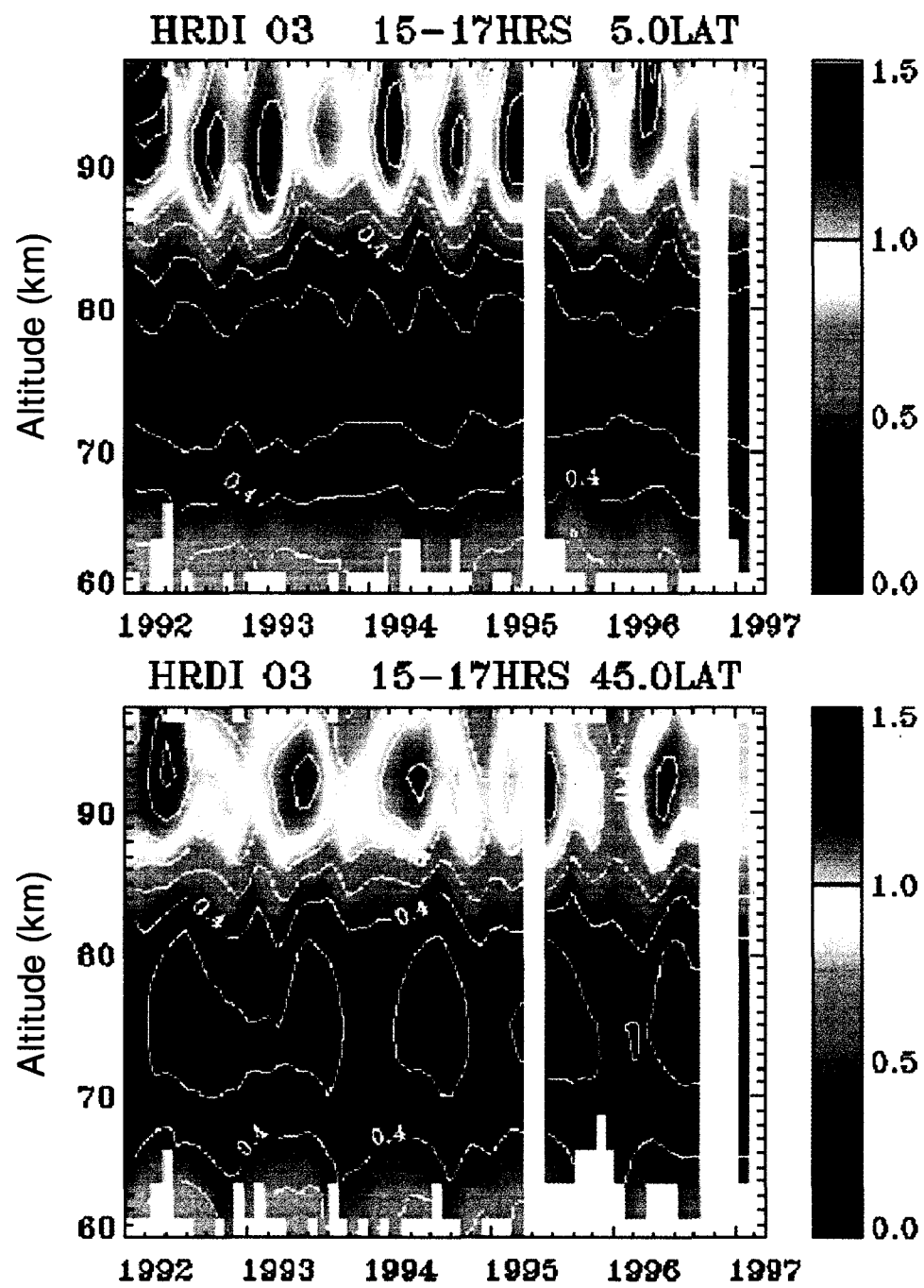
Figure 5.12: Monthly and zonally-averaged HRDI daytime ozone volume mixing ratios in ppm at latitudes of 5°N (top) and 45°N (bottom), between 14 and 16 hrs local time, and ±5° latitude. Data is smoothed with a three-month-wide triangular filter to highlight seasonal variability, from hrdi.engin.umich.edu/generalinfo/HRDI_ozone.html.

5.2.5 Anomalous structure at 80 km in the northern high latitudes

Every May, between 2004 and 2008, around an altitude of 80 km in the northern high latitudes, ozone densities exhibit a significant local maximum. No other regions of altitude or latitude within the dataset consistently exhibit this seasonal feature. Fig. 5.13 compares the time series at an altitude of 80 km in the northern and southern high latitudes.
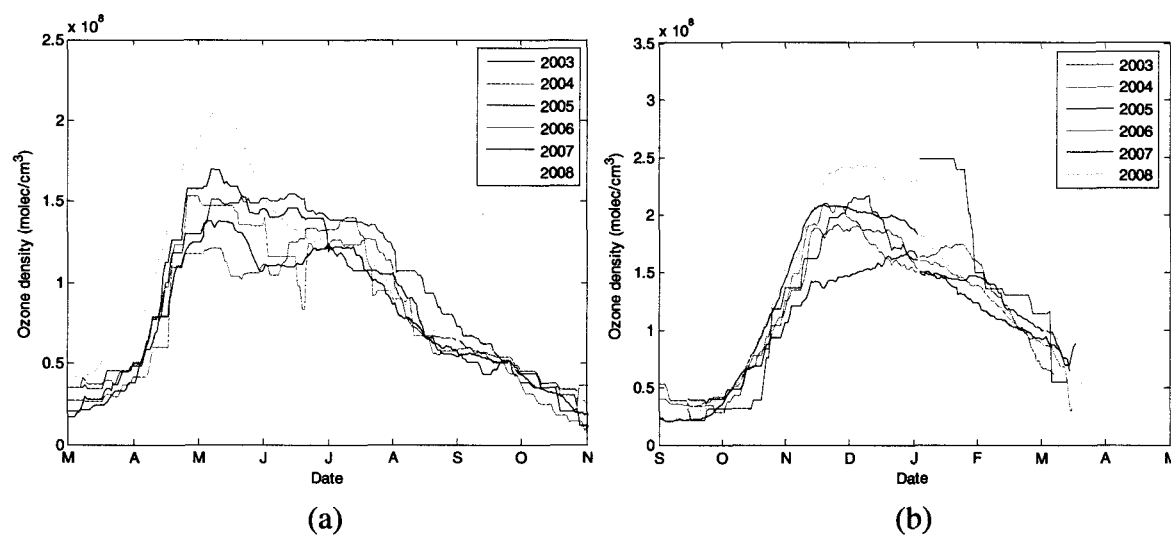
Figure 5.13: Time series of average O_3 densities at an altitude of 80 km for latitudes between (a) 60° and 80° N, and (b) 60° and 80° S. One-day bins represent 30-day averages.

The OSIRIS data was also compared with SABER 9.6 μm channel[2] ozone volume mixing ratios in the same region, seen in Fig. 5.14. Since the SABER observed local time at a given latitude is not constant, only nighttime conditions of the high latitudes for April and the majority of May are observed. From the limited amount of data it appears as though this feature was observed by both SABER and OSIRIS in 2008, the year in which the

---

[2] The SABER instrument is discussed in greater detail in Chapter 6.
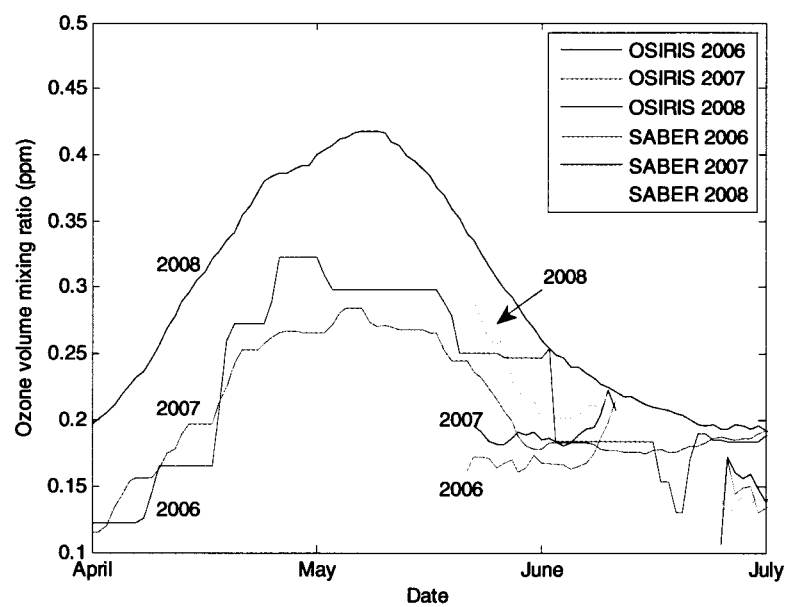
Figure 5.14: Zonally-averaged daytime ozone volume mixing ratios at an altitude of 80 km and for latitudes between 60°N – 80°N as observed by OSIRIS and SABER. OSIRIS data represent 30-day averages, whereas SABER data represent daily averages.

feature is most enhanced; however, it is unclear whether or not it is present in the SABER data in other years.

One possible explanation for this feature could be the presence of polar mesospheric clouds (PMCs). These clouds tend to form in the summer hemisphere at high latitudes, typically at an altitude of 80 km [*Gadsen*, 1989]; and the presence of a PMC in the OSIRIS field-of-view would scatter more sunlight at all wavelengths within the OSIRIS line-of-sight than an atmosphere free of PMCs. However, if this feature was due to the presence of PMCs, one would also expect to see an enhancement in both hemispheres. As well, *Petelina et al.* [2007] show that PMCs are rarely detected by OSIRIS before June 1st, and the highest frequency of detected PMCs consistently occurs at or within a few

124

days of summer solstice. These factors seem to indicate that this observed feature is not due to the presence of PMCs. Further investigation is needed in order to determine its origin.

Chapter 6

Comparisons of results

6.1 Comparisons between OSIRIS and SABER

6.1.1 The SABER instrument aboard the TIMED satellite

The Thermosphere-Ionosphere-Mesosphere Energetics and Dynamics (TIMED) satellite was launched into orbit at an altitude of 625 km and an inclination of 74.1° in December of 2001. The Sounding of the Atmosphere using Broadband Emission Radiometry (SABER) instrument on board TIMED observes the Earth's limb perpendicular to its orbital plane scanning tangent heights between the surface and >400 km every 58 seconds. The nominal latitudinal coverage is between 83°N and 83°S, and, unlike OSIRIS, observations of latitudinal circles between orbits are not at constant local times. It takes 60 days for SABER to cover 24 hours of local time, which intertwines the effects of diurnal and seasonal variations. The radiometer observes radiances using 10 different infrared channels, two of which observe ozone-related emissions—the O_2 Infrared Atmospheric Band at 1.27 µm, and the O_3 9.6 µm band. However, the methods of

inferring ozone concentrations from observations of these bands both have their difficulties. For instance, both methods require taking into account non-LTE effects.

A description of the ozone retrieval method from the 9.6 μm channel is given by *Rong et al.* [2009]. The filter for this channel allows for a spectral window of ~9 – 11 μm and coincides with both the O_3 symmetric and asymmetric stretch vibrational modes at 9.06 μm and 9.6 μm respectively, and with the CO_2 9.4 μm "hot band". Of these three sources, the O_3 asymmetric stretch mode is the dominant source of emission. Above altitudes of 50 km, both O_3 and CO_2 diverge from LTE as collisions become less frequent and the population distribution between energy levels becomes more dependent on radiative processes. The retrieval method employs a non-LTE forward model that determines the vibrational temperature of 11 separate O_3 vibrational-rotational bands and the CO_2 "hot band". Currently, SABER 9.6 μm channel ozone retrievals have only been validated in the altitude range of 15 – 70 km.

A non-LTE forward model is also required in SABER ozone retrievals in the Infrared Atmospheric Bands, as described in *Mlynczak et al.* [2007]. However, this is only required for altitudes below ~70 km. Above 70 km absorption within the band is assumed to be negligible. Also, in regions where $O_2(a^1\Delta)$ is not in steady-state, due to its long radiative lifetime (approximately an hour and 15 minutes [*Mlynczak et al.*, 2007]) and the transport mechanisms in the mesosphere, $O_2(a^1\Delta)$ emission is not necessarily an accurate indicator of the current local ozone densities. The problem requires determining time-dependent solutions of the coupled differential equations for $O_2(a^1\Delta)$ densities. Many different approaches to solving these equations have been developed, as discussed in

127

Khabibrakhmanov et al. [2002]. Another approach is to reinterpret the observations in order to directly determine the derivative $\frac{d[O_2(a^1\Delta)]}{dt}$, as in *Wiensz* [2005]. This, however, is generally not an issue for SABER retrievals, as the majority of MLT observations are far away enough from twilight on the day side to be able to consider $O_2(a^1\Delta)$ in steady state.

6.1.2 Coincident observations

OSIRIS ozone densities were compared with the Version 1.07 SABER data, which includes retrieved ozone density profiles from both the 1.27 and 9.6 μm channels. The data was downloaded directly from the SABER website at saber.gats-inc.com/index.php.

Since retrievals in the upper mesosphere commonly involve significant sources of error, conditions for coincidence were rather strict with $\Delta lat < 2°$, $\Delta lon < 3°$, $\Delta\chi < 2°$, and $\Delta UT < 1$ hour. On a month-to-month basis coincident observations are not always possible due to the viewing characteristics of the two instruments. In the earlier years of the mission OSIRIS was only making mesospheric observations roughly once every 10 days at consistent local times, whereas SABER nearly consistently observes the mesosphere. However, as noted above, due to TIMED's orbit, SABER takes 60 days to cover a full 24 hours of local time. Both datasets have a vertical resolution of ~2 km and therefore vertical smoothing of one dataset by the other's averaging kernels was not required.

Nine coincident scans from throughout the dataset were chosen at random and are plotted in Fig. 6.1[3]. A couple of the retrieved ozone profiles from the SABER 1.27 μm channel were negative and are therefore not presented in these plots.

---

[3] Figures in Chapter 4, starting with Fig. 4.4, correspond to the same scans as those of Fig. 6.1.
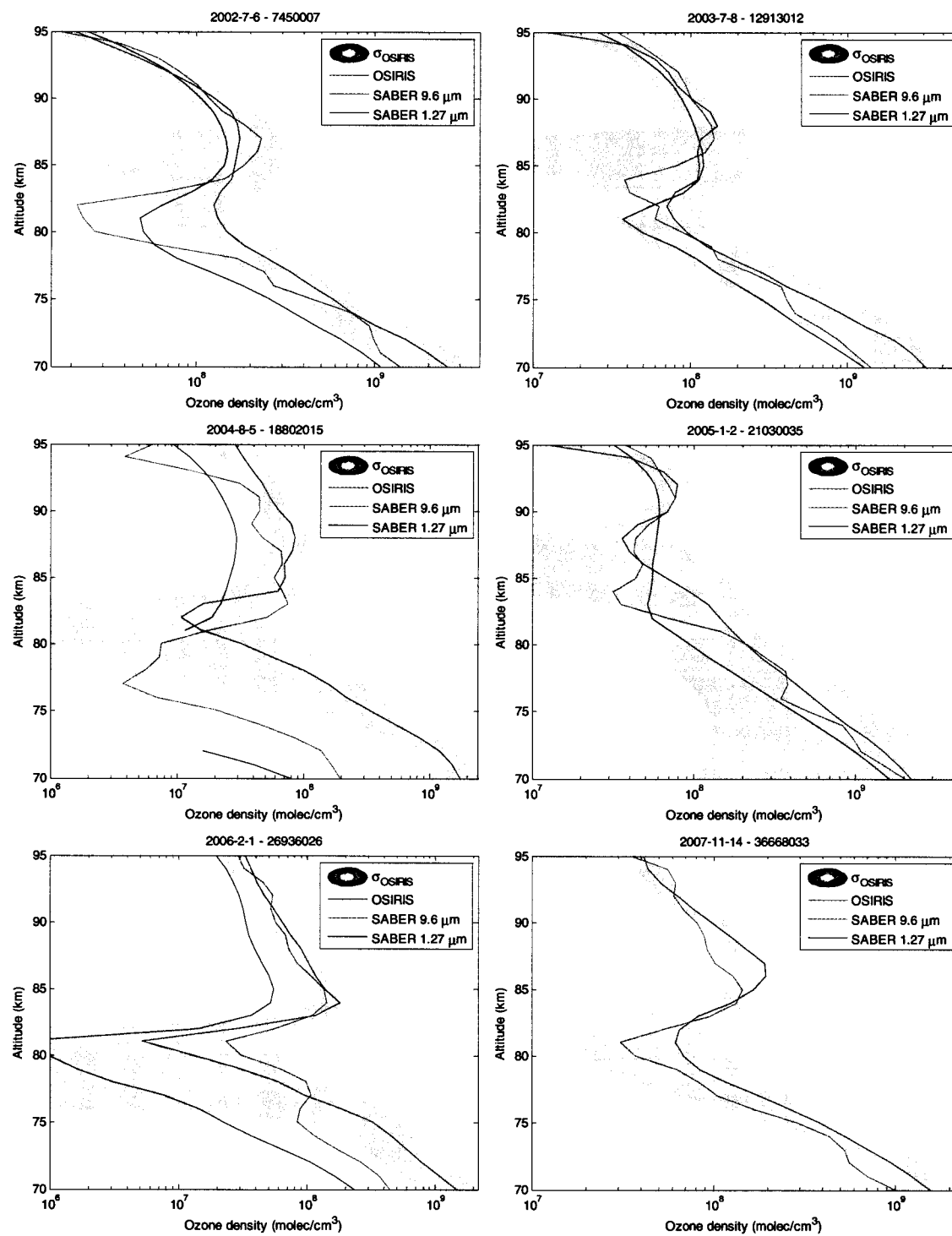
Figure 6.1: Comparisons between ozone density profiles retrieved from OSIRIS, SABER 9.6 μm, and SABER $O_2(a^1\Delta)$ for OSIRIS scans corresponding to those of Fig. 4.4.
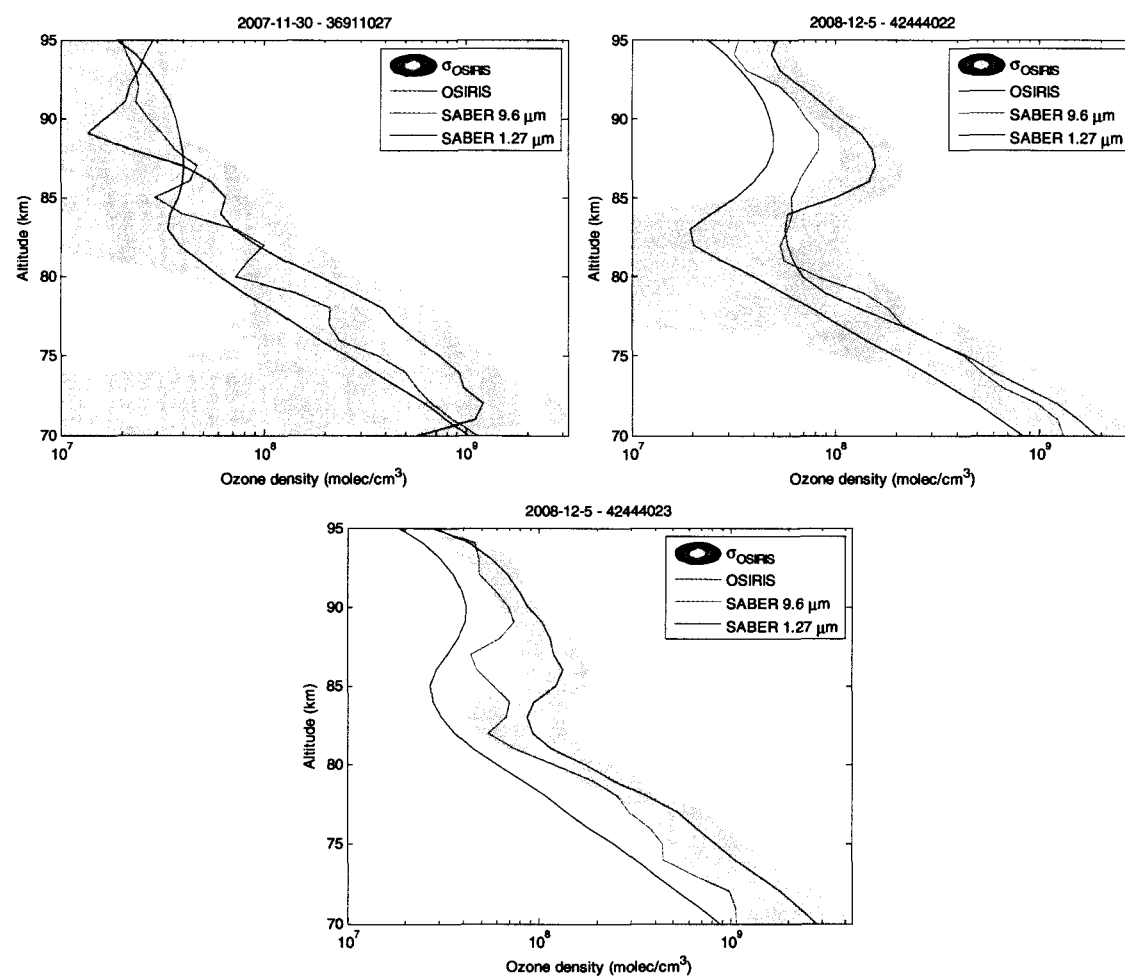
Figure 6.1: Comparisons between ozone density profiles retrieved from OSIRIS, SABER 9.6 μm, and SABER $O_2(a^1\Delta)$ for OSIRIS scans corresponding to those of Fig. 4.4 (cont'd).

The publicly available Version 1.07 SABER data unfortunately does not give any estimate of the uncertainties in either the 9.6 or 1.27 μm channel data. Due to the difficulties in the retrieval methods of these data it is assumed that the uncertainties would not be insignificant. An ad hoc estimate of the minimum uncertainty in the two methods was assumed and was taken as the percent difference between the two channels, *i.e.*,

$$\delta[O_3]_{SABER} \geq \frac{200 \times |[O_3]_{9.6} - [O_3]_{1.27}|}{[O_3]_{9.6} + [O_3]_{1.27}}. \tag{6.1}$$

Fig. 6.2 plots the percent difference between OSIRIS ozone densities and ozone densities from the separate SABER channels, as well as the assumed SABER uncertainty, $\delta[O_3]_{SABER}$.
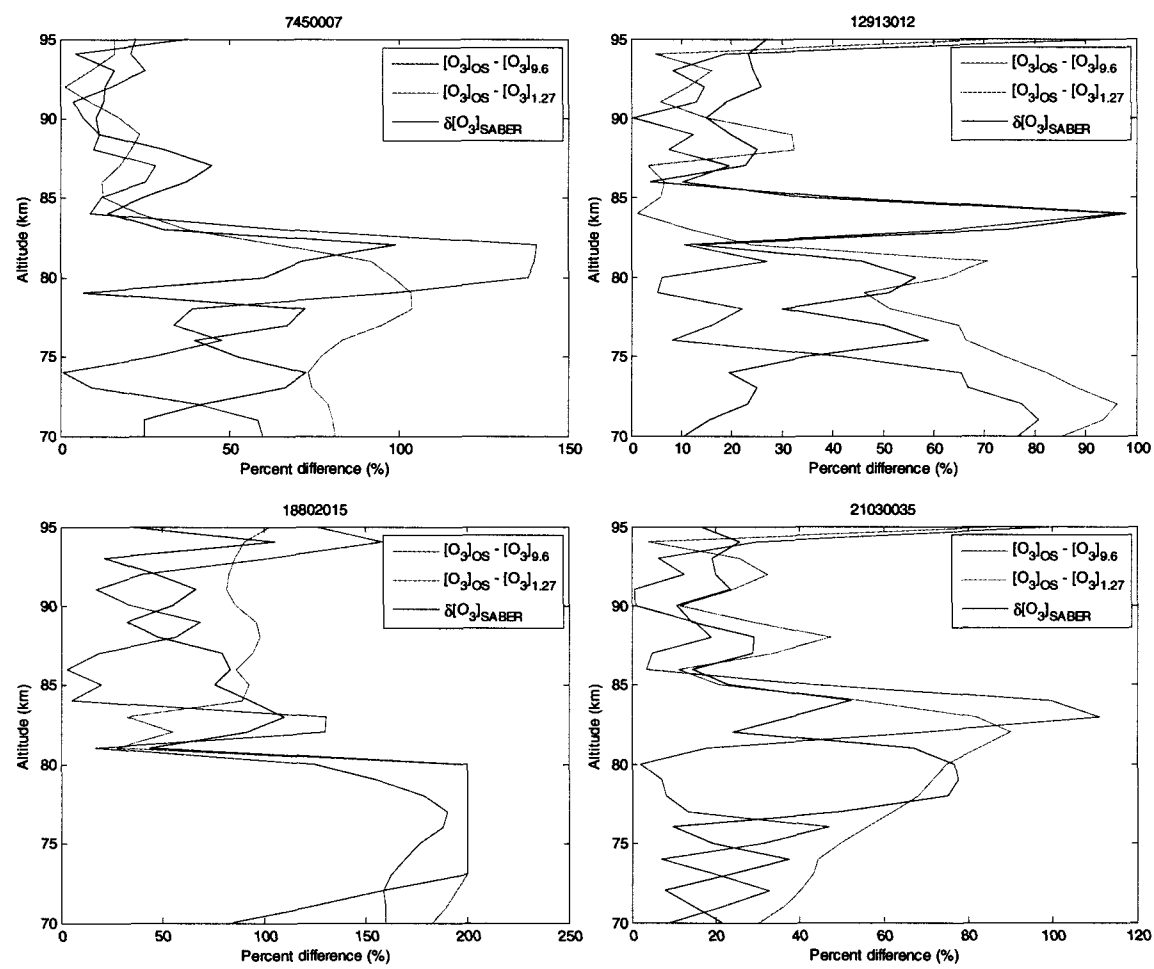
Figure 6.2: Percent differences between OSIRIS and the two SABER channels compared with the assumed SABER uncertainty for scans corresponding to those of Fig. 4.4.
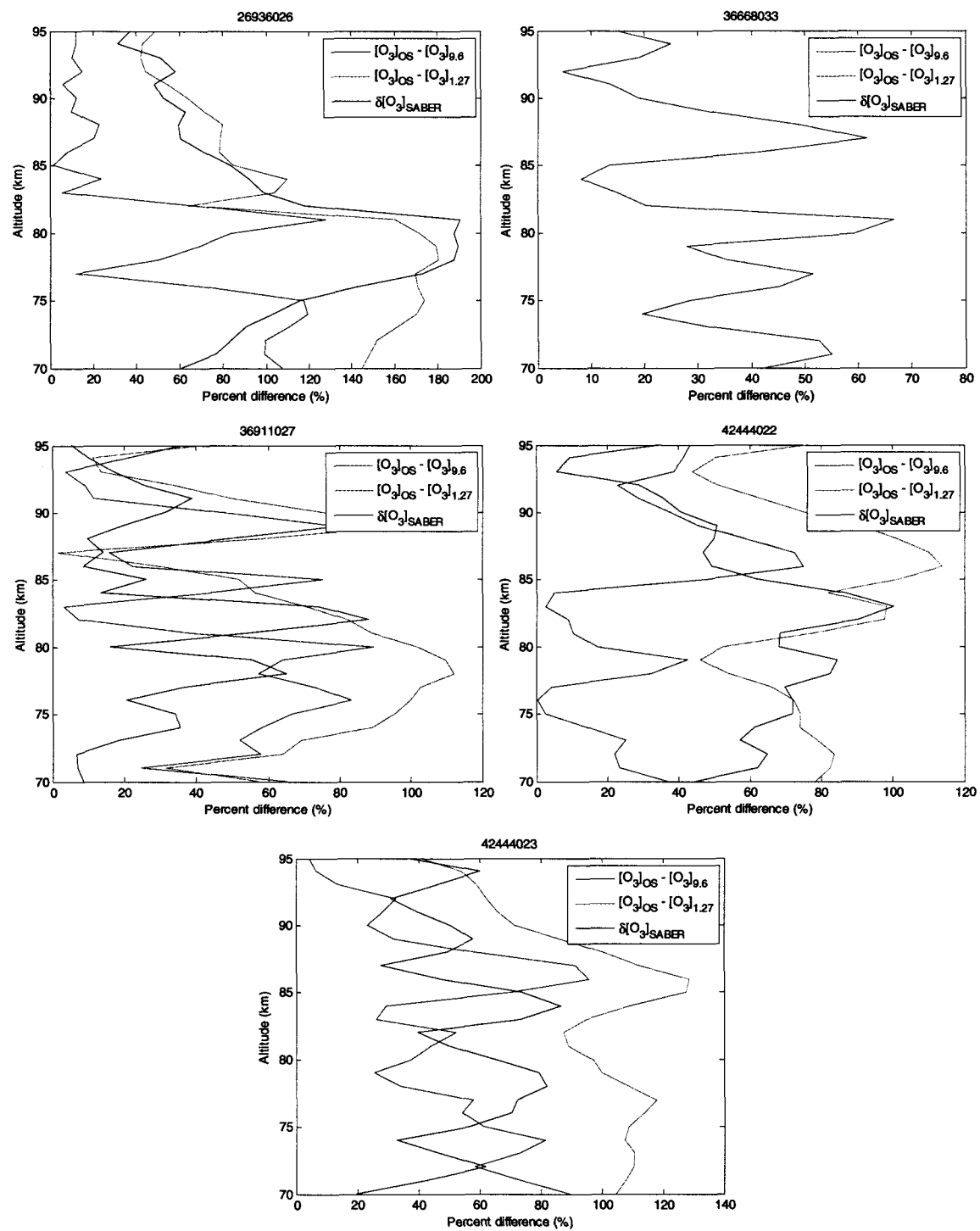
Figure 6.2: Percent differences between OSIRIS and the two SABER channels compared with the assumed SABER uncertainty[4] for scans corresponding to those of Fig. 4.9.

---

[4] The plot for scan 36668033 in Fig. 6.2 does not show the percent difference with 1.27 μm or the SABER error as the corresponding 1.27 μm ozone retrieval was largely negative.

When comparing the OSIRIS and SABER datasets the region with the greatest number of coincident scans was in the Northern hemisphere summer (May – August) in the high latitudes (>65°). 47 coincident scans in this region were compared, and Fig. 6.3 shows the mean percent difference between the OSIRIS and SABER scans, along with the standard deviation of the percent differences and the mean combined uncertainty of the two sets. It can clearly be seen from Fig. 6.3 that there is better agreement between OSIRIS and the 9.6 μm channel ozone retrievals than there is between those of OSIRIS and the 1.27 μm channel at all altitudes except near 85 km, where both show an average percent difference around 40%. However, comparisons between both OSIRIS and the SABER 9.6 μm and OSIRIS and the SABER 1.27 μm channel show that the standard deviation of the percent differences are typically below or on the same order as the combined uncertainties, which indicates that both SABER channel datasets are in agreement with the OS data.
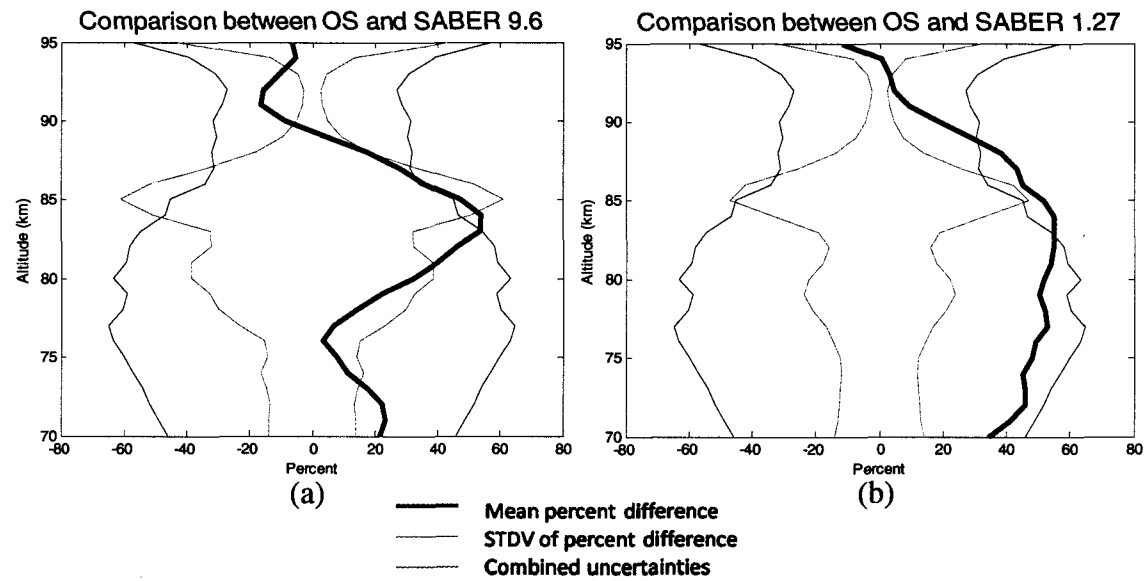
Figure 6.3: Comparisons of high latitude summer ozone between OSIRIS and (a) SABER 9.6 μm channel and (b) SABER 1.27 μm channel. 47 sets of coincident scans were compared in the analysis.

6.2 Comparison of retrieved O densities

As discussed in Chapter 4, atomic oxygen density profiles are inferred from the retrieved ozone profiles. Unfortunately, there are very few daytime mesospheric atomic oxygen databases to which a comparison with OSIRIS retrievals could be made. There are two main reasons for the lack of daytime mesospheric atomic oxygen density measurements. First, as with any mesospheric parameter, *in situ* measurements are difficult, as discussed in Chapter 2. Second, the indirect spectroscopic methods of inferring O densities typically rely on observations of emission features, such as the O(^{1}S) green line at 557.7 nm and various OH emission lines [*e.g. Shepherd et al.*, 1993; *Russell et al.*, 2005]. These lines are relatively weak in the mesosphere and are typically not visible against the solar background at altitudes below roughly 80 km. However, these methods can be used to

retrieve nighttime O densities.

The method of inferring daytime O densities from ozone is often exploited whenever O_3 densities are being retrieved. SABER, whose observations are regularly coincident with those of OSIRIS, utilizes this method and incorporates atomic oxygen densities inferred from the 1.27 μm channel in the Version 1.07 data. However, comparisons between SABER and OSIRIS results will not be made here, as direct comparisons of retrieved ozone concentrations from the two instruments have already been examined.

An atomic oxygen reference model was given by *Llewellyn and McDade* [1996], in which atomic oxygen densities were inferred from measured ozone densities using a similar method to that of this study. The ozone densities were taken from the ozone reference model of *Keating et al.* [1990], which were mean values from five different satellite-based instruments; however, the only instrument that measured ozone densities in the MLT was the SME 1.27 μm channel. These densities ranged from below an altitude of 70 km up to approximately 90 km. Above 90 km atomic oxygen densities were smoothed using a cubic spline to fit modelled density values from the MSIS-86 Thermospheric Model [*Hedin*, 1987] up to an altitude of 100 km. Figs. 6.4 – 6.5 compare composite OSIRIS atomic oxygen densities from 2002 – 2008 with atomic oxygen from the reference model. There are two main differences between the two datasets. First, is that the OSIRIS data correspond to an observed local time of roughly 0600, while the local time of the reference model in the MLT is roughly 1600. Second, the derivation of OSIRIS O densities takes into account the destruction of ozone from atomic hydrogen, whereas the reference model does not.

There is very good agreement in the absolute magnitude of the two datasets at all latitudes. Both exhibit an increase in atomic oxygen densities with altitude from $\sim 10^9$ molec/cm^3 at a height of 70 km to $\sim 10^{12}$ molec/cm^3 at 95 km. The seasonal variations in the equatorial region are also in very good agreement with a semi-annual oscillation peaking around equinox. At high latitudes, there is also agreement in the seasonal structure. Above ~ 82 km both datasets show a peak in atomic oxygen around summer solstice and a semi-annual oscillation below ~ 82 km peaking around equinox. However the seasonal structure of the two datasets at mid-latitudes do not agree. OSIRIS observes annual peaks in oxygen around summer solstice, whereas the reference model exhibits annual peaks around winter solstice.
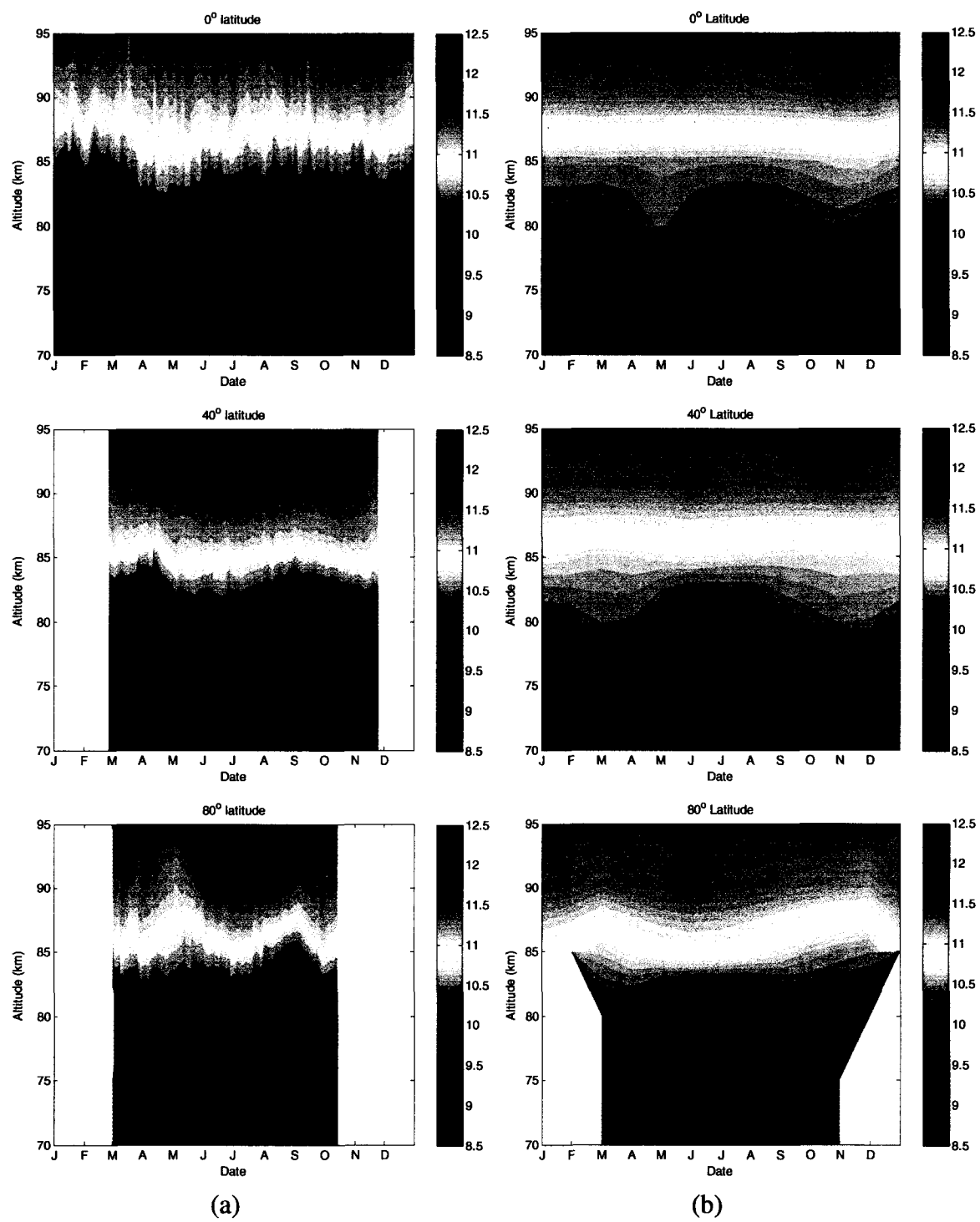
Figure 6.4: Vertical profiles at various latitudes in the northern hemisphere of the log of atomic oxygen densities in molec/cm^3 from (a) zonally-averaged OSIRIS data smoothed by a 5-day running average and (b) the reference model monthly averages.
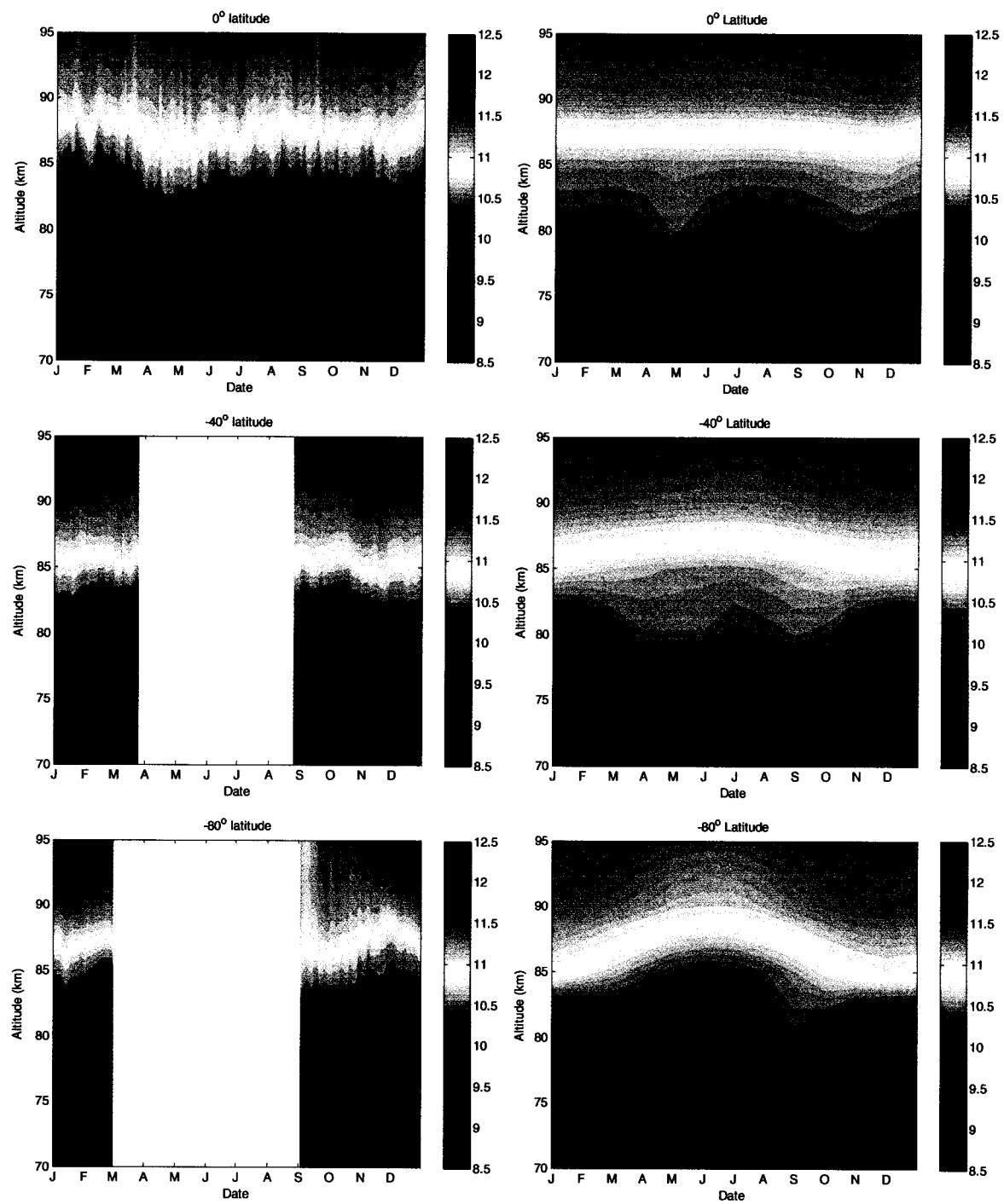
Figure 6.5: Same conditions as Fig. 6.4 only for latitudes in the southern hemisphere.

138

The difference in the seasonal structures exhibited in the two datasets is in part due to the incorporation of the destruction of ozone through atomic hydrogen in the derivation of OSIRIS O densities. For the destruction of ozone by atomic hydrogen to be insignificant in comparison to photolysis, it can be seen from Equation 4.33 that this would require $J_3 \ll k_{O3}[H]$. The values of $k_{O3}[H]/J_3$ are plotted in Fig. 6.6 assuming a constant J_3 value of 7.1×10^{-3} s^{-1} and using MSIS hydrogen densities and kinetic temperatures for the year 2004 at a latitude of 45°N, a longitude of 0°, and an altitude of 78 km. It can be seen that incorporating H in the derivation does increase derived O densities by roughly 5% in the winter and over 8% in the summer.
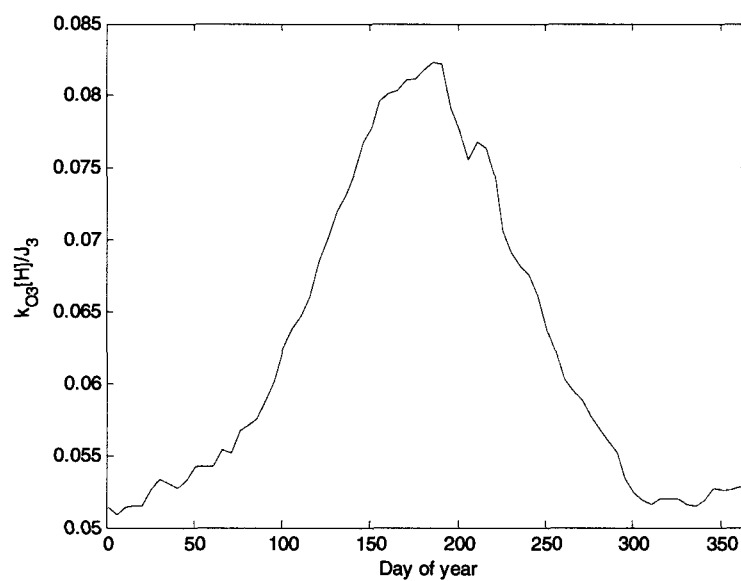
Figure 6.6: Calculated $k_{O3}[H]/J_3$ values for 2004 assuming an MSIS background atmosphere at 45°N latitude, 0° longitude, 78 km altitude, and local noon.

When the SME and OSIRIS ozone time series are directly compared in the mid-latitudes, below 82 km there is excellent agreement in the absolute magnitude of the

volume mixing ratios, although, as expected, there is a clear disagreement in the seasonal variations. At mid-latitudes, at an altitude of 80 km, the SME time series, as seen in Fig. 6.7, exhibits a strong semi-annual oscillation with ozone mixing ratios peaking in April and October and at a minimum around August, whereas the OSIRIS time series shows a strong annual oscillation peaking around early July.
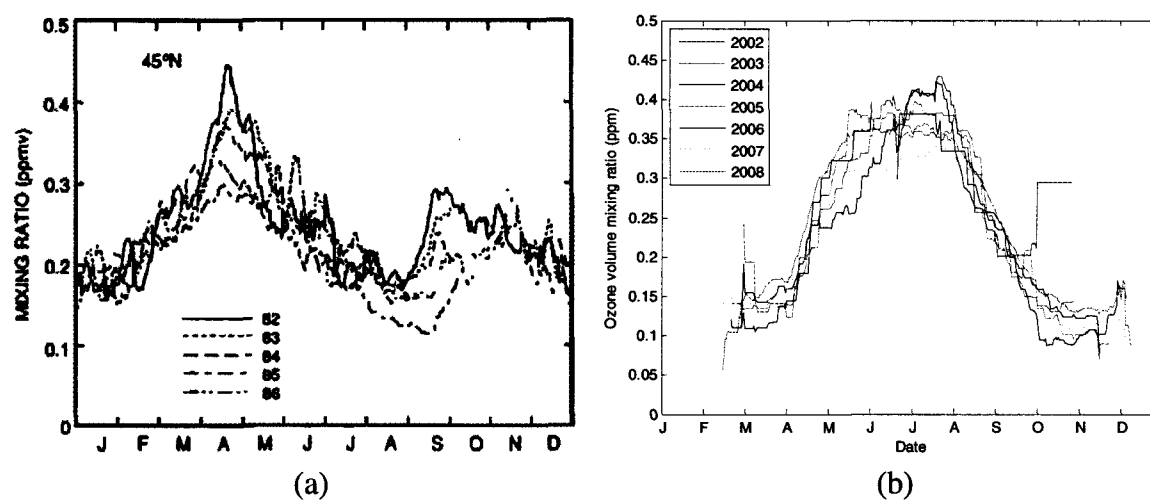
Figure 6.7: Zonally-averaged ozone volume mixing ratios at a height of 80 km and a latitude of 45°N derived from (a) the SME 1.27 μm channel, data has been smoothed by a 7-day running average, from *Thomas* [1990], and (b) OSIRIS, daily bins represent 30-day averages.

Chapter 7

Conclusions

7.1 Summary

A forward model that simulates OSIRIS limb irradiance observations in the O_2 A-band region has been developed. The forward model exploits the A-band volume emission rates predicted by a kinetic-photochemical model of the emission of A-band dayglow that has also been developed. The kinetic-photochemical model takes into account the most current measurements of the relevant reaction coefficients and A-band parameters.

For the first time, OSIRIS observations of the O_2 A-band dayglow, along with the simulated limb irradiance profiles of the forward model, have been used in an iterative Newtonian-optimal estimation technique to retrieve daytime ozone densities in the mesosphere. The retrievals form a new OSIRIS data product, a database of mesospheric ozone densities from July 2002 to December 2008, within an altitude range of 70 – 95 km. Results of an error analysis study show that uncertainties in the retrieved ozone densities are in the range of 10 – 100%, which is typical of modern upper-mesospheric

141

retrievals.

The OSIRIS retrieved ozone densities are in relatively good agreement with near-coincident SABER measurements retrieved from the O_3 9.6 μm band. OSIRIS retrievals and SABER 1.27 μm channel measurements of ozone densities have also been compared and exhibit poorer agreement between the two datasets than between those of OSIRIS and the SABER 9.6 μm channel. Atomic oxygen densities have been inferred from the retrieved ozone densities, and results have been compared to the atomic oxygen densities presented in the reference model of *Llewellyn and McDade*, [1996]. For the most part the two datasets are in good agreement, where the only significant differences are isolated to mid-latitudes near altitudes of ~80 km.

7.2 Future work

Although the retrieval method discussed in this study is currently in use and retrieving ozone density profiles with encouraging results, naturally, there are a great number of areas that could be further explored and/or improved. A list of some of the more pressing areas is given below.

- It was shown in Chapter 4 that the retrieval response is typically very close to unity, and therefore the retrieval results are not greatly dependent on the assumed values of the *a priori*. Therefore an updated *a priori* profile would not have much of an effect on the actual retrieval results, however, using a modelled *a priori* profile from a climatological model (*e.g.* SOCRATES 2-D, or TIME-GCM [*Robel*, 1995]) that would vary from month to month, could potentially significantly speed up

convergence within the optimal estimation routine.

- A significant source of error within the retrieval is due to uncertainty in the A-band g-factors. The incorporation of an on-line calculation of the g-factors into the kinetic-photochemical model would decrease forward model parameter error, with the trade-off being moderately increased computational time within the retrieval.

- In 2008 the 2008 edition of the HITRAN spectroscopic database [*Rothman et al.*, 2009] was made available. O_2 A-band line strengths could be updated for more accurate transmission calculations.

- The retrieved ozone density time series should be made available for download through the OSIRIS website.

- A cross-validation study between OSIRIS mesospheric ozone and that of other instruments is needed. However, this is difficult due to a lack of instruments that currently perform mesospheric ozone retrievals. Comparisons between OSIRIS and SABER have been made in Chapter 6, however a true cross-validation study would first require the separate instruments be independently validated. Validation between OSIRIS and ACE-FTS is also a possibility, although due to the two instruments' viewing geometries coincident coverage is most likely limited.

- Both retrieved ozone and atomic oxygen densities could be compared to CMAM (Canadian Middle Atmosphere Model) data [*Shepherd*, 1995] for validation purposes.

- The retrieved ozone densities could be used to model $O_2(a^1\Delta)$ 1.27 μm volume emission rates observed by the OSIRIS IR imager. Currently, there are no tomographic inversions of the IR data for coincident OS and IR observations. IR data

143

for these observations would need to be inverted before this type of validation study could be exploited.

- Further investigation should be made into the cause of the ozone peak in the northern high latitudes at altitudes near 80 km.

- Polar mesospheric clouds are common features of the summer upper mesosphere, typically forming at an altitude of ~80 km. Although the effects of a PMC in the OSIRIS line-of-sight are not as significant in the A-band as they are in other regions of the solar spectrum, increases in the observed radiance in the A-band due to the presence of PMCs are observed. An investigation of the retrieval process in the presence of a PMC would be of great interest. Currently, a study is underway to retrieve PMC particle sizes from OSIRIS observations in the Hartley band. This study is incorporating monthly averaged retrieved ozone profiles of this study to account for ozone absorption, which is not insignificant at altitudes of 80 – 85 km.

Appendix A

Derivation of optimal estimate equation

In Section 4.2.1 it was stated that the solution for the optimal estimate is given by,

$$\mathbf{x}_{n+1} = (\mathbf{S}_x^{-1} + \mathbf{K}_n^T \mathbf{S}_\varepsilon^{-1} \mathbf{K}_n)^{-1} [\mathbf{S}_x^{-1} \mathbf{x}_a + \mathbf{K}_n^T \mathbf{S}_\varepsilon^{-1} (\mathbf{y} - \mathbf{y}_n + \mathbf{K}_n \mathbf{x}_n)], \qquad (4.26)$$

which is equivalent to the final solution,

$$\mathbf{x}_{n+1} = \mathbf{x}_a + \mathbf{S}_x \mathbf{K}_n^T (\mathbf{S}_\varepsilon + \mathbf{K}_n \mathbf{S}_x \mathbf{K}_n^T)^{-1} [(\mathbf{y} - \mathbf{y}_n) - \mathbf{K}_n (\mathbf{x}_a - \mathbf{x}_n)]. \qquad (4.27)$$

What follows is a proof that Equations 4.26 and 4.27 are indeed equivalent.

Given the identity,

$$\mathbf{K}_n^T \mathbf{S}_\varepsilon^{-1} (\mathbf{S}_\varepsilon + \mathbf{K}_n \mathbf{S}_x \mathbf{K}_n^T) = (\mathbf{S}_x^{-1} + \mathbf{K}_n^T \mathbf{S}_\varepsilon^{-1} \mathbf{K}_n) \mathbf{S}_x \mathbf{K}_n^T \qquad (A.1)$$

$$\Leftrightarrow (\mathbf{S}_x^{-1} + \mathbf{K}_n^T \mathbf{S}_\varepsilon^{-1} \mathbf{K}_n)^{-1} \mathbf{K}_n^T \mathbf{S}_\varepsilon^{-1} = \mathbf{S}_x \mathbf{K}_n^T (\mathbf{S}_\varepsilon + \mathbf{K}_n \mathbf{S}_x \mathbf{K}_n^T)^{-1}. \qquad (A.2)$$

Start with the covariance matrix,

$$\hat{\mathbf{S}} = (\mathbf{S}_x^{-1} + \mathbf{K}_n^T \mathbf{S}_\varepsilon^{-1} \mathbf{K}_n)^{-1}. \qquad (A.3)$$

Using Equation A.2,

$$\hat{\mathbf{S}} = \mathbf{S}_x \mathbf{K}_n^T (\mathbf{S}_\varepsilon + \mathbf{K}_n \mathbf{S}_x \mathbf{K}_n^T)^{-1} \mathbf{S}_\varepsilon \mathbf{K}_n^{T^{-1}} \qquad (A.4)$$

$$= \mathbf{S}_x \mathbf{K}_n^T (\mathbf{S}_\varepsilon + \mathbf{K}_n \mathbf{S}_x \mathbf{K}_n^T)^{-1} \left[(\mathbf{S}_\varepsilon + \mathbf{K}_n \mathbf{S}_x \mathbf{K}_n^T) \mathbf{K}_n^{T^{-1}} - \mathbf{K}_n \mathbf{S}_x \right] \qquad (A.5)$$

145

$$= \mathbf{S}_x - \mathbf{S}_x \mathbf{K}_n^T (\mathbf{S}_\varepsilon + \mathbf{K}_n \mathbf{S}_x \mathbf{K}_n^T)^{-1} \mathbf{K}_n \mathbf{S}_x. \tag{A.6}$$

The optimal estimate given by Equation 4.26,

$$\mathbf{x}_{n+1} = (\mathbf{S}_x^{-1} + \mathbf{K}_n^T \mathbf{S}_\varepsilon^{-1} \mathbf{K}_n)^{-1} [\mathbf{S}_x^{-1} \mathbf{x}_a + \mathbf{K}_n^T \mathbf{S}_\varepsilon^{-1} (\mathbf{y} - \mathbf{y}_n + \mathbf{K}_n \mathbf{x}_n)] \tag{A.7}$$

$$= \hat{\mathbf{S}} \, \mathbf{S}_x^{-1} \mathbf{x}_a + \hat{\mathbf{S}} \, \mathbf{K}_n^T \mathbf{S}_\varepsilon^{-1} (\mathbf{y} - \mathbf{y}_n + \mathbf{K}_n \mathbf{x}_n). \tag{A.8}$$

Substituting in the r.h.s of Equation A.6 and the r.h.s. of Equation A.4 for the respective

$\hat{\mathbf{S}}$ values in Equation A.8 gives,

$$\mathbf{x}_{n+1} = \mathbf{x}_a - \mathbf{S}_x \mathbf{K}_n^T (\mathbf{S}_\varepsilon + \mathbf{K}_n \mathbf{S}_x \mathbf{K}_n^T)^{-1} \mathbf{K}_n \mathbf{x}_a$$
$$+ \mathbf{S}_x \mathbf{K}_n^T (\mathbf{S}_\varepsilon + \mathbf{K}_n \mathbf{S}_x \mathbf{K}_n^T)^{-1} (\mathbf{y} - \mathbf{y}_n + \mathbf{K}_n \mathbf{x}_n) \tag{A.9}$$

$$\mathbf{x}_{n+1} = \mathbf{x}_a + \mathbf{S}_x \mathbf{K}_n^T (\mathbf{S}_\varepsilon + \mathbf{K}_n \mathbf{S}_x \mathbf{K}_n^T)^{-1} [(\mathbf{y} - \mathbf{y}_n) - \mathbf{K}_n (\mathbf{x}_a - \mathbf{x}_n)], \quad q.e.d. \tag{A.10}$$

146

Appendix B

Derivation of the optimal estimate solution

using Bayes' Theorem

Considering both the *a priori* information and the measurement as probability density functions, PDFs, Bayes' Theorem provides a method of mapping the measurement from measurement space into state space. The method calculates a posterior PDF by using the measurement PDF to update the prior PDF. *Rodgers* [2008] shows that the normalized solution to the Bayesian method is given by,

$$P(\mathbf{x}|\mathbf{y}) = P(\mathbf{y}|\mathbf{x})P(\mathbf{x}), \tag{B.1}$$

where, $P(\mathbf{x}|\mathbf{y})$ is the conditional PDF of $\mathbf{x}$ given $\mathbf{y}$, where $P(\mathbf{x}|\mathbf{y})\mathrm{d}\mathbf{x}$ is the probability that $\mathbf{x}$ lies within $\mathbf{x}$ and $\mathbf{x} + \mathrm{d}\mathbf{x}$, given $\mathbf{y}$; $P(\mathbf{y}|\mathbf{x})$ is the conditional PDF of $\mathbf{y}$ given $\mathbf{x}$, where $P(\mathbf{y}|\mathbf{x})\mathrm{d}\mathbf{y}$ is the probability that $\mathbf{y}$ lies within $\mathbf{y}$ and $\mathbf{y} + \mathrm{d}\mathbf{y}$, given $\mathbf{x}$; and $P(\mathbf{x})$ is the PDF of the state, where $P(\mathbf{x})\mathrm{d}\mathbf{x}$ is the probability that $\mathbf{x}$ lies within $\mathbf{x}$ and $\mathbf{x} + \mathrm{d}\mathbf{x}$ prior to making any measurements.

147

Given these definitions, $P(\mathbf{x}|\mathbf{y})$ is the posterior PDF of the state given the measurement $\mathbf{y}$, $P(\mathbf{x})$ is the prior PDF, and obtaining $P(\mathbf{y}|\mathbf{x})$ requires knowledge of the measurement error and the forward model of the state. When solving for the optimal estimate of the state, for the sake of simplicity, the problem will be assumed to be linear, and the assumed probability density functions will be Gaussian distributions. The Gaussian distribution of a vector $\mathbf{z}$, with a covariance of $\mathbf{S}_z$, is given by,

$$P(\mathbf{z}) = \frac{1}{(2\pi)^{\frac{n}{2}}|\mathbf{S}_z|^{\frac{1}{2}}} \exp\left[-\frac{1}{2}(\mathbf{z} - \bar{\mathbf{z}})^T \mathbf{S}_z^{-1}(\mathbf{z} - \bar{\mathbf{z}})\right]. \tag{B.2}$$

Taking the optimal estimate of the state, $\hat{\mathbf{x}}$, as the maximum probability value or the expected value of $\mathbf{x}$ yields the same result of $\hat{\mathbf{x}} = \bar{\mathbf{x}}$, as the PDF is symmetric about and peaks at $\mathbf{x} = \bar{\mathbf{x}}$. Therefore,

$$-2\ln P(\mathbf{x}|\mathbf{y}) = (\mathbf{x} - \hat{\mathbf{x}})^T \hat{\mathbf{S}}^{-1}(\mathbf{x} - \hat{\mathbf{x}}) + c_1, \tag{B.3}$$

where c_1 is independent of $\mathbf{x}$. As in Section 4.2, for the linear problem,

$$\mathbf{y} = \mathbf{F}(\mathbf{x}) = \mathbf{K}\mathbf{x}, \tag{B.4}$$

where the covariance matrix of $\mathbf{y}$ is $\mathbf{S}_\varepsilon$, given experimental error ε. Hence,

$$-2\ln P(\mathbf{y}|\mathbf{x}) = (\mathbf{y} - \mathbf{K}\mathbf{x})^T \mathbf{S}_\varepsilon^{-1}(\mathbf{y} - \mathbf{K}\mathbf{x}) + c_2. \tag{B.5}$$

The prior state PDF is given by,

$$-2\ln P(\mathbf{x}) = (\mathbf{x} - \mathbf{x}_a)^T \mathbf{S}_x^{-1}(\mathbf{x} - \mathbf{x}_a) + c_3. \tag{B.6}$$

Substituting Equations B.5 and B.6 into Equation B.1 gives the posterior PDF as,

$$-2\ln P(\mathbf{x}|\mathbf{y}) = (\mathbf{y} - \mathbf{K}\mathbf{x})^T \mathbf{S}_\varepsilon^{-1}(\mathbf{y} - \mathbf{K}\mathbf{x}) + (\mathbf{x} - \mathbf{x}_a)^T \mathbf{S}_x^{-1}(\mathbf{x} - \mathbf{x}_a) + c_4. \tag{B.7}$$

Equating terms in Equations B.3 and B.7 that are quadratic in $\mathbf{x}$ yields,

$$\mathbf{x}^T \hat{\mathbf{S}}^{-1} \mathbf{x} = \mathbf{x}^T \mathbf{K}^T \mathbf{S}_\varepsilon^{-1} \mathbf{K} \mathbf{x} + \mathbf{x}^T \mathbf{S}_x^{-1} \mathbf{x} \tag{B.8}$$

$$\hat{\mathbf{S}}^{-1} = \mathbf{K}^T \mathbf{S}_\varepsilon^{-1} \mathbf{K} + \mathbf{S}_x^{-1}, \tag{B.9}$$

which is analogous to the non-linear solution of the retrieval covariance given by Equation 4.24. Similarly, equating terms in Equations B.3 and B.7 that are linear in $\mathbf{x}^T$ yields,

$$\mathbf{x}^T \hat{\mathbf{S}}^{-1} \hat{\mathbf{x}} = \mathbf{x}^T \mathbf{K}^T \mathbf{S}_\varepsilon^{-1} \mathbf{y} + \mathbf{x}^T \mathbf{S}_x^{-1} \mathbf{x}_a \tag{B.10}$$

$$\hat{\mathbf{x}} = \hat{\mathbf{S}}(\mathbf{K}^T \mathbf{S}_\varepsilon^{-1} \mathbf{y} + \mathbf{S}_x^{-1} \mathbf{x}_a). \tag{B.11}$$

Substituting Equation B.9 into Equation B.11 and rearranging terms gives,

$$\hat{\mathbf{x}} = \mathbf{x}_a + \mathbf{S}_x \mathbf{K}^T (\mathbf{S}_\varepsilon + \mathbf{K} \mathbf{S}_x \mathbf{K}^T)^{-1} (\mathbf{y} - \mathbf{K} \mathbf{x}_a), \tag{B.12}$$

which is analogous to the non-linear solution of the optimal estimate given by Equation 4.27.

Appendix C

Calculated *g*-factor values

The values of the *g*-factors, displayed in Tables C.1 and C.2 in units of s^{-1}, were calculated using the method described in Section 3.3.5. The *g*-factor values in the model were calculated for altitudes between 40 and 120 km in 1 km intervals and for solar zenith angles of 0 to 90° in 1° intervals, however are only shown here between 60 – 95 km and in solar zenith angle intervals of 5°.

Altitude (km)	0°	5°	10°	15°	20°	25°	30°	35°
60	5.42E-09	5.42E-09	5.41E-09	5.40E-09	5.38E-09	5.35E-09	5.31E-09	5.27E-09
61	5.51E-09	5.51E-09	5.50E-09	5.49E-09	5.47E-09	5.45E-09	5.41E-09	5.37E-09
62	5.59E-09	5.59E-09	5.58E-09	5.57E-09	5.56E-09	5.53E-09	5.51E-09	5.47E-09
63	5.66E-09	5.66E-09	5.66E-09	5.65E-09	5.63E-09	5.61E-09	5.59E-09	5.56E-09
64	5.73E-09	5.73E-09	5.72E-09	5.71E-09	5.70E-09	5.68E-09	5.66E-09	5.63E-09
65	5.79E-09	5.78E-09	5.78E-09	5.77E-09	5.76E-09	5.75E-09	5.73E-09	5.70E-09
66	5.84E-09	5.84E-09	5.83E-09	5.83E-09	5.82E-09	5.80E-09	5.79E-09	5.76E-09
67	5.88E-09	5.88E-09	5.88E-09	5.87E-09	5.86E-09	5.85E-09	5.84E-09	5.82E-09
68	5.92E-09	5.92E-09	5.92E-09	5.91E-09	5.91E-09	5.90E-09	5.88E-09	5.87E-09
69	5.96E-09	5.96E-09	5.95E-09	5.95E-09	5.94E-09	5.93E-09	5.92E-09	5.91E-09
70	5.99E-09	5.99E-09	5.98E-09	5.98E-09	5.97E-09	5.97E-09	5.96E-09	5.94E-09
71	6.01E-09	6.01E-09	6.01E-09	6.01E-09	6.00E-09	6.00E-09	5.99E-09	5.98E-09
72	6.04E-09	6.04E-09	6.04E-09	6.03E-09	6.03E-09	6.02E-09	6.01E-09	6.01E-09
73	6.06E-09	6.06E-09	6.06E-09	6.05E-09	6.05E-09	6.05E-09	6.04E-09	6.03E-09
74	6.08E-09	6.08E-09	6.07E-09	6.07E-09	6.07E-09	6.06E-09	6.06E-09	6.05E-09
75	6.09E-09	6.09E-09	6.09E-09	6.09E-09	6.09E-09	6.08E-09	6.08E-09	6.07E-09
76	6.10E-09	6.10E-09	6.10E-09	6.10E-09	6.10E-09	6.10E-09	6.09E-09	6.09E-09
77	6.12E-09	6.12E-09	6.12E-09	6.11E-09	6.11E-09	6.11E-09	6.11E-09	6.10E-09
78	6.13E-09	6.13E-09	6.13E-09	6.12E-09	6.12E-09	6.12E-09	6.12E-09	6.11E-09
79	6.13E-09	6.13E-09	6.13E-09	6.13E-09	6.13E-09	6.13E-09	6.13E-09	6.12E-09
80	6.14E-09	6.14E-09	6.14E-09	6.14E-09	6.14E-09	6.14E-09	6.14E-09	6.13E-09
81	6.15E-09	6.15E-09	6.15E-09	6.15E-09	6.15E-09	6.14E-09	6.14E-09	6.14E-09
82	6.15E-09	6.15E-09	6.15E-09	6.15E-09	6.15E-09	6.15E-09	6.15E-09	6.15E-09
83	6.16E-09	6.16E-09	6.16E-09	6.16E-09	6.16E-09	6.16E-09	6.15E-09	6.15E-09
84	6.16E-09	6.16E-09	6.16E-09	6.16E-09	6.16E-09	6.16E-09	6.16E-09	6.16E-09
85	6.17E-09	6.17E-09	6.17E-09	6.16E-09	6.16E-09	6.16E-09	6.16E-09	6.16E-09
86	6.17E-09	6.17E-09	6.17E-09	6.17E-09	6.17E-09	6.17E-09	6.17E-09	6.16E-09
87	6.17E-09	6.17E-09	6.17E-09	6.17E-09	6.17E-09	6.17E-09	6.17E-09	6.17E-09
88	6.17E-09	6.17E-09	6.17E-09	6.17E-09	6.17E-09	6.17E-09	6.17E-09	6.17E-09
89	6.17E-09	6.17E-09	6.17E-09	6.17E-09	6.17E-09	6.17E-09	6.17E-09	6.17E-09
90	6.18E-09	6.18E-09	6.18E-09	6.17E-09	6.17E-09	6.17E-09	6.17E-09	6.17E-09
91	6.18E-09	6.18E-09	6.18E-09	6.18E-09	6.18E-09	6.18E-09	6.18E-09	6.17E-09
92	6.18E-09	6.18E-09	6.18E-09	6.18E-09	6.18E-09	6.18E-09	6.18E-09	6.18E-09
93	6.18E-09	6.18E-09	6.18E-09	6.18E-09	6.18E-09	6.18E-09	6.18E-09	6.18E-09
94	6.18E-09	6.18E-09	6.18E-09	6.18E-09	6.18E-09	6.18E-09	6.18E-09	6.18E-09
95	6.18E-09	6.18E-09	6.18E-09	6.18E-09	6.18E-09	6.18E-09	6.18E-09	6.18E-09

Table C.1: Calculated g-factor values for the O_2 A-band in units of s^{-1}.

Altitude (km)	40°	45°	50°	55°	60°	65°	70°	75°
60	5.21E-09	5.14E-09	5.05E-09	4.93E-09	4.77E-09	4.56E-09	4.27E-09	3.85E-09
61	5.32E-09	5.26E-09	5.18E-09	5.07E-09	4.93E-09	4.73E-09	4.46E-09	4.07E-09
62	5.42E-09	5.37E-09	5.29E-09	5.20E-09	5.07E-09	4.89E-09	4.64E-09	4.28E-09
63	5.52E-09	5.46E-09	5.40E-09	5.31E-09	5.20E-09	5.04E-09	4.81E-09	4.48E-09
64	5.60E-09	5.55E-09	5.49E-09	5.41E-09	5.31E-09	5.17E-09	4.96E-09	4.66E-09
65	5.67E-09	5.63E-09	5.58E-09	5.51E-09	5.42E-09	5.29E-09	5.10E-09	4.83E-09
66	5.73E-09	5.70E-09	5.65E-09	5.59E-09	5.51E-09	5.40E-09	5.23E-09	4.98E-09
67	5.79E-09	5.76E-09	5.72E-09	5.67E-09	5.59E-09	5.49E-09	5.35E-09	5.12E-09
68	5.84E-09	5.82E-09	5.78E-09	5.73E-09	5.67E-09	5.58E-09	5.45E-09	5.25E-09
69	5.89E-09	5.86E-09	5.83E-09	5.79E-09	5.74E-09	5.66E-09	5.54E-09	5.36E-09
70	5.93E-09	5.91E-09	5.88E-09	5.84E-09	5.79E-09	5.73E-09	5.62E-09	5.47E-09
71	5.96E-09	5.94E-09	5.92E-09	5.89E-09	5.85E-09	5.79E-09	5.70E-09	5.56E-09
72	5.99E-09	5.98E-09	5.96E-09	5.93E-09	5.89E-09	5.84E-09	5.76E-09	5.64E-09
73	6.02E-09	6.01E-09	5.99E-09	5.96E-09	5.93E-09	5.89E-09	5.82E-09	5.71E-09
74	6.04E-09	6.03E-09	6.01E-09	5.99E-09	5.97E-09	5.93E-09	5.87E-09	5.78E-09
75	6.06E-09	6.05E-09	6.04E-09	6.02E-09	6.00E-09	5.96E-09	5.91E-09	5.83E-09
76	6.08E-09	6.07E-09	6.06E-09	6.04E-09	6.02E-09	5.99E-09	5.95E-09	5.88E-09
77	6.09E-09	6.09E-09	6.08E-09	6.06E-09	6.05E-09	6.02E-09	5.98E-09	5.92E-09
78	6.11E-09	6.10E-09	6.09E-09	6.08E-09	6.07E-09	6.04E-09	6.01E-09	5.96E-09
79	6.12E-09	6.11E-09	6.11E-09	6.10E-09	6.08E-09	6.07E-09	6.04E-09	5.99E-09
80	6.13E-09	6.12E-09	6.12E-09	6.11E-09	6.10E-09	6.08E-09	6.06E-09	6.02E-09
81	6.14E-09	6.13E-09	6.13E-09	6.12E-09	6.11E-09	6.10E-09	6.08E-09	6.05E-09
82	6.14E-09	6.14E-09	6.14E-09	6.13E-09	6.12E-09	6.11E-09	6.09E-09	6.07E-09
83	6.15E-09	6.15E-09	6.14E-09	6.14E-09	6.13E-09	6.12E-09	6.11E-09	6.08E-09
84	6.16E-09	6.15E-09	6.15E-09	6.15E-09	6.14E-09	6.13E-09	6.12E-09	6.10E-09
85	6.16E-09	6.16E-09	6.16E-09	6.15E-09	6.15E-09	6.14E-09	6.13E-09	6.11E-09
86	6.16E-09	6.16E-09	6.16E-09	6.16E-09	6.15E-09	6.15E-09	6.14E-09	6.12E-09
87	6.17E-09	6.17E-09	6.16E-09	6.16E-09	6.16E-09	6.15E-09	6.15E-09	6.13E-09
88	6.17E-09	6.17E-09	6.17E-09	6.16E-09	6.16E-09	6.16E-09	6.15E-09	6.14E-09
89	6.17E-09	6.17E-09	6.17E-09	6.17E-09	6.16E-09	6.16E-09	6.16E-09	6.15E-09
90	6.17E-09	6.17E-09	6.17E-09	6.17E-09	6.17E-09	6.16E-09	6.16E-09	6.15E-09
91	6.17E-09	6.17E-09	6.17E-09	6.17E-09	6.17E-09	6.17E-09	6.16E-09	6.16E-09
92	6.18E-09	6.17E-09	6.17E-09	6.17E-09	6.17E-09	6.17E-09	6.17E-09	6.16E-09
93	6.18E-09	6.18E-09	6.18E-09	6.17E-09	6.17E-09	6.17E-09	6.17E-09	6.17E-09
94	6.18E-09	6.18E-09	6.18E-09	6.18E-09	6.18E-09	6.17E-09	6.17E-09	6.17E-09
95	6.18E-09	6.18E-09	6.18E-09	6.18E-09	6.18E-09	6.18E-09	6.17E-09	6.17E-09

Table C.1: Calculated g-factor values for the O_2 A-band in units of s^{-1}.

Altitude (km)	80°	85°	90°
60	3.18E-09	2.07E-09	5.92E-10
61	3.43E-09	2.31E-09	6.77E-10
62	3.67E-09	2.55E-09	7.75E-10
63	3.90E-09	2.81E-09	8.90E-10
64	4.12E-09	3.07E-09	1.02E-09
65	4.33E-09	3.32E-09	1.17E-09
66	4.53E-09	3.57E-09	1.35E-09
67	4.71E-09	3.82E-09	1.54E-09
68	4.88E-09	4.05E-09	1.76E-09
69	5.03E-09	4.27E-09	1.99E-09
70	5.17E-09	4.48E-09	2.24E-09
71	5.29E-09	4.67E-09	2.51E-09
72	5.41E-09	4.85E-09	2.78E-09
73	5.51E-09	5.01E-09	3.06E-09
74	5.60E-09	5.15E-09	3.33E-09
75	5.67E-09	5.29E-09	3.61E-09
76	5.74E-09	5.40E-09	3.87E-09
77	5.81E-09	5.51E-09	4.12E-09
78	5.86E-09	5.60E-09	4.35E-09
79	5.91E-09	5.68E-09	4.57E-09
80	5.95E-09	5.75E-09	4.78E-09
81	5.98E-09	5.82E-09	4.96E-09
82	6.01E-09	5.87E-09	5.13E-09
83	6.04E-09	5.92E-09	5.27E-09
84	6.06E-09	5.96E-09	5.41E-09
85	6.08E-09	5.99E-09	5.52E-09
86	6.10E-09	6.02E-09	5.62E-09
87	6.11E-09	6.05E-09	5.71E-09
88	6.12E-09	6.07E-09	5.79E-09
89	6.13E-09	6.09E-09	5.85E-09
90	6.14E-09	6.11E-09	5.91E-09
91	6.15E-09	6.12E-09	5.95E-09
92	6.15E-09	6.13E-09	5.99E-09
93	6.16E-09	6.14E-09	6.03E-09
94	6.16E-09	6.15E-09	6.05E-09
95	6.17E-09	6.15E-09	6.08E-09

Table C.1: Calculated g-factor values for the O_2 A-band in units of s^{-1}.

153

Altitude (km)	0°	5°	10°	15°	20°	25°	30°	35°
60	3.57E-10	3.57E-10	3.57E-10	3.57E-10	3.57E-10	3.57E-10	3.57E-10	3.57E-10
61	3.58E-10	3.58E-10	3.58E-10	3.58E-10	3.58E-10	3.58E-10	3.57E-10	3.57E-10
62	3.58E-10	3.58E-10	3.58E-10	3.58E-10	3.58E-10	3.58E-10	3.58E-10	3.58E-10
63	3.59E-10	3.59E-10	3.58E-10	3.58E-10	3.58E-10	3.58E-10	3.58E-10	3.58E-10
64	3.59E-10	3.59E-10	3.59E-10	3.59E-10	3.59E-10	3.59E-10	3.59E-10	3.58E-10
65	3.59E-10	3.59E-10	3.59E-10	3.59E-10	3.59E-10	3.59E-10	3.59E-10	3.59E-10
66	3.59E-10	3.59E-10	3.59E-10	3.59E-10	3.59E-10	3.59E-10	3.59E-10	3.59E-10
67	3.59E-10	3.59E-10	3.59E-10	3.59E-10	3.59E-10	3.59E-10	3.59E-10	3.59E-10
68	3.60E-10	3.60E-10	3.60E-10	3.60E-10	3.60E-10	3.59E-10	3.59E-10	3.59E-10
69	3.60E-10	3.60E-10	3.60E-10	3.60E-10	3.60E-10	3.60E-10	3.60E-10	3.60E-10
70	3.60E-10	3.60E-10	3.60E-10	3.60E-10	3.60E-10	3.60E-10	3.60E-10	3.60E-10
71	3.60E-10	3.60E-10	3.60E-10	3.60E-10	3.60E-10	3.60E-10	3.60E-10	3.60E-10
72	3.60E-10	3.60E-10	3.60E-10	3.60E-10	3.60E-10	3.60E-10	3.60E-10	3.60E-10
73	3.60E-10	3.60E-10	3.60E-10	3.60E-10	3.60E-10	3.60E-10	3.60E-10	3.60E-10
74	3.60E-10	3.60E-10	3.60E-10	3.60E-10	3.60E-10	3.60E-10	3.60E-10	3.60E-10
75	3.60E-10	3.60E-10	3.60E-10	3.60E-10	3.60E-10	3.60E-10	3.60E-10	3.60E-10
76	3.60E-10	3.60E-10	3.60E-10	3.60E-10	3.60E-10	3.60E-10	3.60E-10	3.60E-10
77	3.60E-10	3.60E-10	3.60E-10	3.60E-10	3.60E-10	3.60E-10	3.60E-10	3.60E-10
78	3.60E-10	3.60E-10	3.60E-10	3.60E-10	3.60E-10	3.60E-10	3.60E-10	3.60E-10
79	3.61E-10	3.61E-10	3.61E-10	3.61E-10	3.61E-10	3.60E-10	3.60E-10	3.60E-10
80	3.61E-10	3.61E-10	3.61E-10	3.61E-10	3.61E-10	3.61E-10	3.61E-10	3.61E-10
81	3.61E-10	3.61E-10	3.61E-10	3.61E-10	3.61E-10	3.61E-10	3.61E-10	3.61E-10
82	3.61E-10	3.61E-10	3.61E-10	3.61E-10	3.61E-10	3.61E-10	3.61E-10	3.61E-10
83	3.61E-10	3.61E-10	3.61E-10	3.61E-10	3.61E-10	3.61E-10	3.61E-10	3.61E-10
84	3.61E-10	3.61E-10	3.61E-10	3.61E-10	3.61E-10	3.61E-10	3.61E-10	3.61E-10
85	3.61E-10	3.61E-10	3.61E-10	3.61E-10	3.61E-10	3.61E-10	3.61E-10	3.61E-10
86	3.61E-10	3.61E-10	3.61E-10	3.61E-10	3.61E-10	3.61E-10	3.61E-10	3.61E-10
87	3.61E-10	3.61E-10	3.61E-10	3.61E-10	3.61E-10	3.61E-10	3.61E-10	3.61E-10
88	3.61E-10	3.61E-10	3.61E-10	3.61E-10	3.61E-10	3.61E-10	3.61E-10	3.61E-10
89	3.61E-10	3.61E-10	3.61E-10	3.61E-10	3.61E-10	3.61E-10	3.61E-10	3.61E-10
90	3.61E-10	3.61E-10	3.61E-10	3.61E-10	3.61E-10	3.61E-10	3.61E-10	3.61E-10
91	3.61E-10	3.61E-10	3.61E-10	3.61E-10	3.61E-10	3.61E-10	3.61E-10	3.61E-10
92	3.61E-10	3.61E-10	3.61E-10	3.61E-10	3.61E-10	3.61E-10	3.61E-10	3.61E-10
93	3.61E-10	3.61E-10	3.61E-10	3.61E-10	3.61E-10	3.61E-10	3.61E-10	3.61E-10
94	3.61E-10	3.61E-10	3.61E-10	3.61E-10	3.61E-10	3.61E-10	3.61E-10	3.61E-10
95	3.61E-10	3.61E-10	3.61E-10	3.61E-10	3.61E-10	3.61E-10	3.61E-10	3.61E-10

Table C.2: Calculated g-factor values for the O_2 B-band in units of s^{-1}.

Altitude (km)	40°	45°	50°	55°	60°	65°	70°	75°
60	3.57E-10	3.56E-10	3.56E-10	3.55E-10	3.55E-10	3.54E-10	3.52E-10	3.49E-10
61	3.57E-10	3.57E-10	3.56E-10	3.56E-10	3.55E-10	3.54E-10	3.53E-10	3.51E-10
62	3.58E-10	3.57E-10	3.57E-10	3.57E-10	3.56E-10	3.55E-10	3.54E-10	3.52E-10
63	3.58E-10	3.58E-10	3.57E-10	3.57E-10	3.57E-10	3.56E-10	3.55E-10	3.53E-10
64	3.58E-10	3.58E-10	3.58E-10	3.58E-10	3.57E-10	3.56E-10	3.56E-10	3.54E-10
65	3.59E-10	3.58E-10	3.58E-10	3.58E-10	3.58E-10	3.57E-10	3.56E-10	3.55E-10
66	3.59E-10	3.59E-10	3.59E-10	3.58E-10	3.58E-10	3.57E-10	3.57E-10	3.56E-10
67	3.59E-10	3.59E-10	3.59E-10	3.59E-10	3.58E-10	3.58E-10	3.57E-10	3.56E-10
68	3.59E-10	3.59E-10	3.59E-10	3.59E-10	3.59E-10	3.58E-10	3.58E-10	3.57E-10
69	3.59E-10	3.59E-10	3.59E-10	3.59E-10	3.59E-10	3.59E-10	3.58E-10	3.57E-10
70	3.60E-10	3.60E-10	3.59E-10	3.59E-10	3.59E-10	3.59E-10	3.58E-10	3.58E-10
71	3.60E-10	3.60E-10	3.60E-10	3.60E-10	3.59E-10	3.59E-10	3.59E-10	3.58E-10
72	3.60E-10	3.60E-10	3.60E-10	3.60E-10	3.60E-10	3.59E-10	3.59E-10	3.59E-10
73	3.60E-10	3.60E-10	3.60E-10	3.60E-10	3.60E-10	3.60E-10	3.59E-10	3.59E-10
74	3.60E-10	3.60E-10	3.60E-10	3.60E-10	3.60E-10	3.60E-10	3.59E-10	3.59E-10
75	3.60E-10	3.60E-10	3.60E-10	3.60E-10	3.60E-10	3.60E-10	3.60E-10	3.59E-10
76	3.60E-10	3.60E-10	3.60E-10	3.60E-10	3.60E-10	3.60E-10	3.60E-10	3.60E-10
77	3.60E-10	3.60E-10	3.60E-10	3.60E-10	3.60E-10	3.60E-10	3.60E-10	3.60E-10
78	3.60E-10	3.60E-10	3.60E-10	3.60E-10	3.60E-10	3.60E-10	3.60E-10	3.60E-10
79	3.60E-10	3.60E-10	3.60E-10	3.60E-10	3.60E-10	3.60E-10	3.60E-10	3.60E-10
80	3.61E-10	3.60E-10	3.60E-10	3.60E-10	3.60E-10	3.60E-10	3.60E-10	3.60E-10
81	3.61E-10	3.61E-10	3.61E-10	3.60E-10	3.60E-10	3.60E-10	3.60E-10	3.60E-10
82	3.61E-10	3.61E-10	3.61E-10	3.61E-10	3.61E-10	3.60E-10	3.60E-10	3.60E-10
83	3.61E-10	3.61E-10	3.61E-10	3.61E-10	3.61E-10	3.61E-10	3.60E-10	3.60E-10
84	3.61E-10	3.61E-10	3.61E-10	3.61E-10	3.61E-10	3.61E-10	3.61E-10	3.60E-10
85	3.61E-10	3.61E-10	3.61E-10	3.61E-10	3.61E-10	3.61E-10	3.61E-10	3.60E-10
86	3.61E-10	3.61E-10	3.61E-10	3.61E-10	3.61E-10	3.61E-10	3.61E-10	3.61E-10
87	3.61E-10	3.61E-10	3.61E-10	3.61E-10	3.61E-10	3.61E-10	3.61E-10	3.61E-10
88	3.61E-10	3.61E-10	3.61E-10	3.61E-10	3.61E-10	3.61E-10	3.61E-10	3.61E-10
89	3.61E-10	3.61E-10	3.61E-10	3.61E-10	3.61E-10	3.61E-10	3.61E-10	3.61E-10
90	3.61E-10	3.61E-10	3.61E-10	3.61E-10	3.61E-10	3.61E-10	3.61E-10	3.61E-10
91	3.61E-10	3.61E-10	3.61E-10	3.61E-10	3.61E-10	3.61E-10	3.61E-10	3.61E-10
92	3.61E-10	3.61E-10	3.61E-10	3.61E-10	3.61E-10	3.61E-10	3.61E-10	3.61E-10
93	3.61E-10	3.61E-10	3.61E-10	3.61E-10	3.61E-10	3.61E-10	3.61E-10	3.61E-10
94	3.61E-10	3.61E-10	3.61E-10	3.61E-10	3.61E-10	3.61E-10	3.61E-10	3.61E-10
95	3.61E-10	3.61E-10	3.61E-10	3.61E-10	3.61E-10	3.61E-10	3.61E-10	3.61E-10

Table C.2: Calculated g-factor values for the O_2 B-band in units of s^{-1}.

Altitude (km)	80°	85°	90°
60	3.44E-10	3.32E-10	2.68E-10
61	3.46E-10	3.35E-10	2.78E-10
62	3.48E-10	3.38E-10	2.87E-10
63	3.50E-10	3.41E-10	2.95E-10
64	3.51E-10	3.44E-10	3.03E-10
65	3.52E-10	3.46E-10	3.10E-10
66	3.53E-10	3.48E-10	3.16E-10
67	3.54E-10	3.49E-10	3.21E-10
68	3.55E-10	3.51E-10	3.26E-10
69	3.56E-10	3.52E-10	3.31E-10
70	3.57E-10	3.53E-10	3.34E-10
71	3.57E-10	3.54E-10	3.38E-10
72	3.58E-10	3.55E-10	3.41E-10
73	3.58E-10	3.56E-10	3.44E-10
74	3.58E-10	3.57E-10	3.46E-10
75	3.59E-10	3.57E-10	3.48E-10
76	3.59E-10	3.58E-10	3.50E-10
77	3.59E-10	3.58E-10	3.51E-10
78	3.59E-10	3.58E-10	3.53E-10
79	3.60E-10	3.59E-10	3.54E-10
80	3.60E-10	3.59E-10	3.55E-10
81	3.60E-10	3.59E-10	3.56E-10
82	3.60E-10	3.60E-10	3.57E-10
83	3.60E-10	3.60E-10	3.57E-10
84	3.60E-10	3.60E-10	3.58E-10
85	3.60E-10	3.60E-10	3.58E-10
86	3.60E-10	3.60E-10	3.59E-10
87	3.60E-10	3.60E-10	3.59E-10
88	3.61E-10	3.60E-10	3.59E-10
89	3.61E-10	3.60E-10	3.60E-10
90	3.61E-10	3.60E-10	3.60E-10
91	3.61E-10	3.61E-10	3.60E-10
92	3.61E-10	3.61E-10	3.60E-10
93	3.61E-10	3.61E-10	3.60E-10
94	3.61E-10	3.61E-10	3.60E-10
95	3.61E-10	3.61E-10	3.60E-10

Table C.2: Calculated g-factor values for the O_2 B-band in units of s^{-1}.

Appendix D

Model code

D.0.1 Code description

The code given here is for the MatLab routine "Orbit_Retrieval". The routine first searches the OSIRIS database for orbits that contain scans that observed the Earth's limb between tangent heights of 70 and 95 km. Once those orbits were found ozone density profiles were retrieved for the scans within those orbits that had an observed tangent height solar zenith angle below $87.5°$. Due to space constraints, certain large tables have been omitted, namely values of the pre-calculated Chapman function, and values of the pre-calculated g-factors for both the A and B bands.

D.0.2 The code

```
function Orbit_Retrieval(startOrbit,stopOrbit,inputDays)

global R chf wavelengthsSRC wavelengthsL wavelengthsO3 LBL FUV MUV...
    gAt gBt OScal

if nargin>2
    x=inputDays;
else
```

```
      x=orbitFind(startOrbit,stopOrbit);
end

R=6378.150;

% chapman function (from 75 to 90 sza, 75=sec(sza), and 45 to 140 km)
chf=[]; % OMITTED

wavelengthsSRC=[130 4.3338E-19; 131 3.9769E-19; 132 1.2667E-18;...
    133 2.1927E-18; 134 2.1259E-18; 135 5.9463E-18; 136 7.6454E-18;...
    137 1.1941E-17; 138 1.3712E-17; 139 1.4223E-17; 140 1.4400E-17;...
    141 1.4414E-17; 142 1.4448E-17; 143 1.4197E-17; 144 1.4198E-17;...
    145 1.3930E-17; 146 1.3677E-17; 147 1.3318E-17; 148 1.2722E-17;...
    149 1.2181E-17; 150 1.1561E-17; 151 1.0839E-17; 152 1.0102E-17;...
    153 9.1462E-18; 154 8.4319E-18; 155 7.8171E-18; 156 7.0138E-18;...
    157 6.2826E-18; 158 5.6509E-18; 159 4.9505E-18; 160 4.4087E-18;...
    161 3.8545E-18; 162 3.3774E-18; 163 2.8838E-18; 164 2.4694E-18;...
    165 2.0481E-18; 166 1.7294E-18; 167 1.4239E-18; 168 1.2029E-18;...
    169 9.7405E-19; 170 7.8503E-19; 171 6.2583E-19; 172 5.0936E-19;...
    173 4.0775E-19; 174 3.1557E-19; 175 2.3291E-19];

wavelengthsL=[121.6 1E-20];

wavelengthsO3=[198 3.32E-19 0.56; 199 3.21E-19 0.58; 200 3.15E-19 0.59;...
    201 3.12E-19 0.61; 202 3.15E-19 0.63; 203 3.22E-19 0.64;...
    204 3.36E-19 0.66; 205 3.56E-19 0.67; 206 3.83E-19 0.69;...
    207 4.18E-19 0.70; 208 4.61E-19 0.71; 209 5.11E-19 0.71;...
    210 5.70E-19 0.72; 211 6.39E-19 0.73; 212 7.18E-19 0.74;...
    213 8.08E-19 0.76; 214 9.10E-19 0.77; 215 1.02E-18 0.78;...
    216 1.14E-18 0.80; 217 1.28E-18 0.82; 218 1.43E-18 0.84;...
    219 1.59E-18 0.86; 220 1.78E-18 0.88; 221 1.97E-18 0.87;...
    222 2.18E-18 0.87; 223 2.41E-18 0.88; 224 2.66E-18 0.89;...
    225 2.92E-18 0.90; 226 3.14E-18 0.87; 227 3.41E-18 0.87;...
    228 3.70E-18 0.87; 229 4.01E-18 0.83; 230 4.34E-18 0.91;...
    231 4.67E-18 0.83; 232 5.03E-18 0.92; 233 5.38E-18 0.92;...
    234 5.73E-18 0.93; 235 6.11E-18 0.92; 236 6.48E-18 0.91;...
    237 6.84E-18 0.91; 238 7.22E-18 0.91; 239 7.57E-18 0.91;...
    240 7.99E-18 0.91; 241 8.36E-18 0.90; 242 8.73E-18 0.89;...
    243 9.04E-18 0.89; 244 9.40E-18 0.90; 245 9.62E-18 0.90;...
    246 9.99E-18 0.90; 247 1.01E-17 0.90; 248 1.04E-17 0.91;...
    249 1.07E-17 0.91; 250 1.08E-17 0.90; 251 1.08E-17 0.90;...
    252 1.12E-17 0.91; 253 1.11E-17 0.91; 254 1.12E-17 0.92;...
    255 1.12E-17 0.92; 256 1.12E-17 0.92; 257 1.10E-17 0.92;...
    258 1.09E-17 0.91; 259 1.11E-17 0.91; 260 1.06E-17 0.91;...
    261 1.07E-17 0.91; 262 1.04E-17 0.92; 263 1.01E-17 0.91;...
    264 9.84E-18 0.91; 265 9.60E-18 0.92; 266 9.31E-18 0.92;...
    267 8.79E-18 0.93; 268 8.59E-18 0.93; 269 8.02E-18 0.92;...
    270 7.87E-18 0.92; 271 7.31E-18 0.92; 272 7.00E-18 0.92;...
    273 6.57E-18 0.92; 274 6.05E-18 0.91; 275 5.75E-18 0.91;...
    276 5.34E-18 0.90; 277 5.00E-18 0.90; 278 4.62E-18 0.89;...
    279 4.26E-18 0.89; 280 3.95E-18 0.89; 281 3.60E-18 0.89;...
    282 3.24E-18 0.88; 283 3.01E-18 0.87; 284 2.73E-18 0.87;...
    285 2.44E-18 0.87; 286 2.21E-18 0.87; 287 2.00E-18 0.88;...
    288 1.76E-18 0.88; 289 1.57E-18 0.88; 290 1.40E-18 0.88;...
    291 1.26E-18 0.89; 292 1.10E-18 0.89; 293 9.90E-19 0.89;...
    294 8.63E-19 0.88; 295 7.67E-19 0.88; 296 6.63E-19 0.88;...
```

```
    297 5.87E-19 0.89; 298 5.07E-19 0.89; 299 4.50E-19 0.88;...
    300 3.90E-19 0.88; 301 3.42E-19 0.88; 302 3.01E-19 0.86;...
    303 2.61E-19 0.86; 304 2.32E-19 0.87; 305 1.98E-19 0.88;...
    306 1.77E-19 0.85; 307 1.53E-19 0.85; 308 1.34E-19 0.78;...
    309 1.21E-19 0.67];

LBL=load('lbl3.mat','lbl3'); % only contains lines where x-section >1e-27
LBL=LBL.lbl3;

OSc=load('OScal.mat','OScal');
OScal=OSc.OScal; % mjd=52197:54732

load('SORCE data/fluxFUV.mat', 'fluxFUV')
load('SORCE data/fluxMUV.mat', 'fluxMUV')
FUV=fluxFUV;
MUV=fluxMUV;

% g factor tables are from sza 0 to 90 deg, 40 to 120 km
% FA=2.75e13; % from SORCE website, 759-775 nm, july 2002 - Dec 2007.
% FB=2.41e13; % from SORCE website, 687-699 nm, july 2002 - Dec 2007.
gAt=[]; % OMITTED
gBt=[]; % OMITTED

tic
for q=1:length(x)
    orbitNum=x(q);

    warning off all
    theList=GetScanList(orbitNum);
    warning on all
    last=length(theList);

    if last>1
        startScan=theList(1);
        stopScan=theList(last);
        disp(num2str(orbitNum))

        for scanNum=startScan:stopScan
%               disp(['  ' num2str(scanNum)])

            warning off all
            info=GetScanInfo(scanNum);
            warning on all

            if isfield(info,'MaxAltitude')
            if (info.MaxAltitude>95 && info.MinAltitude<70)

                warning off all
                scan=OS_L1_load(scanNum);
                warning on all

                if ~isempty(scan)
                if mean([scan.sza])<87.5
                if max([scan.alt])>95 && min([scan.alt])<70

                    if ~isdir(['retrievals/' num2str(orbitNum)])
```

159

```matlab
                            mkdir(['retrievals/' num2str(orbitNum)]);
                        end

                        first=1;

                        for m=[100 50 10 5 1:-0.1:0.1 0.09:-0.01:0.01]
%                            disp(num2str(m))
                            try
                                O3retrievalF(scan,m,first);
%                                disp(num2str(m))
                                break
                            catch
                                first=0;err=lasterror;
                                if ~isempty(strfind(err.message,'flag'))
%                                    disp('flag')
                                    break
                                elseif ~isempty(strfind(err.message,'absorp'))
%                                    disp('absorption')
                                    break
                                end
                            end
                        end
                    else
%                        disp('alt')
                    end
                    else
%                        disp('sza')
                    end
                    end
                end
            end
        end
    end
end
t=toc;
disp([num2str(t/3600) ' hours'])
%------------------------------------------------------------------------

function [data]=orbitFind(startOrbit,stopOrbit)
tic
disp('getting valid orbits...')
data=[];
place=0;
for orbitNum=startOrbit:stopOrbit
    %disp(num2str(orbitNum))

    warning off all
    theList=GetScanList(orbitNum);
    warning on all
    last=length(theList);

    if last>1

        first=ceil(length(theList)*0.33);
        warning off all
        scan=GetScanInfo(theList(first));
```

160

```
            warning on all

        if isfield(scan,'MaxAltitude')
            if (scan.MaxAltitude>95 && scan.MinAltitude<75)
                place=place+1;
                data(place)=orbitNum;
            else
                second=ceil(length(theList)*0.66);
                warning off all
                scan=GetScanInfo(theList(second));
                warning on all
                if isfield(scan,'MaxAltitude')
                    if (scan.MaxAltitude>95 && scan.MinAltitude<75)
                        place=place+1;
                        data(place)=orbitNum;
                    end
                end
            end
        end
    end
end
if isempty(data)
    error('no days here')
end
save(['good orbits\' num2str(startOrbit) '-' num2str(stopOrbit)],'data')
toc
disp('getting data now...')
%-----------------------------------------------------------------------

function [data]=O3retrievalF(scan,Xerr,first)

global MINalt MAXalt Dalt DaltOE L Lt FUV MUV fluxSRC sigmaSRC fluxL...
    sigmaL wavelengthsSRC wavelengthsO3 J2 J3 J3t sigmaO3 QyO3 fluxO3...
    gAt gBt gA gB wavelengthsL Oretrieved Berrf XO2check Og N2g O2g Hg...
    Tg O3g

SZA=mean([scan.sza]);
if SZA>=87.5
    error('sza is too high')
end

mjd=fix(mean([scan.mjd]));
[year,month]=mjd2utc(mjd);

if first
    [Og,N2g,O2g,Hg,Tg,O3g]=MSIS(scan);
end
O=Og; N2=N2g; O2=O2g; H=Hg; T=Tg; O3=O3g;
x=[scan.alt];
observed=IRR(scan,SZA);
y=observed(1,:);
err=observed(2,:);

if x(1)>95
    x=flipdim(x,2);
    y=flipdim(y,2);
```

161

```
        err=flipdim(err,2);
end

if year<2003 || and(year==2003,month<6)
    mjd=mjd+365; % sorce data starts in may 2003.
end

fuv=FUV(FUV(:,1)==mjd,3);
muv=MUV(MUV(:,1)==mjd,3);

fluxSRC=fuv(130-116+1:175-116+1);
sigmaSRC=wavelengthsSRC(:,2);

fluxL=fuv(6);
sigmaL=wavelengthsL(2);

fluxO3=muv(198-180+1:309-180+1);
sigmaO3=wavelengthsO3(:,2);
QyO3=wavelengthsO3(:,3);
J3t=sum(sigmaO3.*fluxO3.*QyO3);

if first
    warning off all
    for j=1:-1:-3
        Berr=10^j;
        try
            XO2=O2retrieval(SZA,O2,O3,N2,H,T,x,y,err,Berr);
            XO2check=1;
            Berrf=Berr;
            break
        catch
            if j==-3
                XO2check=0;
%                disp('going with MSIS')
            end
        end
    end
    warning on all
else
    Lts=Lt;
    if XO2check
        XO2=O2retrieval(SZA,O2,O3,N2,H,T,x,y,err,Berrf);
    end
    Lt=Lts;
end

MINalt=70;
MAXalt=95;
TOPalt=ceil(max(x));

xx=x(and(x>MINalt,x<=MAXalt));
xy=x(and(x>MAXalt,x<=TOPalt));
Y=y(and(x>MINalt,x<=MAXalt))';
ERR=err(and(x>MINalt,x<=MAXalt))';

if sum(Y==0)
```

```
        error('absorption');
end

alts=[xx xy TOPalt:140];

Dalt=length(alts);
DaltOE=length(xx);

O3above=[spline(MAXalt:TOPalt,O3(MAXalt+1:TOPalt+1),xy)';...
    O3(TOPalt+1:141)];
O3above(O3above<0)=0;

denC=1;

O=[spline(MINalt:TOPalt,O(MINalt+1:TOPalt+1),[xx xy])'; O(TOPalt+1:141)];
N2=[spline(MINalt:TOPalt,N2(MINalt+1:TOPalt+1),[xx xy])';...
    N2(TOPalt+1:141)];
H=[spline(MINalt:TOPalt,H(MINalt+1:TOPalt+1),[xx xy])'; H(TOPalt+1:141)];
T=[spline(MINalt:TOPalt,T(MINalt+1:TOPalt+1),[xx xy])'; T(TOPalt+1:141)];

if XO2check
    O2=[spline(MINalt:MAXalt,O2(MINalt+1:MAXalt+1),xx)'*denC; XO2];
else
    O2=[spline(MINalt:TOPalt,O2(MINalt+1:TOPalt+1),[xx xy])';...
        O2(TOPalt+1:141)];
    O2(1:DaltOE)=O2(1:DaltOE)*denC;
end
N2(1:DaltOE)=N2(1:DaltOE)*denC;

data.O=O;
data.N2=N2;
data.O2=O2;
data.H=H;
data.T=T;

X=spline(MINalt:MAXalt,O3(MINalt+1:MAXalt+1),xx)';

L=path_lengths(alts);
if first
    [Tnear,Tfar]=transmission(O2,T);
    Lt=L.*(Tnear+Tfar);
end

J3=[];
gA=[];
gB=[];

J2=J2calc(O2,SZA);
J3(1:Dalt,1)=J3t;

for j=1:length(alts)
    if round(alts(j))<=81
        gA(j,1)=gAt(round(alts(j)),round(SZA));
        gB(j,1)=gBt(round(alts(j)),round(SZA));
    else
        gA(j,1)=gAt(81,round(SZA));
```

163

```
            gB(j,1)=gBt(81,round(SZA));
    end
end

O2r=0;
modelAP=Forward_Model(N2,O2,H,T,X,SZA,O3above,O2r);  % with a priori

dy=ERR./Y;
Sy=diag((log(Y).*dy).^2);
Sx=Xerr*diag(log(X).^2);

X=log(X);
Xo=X;
Y=log(Y);

TOL=0.001*ones(DaltOE,1);
iter=0;
check=1;
K=zeros(DaltOE);

% solve stuff
while check

    iter=iter+1;
    Xn=X;

    if iter==500
        error('not converging') % not converging.
    end

    % weighting function K, calculated numerically at first iteration
    if iter==1
        for m=0:DaltOE  % 0 run for Yn undisturbed by X
            Q=Xn;
            if m
                Q(m)=Q(m)*1.25; % disturb O3 at each height
                dQ=Q(m)-Xn(m);
            end
            Z=log(Forward_Model(N2,O2,H,T,exp(Q),SZA,O3above,O2r));

            if ~m
                Yn=Z; % when m=0 the model is run with no disturbance in X
            else
                dZ=Z-Yn;
                K(m,:)=(dZ/dQ)';
            end
        end
    else
        Yn=log(Forward_Model(N2,O2,H,T,exp(X),SZA,O3above,O2r));
    end

    X=Xo+Sx*K'*inv(K*Sx*K'+Sy)*((Y-Yn)-K*(Xo-Xn));

    if or(imag(X)~=0,isnan(X))
        error('kablooee!!') % OE is blowing up.
    end
```

164

```
        pd=abs((X-Xn)./X);
        check=sum(pd>TOL);
end
% disp(num2str(iter))

S=inv(inv(Sx)+K'*inv(Sy)*K);
sigma=sqrt(diag(S))./X; % relative stdv

X=exp(X);
Xo=exp(Xo);
Y=exp(Y);
Yn=exp(Yn);

checkf=abs(Y-Yn)./Y;
if ~isempty(find(checkf>0.1,1))
    error('not a useful solution')
end

G=Sx*K'*inv(K*Sx*K'+Sy); % gain matrix = inv(inv(Sx)+K'inv(Sy)K))K'inv(Sy)
avgKer=G*K;

LON=[scan.lon];
lon=LON(fix(length(LON)/2)); % not mean, OSIRIS could cross prime meridian

LAT=[scan.lat];
if LAT(1)<LAT(2)
    AMPM=0;  % ascending node (18:00)
else
    AMPM=1;  % descending node (06:00)
end

data.scanNumber=mean([scan.scannumber]);
data.mjd=mean([scan.mjd]);
data.time=AMPM;
data.lat=mean([scan.lat]);
data.lon=lon;
data.sza=mean([scan.sza]);
data.alt=alts';
data.retrieval_alts=alts(1:DaltOE)';
data.observed=Y;
data.aPriori=Xo;
data.modelAP=modelAP;
data.Xerr=Xerr;
data.Sx=Sx;
data.Sy=Sy;
data.S=S;
data.sigma=sigma;
data.s_interp=interp1(xx,data.sigma,MINalt:MAXalt,'pchip','extrap')';
data.WeightingFunc=K;
data.AvgKernel=avgKer;
data.final=Yn;
data.O3=X;
data.O3interp=interp1(xx,X,MINalt:MAXalt,'pchip','extrap')';
MM=1:DaltOE;
data.VMR=X./(data.O2(MM)+data.N2(MM)+data.O(MM)+data.H(MM)+X)*1e6;
```

```
data.VMRinterp=interp1(xx,data.VMR,MINalt:MAXalt,'pchip','extrap')';
data.Oretrieved=Oretrieved(1:DaltOE);

orbit=fix(data.scanNumber/1000);
save(['retrievals\' num2str(orbit) '\' num2str(data.scanNumber)],'data')

% figure % plots a priori and retrieved ozone
% semilogx(Xo,xx,X,xx)
%
% figure  % plots the final weighting functions
% for k=1:length(K)
%      plot(K(k,:),xx)
%      hold all
% end
% hold off
%
% figure  % plots the final averaging kernel
% for k=1:length(avgKer)
%      plot(avgKer(k,:),xx)
%      hold all
%      plot(sum(avgKer),xx)
% end
% hold off
%
% figure  % plot observed, model with a priori, and final estimate
% semilogx(Y,xx,modelAP,xx,Yn,xx)
%-----------------------------------------------------------------------

function [data]=Forward_Model(N2,O2,H,T,O3,SZA,Oabove,O2r)

% forward models what OSIRIS will see based on the volume emission rates
% from fuction VER and pathlengths from function path_lengths

global Dalt DaltOE Lt

if O2r
    O2=[O2; Oabove];
else
    O3=[O3; Oabove];
end

V=flipdim(VER(N2,O2,H,T,round(SZA),O3,O2r),1)';
for Hsh=1:Dalt % pathlength matrix first entry is MAXalt
    Vm(Hsh,:)=V;
end

dataTemp=flipdim(sum((Lt.*Vm),2),1);
data=dataTemp(1:DaltOE); % only want xx
%-----------------------------------------------------------------------

function [data]=VER(N2,O2,H,T,sza,O3,O2r)

% calculates the expected volume emission rates for Vres, Vbarth, and
% VO1D from O2 and O3

global J2 J3 gA gB Oretrieved
```

```
A=0.085;
A1D=6.81e-3;
phi=0.95;
Fc=0.93;

k0=1.8e-15.*exp(45./T);    % O2(b)+N2-->O2
k1=3.3e-11.*exp(55./T);    % O(1D)+O2-->O
k2=2.15e-11.*exp(110./T);  % O(1D)+N2-->O
k3=3.5e-11.*exp(135./T);   % O2(b)+O3-->O2
k4=3.9e-17;                % O2(b)+O2-->O2
k5=4.7e-33.*(300./T).^2;   % O+O+M
k7=8e-14;                  % O2(b)+O

% B-band
A7=7.0e-2;
k0b=4.5e-12;
k1b=4.2e-11*exp(-312./T);
k2b=5e-13;
k3b=3e-10;

% Barth mechanism
Co2=7.5;
Co=33;
k6=5.0e-13;
ab=0.8;
Astar=0.002;
C3=Astar/ab/k6;

if O2r
    J2=J2calc(O2,sza);
end
M=O2+N2;

Ok2=6.0e-34*exp(T/300).^2.4;  % calculate O from O3
Ok3=2.2e-11*exp(120./T);
O=O3.*(J3+Ok3.*H)./(Ok2.*O2.*M);

Q=A./(A + k0.*N2 + k4.*O2 + k3.*O3 + k7.*O);
K=k0b*O+k1b.*O2+k2b*N2;

Pres=gA.*O2;
PresB=K.*gB.*O2./(K+A7+k3b.*O3);
Pbarth=(k5.*O.^2.*O2.*M)./(C3+Co2.*O2+Co.*O);
Po1d=phi.*k1.*O2.*((J2.*O2+J3.*O3)./(A1D+k2.*N2+k1.*O2));

Oretrieved=O;
data=Fc.*Q.*(Pres+Pbarth+Po1d+PresB);
%-----------------------------------------------------------------------

function [data]=path_lengths(alts)

% calculates the pathlengths radiation travels in each equally spaced shell
% of shellsize between tangent heights of altMin and altMax

%                      shell
```

```
%           __ max              min __
%   max   |  x    0    0    0    0   |
%         |  x    x    0    0    0   |
% th      |  x    x    x    0    0   |
%         |  x    x    x    x    0   |
%   min   |__x    x    x    x    x __|

global R level

size=length(alts);
dataT=zeros(size);
level=zeros(size+1,1);

for j=1:size+1
    if j==1
        level(j)=alts(j)-(alts(j+1)-alts(j))/2;
    elseif j==size+1
        level(j)=alts(j-1)+(alts(j-1)-alts(j-2))/2;
    else
        level(j)=alts(j)-(alts(j)-alts(j-1))/2;
    end
end

for j=1:size
    th=level(j);
    for k=j:size
        sh=level(k+1);

        dataT(size-j+1,size-k+1)=sqrt((R+sh)^2-(R+th)^2)...
            -sum(dataT(size-j+1,:),2);
    end
end
data=dataT*1e5; % convert from km to cm
%-----------------------------------------------------------------------
function [Tnear,Tfar]=transmission(O2,T)

% changed weight from emission to absorption

global Dalt L LBL

Tnear=zeros(Dalt);
Tfar=zeros(Dalt);

for r=1:Dalt
    for c=1:r
        sh=Dalt+1-c; % shell

        if T(sh)>500
            j=351;
        elseif T(sh)<150
            j=1;
        else
            j=round(T(sh))-149;
        end

        if c==1
```

```matlab
            Tnear(r,c)=sum(LBL{j}/sum(LBL{j}).*exp(-O2(sh)*L(r,c)*LBL{j}));
        else
            Tnear(r,c)=Tnear(r,c-1)*sum(LBL{j}/sum(LBL{j})...
                .*exp(-O2(sh)*L(r,c)*LBL{j}));
        end
    end
end

for r=Dalt:-1:1
    for c=r:-1:1
        sh=Dalt+1-c; % shell

        if T(sh)>500
            j=351;
        elseif T(sh)<150
            j=1;
        else
            j=round(T(sh))-149;
        end

        if c==r
            Tfar(r,c)=Tnear(r,c)*sum(LBL{j}/sum(LBL{j})...
                .*exp(-O2(sh)*L(r,c)*LBL{j}));
        else
            Tfar(r,c)=Tfar(r,c+1)*sum(LBL{j}/sum(LBL{j})...
                .*exp(-O2(sh)*L(r,c)*LBL{j}));
        end
    end
end
%-------------------------------------------------------------------------

function [J2]=J2calc(O2,SZA)

% wavelength matrices are [wavelength(nm) ab.c.s.(cm2/molec)]
% and the 3rd column for O3 is quantum yield.

global Dalt fluxSRC sigmaSRC fluxL sigmaL chf level

for j=1:Dalt

    h=round(level(j)-45)+1; % chf starts at alt of 45 km

    if round(SZA)>75
        ch=chf(h,round(SZA)-74); % chapman function
    else
        ch=sec(SZA*pi/180);
    end

    tauSRC=0;
    tauL=0;
    for k=j:Dalt
        tauSRC=tauSRC+sigmaSRC*O2(k)*ch*(level(k+1)-level(k))...
            *1e5; %convert to cm
        tauL=tauL+sigmaL*O2(k)*ch*(level(k+1)-level(k))*1e5;
    end
```

169

```matlab
        phiSRC=fluxSRC.*exp(-tauSRC);
        phiL=fluxL.*exp(-tauL);

        % Qy of 1 (@ Lya,=0.48), values at 1nm interval
        J2(j,1)=sum(sigmaSRC.*phiSRC)+0.48*sigmaL*phiL;
end
%-------------------------------------------------------------------------

function [data]=IRR(temp,sza)

global OScal

% calculates irradiance in the A-band (pixels 1215:1238), and its error, as
% seen by OSIRIS. error of each pixel can be assumed independent, hence
% added in quadrature.

a=[temp.data];
scans=size(a,2);
errTemp=[temp.error];

MJD=mean([temp.mjd]);
if MJD>54732
    MJD=54732;
end
OScorr=OScal(:,floor(MJD)-52196); % mjd=52197:54732


flag=[temp.flags];
moon=[temp.mooninFOV];
satSAA=[temp.satinSAA];
flag=flag(1200:1252,:);
if ~isempty(find(flag,1)) || ~isempty(find(moon,1))...
        || ~isempty(find(satSAA,1))
    error('at least one pixel was flagged')
end

for scan=1:scans
    ALT=temp(scan).alt;
    set=a(1200:1252,scan);
    subset=[set(1:14)' set(41:53)'];
    places=[1:14 41:53];

    n=length(subset);
    x=sum(places);
    y=sum(subset);
    xy=sum(places.*subset);
    x2=sum(places.^2);

    m=(n*xy-x*y)/(n*x2-x^2);
    b=(y*x2-x*xy)/(n*x2-x^2);

    line=m*(1:53)+b;

    f=0.0013*exp(0.1157*ALT);
    Tband=exp(sec(sza*pi/180)*log(0.95))* 0.95;
    percent=1-(1-Tband)/(1+1/f);
```

```
        final=set-percent*line';

        errBkgd=0.05*sum(percent*line)/sum(final);

        if sum(final(15:38))<0 % reject where absorbtion is observed
            data(1,scan)=0;
            data(2,scan)=0;
        else
            data(1,scan)=sum(final(15:38).*OScorr)*0.4049*4*pi; % dlamda/dp, sr
            sqERR=(errTemp(1215:1238,scan).*OScorr*0.4049*4*pi).^2;
            data(2,scan)=sqrt(sum(sqERR)+(errBkgd*data(1,scan))^2);
        end
end
%--------------------------------------------------------------------------

function [O,N2,O2,H,T,O3]=MSIS(scan)

[year,month,day,hour,minute,secs]=mjd2utc(mean([scan.mjd]));
MJD=fix(mean([scan.mjd]));
DOY=MJD-utc2mjd(1,1,year,0,0,0,0)+1;

if month==day
%      just trying to use everything I've declared. yipee.
end

yearANDday=rem(year,100)*1000+DOY;
LAT=round(mean([scan.lat]));
LON=round(mean([scan.lon]));
UT=hour*3600+minute*60+secs;

[ap,f107A,f107]=APFcalc(year,DOY,hour);
theInput=[yearANDday LAT LON UT f107A f107];

fid=fopen('theIN.txt','w');
fprintf(fid,'%5g %4g %4g %6g %12g %12g',theInput);
fclose(fid);

fid=fopen('theAP.txt','w');
fprintf(fid,'%7g %7g %7g %7g %7g %7g %7g',ap);
fclose(fid);

system('msis00.exe');

fid=fopen('theOUT.txt');
C2=textscan(fid,'%f %f %f %f %f');
O=C2{1};
N2=C2{2};
O2=C2{3};
H=C2{4};
T=C2{5};
fclose(fid);

O3=[1.0000E+03 1.0000E+04 1.0000E+05 1.0000E+06 1.0000E+07 1.0000E+08...
    1.0000E+09 1.0000E+10 3.0000E+10 9.0000E+10 1.0000E+11 1.3124E+11...
    1.6432E+11 1.9428E+11 2.4816E+11 3.5000E+11 4.7184E+11 7.5572E+11...
    1.0937E+12 1.6178E+12 2.1000E+12 2.6428E+12 3.2000E+12 3.7115E+12...
```

```
    4.1000E+12 4.3000E+12 4.3500E+12 4.4000E+12 4.3865E+12 4.2000E+12...
    3.8000E+12 3.2575E+12 2.5237E+12 2.0039E+12 1.5034E+12 1.2874E+12...
    1.0013E+12 8.0020E+11 6.4942E+11 4.7427E+11 4.0000E+11 2.9901E+11...
    2.3234E+11 1.8817E+11 1.5466E+11 1.2000E+11 9.4560E+10 7.5500E+10...
    6.0155E+10 4.8873E+10 5.0817E+10 4.1545E+10 3.6281E+10 2.9560E+10...
    2.3993E+10 2.0832E+10 1.6806E+10 1.4540E+10 1.1652E+10 9.2881E+09...
    7.9687E+09 6.3003E+09 5.3600E+09 4.1696E+09 3.2189E+09 2.7000E+09...
    2.0594E+09 1.7076E+09 1.2766E+09 9.4392E+08 7.6569E+08 5.5024E+08...
    4.3662E+08 3.0528E+08 2.1297E+08 1.6835E+08 1.2007E+08 9.7194E+07...
    7.2878E+07 5.7592E+07 5.1206E+07 4.6779E+07 4.7634E+07 5.4148E+07...
    6.4616E+07 7.2330E+07 8.2645E+07 8.5863E+07 8.3951E+07 7.6666E+07...
    6.9768E+07 5.7727E+07 4.9288E+07 3.7008E+07 2.6203E+07 2.0211E+07...
    1.3131E+07 9.5900E+06 5.7286E+06 3.2133E+06 2.0878E+06 1.7429E+06...
    1.0825E+06 6.4050E+05 3.3903E+05 2.0000E+05 1.2037E+05 6.7100E+04...
    3.7140E+04 1.7460E+04 1.0000E+04 zeros(1,30)]';


function [apOUT,f107AOUT,f107OUT]=APFcalc(year,day,hour)

fid=fopen(['AP F107 data/' num2str(year) '.txt']);
try
    C=textscan(fid,'%71c');
    x=char(C{1});

    place=0;
    q=0;
    AP=[];
    for j=day-90:day
        place=place+1;
        if j>day-4
            q=q+1;
        end
        if j<1
            if or(year-1==2000,year-1==2004)
                jj=j+366;
            else
                jj=j+365;
            end
            POOP=fopen(['AP F107 data/' num2str(year-1) '.txt']);
            C=textscan(POOP,'%71c');
            fclose(POOP);
            y=char(C{1});

            f107(place,1)=str2double(y(jj,66:70));
            if j>day-4
                ap(q,1:4)=[y(jj,32:34) ' '];
                ap(q,5:8)=[y(jj,35:37) ' '];
                ap(q,9:12)=[y(jj,38:40) ' '];
                ap(q,13:16)=[y(jj,41:43) ' '];
                ap(q,17:20)=[y(jj,44:46) ' '];
                ap(q,21:24)=[y(jj,47:49) ' '];
                ap(q,25:28)=[y(jj,50:52) ' '];
                ap(q,29:32)=[y(jj,53:55) ' '];
                ap(q,33:36)=[y(jj,56:58) ' '];
            end
        else
```

```
                     f107(place,1)=str2double(x(j,66:70));
                     if j>day-4
                         ap(q,1:4)=[x(j,32:34) ' '];
                         ap(q,5:8)=[x(j,35:37) ' '];
                         ap(q,9:12)=[x(j,38:40) ' '];
                         ap(q,13:16)=[x(j,41:43) ' '];
                         ap(q,17:20)=[x(j,44:46) ' '];
                         ap(q,21:24)=[x(j,47:49) ' '];
                         ap(q,25:28)=[x(j,50:52) ' '];
                         ap(q,29:32)=[x(j,53:55) ' '];
                         ap(q,33:36)=[x(j,56:58) ' '];
                     end
                 end

                 if j>day-4
                     apt=strread(ap(q,:),'%f')';
                     AP(q,:)=apt(1:8);
                     APD(q,1)=round(mean(AP(q,:))*10)/10;
                 end
             end

             apT=[AP(1,:) AP(2,:) AP(3,:) AP(4,:)];
             first=24+fix(hour/3)+1;

             apOUT=[APD(4) apT(first) apT(first-1) apT(first-2) apT(first-3)...
                 round(mean(apT(first-11:first-4))*10)/10 ...
                 round(mean(apT(first-19:first-12))*10)/10];
             f107AOUT=mean(f107(1:length(f107)-1));
             f107OUT=f107(length(f107)-1);

             fclose(fid);
catch
             fclose(fid);
             error('MSIS error')
end
%------------------------------------------------------------------------

function [data]=O2retrieval(SZA,O2,O3,N2,H,T,x,y,err,Berr)

global Dalt DaltOE Lt J3 J3t gAt gBt gA gB

O2r=1;
MINalt=95;
MAXalt=ceil(max(x));

xx=x(and(x>MINalt,x<=MAXalt));
Y=y(and(x>MINalt,x<=MAXalt))';
ERR=err(and(x>MINalt,x<=MAXalt))';
alts=[xx MAXalt:140];

Dalt=length(alts);
DaltOE=length(xx);

O2above=O2(MAXalt+1:141);
J3=[];
J3(1:Dalt,1)=J3t;
```

```
gA=[];
gB=[];
for j=1:length(alts)
    if round(alts(j))<=81
        gA(j,1)=gAt(round(alts(j)),round(SZA));
        gB(j,1)=gBt(round(alts(j)),round(SZA));
    else
        gA(j,1)=gAt(81,round(SZA));
        gB(j,1)=gBt(81,round(SZA));
    end
end

O3=[spline(MINalt:MAXalt,O3(MINalt+1:MAXalt+1),xx)'; O3(MAXalt+1:141)];
N2=[spline(MINalt:MAXalt,N2(MINalt+1:MAXalt+1),xx)'; N2(MAXalt+1:141)];
H=[spline(MINalt:MAXalt,H(MINalt+1:MAXalt+1),xx)'; H(MAXalt+1:141)];
T=[spline(MINalt:MAXalt,T(MINalt+1:MAXalt+1),xx)'; T(MAXalt+1:141)];

X=spline(MINalt:MAXalt,O2(MINalt+1:MAXalt+1),xx)';

Lt=2*path_lengths(alts);

Sy=diag(ERR.^2);
Sx=zeros(DaltOE);
beta=0.95;
Xerr=Berr;
for j=1:DaltOE
    for k=1:DaltOE
        % variances between levels are correlated
        Sx(j,k)=beta^(2*abs(j-k))*(Xerr*X(DaltOE))^2;
    end
end

X=log(X);
Xo=X;
Y=log(Y);

TOL=0.001;
iter=0;
pd=1;
K=zeros(DaltOE);

% solve stuff
while pd>TOL

    iter=iter+1;
    Xn=X;

    if iter==500
        error('O2 retrieval') % not converging.  no point, sucka.
    end

    % weighting function K, calculated numerically at first iteration
    if iter==1
        for m=0:DaltOE  % 0 run for Yn undisturbed by X
            Q=Xn;
```

174

```
            if m
                Q(m)=Q(m)*1.05; % disturb O by 5% at each height
                dQ=Q(m)-Xn(m);
            end
            Z=log(Forward_Model(N2,exp(Q),H,T,O3,SZA,O2above,O2r));

            if ~m
                Yn=Z; % when m=0 the model is run with no disturbance in X
            else
                dZ=Z-Yn;
                K(m,:)=(dZ/dQ)';
            end
        end
    else
        Yn=log(Forward_Model(N2,exp(X),H,T,O3,SZA,O2above,O2r));
    end

    X=Xo+Sx*K'*inv(K*Sx*K'+Sy)*((Y-Yn)-K*(Xo-Xn));
    if or(imag(X)~=0,isnan(X))
        error('O2 retrieval, kablooee!!')
    end

    for j=1:length(O2above)
        O2above(j)=exp(X(length(X)))*exp(-j/7); % assume 7 km scale height
    end

    pd=mean(abs((X-Xn)./X));
end
X=exp(X);
Y=exp(Y);
Yn=exp(Yn);

checkf=abs(Y-Yn)./Y;
if ~isempty(find(checkf>0.1,1))
    error('O2 retrieval, not a useful solution')
end

data=[X; O2above];
%------------------------------------------------------------------------
%------------------------------------------------------------------------
```

References

Andrews, D. G., J. R. Holton, and C. B. Leovy, Middle Atmosphere Dynamics, *Academic Press, New York*, 1987.

Bates, D. R., and M. Nicolet, The photochemistry of atmospheric water vapor, *J. Geophys. Res., Vol. 55, No. 3*, 301-327, 1950.

Bevilacqua, R., D. Strobel, M. Summers, J. Olivero, and M. Allen, The Seasonal Variation of Water Vapor and Ozone in the Upper Mesosphere: Implications for Vertical Transport and Ozone Photochemistry, *J. Geophys. Res., Vol. 95, D1*, 883-893, 1990.

Brasseur, G. P., and S. Solomon, Aeronomy of the middle atmosphere: chemistry and physics of the stratosphere and mesosphere, *Springer, Dordrecht*, 2005.

Brewer, A. W., J. R. Milford, The Oxford-Kew Ozone Sonde, *Proc. R. Soc. Lond., A, Vol. 256*, 470-495, 1960.

Brian, J., A. Chakir, D. Daumont, J. Malicet and C. Parisse, High-resolution laboratory

absorption cross-section of O_3 temperature effect, *Chem. Phys. Lett., Vol. 213, No. 5,* 610-612, 1993.

Bucholtz, A., W. R. Skinner, V. J. Abreu, and P. B. Hays, The dayglow of the O_2 atmospheric band system, *Planet. Space Sci., Vol. 34, No. 11,* 1031-1035, 1986.

Burch, D. E., and D. A. Gryvnak, Strengths, widths, and shapes of oxygen lines near 13,100 cm^{-1} (7620 Å), *Appl. Opt., Vol. 8, No. 7,* 1493, 1969.

Burrage, M., M. Hagan, W. Skinner, D. Wu, and P. Hays, Long-Term Variability in the Solar Diurnal Tide Observed by HRDI and Simulated by the GSWM, *Geophys. Res. Lett., Vol. 22, No.19,* 2641-2644, 1995.

Campbell, I. M., and C. N. Gray, Rate constants for $O(^3P)$ recombination and association with $N(^4S)$, Chem. Phys. Lett., Vol. 18, No. 4, 607-609, 1973.

Castle K. J., K. M. Kleissas, J. M. Rhinehart, E. S. Hwang, and J. A. Dodd, Vibrational relaxation of $CO_2(v_2)$ by atomic oxygen, *J. Geophys. Res., Vol. 111,* A09303, 2006.

Chapman, S., On ozone and atomic oxygen in the upper atmosphere, *Philosophical Magazine, Vol. 10, No. 64,* 369-383, 1930.

Cornu, A., Sur l'absorption par l'atmosphère des radiations ultra-violettes, *C. R. Acad. Sci. Paris, 88,* 1285–1290, 1879.

Cunnold, D. M., C. R. Gray, D. C. Merritt, Stratospheric Aerosol Layer Detection, *J.*

Geophys. Res., Vol. 78, No. 6, 920-931, 1973.

Daumont, D., J. Brion, J. Charbonnier, and J. Malicet, Ozone UV spectroscopy I: Absorption cross-sections at room temperature, *J. Atmos. Chem., Vol. 15, No. 2*, 145-155, 1992.

Degenstein, D. A., R. L. Gattinger, N. D. Lloyd, A. E. Bourassa, J. T. Wiensz, and E. J. Llewellyn, Observations of an Extended Mesospheric Tertiary Ozone Peak, *J. Atm. Solar-Terr. Phys., Vol. 67, No. 5*, 1395-1402, 2005.

Dobson, G. M. B., 40 Years of Research on Atmospheric Ozone at Oxford – A History, *Appl. Opt., Vol. 7, No. 3*, 387, 1968.

Dobson, G. M. B., and D.N. Harrison, Measurements of the amount of ozone in the Earth's atmosphere and its relation to other geophysical conditions, *Proc. R. Soc. Lond., A, Vol. 110*, 660-693, 1926.

Evans, W. F. J., E. J. Llewellyn, Atomic-Hydrogen Concentrations in Mesosphere and Hydroxyl Emissions, *J. Geophys. Res., Vol. 78, No. 1*, 323-326, 1973.

Fabry, C., and H. Buisson, A study of the ultraviolet extremity of the solar spectrum, *Journal De Physique et le Radium, Vol. 2*, 197-226, 1921.

Frisk, U., M. Hagstrom, J. Ala-Laurinaho, S. Andersson, J. C. Berges, J. P. Chabaud, M. Dahlgren, A. Emrich, H. G. Floren, G. Florin, M. Fredrixon, T. Gaier, R. Haas, T. Hirvonen, A. Hjalmarsson, B. Jakobsson, P. Jukkala, P. S. Kildal, E. Kollberg, J. Lassing,

A. Lecacheux, P. Lehikoinen, A. Lehto, J. Mallat, C. Marty, D. Michet, J. Narbonne, M. Nexon, M. Olberg, A. O. H. Olofsson, G. Olofsson, A. Origne, M. Petersson, P. Piironen, R. Pons, D. Pouliquen, I. Ristorcelli, C. Rosolen, G. Rouaix, A. V. Raisanen, G. Serra, F. Sjoberg, L. Stenmark, S. Torchinsky, J. Tuovinen, C. Ullberg, E. Vinterhav, N. Wadefalk, H. Zirath, P. Zimmermann, and R. Zimmermann, The Odin satellite I. Radiometer design and test, *Astronomy and Astrophysics, 402*, L27–L34, 2003.
Geophys. Res. Lett., Vol. 10, No. 4, 245-248, 1983.

Gadsden, M., Noctilucent clouds, *Springer, Berlin*, 1989.

Goody, R.M., and Y.L. Yung, Atmospheric radiation: theoretical basis, *Oxford University Press, New York*, 1989.

Green, J. G., J. Shi, and J. R. Barker, Photochemical kinetics of vibrationally excited ozone produced in the 248 nm photolysis of O_2/O_3 mixtures, *J. Phys. Chem., Vol. 104, No. 26*, 6218-6226, 2000.

Gruzdev, A. N., and G. P. Brasseur, Long-term changes in the mesosphere calculated by a two-dimensional model, *J. Geophys. Res., Vol. 110, D3*, D03304, 2005.

Haley, C. S., and C. E. Sioris, OS Level 0 → 1 Processing and Error Approximation, *OSIRIS internal report, York University, Toronto*, 2001.

Haley, C. S., S. M. Brohede, C. E. Sioris, E. Griffioen, D. P. Murtagh, I. C. McDade, P. Eriksson, E. J. Llewellyn, A. Bazureau, and F. Goutail, Retrieval of stratospheric O_3 and

NO$_2$ profiles from Odin Optical Spectrograph and Infrared Imager System (OSIRIS) limb-scattered sunlight measurements, *J. Geophys. Res., Vol. 109*, D16303, 2004.

Haley, C. S., Retrieval of Stratospheric Ozone and Nitrogen Dioxide Profiles From Odin Optical Spectrograph and Infrared Imager System (OSIRIS) Limb-Scattered Sunlight Measurements, *Ph. D. Thesis, York University, Toronto*, 2008.

Hartley, W. N., On the Probable Absorption of the Solar Ray by Atmospheric Ozone, *Chem. News, Vol. 42*, 268, 1880.

Hays, P., V. Abreu, M. Dobbs, D. Gell, H. Grassl, and W. Skinner, The High-Resolution Doppler Imager on the Upper Atmosphere Research Satellite, *J. Geophys. Res., Vol. 98, D6*, 10713-10723, 1993.

Heath, D. F., A. J. Krueger, H. R. Roeder, and B. D. Henderson, The solar backscatter ultraviolet and total ozone mapping spectrometer (SBUV/TOMS) for Nimbus G, *Optical Engineering, 14*, 323-331, 1975.

Hedin, A. E., Extension of the MSIS Thermosphere Model into the Middle and Lower Atmosphere, *J. Geophys. Res., Vol. 96, A2*, 1159-1172, 1991.

Hedin, A. E., MSIS-86 Thermospheric Model, *J. Geophys. Res., Vol. 92, A5*, 4649-4662, 1987.

Heller, J., A. Christensen, J. Yee, and W. Sharp, Mesospheric Temperature Inferred from Daytime Observation of the O2 Atmospheric (0, 0) Band System, *J. Geophys. Res., Vol.*

96, A11, 19,499-19,505, 1991.

Herzberg, G., Molecular Spectra and Molecular Structure: I. Spectra of Diatomic Molecules, *Van Nostrand Company, New York,* 1950.

Hocke, K., Phase estimation with the Lomb-Scargle periodogram method, *Ann. Geophys., Vol. 16, No. 3,* 356-358, 1998.

Holton, J. R., The role of gravity-wave induced drag and diffusion in the momentum budget of the mesosphere, *J. Atmos. Sci., Vol. 39, No. 4,* 791-799, 1982.

Keating, G. M., M. C. Pitts, and D. F. Young, Ozone reference models for the middle atmosphere, *Adv. Space Res., Vol. 10, No. 12,* 317-355, 1990.

Kernahan, J. A., and P. H. L. Pang, Experimental Determination of Absolute A Coefficients for Forbidden Atomic Oxygen Lines, *Can. J. Phys. Vol. 53, No. 5,* 455-458 , 1975.

Khabibrakhmanov, I. K., D. A. Degenstein, and E. J. Llewellyn, Mesospheric ozone: Determination from orbit with the OSIRIS instrument on Odin, *Can J. Phys., Vol. 80, No. 4,* 493-504, 2002.

Kyrola, E, J. Tamminen, G. W. Leppelmeier , V. Sofieva, S. Hassinen, J. L. Bertaux, A. Hauchecorne, F. Dalaudier, C. Cot, O. Korablev, O. Fanton d'Andon, G. Barrot, A. Mangin, B. Theodore, M. Guirlet, F. Etanchaud, P. Snoeij, R. Koopman, L. Saavedra, R. Fraisse, D. Fussen, and F. Vanhellemont, GOMOS on Envisat: an overview, *Adv. Space.*

Res., Vol. 33, 1020–1028, 2004.

Lacoursiere, J., S. A. Meyer, G. W. Faris, T. G. Slanger, B. R. Lewis, and S. T. Gibson, The O(^{1}D) yield from O_2 photodissociation near H Lyman-α (121.6 nm), *J. Chem. Phys., Vol. 110, No. 4*, 1949-1958, 1999.

Lee, L. C., T. G. Slanger, Observations on O(^{1}D → ^{3}P) and O_2($b^1\Sigma$ → $X^3\Sigma$) following O_2 photodissociation, *J. Chem. Phys., Vol. 69, No. 9*, 4053-4060, 1978.

Lindzen, R. S., Turbulence and Stress Owing to Gravity Wave and Tidal Breakdown, *J. Geophys. Res., Vol. 86, C10*, 9707-9714, 1981.

Llewellyn, E. J., and I. C. McDade, A reference model for atomic oxygen in the terrestrial atmosphere, *Adv. Space. Res., Vol. 12, No. 9*, 209-226.

Llewellyn, E. J., and R. L. Gattinger, Estimated OSIRIS UVIS Baffle On-Orbit Performance, *OSIRIS Internal report*, University of Saskatchewan, Saskatoon, 1998.

Llewellyn, E. J., N. D. Lloyd, D. A. Degenstein, R. L. Gattinger, S. V. Petelina, A. E. Bourassa, J. T. Wiensz, E. V. Ivanov, I. C. McDade, B. H. Solheim, J. C. McConnell, C. S. Haley, C. von Savigny, C. E. Sioris, C. A. McLinden, E. Griffioen, J. Kaminski, W. F. J. Evans, E. Puckrin, K. Strong, V. Wehrle, R. H. Hum, D. J. W. Kendall, J. Matsushita, D. P. Murtagh, S. Brohede, J. Stegman, G. Witt, G. Barnes, W. F. Payne, L. Piché, K. Smith, G. Warshaw, D. L. Deslauniers, P. Marchand, E. H. Richardson, R.A. King, I. Wevers, W. McCreath, E. Kyrola, L. Oikarinen, G. W. Leppelmeier, H. Auvinen, G.

Mégie, A. Hauchecorne, F. Lefèvre, J. de La Nöe, P. Ricaud, U. Frisk, F. Sjoberg, F. von Schéele, and L. Nordh, The OSIRIS instrument on the Odin spacecraft, *Can. J. Phys., 82*, 411-422, 2004.

Lopez-Gonzalez, M. J, J. J. Lopez-Moreno, and R. Rodrigo, Altitude profiles of the atmospheric system of O_2 and of the green line emission, *Planet. Space Sci., Vol. 40, No. 6*, 783-795, 1992.

Lopez-Puertas, M. and F. W. Taylor, Non-LTE Radiative Transfer in the Atmosphere, *World Scientific Publishing Co., Singapore*, 2001.

Lopez-Puertas, M., G. Zaragoza, M. Lopez-Valverde, and F. Taylor, Non local thermodynamic equilibrium (LTE) atmospheric limb emission at 4.6 µm 1. An update of the CO_2 non-LTE radiative transfer model, *J. Geophys. Res., Vol. 103, D7*, 8499-8513, 1998.

Lossow, S., J. Urban, J. Gumbel, P. Eriksson, and D. Murtagh, Observations of the mesospheric semi-annual oscillation (MSAO) in water vapour by Odin/SMR, *Atmos. Chem. Phys., Vol. 8*, 6257-6540, 2008.

Malicet, J., D. Daumont, J. Charbonnier, C. Parisse, A. Chakir, and J. Brion, Ozone UV spectroscopy II: Absorption cross-sections and temperature dependence, *J. Atmos. Chem., Vol. 21, No. 3*, 263-273, 1995.

Marsh, D., A. Smith, and E. Noble, Mesospheric ozone response to changes in water

vapor, *J. Geophys. Res., Vol. 108, D3*, 4109, 2003.

Marsh, D. R., W. R. Skinner, A. R. Marshall, P. B. Hays, D. A. Ortland, and J. H. Yee, High Resolution Doppler Imager observations of ozone in the mesosphere and lower thermosphere, *J. Geophys. Res., Vol. 107, D19*, 4390, 2002.

Marshall, B. T., L. L. Gordley, and D. A. Chu, BANDPAK: algorithms for modeling broadband transmission and radiance, *J. Quant. Spectrosc. Radiat. Transfer, Vol. 52, No. 5*, 581-599, 1994.

McClatchey, R.A., W. S. Benedict, S. A. Clough, D. E. Burch, R. F. Calfee, K. Fox, L. S Rothman, and J. S. Garing, ARCRL atmospheric absorption line parameters compilation, *environmental research papers, National Technical Information Service, Virginia, No. 434*, AFCRL-TR-73-0096, 1973.

McCormick, M. P., J.M. Zawodny, R. E. Veiga, J. C. Larson, and P. H. Wang, An overview of SAGE-I and SAGE-II ozone measurements, *Planet. Space Sci., Vol. 37, No. 12*, 1567-1586, 1989.

McDade, I. C., D. P. Murtagh, R. G. H. Greer, P. H. G. Dickinson, G. Witt, J. Stegman, E. J. Llewellyn, L. Thomas, and D. B. Jenkins, ETON 2: Quenching parameters for the proposed precursors of $O_2(b^1\Sigma_g^+)$ and $O(^1S)$ in the terrestrial nightglow, *Planet. Spuce Ser., Vol. 34, No. 9*, 789-800, 1986.

McElroy, T. C., C. R. Nowlan, J. R. Drummond, P. F. Bernath, D. V. Barton, D. G.

Dufour, C. Midwinter, R. B. Hall, A. Ogyu, A. Ullberg, D. I. Wardle, J. Kar, J. Zou, F. Nichitiu, C. D. Boone, Kaley A. Walker, and N. Rowlands, The ACE-MAESTRO instrument on SCISAT: description, performance, and preliminary results, *Appl. Opt., Vol. 46, No. 20,* 2007.

McLandress, C., The seasonal variation of the propagating diurnal tide in the mesosphere and lower thermosphere. Part I: the role of tidal heating and zonal mean winds, *J. Atmos. Sci., Vol. 59,* 907–922, 2002.

Mlynczak M. G., B. T. Marshall, F. J. Martin-Torres, J. M. Russell III, R. E. Thompson, E. E. Remsberg, L. L. Gordley, Sounding of the Atmosphere using Broadband Emission Radiometry observations of daytime mesospheric $O_2(^1\Delta)$ 1.27 µm emission and derivation of ozone, atomic oxygen, and solar and chemical energy deposition rates, *J. Geophys. Res., Vol. 112,* D15306, 2007.

Mlynczak, M. G., An Evaluation of the Rate of Absorption of Solar-Radiation in the $O_2(X^3\Sigma_g - b^1\Sigma_g)$ Transition, *Geophys. Res. Lett., Vol. 20, No. 14,* 1439-1442, 1993.

Mlynczak, M. G., and S. Solomon, A detailed evaluation of the heating efficiency in the middle atmosphere, *J. Geophys. Res., Vol. 98, D6,* 10517-10541, 1993.

Mlynczak, M. G., Energetics of the Mesosphere and Lower Thermosphere and the SABER Experiment, *Adv. Space Res. Vol. 20, No. 6,* 1177-1183, 1997.

Mlynczak, M., R. Garcia, R. Roble, and M. Hagan, Solar energy deposition rates in the

mesosphere derived from airglow measurements: Implications for the ozone model deficit problem, *J. Geophys. Res., Vol. 105, D13*, 17527-17538, 2000.

Murtagh, D., U. Frisk, F. Merino, M. Ridal, A. Jonsson, J. Stegman, G. Witt, P. Eriksson, C. Jiménez, G. Megie, J. de la Noë, P. Ricaud, P. Baron, J. R. Pardo, A. Hauchcorne, E. J. Llewellyn, D. A. Degenstein, R. L. Gattinger, N. D. Lloyd, W. F. J. Evans, I. C. McDade, C. S. Haley, C. Sioris, C. von Savigny, B. H. Solheim, J. C. McConnell, K. Strong, E. H. Richardson, G. W. Leppelmeier, E. Kyrölä, H. Auvinen, and L. Oikarinen, An overview of the Odin atmospheric mission, *Can J. Phys., 80, No. 4*, 309-319, 2002.

Nappo, C. J., An introduction to atmospheric gravity waves, *Academic Press, San Diego*, 2002.

Nicholls, R. W., Franck-Condon factors to high vibrational quantum numbers V: O_2 band systems, *J. Res. NBS, Vol. A 69, No. 4*, 369, 1965.

Nishida, S., F. Taketani, K. Takahashi, and Y. Matsumi, Quantum yield for $O(^1D)$ production from ozone photolysis in the wavelength range of 193-225 nm, *J. Phys. Chem., Vol. 108, No. 14*, 2710-2714, 2004.

Noxon, J. F., Twilight Enhancement in $O_2(b^1\Sigma_g)$ Airglow Emission, *J. Geophys. Res. Vol. 80, No. 10*, 1370-1373, 1975.

Petelina, S. V., E. J. Llewellyn, D. A. Degenstein, N. D. Lloyd, R. L. Gattinger, C. S. Haley, C. von Savigny, E. Griffioen, I. C. McDade, W. F. J. Evans, D. P. Murtagh, and J.

de La Noe, Comparison of the Odin/OSIRIS stratospheric ozone profiles with coincident POAM III and ozonesonde measurements, *Geophys. Res. Lett., Vol. 31*, L07104, 2004.

Petelina, S. V., E. J. Llewellyn, D. A. Degenstein, Properties of Polar Mesospheric Clouds measured by Odin/OSIRIS in the Northern Hemisphere in 2002-2005, *Can. J. Phys., Vol. 85*, 1143-1158, 2007.

Press, W. H., and Rybicki, G. B., Fast Algorithm for Spectral Analysis of Unevenly Sampled Data, *Astrophys. J., Vol. 338*, 227-280, 1989.

Ratnam, M. V., C. M. Shen, W. N. Chen, and J. B. Nee, Study on oxygen atmospheric band dayglow: global and seasonal variations deduced from high-resolution Doppler imager observations, *J. Atm. Solar-Terr. Phys., Vol. 66*, 209-218, 2004.

Reddmann, T, and R. Uhl, The H Lyman-α actinic flux in the middle atmosphere, *Atmos. Chem. Phys., Vol. 3*, 225-231, 2003.

Regener, V. H., On a Sensitive Method for the Recording of Atmospheric Ozone, *J. Geophys. Res., Vol. 65, No. 12*, 3975-3977, 1960.

Remsber, E., J. M. Russell, J. C. Gille, L. L. Gordley, P. L. Bailey, W. G. Planet, and J. E. Harries, The Validation of NIMBUS 7 LIMS Measurements of Ozone, *J. Geophys. Res., Vol. 89, D4*, 5161-5178, 1984.

Roble R. G., Energetics of the mesosphere and thermosphere. In: R. M. Johnson and T. L. Killeen, The Upper Atmosphere and Lower Thermosphere: A Review of Experiment

and Theory, *American Geophysical Union, Washington D. C.*, 1995.

Rodgers, C. D., Inverse methods for atmospheric sounding, *World Scientific Publishing Co., Singapore*, 2008.

Rong P. P., J. M. Russell III, M. G. Mlynczak, E. E. Remsberg, B. T. Marshall, L. L. Gordley, M. Lopez-Puertas, Validation of Thermosphere Ionosphere Mesosphere Energetics and Dynamics/Sounding of the Atmosphere using Broadband Emission Radiometry (TIMED/SABER) v1.07 ozone at 9.6 μm in altitude range 15–70 km, *J. Geophys. Res., Vol. 114*, D04306, 2009.

Rothman, L. S., D. Jacquemarta, A. Barbeb, D. Chris Bennerc, M. Birkd, L. R. Browne, M. R. Carleerf, C. Chackerian Jr., K. Chancea, L. H. Couderth, V. Danai, V. M. Devic, J. M. Flaudh, R. R. Gamachej, A. Goldmank, J. M. Hartmannh, K. W. Jucks, A. G. Makim, J. Y. Mandini, S. T. Massien, J. Orphalh, A. Perrinh, C. P. Rinslando, M. A. H. Smitho, J. Tennysonp, R. N. Tolchenovp, R. A. Tothe, J. Vander Auweraf, P. Varanasiq, and G. Wagnerd, The HITRAN 2004 molecular spectroscopic database, *J. Quant. Spectrosc. Radiat. Transfer, Vol. 96*, 139–204, 2005.

Rothman, L. S., I. E. Gordon, A. Barbe, D. Chris Benner, P. F. Bernath, M. Birk, V. Boudon, L. R. Brown, A. Campargue, J. P. Champion, K. Chance, L. H. Coudert, V. Danaj, V. M. Devi, S. Fally, J. M. Flaud, R. R. Gamache, A. Goldmanm, D. Jacquemart, I. Kleiner, N. Lacome, W. J. Lafferty, J. Y. Mandin, S. T. Massie, S. N. Mikhailenko, C. E. Miller, N. Moazzen-Ahmadi, O. V. Naumenko, A. V. Nikitin, J. Orphal, V. I.

Perevalov, A. Perrin, A. Predoi-Cross, C. P. Rinsland, M. Rotger, M. Simeckova, M. A. H. Smith, K. Sung, S. A. Tashkun, J. Tennyson, R. A. Toth, A. C. Vandaele, and J. Vander Auwera, The HITRAN 2008 molecular spectroscopic database, *J. Quant. Spectrosc. Radiat. Transfer, Vol. 110*, 533-572, 2009.

Rubin, M. B., The History of Ozone. The Schonbein Period, 1839-1868, *Bull. Hist. Chem., Vol. 26, No. 1*, 2001.

Russell J. P., W. E. Ward, R. P. Lowe, R. G. Roble, G. G. Shepherd, B. Solheim, Atomic oxygen profiles (80 to 115 km) derived from Wind Imaging Interferometer/Upper Atmospheric Research Satellite measurements of the hydroxyl and greenline airglow: Local time–latitude dependence, *J. Geophys. Res., Vol. 110*, D15305, 2005.

Rusch, D. W., G. H. Mount, C. A. Barth, R. J. Thomas, and M. T. Callan, Solar Mesosphere Explorer Ultraviolet Spectrometer Measurements of Ozone in the 1.0-0.1 mbar Region, *J. Geophys. Res., Vol. 89*, 11,677-11,687, 1984.

Sander, S. P., R. R. Fried, A. R. Ravishankara, D. M. Golden, C. E. Kolb, M. J. Kurylo, M. J. Molina, G. K. Moortgat, H. Keller-Rudek, B. J. Finlayson-Pitts, P. H. Wine, R. E. Huie, and V. L. Orkin, Chemical Kinetics and Photochemical Data for Use in Atmospheric Studies Evaluation Number 15, *JPL Publication, 06-2*, 2006.

Schonbein, C. F., On the Odour Accompanying Electricity, and on the Probability of Its Dependence on the Presence of a New Substrate, *Philos. Trans. R. Soc. Lond., Vol. 4*, 226, 1840.

Shepherd, G. G., G. Thuillier, B. H. Solheim, S. Chandra, L. L. Cogger, M. L. Duboin, W. F. J. Evans, R. L. Gattinger, W. A. Gault, M. Herse, A. Hauchecorne, C. Lathuilliere, E. J. Llewellyn, R. P. Lowe, H. Teitelbaum, and F. Vial, Longitudinal structure in atomic oxygen concentrations observed with WINDII on UARS, *Geophys. Res. Lett., Vol. 20, No. 12*, 1303-1306, 1993.

Shepherd, T. G., The Canadian MAM project, *CMOS Bulletin, Vol. 23*, 3-12, 1995.

Sica, R. J., Inferring Middle-Atmospheric Ozone Height Profiles from Ground-Based Measurements of Molecular-Oxygen Emission Rates. 1: Model Description and Sensitivity to Inputs, *Can. J. Phys., Vol. 69, No. 8*, 1069-1075, 1991.

Sica, R.J., Inferring middle atmospheric ozone height profiles from ground-based measurements of molecular-oxygen emission rates. 3: Can twilight measurements of the atmospheric band be used to retrieve an ozone density profile, *J. Geophys. Res., Vol. 98, D1*, 1057-1067, 1993.

Siskind, D. E., G. E. Nedoluha, M. E. Summers, and J. M. Russell III, A search for an anticorrelation between H_2O and O_3 in the lower mesosphere, *J. Geophys. Res., Vol. 107 D20*, 4435, 2002.

Skinner, W. R., and P. B. Hays, Brightness of the O_2 Atmospheric Bands in the Daytime Thermosphere, *Planet. Space Sci., Vol. 33, No. 1*, 17-22, 1985.

Slanger, T.G, and G. Black, $O(^1S)$ in the lower thermosphere Chapman vs. Barth, *Planet.*

Space Sci., Vol. 25, No. 1, 79-88, 1977.

Slanger, T. G., D. L. Huestis, D. E. Osterbrock, and J. P. Fulbright, The isotopic oxygen nightglow as viewed from Mauna Kea, *Science, Vol. 277*, 1485-1488, 1997.

Smith, A. K., Physics and chemistry of the mesopause region, *Journal of Atmospheric and Solar-Terrestrial Physics, Vol. 66, No. 10*, 839-857, 2004.

Smith, F., III, and C. Smith, Numerical Evaluation of Chapman's Grazing Incidence Integral ch(x, χ), *J. Geophys. Res., Vol. 77, No. 19*, 3592-3597, 1972.

Sparn, T. P., G. Rottman, T. N. Woods, B. D. Boyle, R. Kohnert, S. Ryan, R. Davis, R. Fulton, and William Ochs, The SORCE spacecraft and operations, *Solar Phys., Vol. 230, No. 1*, 71-89, 2005.

Takahashi K., S. Hayashi, Y. Matsumi, N. Taniguchi, and S. Hayashida, Quantum yields of O(^{1}D) formation in the photolysis of ozone between 230 and 308 nm, *J. Geophys. Res., Vol. 107, D20*, 4440, 2002.

Talukdar, R., C. Longfellow, M. Gilles, and A. Ravishankara, Quantum Yields of O(^{1}D) in the Photolysis of Ozone Between 289 and 329 nm as a Function of Temperature, *Geophys. Res. Lett., Vol. 25, No. 2*, 143-146, 1998.

Thomas, R. J., C. A. Barth, G. J. Rottman, D. W. Rusch, G. H. Mount, G. M. Lawrence, R. W. Sanders, G. E. Thomas, and L. E. Clemens, Ozone density distribution in the mesosphere (50-90 km) measured by the SME limb scanning near infrared spectrometer,

J. Geophys. Res., Vol. 10, No. 4, 245-248, 1983.

Thomas, R., Seasonal Ozone Variations in the Upper Mesosphere, *J. Geophys. Res., Vol. 95, D6,* 7395-7401, 1990.

Torr, M. R., B. Y. Welsh, D. G. Torr, The O_2 Atmospheric Dayglow in the Thermosphere Venkat Ratnam, M., C. M. Shen, W. N. Chen, and J. B. Nee, Study on oxygen atmospheric band dayglow: global and seasonal variations deduced from high-resolution Doppler imager observations, *Journal of Atmospheric and Solar-Terrestrial Physics, Vol. 66, No. 3,* 209-218, 2004.

von Savigny, C., C. S. Haley, C. E. Sioris, I. C. McDade, E. J. Llewellyn, D. Degenstein, W. F. J. Evans, R. L. Gattinger, E. Griffioen, E. Kyrola, N. D. Lloyd, J. C. McConnell, C. A. McLinden, G. Megie, D. P. Murtagh, B. Solheim, and K. Strong, Stratospheric ozone profiles retrieved from limb scattered sunlight radiance spectra measured by the OSIRIS instrument on the Odin satellite, *Geophys. Res. Lett., Vol. 30, No. 14,* 1755, 2003.

von Savigny, C., Retrieval of Stratospheric Ozone Density Profiles from OSIRIS Scattered Sunlight Observations, *Ph. D. Thesis, York University, Toronto,* 2002.

Walker, K. A., C. E. Randall, C. R. Trepte, C. D. Boone, and P. F. Bernath, Initial validation comparisons for the Atmospheric Chemistry Experiment (ACE-FTS), *Geophys. Res. Lett., Vol. 32,* L16S04, 2005

Wallace, L., and D. M. Hunten, Dayglow of the Oxygen A Band, *J. Geophys. Res., Vol.*

73, No. 15, 4813-4834, 1968.

Warshaw, G. D., D. L. Desaulniers, and D. Degenstein, Optical design and performance of the Odin UV/Visible spectrograph and infrared imager instrument, *Proc. 12th Annual AIAA/USU Conference on Small Satellites*, 1998.

Wiensz, J. T., Ozone Retrievals from the Oxygen Infrared Channels of the OSIRIS Infrared Imager, *M. Sc. Thesis, University of Saskatchewan, Saskatoon*, 2005.

Xu J., A. K. Smith, W. Yuan, H. L. Liu, Q. Wu, M. G. Mlynczak, and J. M. Russell III, Global structure and long-term variations of zonal mean temperature observed by TIMED/SABER, *J. Geophys. Res., Vol. 112,* D24106, 2007.

Yankovsky, V. A., and R. O. Manuilova, Model of daytime emissions of electronically-vibrationally excited products of O_3 and O_2 photolysis: application to ozone retrieval, *Ann. Geophys., Vol. 24, No. 11*, 2823-2839, 2006.

Yoshino, K., W. H. Parkinson, K. Ito, and T. Matsui, Absolute absorption cross-section measurements of Schumann-Runge continuum of O_2 at 90 and 295 K, *J. Molec. Spectrosc., Vol. 229*, 238-243, 2005.